Modelling the Effect of Step and Roughness Features on Swept Wing Boundary Layer Instabilities

a thesis presented for the degree of

Doctor of Philosophy of Imperial College London

and the

Diploma of Imperial College

by

Emma Cooke

Department of Mathematics

Imperial College

180 Queen's Gate, London SW7 2BZ

August 2020

I, Emma Cooke, certify that this thesis, and the research to which it refers, are the product of my own work, and that any ideas or quotations from the work of other people, published or otherwise, are fully acknowledged in accordance with the standard referencing practices of the discipline.

Signed: _____

Copyright

The copyright of this thesis rests with the author and is made available under a Creative Commons Attribution Non-Commercial No Derivatives licence. Researchers are free to copy, distribute or transmit the thesis on the condition that they attribute it, that they do not use it for commercial purposes and that they do not alter, transform or build upon it. For any reuse or redistribution, researchers must make clear to others the licence terms of this work.

Modelling the Effect of Step and Roughness Features on Swept Wing Boundary Layer Instabilities

Abstract

Destabilisation effects of forward facing steps, backward facing steps and bumps on stationary and travelling crossflow disturbances are investigated computationally for a 40° infinitely swept wing. Step and bump heights range from 18% to 82% of the boundary layer thickness and are located at 3%, 10% and 20% chord. The spectral/hp element solver, Nektar++, is used to compute base flow profiles with an embedded swept wing geometry. Parabolised Stability Equations (PSE) and Linearised Harmonic Navier-Stokes (LHNS) models are used to evaluate growth of convecting instabilities. The presence of surface step features impose an extremely rapidly varying flow field locally, which requires accurate resolution of the perturbed flow field. Derivations of these PSE and LHNS models incorporating the excrescence (PSEh, LHNSh) are elucidated. Unlike the PSE, which suffer from a stream-wise numerical step size restriction, the LHNS are a fully elliptic set of equations which may use an arbitrarily fine grid resolution. Unsurprisingly, the PSE codes fail to capture the effect of abrupt changes in surface geometry introduced by the step features. Results for the LHNS and roughness incorporating LHNSh are given for the varying vertical step and ramped type steps. Comparisons are made between the LHNSh model and direct numerical simulations involving the time-stepping linearised Navier-Stokes solver (NekLNS) in the Nektar++ software framework. Most previous work in the topic area has focused on Tollmien-Schlichting perturbations over two-dimensional flat plate flows or aerofoils, the novelty of this work lies with analysing crossflow instability over a swept wing boundary-layer flow with step features.

PSEh and LHNSh models are tested with convecting Tollmien Schlichting instability over a dimple and randomly distributed roughness on an overall flat plate flow. The dimple case performs very well whereas it is more difficult to obtain converged results with the random roughness case, likely due to large stream-wise velocity gradient changes. A 45° ramped shape roughness is investigated and remarkably good agreement between the LHNSh solution and NekLNS solution is found. Forward facing ramps and steps are found to act as greater amplifiers with increased height, whilst backward facing ramps and steps predict very weak changes in the disturbance development. This is contrary to the wider literature and an argument is made that

backward facing steps and ramps initiate an immediate non-linear interaction which cannot be captured with linear theory. Vertical forward facing step cases also predict greater amplification with increased step height, which is not observed in the backward facing step cases. Again, this is believed to be due to non-linear mode interaction that is immediately triggered by the step. Bump roughness cases agree well qualitatively with experimental work on a 40° swept wing, the AERAST geometry. Good agreement locally to the roughness could not be drawn with the NekLNS solutions, likely due to the presence of strong stream-wise gradients and mesh limitations.

To my Grandad, Robert Edward Cooke. Without whom I wouldn't have made it to Imperial, and certainly wouldn't have had the opportunity to do a PhD. I am forever grateful and indebted.

Acknowledgments

I extend thanks to Airbus Group Central Research and Technology, EPSRC and Imperial College Centre for Doctoral Training in Fluid Dynamics Across Scales for financially supporting this research.

I would like to thank my supervisor Dr. Shahid Mughal for his continued support, patience and many hours of discussion. His technical insight and experience was essential to the completion of this work.

Many thanks to my secondary supervisor Professor Spencer Sherwin for whom his technical advice was essential and his enthusiasm inspiring.

I am extremely grateful to my Airbus supervisors Dr. Richard Ashworth and Dr. Stephen Rolston for a fascinating introduction to the commercial world and their continued up-beat support.

I would then like to express my sincere gratitude to my colleagues and friends at Imperial, Raquel, Ruben, Max and Jordan for providing a fun problem solving environment.

I would also like to extend this gratitude to my Airbus colleagues and friends, Henrique, Richard, Dean and Martin for our many fruitful tea-break discussions. Particularly, for providing physical fitness competition which I found essential for maintaining a healthy state of mind throughout the PhD.

A special thanks goes to my dear friend Alice, who continues to give friendly support, ever constructive advice and always pushes me to improve on everything I do.

I am extremely grateful to my mother and father for always reminding me that the best I can do, is good enough. I especially thank my father for his continual berating

over writing this thesis.

Above all, I thank my boyfriend Sam. Through the peaks and the troughs he has been my rock. Convincing me never to give up and encouraging me in times when the world feels like it is falling apart.

List of figures

List of tables

Contents

CHAPTER 1

Introduction

1.1 Motivation for maintaining Laminar Boundary Layers

Drag reduction is one of the most important objectives in the aircraft manufacturing industry today. An aircraft with lower drag, is not only more economical but also more environmentally friendly, which is inevitably becoming an ever growing global concern. Fuel efficiency can be increased through a number of modifications to the aircraft, such as replacement of aluminium with carbon fibre for allowing stronger, lighter wings to be built, but a major focus is on the construction of a swept laminar flow wing[38].

Viscous effects play a very important role within a thin layer of fluid in the neighbourhood of the surface geometry, as found by Prandtl in 1904[3]. This thin layer of fluid is named a boundary layer. Flows with zero pressure gradient, such as flow over a flat plate, are initially laminar and described by the Blasius solution[86]. However, when traversing downstream, away from the leading edge of the flat plate, an unsteadiness establishes itself within the boundary layer in the form of a so called Tollmien-Schlichting wave. These Tollmien-Schlichting (TS) waves cause the steady Blasius flow to become weakly unsteady and initially have an amplitude too small to cause notable changes in the boundary layer. As they grow downstream these waves increase in amplitude and eventually cause the flow to notably transition from laminar to turbulent[86]. Maintaining a laminar boundary layer and delaying the onset of turbulence over the wing is crucial for minimising fuel consumption. The presence of

turbulence increases shear stress on the surface which in turn increases drag and hence increases fuel consumption. Large aircraft of today feature turbulent boundary layers on the majority of the exposed wetted surface, resulting in viscous drag that is five to ten times larger than a laminar boundary layer[10].

Achieving and maintaining laminar flow on a wing is hindered by surface imperfections which may be present on the wing. These imperfections can act as flow destabilisation sites and may arise from rivets, leading edge to wing box junction tolerances, or even insect contamination. The presence of a roughness, or very localized surface imperfection which occur primarily in the form of steps or bumps, induces a local flow modification which can destabilise pre-existing instabilities within the laminar boundary layer. This promoted destabilisation of the instability leads to earlier transition and can completely eradicate any drag reduction benefit obtained from the laminar flow wing. The size of the typical roughness, or excrescence, in question can range from of ten to two hundred micrometres in depth and up to a few centimetres in length on a wing that is potentially several metres wide and ten times that long.

For design purposes, industry is interested in numerically simulating how disturbances are further destabilised by the presence of such a roughness feature. This can be achieved by direct numerical simulation (DNS) but at huge computational expense. DNS calculations may take days or weeks to run over extensive central processing unit (CPU) resources meaning this is an infeasible option for day to day use within industry. Instead, a rapid tool is required. Currently industry have a fast but semi-empirical tool, the e^N method, for predicting the growth of transition within seconds. However, the tool is based upon Linear Stability Theory (LST), and neglects many crucial non-parallel and non-linear effects in the transition process. Two superior methods, the Parabolised Stability Equations (PSE) and Linearised Navier-Stokes (LHNS) equations, which do encapsulate non-parallelism and some non-linear effects, can replace LST. These have been around for a few decades but only recently has the PSE began to be adopted by industry due to cheaper compute power, with fast CPU processing and increased random access memory (RAM). The LHNS even has the capability to model how a disturbance can be generated within the boundary layer, receptivity. However, due to being rapid computational tool sets, they do not solve for the equation set describing the roughness geometry. The bump is only introduced through the base flow.

The purpose of this work is to develop rapid perturbation prediction tools which better capture the roughness geometry and give more insight into the flow physics around the excrescence locally. A better understanding of the mechanisms at play around a roughness will help with establishing better criteria for design tolerances.

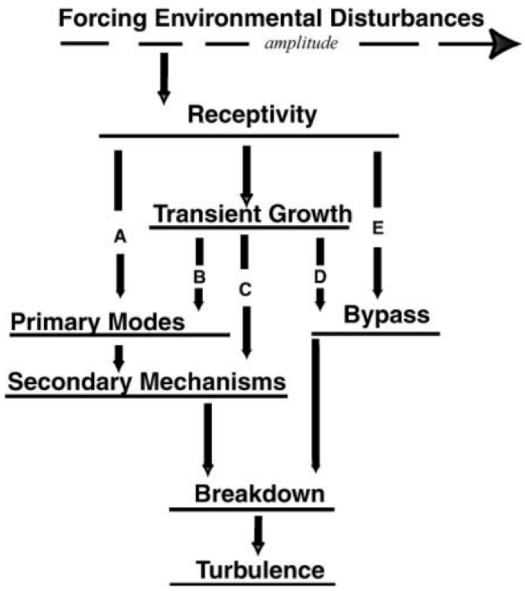

Figure 1.1: Varying transition pathways from laminar to turbulent flow[84]

1.2 Background and state-of-the-art

Instabilities within the boundary layer are influenced greatly by factors both internal and external to the boundary layer. Depending on the intensity of the environmental disturbances, transition may take a variety of routes before assuming the turbulent regime. These pathways usually occur via three main steps: receptivity, instability and breakdown.

Receptivity is the first building block of transition and occurs due to an environmental forcing such as surface roughness, acoustic waves or vorticity from free stream turbulence entering the boundary layer. If the external forcing resonates with natural eigenmodes of the boundary layer then a receptivity mechanism takes place. If the environmental forcing scales are not well matched with the natural boundary layer eigenmodes then these disturbances have a lesser chance of propagating within the boundary layer. Imagine a broadband noise in the free-stream which generates a sea of disturbances, only a few select frequencies may resonate with the natural eigenmodes. The receptivity process provides the essential initial conditions of amplitude, phase and frequency for the break down to turbulent state[73]. As this initial disturbance amplitude increases different instabilities occur depending on varying Reynolds number, sweep, roughness and other factors. The varying pathways are well described by Morkovin and depicted in figure 1.1.

When the disturbance is of a weak amplitude the initial growth of the instability is linear and follows path A of figure 1.1. Since the growth is linear the perturbation

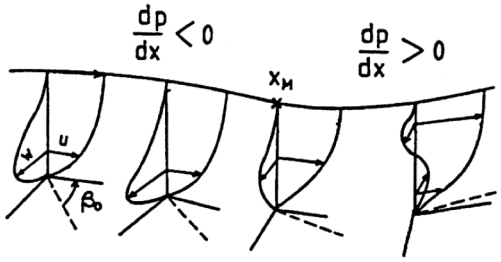

Figure 1.2: Graphic of crossflow by Arnal and Casalis[5]

can be modelled by linear stability theory and grows slowly over a long stream-wise length scale[84]. For two dimensional boundary layers the instability takes the form of a Tollmien-Schlichting (TS) wave and is usually triggered by free-stream acoustic waves or turbulence[55]. Secondary instabilities, arising from primary instabilities, begin to play a role when the amplitude grows in the form of non-linear effects and three dimensional disturbances. This usually occurs when the amplitude of the TS wave is greater than 0.3% to 1% of the free stream velocity U_∞ [56]. For swept wing flow configurations there are varying types of instability which arise: attachment line instability, centrifugal instability and crossflow instability[72]. The first type of instability occurs in the attachment-line boundary layer which can become unstable or contaminated by wing-root turbulence. Generally this type of instability affects swept wings with large leading-edge radii[85]. Centrifugal instabilities arise in the shear flow with the presence of concave surfaces in the form of Gortler Vortices which counter-rotate[40,83]. Crossflow vortices tend to arise on wings with a substantial amount of sweep in regions of strong pressure gradients, see figure 1.2[72]. The crossflow velocity is perpendicular to the direction of the inviscid streamline and exhibits an inflection point, ensuring that the crossflow component vanishes at the wall and at the boundary layer edge, all vortices rotate in the same direction[5]. At the secondary instability stage the disturbance growth is very rapid and breakdown to turbulence quickly ensues, completing pathway A. This is the pathway generally accepted to best model transport flight[74].

Transient growth occurs when two, non-orthogonal, stable modes interact, grow algebraically, and then decay exponentially; depicted by paths B, C and D. This mechanism seems to be highly influenced by stream-wise and wall-normal vorticity. Depending on the amplitude of the initial disturbance, transient growth can lead to span-wise modulations of two-dimensional waves, path B, a direct distortion to the basic state which leads to secondary or sub-critical instabilities, path C, or when the amplitude is large enough that the transient growth will progress directly to breakdown, path D[84]. Transient growth usually occurs in regimes with an increased amount of free-stream turbulence or in regimes with distributed surface roughness[74].

Finally, the receptivity process can immediately induce bypass transition when the

initial disturbance amplitude is extremely strong, pathway E. Although pathways B, C and D are still not completely understood, bypass induced transition tripping remains the most mysterious despite various numerical, computational and analytical studies[102].

For effective generation of TS waves the forcing environmental disturbance needs to resonate with the natural flow oscillations in the boundary layer. This condition must be satisfied for both frequency and wavelength of the perturbation. It has been shown, through application of triple deck theory, that roughness elements in conjunction with acoustic waves trigger TS instabilities by Ruban[78] and Goldstein[35]. Assuming that the stream-wise length scale of the roughness is of the order of the TS wavelength, the flow around the roughness can be described by triple deck theory. They found that the mean flow over the roughness could provide the spatial scale, wavelength, and the acoustic forcing provides the frequency. When the two are proportional, the acoustic wave and the Fourier transform of the roughness element, they can give rise to the generation of a TS wave. Free stream turbulence has also been shown to play a large role by Duck et al.[23]. Here they represented the disturbance field as a superposition of vorticity waves. The boundary layer interacts differently with vorticity waves as they are unable to carry pressure perturbations, contrary to acoustic waves, and so cannot penetrate the boundary layer. With the presence of wall roughness, since wall roughness not only produces perturbations within the boundary layer but also outside, in the upper tier of triple deck theory, non-linear interactions of the steady perturbations in the upper tier with vorticity waves create the necessary resonance conditions for TS wave generation.

Transition prediction schemes used by industry often assume that the transition pathway follows that of path A. Only the linear regime of this pathway is accounted for, under the assumption that flow in the free stream has weak disturbances and the stream-wise linear growth region is large compared to that of the non-linear. Arnal and Casalis[5] state that for flat plate conditions the extent of the linear amplification in the stream-wise direction covers 75% to 85% of the plate, between the leading edge to the point of transition. Comparisons between two cases can only be made when the environmental conditions are similar since receptivity is not captured within the model.[84]

Capturing the receptivity process, free-stream disturbances superimposing the basic state, is crucial to understanding the type of transition pathway activated and therefore the propagation of the instability before breaking down to turbulence.

1.2.1 Tollmien Schlichting Instability

Research is rich in the area of unswept flat plates[100,33,103,64,75,107] and aerofoil geometries[17,94,7] where the boundary layer becomes unstable due to TS waves. TS instability is generally the dominant mechanism for two dimensional flows. TS waves can be generated in the presence of acoustic noise or surface roughness. Already convecting TS waves within the boundary layer can also be further destabilised by surface roughness. Varying step features such as forward facing steps, backward facing steps, dimples and pimples have been simulated, either experimentally or numerically, to study how the presence of the excrescence destabilises a convecting two dimensional perturbation. It remains of strong interest to try and characterise a destabilising step height in order to better understand how severe aircraft manufacturing tolerances are required to be. However, there seems to be quite some variation on this critical characterisation within the literature.

Wang and Gaster[100] looked at the effect of varying forward facing and backward facing step heights on transition location by hot wire anemometry on a flat plate. They found that increasing step height / depth caused earlier transition onset for the backward facing step than for the forward facing step. Wörner et al.[103] looked at direct numerical simulation of bumps with sharp and rounded corners at varying heights, between 37% to 97% of the boundary layer, and widths, ranging between half and double the TS wavelength introduced. They observed that sharper corners produce a greater destabilisation than more rounded corners, the width of the bump does not impact the flow nearly as much as increasing the height and even observed a stabilisation from their forward facing step case. Park and Park[64] decided to model bumps and dimples numerically using some of the tool sets, PSE, which will be used in this work. They computed baseflows over two dimensional smooth symmetric humps by solving the time iterative parabolised Navier-Stokes equations, involving a splitting of the stream-wise flux vector[92]. They found that the influence of a dimple instead of a bump can be just as impacting on the flow as a bump. They displayed linear PSE results for attached and separated flows but only showcased results for non-linear PSE computations for the attached cases. This raises an interesting question as to if the non-linear PSE are able to converge in the presence of a laminar separation bubble.

Xu et al.[106] looked at staggering forward facing steps between 3% to 30% of the boundary layer thickness, with a width length scale comparable to the TS wavelength. They found that smooth steps are considered safe, exhibiting the same growth as that of a flat plate boundary layer, as long as the convecting TS wave has a high frequency and the step is rather small. When the step is larger than 20% of the boundary layer they observed a destabilising effect. Sharp steps were shown to be

much more dangerous, which they attributed to the presence of a separation bubble, to be discussed in section 1.2.3. Later, Xu et al.[107] looked at two dimensional and three dimensional dimples cases which ranged from 40% to 60% of the boundary layer. They discovered that the presence of a two dimensional dimple is much more degrading to the TS wave stability than a three dimensional dimple and credit the destabilisation mechanism to the inflectional instability present from the separated shear layer.

Sumariva and Hein[89] have looked computationally at the effect of smooth and sharp corners on bump shaped roughness of a height 35% of the boundary layer thickness. They apply a similar approach to that presented in this work but section off the computational domain into areas without roughness, which are solved with PSE, and an area with the roughness, which are solved with what they coin the adaptive harmonic linearised Navier-Stokes equations (AHLNS). They found that the PSE were unable to be used for such sharp cornered geometries, even with 'smooth' corners, as this introduces large stream-wise gradient changes which the PSE are unable to converge with. They were however, able to gain good agreement from the AHLNS code with experimental results when comparing transition indicators, such as N-factors, and found the sharp cornered bump to be much more destabilising. Sumariva and Hein[89] also studied the effect of varying the width of the hump and found that this had a more significant effect than that found by Wörner et al.[103], but they are both agreed that the height of the bump plays a greater role for destabilisation than the width.

Costantini et al.[17] began looking at a span-wise invariant wing geometry featuring a step that ranged to 1.45% of the boundary layer thickness. They found a correlation between increasing the Reynolds number at the step location and the relative step height (compared with the boundary layer thickness), causing a forward movement in transition location. They observed a movement in transition even with their smallest step height. Thomas et al.[94] investigated gap features on a symmetric wing. They generated the steady flow fields using Reynolds Averaged Navier Stokes (RANS) solutions and conducted analysis by solving PSE and LHNS equations. They found that although there was a destabilisation at the smallest depth, upon increasing the depth they observed a plateau in the forward movement of transition. They attribute this to the re-circulatory flow inside the gap, maintaining an almost constant depth; the bubble shear layer assimilates a wall boundary condition. They had difficulty obtaining converged solutions in the presence of laminar separation bubbles due to the stream-wise marching inherent in the PSE, the LHNS does not suffer this restriction.

Wu and Dong[104] looked at the impact of a roughness on a TS wave and show that when the length scale of a roughness is comparable with the characteristic length of the TS wave, the TS wave undergoes a scattering effect though the mean flow distortion (MFD), caused by the roughness. Essentially they compose the flow of a scattering set

of equations and the MFD through the application of triple-deck theory. They introduce a transmission coefficient, dependent on the height and shape of the roughness and the frequency of the incident TS wave, which accounts for the scattering effect. This introduces a forcing which is in resonance with the TS wave and so produces an even larger correction term to the equation sets. The transmission coefficient is an unknown quantity to be solved for and happens to occur as an eigenvalue in the discretised equation system. They incorporate this transmission coefficient into the usual LST or PSE theory in order to account for the local roughness. Wu and Dong [104] find that humps and dimples have an absolute transmission coefficient greater than one, meaning they cause amplification of the TS wave. This amplification is exacerbated if the width or height of the roughness is increased. This scattering effect is also encapsulated in our LHNS stability tool.

TS waves may be present in swept wing flows but generally the wing geometry can be constructed in such a way that it maintains a favourable stream-wise pressure gradient. Favourable stream-wise pressure gradients have a stabilising effect on TS waves but adverse ones destabilise them, such as in separated flows.

1.2.2 Crossflow Instability

Since almost all transport aircraft feature swept wings with favourable pressure gradients, the applicability of TS focused studies for transport aircraft is limited. Research has, instead, begun to grow in the area of crossflow instability (CFI) which can be destabilised in regions of adverse or favourable pressure gradients. CFI features a velocity profile within the boundary layer which is zero at the wall and the free stream but has an inflection point, due to a local maximum, at some wall-normal position. These instabilities can be of a stationary or travelling nature. The size of the environmental forcing relative to surface quality, receptivity to free-stream turbulence and surface roughness, determines which may dominate the boundary layer.

Stationary CFI modifies the mean flow, and hence the stability of the boundary layer, by pulling low momentum flow from low in the boundary layer and displacing it upwards in areas of higher momentum flow. The contrary process is also happening, pulling the upper high momentum flow closer to the low momentum flow closer to the wall, resulting in a boundary layer that has high velocity shears [11]. This can be seen as a saw-tooth like profile in experiments. Travelling crossflow does not exhibit this observable feature, but has a more uniform front [19]. Although acoustic perturbations have been found to leave crossflow unaffected [70], both stationary and travelling crossflow is highly receptive to surface roughness.

Recent studies of swept flows over flat plates and wings with steps has shown that

an excrescence present in the shape of a backward facing step (BFS) has a more detrimental effect on boundary layer transition than a forward facing step (FFS). Duncan Jr. et al.[24] and Perraud et al.[68] suggest that the transition location is generally unaffected by small steps but then suddenly jumps to the step implying there exists a critical step height. Duncan Jr. et al.[24], who experimentally investigated a 30° swept wing with forward and backward facing steps located at 15% chord, observed that the FFS impacted the flow much further upstream than that of the BFS. The FFS caused the flow to begin decelerating as far upstream as 2% chord in comparison to the clean case, whereas the BFS only caused the flow to accelerate a 12% chord. The change in magnitude of the pressure coefficient (C_p) was also greater in magnitude for the FFS. Perraud et al.[68] looked at steps in 2D and 3D flows with varying sweep, between 30° or 50°, and at varying angles of attack. They apply the R_h criteria, an empirical criteria first introduced by Nenni and Gluyas[62] in 1966, which defines a critical height for steps at which a significant displacement of the transition location is observed.

$$Re_h = \frac{hU_e}{\nu}. \tag{1.1}$$

Where h denotes the step height, U_e is the velocity at the boundary layer edge at the step location, and ν is the kinematic viscosity. The critical values are $Re_h = 900$ for a BFS and $Re_h = 1800$ for a FFS. However, when applying this criteria Perraud et al.[68] find it not to be a very precise prediction method. Although, they did agree with an element of the criteria, being that FFSs are half as dangerous as equivalent depth BFSs. Saeed et al.[82] experimentally studied the impact of two-dimensional bump like features placed at 3%, 10% and 20% chord on a 40° swept wing geometry. Beyond a certain height, waviness and jaggedness was observed within the transition front, charactering crossflow instability. A further movement of the transition front towards the bump location was observed for increasing bump heights and bumps located further down stream. They attributed this to the stationary CFI being more established further downstream and then interacting with the travelling disturbance, causing the transition front to move close to the bump.

Further characterisations have been made for critical step heights, those causing a large forward movement in the transition front, for forward facing steps on swept wing flows. This could be extremely useful for design of wing tolerances however the critical step height varies from paper to paper due to the variety of flow configurations. It is important to note that the separation bubble in swept flows is not a closed 2D recirculation but an open 3D flow due to the span-wise component, see figure 1.3. Generally these are helical flows which flow from the wing route to wing tip, contrary to the span-wise crossflow direction which flows tip to root[95]. Vidales et al.[98] experimentally, and Tufts et al.[95] numerically, studied a 45° swept wing with a FFS

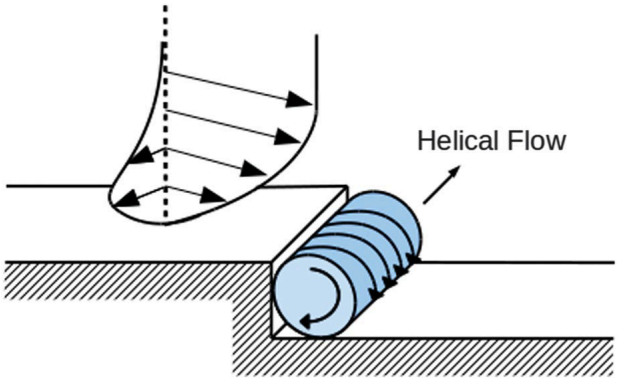

Figure 1.3: Cartoon for backward facing step featuring CFI and a three dimensional laminar separation bubble from Tufts et al.[95].

placed at 20% and 15% chord respectively. They propose the critical height for a FFS is determined by the core of the crossflow vortex height (y_c) and the height of the step (h). If the clean case crossflow vortex height is greater than the step height then the convecting crossflow instability will remain stable and not be amplified by the step. Otherwise there is a destructive interaction between the crossflow and helical downstream flow that is the separation bubble. The height of the core of the stationary crossflow can be determined by finding the CFI wavelength with the largest N-factor at the step location and then finding the maximum of the v-perturbation shape function. If $h > y_c$ the interaction is constructive, amplifies the stationary crossflow and the transition front moves towards the step. Vidales et al.[98] also note that an increase in the ratio of the step height with the boundary layer thickness at the step (h/δ_h) results in a higher critical N-factor reduction for a fixed y_c/h ratio. Tufts et al.[95] confirm the interaction with the separation bubble with a trial experiment. They artificially reduced the size of the separation bubble on top of the step but kept the step hight the same by modifying the numerical boundary conditions. When doing this they found that the step produced similar disturbance profiles, amplitudes and shapes, to that of those from sub-critical step heights when it should have exhibited critical behaviour.

Tufts et al.[95] also investigated the BFS which exhibits a larger recirculation region than in the FFS case. They observed that increasing the step height results in a gradual movement of transition towards the step, rather than a quick jump making it difficult to characterise a critical height. They reason this is because, although the stationary crossflow itself was not amplified by the BFS, the presence of a travelling mode found in the recirculation bubble interacts with the stationary CFI causing a faster breakdown to turbulence. Generally, they found that critical FFS heights were larger than those for the equivalent BFS's with the same flow conditions, implying the BFSs are more dangerous.

Eppink has investigated various FFSs and BFSs on a flat plate experimentally[26,29,27,30,31]

for step heights ranging from 53 to 71% of the boundary layer. Eppink applied the same criteria for predicting the FFS critical step height as Tufts et al.[95] and although results agreed well qualitatively, Tufts et al. predicted a critical step height 15% larger than what Eppink found in experiments. Eppink[27] reasons that upstream of the step the primary incoming stationary crossflow vortices are lifted up significantly from the wall and do not directly impact the step. There are a second set of vortices, rotating in the opposite direction, which form underneath the primary set. Due to their rotation in the opposite direction, their interaction with the downstream helical flow should not be constructive. Eppink believes the crossflow reversal region plays a crucial role in the transition process, firstly because of the effect of the near wall vortex, caused by the crossflow reversal, on the growth of wall-normal perturbations near the wall. Secondly due to the strong streamline curvature induced from the positive crossflow component which causes the two vortices to eventually merge, consequent of which is a large stationary crossflow growth downstream. The crossflow reversal region may be a good indicator of critical cases. The BFS's considered by Eppink et al.[31] ranged from 36% to 49% of the boundary layer and considered both steady and unsteady CFI. She found that the presence of the step only had a very small localised impact on the stationary crossflow growth, whereas the amplitude of the unsteady disturbance increased with larger step depths. Eppink elucidates that the stationary crossflow vortices, although not hugely dangerous on their own, interact with the unsteady disturbances non-linearly, aiding in the breakdown to turbulent state. Overall, the travelling modes seem to be the most dangerous in the breakdown mechanism. Eppink and Yao[29] have further delved into the impact of the 49% BFS on stationary CFI through the use of time-resolved particle image velocimetry. They discovered three unsteady disturbances in the flow downstream of the roughness and characterised them as a travelling CFI, a TS wave and a shear layer instability. Large velocity peaks were observed in the frequency spectra which they attributed to the interaction of these modes. They believe the stream-wise velocity is modulated by the stationary crossflow instability. The span-wise wavelength of the unsteady CFI is similar to that of the stationary crossflow and so also enhances the stream-wise velocity modulation further. On top of this there is the TS mode which is almost phase aligned with the travelling CFI causing even more velocity modulation and even larger amplitude velocity spikes. Eppink and Yao[29] go on to say the velocity spikes cannot be caused by this interaction alone since the spikes are not observed for 180° phase shift of the travelling CFI and TS wave. The result of this interaction results in breakdown.

Recently Eppink and Casper[28] have also looked at the effect of varying shapes of ramps and FFS's placed on a swept flat plate in the presence of a three dimensional pressure body, to simulate an infinitely swept wing flow. The ramp height was 81% of the

boundary layer thickness with an angle of 30° or 45° slope. The ramps delayed transition further as their angle was decreased due to the reduction, or even eradication, of the separation bubble downstream of the step. Although reducing the amplification of CFI locally to the step region, downstream of this there is a second strong region of growth. Eppink shows that downstream of the step there are multiple stationary modes present which are modified in varying ways by the mean flow. Some being destabilised near the step, growing to large amplitudes and then decaying, and others which increase in amplitude from the step or end of the separation region. These can overtake the initial dominant mode. During the flow recovery region unsteady disturbances are amplified, implying significance of non-linear interactions within this region.

Groot et al.[37] apply a numerical and experimental approach to analyse the growth of stationary CFI and the development of secondary high-frequency instabilities of type one and two in swept wing boundary layers. This work focusses mainly on the latter stages of transition and breakdown with crossflow inducing this result. The model was swept to 45° and had a 3° incidence in order to augment the generation of the CFI. The stationary CFI advects fluid about its vortical axis to redistribute fluid momentum across the boundary layer. One side of the vortex draws fluid up and the other draws fluid down causing high and low speed flow in an otherwise homogeneous boundary layer. This leads to forward and backward streaky structures in the flow, named Klebanoff modes[97]. The span-wise shear layer with the basic state in the upwash region of the primary vortex generates type one modes and the wall normal shear with the basic state generates the type two modes. The type two mode remains on the top of the primary vortex. These modes, also named z-type and y-type modes by Malik and Li F.[53], are of interest since they are responsible for turbulent breakdown. Klebanoff, or K-modes, usually take the form of a lambda structure which is aligned with the free stream direction. They cause span-wise modulation with a distinctive span-wise wavelength. Xu et al.[106] document a good image of these over a flat plate and also H-type modes which are staggered to the free stream.

Groot et al.[37] measure the base flow and mean flow distortion from the primary vortex directly, as opposed to the usual method of computing the secondary instabilities with non-linear Parabolised Navier-Stokes Equations. Here the base flow and distorted mean flow obtained from three dimensional PIV measurements are used as the base flow for secondary stability analysis. They show that resolving the shear layer allows for extracting stability data without having to examine the receptivity of the primary vortices with a computational approach.[37,87]

1.2.3 Laminar Separation Bubble Instabilities

Backward facing steps and bump excrescences generally feature a large region of reverse flow downstream of the excrescence, a laminar separation bubble. This is due to the strong adverse pressure gradient created by the presence of the step. The re-attachment of the free-stream flow can be rather unsteady, being subject to low-frequency oscillations of the separation bubble. The bubble may then become an amplifier and oscillator to already convecting instabilities within the boundary layer.

Watmuff[101] looked at separation bubbles over a flat plate, initiated by generating an adverse pressure gradient. Watmuff found that what previously was being referred to as a TS wave packet, should really be referred to as a Kelvin-Helmholtz wave packet. After the separated flow region, the wave amplitude grows due the Kelvin-Helmholtz instability in the shear layer, exhibits classical roll-up formation leading to large scale vortex loops near reattachment.

Hasan[43], who looked at varying roughness geometries on the leading edge of flat plates to generate re-attaching shear layers, found that the shear layer instability does not seem to correlate with roughness height but does correlate with boundary layer momentum thickness for large roughness. This seems to be in line with the findings from Diwan and Ramesh[20] who studied separation bubbles on a flat plate generated from an imposed pressure gradient. They found that in the frontal region of the bubble, the so-called dead-air region, instability amplitudes are small and reach their maximum towards the end of the bubble, at reattachment. They introduced a small wave packet upstream of the bubble and observed its modification as it advected downstream. Diwan and Ramesh[20] argue that the separation bubble exhibits an inviscid inflectional instability due to the separated shear layer, which should be seen as an appendage of the upstream instability in the attached adverse pressure region. Only when the separated shear layer has moved substantially away from the wall, one can assume the instability originates from the bubble and evolves into the Kelvin-Helmholtz instability scenario.

There are also other mechanisms at play which can cause global instability. In 1998, Hammond and Redekopp[41] further built on work from Huerre and Monkewitz[47] and found that flows with a laminar separation bubble have the potential of becoming absolutely unstable. They showed that if the peak reverse flow velocity was in excess of 30% of the basic flow then the boundary layer would suffer absolute instability. Alam and Sandham[2] looked into the effect of laminar separation bubbles on global instability. They found the peak reverse flow only had to be 15-20% of the freestream velocity to instigate an absolutely unstable flow, which was also similar to Gaster's[34] findings of peak reverse flow of 15%. Alam and Sandham[2] also found that convective

instabilities may be present if the reverse flow region reaches 8% of the freestream flow.

The causes of unsteadiness and three-dimensionality of unforced two dimensional separated flows have been investigated by Rodríguez et al.[77]. The two main contributors are a global oscillator due to regions of absolute inflectional instability and a centrifugal instability leading to three dimensionality of the base laminar separation bubble. They study a variety of separation bubbles and discover that absolute instability does not exist for two dimensional bubbles with a peak reverse flow of less than 12% of the free stream velocity. The three dimensional instability, however, comes into play with reverse flow as little at 7% of the free stream. Having applied the peak reverse flow criteria to gauge the strength of the bubble, they believe this is not the best way to parametrise the absolute or convective instability. They find that for local parallel analysis the maximum displacement thickness is a more adequate measure for onset of absolute instability than the previous basis of peak reverse flow by Huerre and Monkewitz[47].

Hosseinverdi and Fasel[46] have recently carried out an in-depth study of laminar separation bubbles using direct numerical simulation. Simulations without free stream turbulence usually follow the path of Kelvin-Helmholtz instability of the separated shear layer before transitioning to turbulence. Bubbles subjected to freesteam turbulence, penetrating the boundary layer upstream of the separation, promote slowly growing low frequency modes, Klebanoff modes. They find that the transition process is composed of two mechanisms, high frequency disturbances which are strongly amplified and low frequency Klebanoff modes instigated by the free stream turbulence. Transition is accelerated with increased free stream turbulence and the span-wise roll-up of the Kelvin-Helmholtz modes into vortical structure which eventually break down. This break down resultantly aids with the re-attachment process.

1.3 Outline

The arrangement of this thesis will begin with a numerical methods chapter, chapter 2, based upon stability methods. This will first cover the pre-existing tools, such as linear stability theory, the e^N method (utilised by industry), PSE and LHNS equations. Their limitations and computational implementation will also be divulged. The LHNS equations have only recently been utilised in industry, with only ourselves and now others[89] replicating this ability. The chapter will then go on to explain the contribution of this work to modify these stability equation sets to correctly solve the region local to the roughness, these are coined PSEh and LHNSh.

Chapter 3 will expand upon the direct numerical simulation tool set, Nektar++, describing the high order spectral / hp element method utilised by the incompressible Navier-Stokes and linearised Navier-Stokes time iterating solvers. Due to there being a huge change in scaling of the mesh in the far field, which can be very coarse, to the mesh local to the roughness, which requires extremely fine elements, an embedded domain approach is adopted. The embedded domain approach for generating base flows to enable the use of the extremely rapid stability tools PSE and LHNS is described. The pipeline for the meshing of varying types of roughness and the tests completed to ensure steady convergence will then be discussed. Due to the presence of separated flow induced by the roughness, Prandtl Boundary layer equations cannot be used to extract the base flow profiles. Finally, this chapter will explain the method applied to extract boundary layer profiles from the steady DNS solutions and the limitations of the methodology.

Two dimensional flow problems featuring a dimple case and an undulating random roughness case will be presented in chapter 4. The varying, newly derived, stability tool sets, PSEh and LHNSh, in the linear and non-linear form, will be applied to these cases and their merits and limitations discussed. Generally both codes are in good agreement for the dimple case, with some variation for larger dimple depths. This is likely due to the PSEh struggling to attain space marching convergence in the presence of a large separated flow region. The LHNSh solutions compare exceptionally well with experimental results[36], demonstrating the importance of the corrected model. It is extremely difficult to obtain linear stability analysis convergence for the random roughness case. Non-linear interaction was unable to be modelled. We reason this is due to multiple reverse flow regions present in the deeper roughness cases and there being huge stream-wise gradient changes, making it extremely difficult for either code to converge.

Following on from here is a three dimensional flow problem for an infinitely swept wing geometry in chapter 5. This elucidates the experimental work of Saeed et al.[82] upon which the majority of this numerical work is based upon. The clean geometry, featuring no excrescence, and the boundary layer profiles extracted from the DNS are validated with the Prandtl Boundary Layer equations. Remarkably good agreement is obtained between the PSE, LHNS and Nektar++ time stepping LNS equations.

Satisfied with the validation of the clean case, varying roughness shapes are then introduced to the embedded clean geometry. These are based upon the experimental investigation of Saeed et al.[82] who placed bump shaped roughness of varying heights on an infinitely swept wing. In chapter 6 we begin by relaxing the severity of the vertical bump with a 45° ramp case and consider only the largest height from the work of Saeed et al.[82]. This is also decomposed into its corresponding forward facing ramp (FFR)

and backward facing ramp (BFR) components and numerically simulated. The PSEh fail to accurately converge for these regimes due to the length scale of the bump being too short compared to the crossflow[104] and the sharp stream-wise gradient changes. Again, excellent agreement is obtained between the LHNSh and NekLNS equations, especially locally to the roughness. We find that the FFR triggers amplified growth of the stationary CFI, where as the BFR component does not seem to provide any growth increase; this is in-line with experimental observations[28,81].

The encouraging results from the ramp cases leads us to investigate the vertical bump, FFS and BFS cases for all height and locations considered by Saeed et al.[82] in chapter 7. Again the PSEh are unable to capture the presence of the excrescence due to the reasons mentioned above. The LHNSh predict an increased destabilisation with increasing step height for both stationary and travelling disturbances for the FFS and bump excrescences, which are in-line with the literature. We see that the 10% chord located roughness causes further destabilisation than the 20% chord cases, which is in agreement with the experimental work[82,81]. The BFS however, predicts a stabilisation which is contrary to much of the literature. We attribute this to either an immediate triggering of non-linear mode interaction that we are unable to capture with linear growth mechanisms, or a limitation of the problem construction due to the severity of the vertical step. Comparisons are drawn with NekLNS solutions however we do not see very good agreement between the models. Limitations of the methodology are discussed to elucidate why this may be.

Finally, conclusions will be summarised and recommendations for future work will be given in chapter 8.

CHAPTER 2

Numerical Methods

2.1 Review of previous methods

In 1908 Orr and Sommerfeld derived an equation based upon the small amplitude growth of a disturbance, limiting the solution to the initial stage of transition. They analysed flows where the streamlines ran parallel to one another meaning the partial differential equation can be reduced to an ordinary differential, coined the Orr-Sommerfeld equation (OSE). This equation is still widely used for stability analysis of Tollmien-Schlichting, amongst other, waves today and is popularly coupled with the e^N method. There have been many other derivations for compressible flow and attempts to incorporate non-linear theory in order to obtain better agreement with experimental results. However, it wasn't until Herbert[44,45], introducing the Parabolised Stability Equations (PSE), that the interaction of modes was better captured and provided good agreement with experiments. Similarly to Linear Stability Theory, the PSE still require the input of an initial starting amplitude, they do not have any capability of modelling receptivity. One option to obtain the initial amplitude is to use analytical theory or another could be to solve various receptivity modelling tool sets, such as the Linearised Harmonic Navier-Stokes (LHNS). The LHNS are another stability analysis tool which enable significant insight into the detailed flow physics by overcoming many of the simplifications in the earlier methods. These aforementioned equation sets come at a fraction of the cost of DNS computations and are used abundantly in this work. These will now be discussed in detail, along with contribution of this work.

2.1.1 Governing Equations of Fluid Motion

The incompressible Navier-Stokes equations, neglecting body forces, are commonly denoted as

$$\frac{\partial \mathbf{u}'}{\partial t'} + \big(\mathbf{u}'.\nabla'\big)\mathbf{u}' = -\frac{1}{\rho}\nabla'\mathbf{p}' + \nu\nabla'^2\mathbf{u}', \tag{2.1a}$$

$$\nabla'.\mathbf{u}' = 0, \tag{2.1b}$$

where $\mathbf{u}$ is the velocity vector composed of u, v and w taken in the Cartesian x, y and z direction respectively and $\mathbf{p}$ is the pressure vector. Time is represented by t and kinematic viscosity with ν. These equations are made dimensionless with the variables,

$$\begin{aligned} x' &= xL, & y' &= yL, & z' &= zL, \\ u' &= uU_\infty, & v' &= vU_\infty, & w' &= wU_\infty, \\ t' &= t\frac{U_\infty}{L}, & p' &= \rho_\infty U_\infty^2 p, \end{aligned}$$

where U_∞ is the free stream velocity and L is the length of the chord. The dimensionless incompressible Navier-Stokes equations are then,

$$\frac{\partial \mathbf{u}}{\partial t} + \big(\mathbf{u}.\nabla\big)\mathbf{u} = -\nabla\mathbf{p} + \frac{1}{R_e}\nabla^2\mathbf{u}, \tag{2.2a}$$

$$\nabla'.\mathbf{u}' = 0, \tag{2.2b}$$

where $R_e = \frac{U_\infty L}{\nu}$ is the usual Reynolds number.

The Navier-Stokes Equations are recast into a body-fitted co-ordinate system (x, n, q) for an aerofoil such that, x, follows the chord geometry, n, is the normal direction to the aerofoil surface and q is the span-wise direction. For simplicity the velocity components in the curve linear co-ordinate system will retain the same notation u, v and w. Assuming the body has a cylindrical surface the curvature of the body contour can be defined as $\kappa(x) = \frac{1}{R}$, where R is the radius of curvature.

The transformation from the Cartesian co-ordinate frame to the body-fitted co-ordinate system, well described in the literature[80], gives the body fitted Navier-Stokes equations 2.3.

$$\begin{aligned} R_e\big[u_t - uv\kappa\chi + u\chi u_x + vu_n + wu_q\big] &= -R_e\chi p_x - u\kappa^2\chi^2 - \kappa\chi u_n + u_{nn} \\ &\quad + u_{qq} + \chi^2 u_{xx} - 2\kappa\chi^2 v_x - v\chi^2(1 + n\kappa\chi)\kappa_x + n\chi^3 u_x\kappa_x, \end{aligned} \tag{2.3a}$$

$$\begin{aligned} R_e\big[v_t + u^2\kappa\chi + u\chi v_x + vv_n + wv_q\big] &= -R_e p_n - v\kappa^2\chi^2 - \kappa\chi v_n + v_{nn} \\ &\quad + v_{qq} + \chi^2 v_{xx} + 2\kappa\chi^2 u_x + u\chi^2(1 + n\kappa\chi)\kappa_x + n\chi^3 v_x\kappa_x, \end{aligned} \tag{2.3b}$$

$$R_e\big[w_t + u\chi w_x + vw_n + ww_q\big] = -R_e p_q - \kappa\chi w_n + w_{nn} + w_{qq} + \chi^2 w_{xx} + n\chi^3 w_x\kappa_x, \tag{2.3c}$$

$$\chi u_x + v_n + w_q - v\kappa\chi = 0, \tag{2.3d}$$

where $\chi = \frac{1}{1-n\kappa(x)}$ and subscripts denote derivatives.

In order to linearise the set of equations 2.3 the velocity and pressure components are decomposed into a base flow plus a small perturbation field, such that $\bar{\boldsymbol{\phi}} >> \epsilon\tilde{\boldsymbol{\phi}}$, where $\boldsymbol{\phi}$ represents the variables u, v, w, p, t.

$$\boldsymbol{\phi} = \bar{\boldsymbol{\phi}}(x,n,q) + \epsilon\tilde{\boldsymbol{\phi}}(x,n,q,t) + \mathcal{O}(\epsilon^2), \quad \epsilon \ll 1.$$

Substituting these in and retaining only the order epsilon terms leads to the non-dimensional body fitted incompressible equations.

$$\begin{aligned} R_e\big[&\tilde{u}_t - \bar{u}\tilde{v}\kappa\chi - \tilde{u}\bar{v}\kappa\chi + \tilde{u}\chi\bar{u}_x + \bar{u}\chi\tilde{u}_x + \bar{v}\tilde{u}_n + \tilde{v}\bar{u}_n \\ &+ \bar{w}\tilde{u}_q + \tilde{w}\bar{u}_q\big] = -R_e\chi\tilde{p}_x - \tilde{u}\kappa^2\chi^2 - \kappa\chi\tilde{u}_n + \tilde{u}_{nn} + \tilde{u}_{qq} \\ &+ \chi^2\tilde{u}_{xx} - 2\kappa\chi^2\tilde{v}_x - \tilde{v}\chi^2(1+n\kappa\chi)\kappa_x + n\chi^3\tilde{u}_x\kappa_x, \end{aligned} \tag{2.4a}$$

$$\begin{aligned} R_e\big[&\tilde{v}_t + 2\tilde{u}\bar{u}\kappa\chi + \tilde{u}\chi\bar{v}_x + \bar{u}\chi\tilde{v}_x + \bar{v}\tilde{v}_n + \tilde{v}\bar{v}_n + \bar{w}\tilde{v}_q \\ &+ \tilde{w}\bar{v}_q\big] = -R_e\tilde{p}_n - \tilde{v}\kappa^2\chi^2 - \kappa\chi\tilde{v}_n + \tilde{v}_{nn} + \tilde{v}_{qq} \\ &+ \chi^2\tilde{v}_{xx} + 2\kappa\chi^2\tilde{u}_x + \tilde{u}\chi^2(1+n\kappa\chi)\kappa_x + n\chi^3\tilde{v}_x\kappa_x, \end{aligned} \tag{2.4b}$$

$$\begin{aligned} R_e\big[&\tilde{w}_t + \tilde{u}\chi\bar{w}_x + \bar{u}\chi\tilde{w}_x + \bar{v}\tilde{w}_n + \tilde{v}\bar{w}_n + \bar{w}\tilde{w}_q + \tilde{w}\bar{w}_q\big] \\ &= -R_e\tilde{p}_q - \kappa\chi\tilde{w}_n + \tilde{w}_{nn} + \tilde{w}_{qq} + \chi^2\tilde{w}_{xx} + n\chi^3\tilde{w}_x\kappa_x, \end{aligned} \tag{2.4c}$$

$$\chi\tilde{u}_x + \tilde{v}_n + \tilde{w}_q - \tilde{v}\kappa\chi = 0. \tag{2.4d}$$

These form the main starter block for the incompressible stability derivations to follow.

For the compressible equation set there are the added variables for temperature, density and dynamic viscosity,

$$T' = TT_\infty, \qquad \rho' = \rho\rho_\infty, \qquad \mu' = \mu\mu_\infty,$$

such that the body fitted compressible Navier-Stokes equations are denoted as,

$$\begin{aligned} &R_e(uv\kappa\rho\chi - \chi p_x - v\rho u_n - \rho u_t - w\rho u_q - u\rho\chi u_x) \\ &+ \mu\big(-u\kappa^2\chi^2 - \kappa\chi u_n + u_{nn} + u_{qq} + r\chi^2 u_{xx} - (1+r)\kappa\chi^2 v_x + Q\chi(v_{xn} + w_{xq}) \\ &- rv\chi^2(1+n\kappa\chi)\kappa_x + nr\chi^3 u_x K_x\big) + \big(u\kappa\chi + u_n + \chi v_x\big)\mu_n \\ &+ \big(u_q + \chi w_x\big)\mu_q + \big(r\chi(-v\kappa\chi + \chi u_x) + m\chi(v_n + w_q)\big)\mu_x = 0, \end{aligned} \tag{2.5a}$$

$$
\begin{aligned}
&R_e(-u^2\kappa\rho\chi - p_n - v\rho v_n - \rho v_t - w\rho v_q - u\rho\chi v_x)\\
&\quad + \mu\big(- rv\kappa^2\chi^2 + (1+r)\kappa\chi^2 u_x - r\kappa\chi v_n + rv_{nn} + v_{qq} + \chi^2 v_{xx} + Q(\chi u_{xn} + w_{nq})\\
&\quad + u\chi^2(1+n\kappa\chi)\kappa_x + n\chi^3 v_x K_x\big) + \big(rv_n + m(-v\kappa\chi + \chi u_x + w_q)\big)\mu_n\\
&\quad + \big(v_q + w_n\big)\mu_q + \chi(u\kappa\chi + u_n + \chi v_x)\mu_x = 0,
\end{aligned}
\tag{2.5b}
$$

$$
\begin{aligned}
&R_e(-p_q - v\rho w_n - \rho w_t - w\rho w_q - u\rho\chi w_x) + \mu\big(Q(v_{nq} + \chi(u_{xq} - \kappa v_q)\big)\\
&\qquad - \kappa\chi w_n + w_{nn} + rw_{qq} + \chi^2 w_{xx} + n\chi^3 w_x K_x\big) + \big(v_q + w_n\big)\mu_n\\
&\qquad + \big(m(-v\kappa\chi + \chi u_x + v_n) + rw_q\big)\mu_q + \chi(u_q + \chi w_x)\mu_x = 0,
\end{aligned}
\tag{2.5c}
$$

$$
\begin{aligned}
&M^2(-1+\gamma)\sigma\mu\big((u\kappa\chi + u_n)^2 + u_q^2 - 2mv\kappa\chi v_n + v_q^2 + 2u\kappa\chi^2 v_x + 2\chi u_n v_x + \chi^2 v_x^2\\
&\quad + 2v_q w_n + w_n^2 + 2m(\chi u_x v_n + \chi(-v\kappa + u_x)w_q + v_n w_q) + r\big(\chi^2(-v\kappa + u_x)^2 + v_n^2 + w_q^2\big)\\
&\quad + 2\chi u_q w_x + \chi^2 w_x^2\big) + M^2 R_e(-1+\gamma)\sigma(vp_n + p_t + wp_q + u\chi p_x)\\
&\quad + R_e\rho\sigma(-vT_n - T_t - wT_q - u\chi T_x) + \mu\big(- \kappa\chi T_n + T_{nn} + T_{qq} + \chi^2 T_{xx} + n\chi^3 T_x\kappa_x\big)\\
&\quad + T_n\mu_n + T_q\mu_q + \chi^2 T_x\mu_x = 0,
\end{aligned}
\tag{2.5d}
$$

$$
- \rho v\kappa\chi + \rho\chi u_x + \rho v_n + \rho w_q + v\rho_n + \rho_t + w\rho_q + u\chi\rho_x = 0. \tag{2.5e}
$$

The Prandtl number, defining the ratio of momentum diffusivity to thermal diffusivity, is given by σ, $\gamma = \frac{c_p}{c_v}$ is the ratio of specific heats, μ is the viscosity, M is the Mach number, $m = -2/3$ is the stokes constant, $Q = m + 1$ and $r = m + 2$.

The equations are then linearised with the use of two further laws. The first being the ideal gas law,

$$\gamma M_\infty^2 p = \rho T, \tag{2.6}$$

made non-dimensional though using the same definitions above and using the identities $c = \sqrt{\gamma R^* T_\infty}$ and $M_\infty = \frac{U_\infty}{c}$. Linearising 2.6 in p, ρ and T and substituting the rearrangement of the 2.6 for the basic flow to give $\frac{\gamma M_\infty^2}{\bar{T}} = \frac{\bar{\rho}}{\bar{p}}$ results with,

$$\tilde{\rho} = \bar{\rho}\big[\frac{\tilde{p}}{\bar{p}} - \frac{\tilde{T}}{\bar{T}}\big]. \tag{2.7}$$

This enables the removal of $\tilde{\rho}$ terms and corresponding derivatives from equations 2.5 in place of $\tilde{p}$ and $\tilde{T}$.

For an ideal gas the dynamic viscosity behaves according to Sutherland's Law,

$$\mu' = \mu_\infty\Big(\frac{T_\infty + S}{T' + S}\Big)\Big(\frac{T'}{T_\infty}\Big)^{\frac{3}{2}}, \tag{2.8}$$

where $S = 110.4$ is Sutherland's constant. This equation is made non-dimensional

using $\mu = \frac{\mu'}{\mu_\infty}$ and $T = \frac{T'}{T_\infty}$ and linearised to give

$$\tilde{\mu} = f_T \tilde{T}, \quad \text{where} \quad f_T = \Big(1 + \frac{S}{T_\infty}\Big)\bar{T}^{\frac{1}{2}}\Big(\bar{T} + \frac{S}{T_\infty}\Big)^{-1}\Big(\frac{3}{2} - \frac{\bar{T}}{(\bar{T} + \frac{S}{T_\infty})}\Big), \tag{2.9}$$

and for derivative terms,

$$\tilde{\mu}_x = f_T \tilde{T}_x + f_{TT}\tilde{T}\bar{T}_x, \tag{2.10}$$

where,

$$f_{TT} = 2\Big(1 + \frac{S}{T_\infty}\Big)\bar{T}^{\frac{1}{2}}\Big(\bar{T} + \frac{S}{T_\infty}\Big)^{-1}\Big(\frac{1}{\bar{T}} - \frac{\frac{3}{2}}{(\bar{T} + \frac{S}{T_\infty})} + \frac{\bar{T}}{(\bar{T} + \frac{S}{T_\infty})^2}\Big). \tag{2.11}$$

This means that μ terms and its derivatives may be removed and replaced with T. Applying these gives the following set of equations which form the foundations for deriving the various compressible stability models. These are summarised as follows,

x-momentum :

$$\begin{aligned}
R_e\big[&(\bar{u}\bar{v}\kappa\bar{\rho}(\frac{\tilde{p}}{\bar{p}} - \frac{\tilde{T}}{\bar{T}}) + (\bar{u}\tilde{v} + \tilde{u}\bar{v})\kappa\bar{\rho})\chi - \chi\tilde{p}_x - \bar{v}\bar{\rho}\tilde{u}_n) - (\bar{v}\bar{\rho}(\frac{\tilde{p}}{\bar{p}} - \frac{\tilde{T}}{\bar{T}}) \\
&+ \tilde{v}\bar{\rho})\bar{u}_n - \bar{\rho}\tilde{u}_t - \bar{w}\bar{\rho}\tilde{u}_q - (\bar{w}\bar{\rho}(\frac{\tilde{p}}{\bar{p}} - \frac{\tilde{T}}{\bar{T}}) + \tilde{w}\bar{\rho})\bar{u}_q - \bar{u}\bar{\rho}\chi\tilde{u}_x \\
&- (\bar{u}\bar{\rho}(\frac{\tilde{p}}{\bar{p}} - \frac{\tilde{T}}{\bar{T}}) + \tilde{u}\bar{\rho})\chi\bar{u}_x\big] + \bar{\mu}(-\tilde{u}\kappa^2\chi^2 - \kappa\chi\tilde{u}_n + \tilde{u}_{nn} + \tilde{u}_{qq} + r\chi^2\tilde{u}_{xx} \\
&- (1+r)\kappa\chi^2\tilde{v}_x + Q\chi(\tilde{v}_{nx} + \tilde{w}_{qx}) - r\tilde{v}\chi^2(1 + n\kappa\chi)\kappa_x + nr\chi^3\tilde{u}_x\kappa_x) \\
&+ f_T\tilde{T}(-\bar{u}\kappa^2\chi^2 - \kappa\chi\bar{u}_n + \bar{u}_{nn} + \bar{u}_{qq} + r\chi^2\bar{u}_{xx} - (1+r)\kappa\chi^2\bar{v}_x \\
&+ Q\chi(\bar{v}_{nx} + \bar{w}_{qx}) - r\bar{v}\chi^2(1 + n\kappa\chi)\kappa_x + nr\chi^3\bar{u}_x\kappa_x) \\
&+ (\bar{u}\kappa\chi + \bar{u}_n + \chi\bar{v}_x)(f_T\tilde{T}_n + f_{TT}\tilde{T}\bar{T}_n) + (\tilde{u}\kappa\chi + \tilde{u}_n + \chi\tilde{v}_x)\bar{\mu}_n \\
&+ (\bar{u}_q + \chi\bar{w}_x)f_T\tilde{T}_q + (\tilde{u}_q + \chi\tilde{w}_x)\bar{\mu}_q + (r\chi(-\bar{v}\kappa\chi + \chi\bar{u}_x) \\
&+ m\chi(\bar{v}_n + \bar{w}_q)(f_T\tilde{T}_x + f_{TT}\tilde{T}\bar{T}_x) + (r\chi(-\tilde{v}\kappa\chi + \chi\tilde{u}_x) + m\chi(\tilde{v}_n + \tilde{w}_q)\bar{\mu}_x = 0,
\end{aligned} \tag{2.12a}$$

n-momentum :

$$
\begin{aligned}
R_e\big[&- \bar{u}^2\kappa\bar{\rho}(\frac{\tilde{p}}{\bar{p}} - \frac{\tilde{T}}{\bar{T}}) - 2\bar{u}\tilde{u}\kappa\bar{\rho})\chi - \tilde{p}_n - \bar{v}\bar{\rho}\tilde{v}_n - (\bar{v}\bar{\rho}(\frac{\tilde{p}}{\bar{p}} - \frac{\tilde{T}}{\bar{T}}) + \tilde{v}\bar{\rho})\bar{v}_n \\
&- \bar{\rho}\tilde{v}_t - \bar{w}\bar{\rho}\tilde{v}_q - (\bar{w}\bar{\rho}(\frac{\tilde{p}}{\bar{p}} - \frac{\tilde{T}}{\bar{T}}) + \tilde{w}\bar{\rho})\bar{v}_q - \bar{u}\bar{\rho}\chi\tilde{v}_x \\
&- (\bar{u}\bar{\rho}(\frac{\tilde{p}}{\bar{p}} - \frac{\tilde{T}}{\bar{T}}) + \tilde{u}\bar{\rho})\chi\bar{v}_x\big] + \bar{\mu}(-r\tilde{v}\kappa^2\chi^2 - r\kappa\chi\tilde{v}_n + r\tilde{v}_{nn} + \tilde{v}_{qq} \\
&+ \chi^2\tilde{v}_{xx} + (1+r)\kappa\chi^2\tilde{u}_x + Q\chi(\tilde{u}_{nx} + \tilde{w}_{nq}) - \tilde{u}\chi^2(1+n\kappa\chi)\kappa_x + n\chi^3\tilde{v}_x\kappa_x) \\
&+ f_T\tilde{T}(-r\bar{v}\kappa^2\chi^2 - r\kappa\chi\bar{v}_n + r\bar{v}_{nn} + \bar{v}_{qq} + \chi^2\bar{v}_{xx} + (1+r)\kappa\chi^2\bar{u}_x \\
&+ Q\chi(\bar{u}_{nx} + \bar{w}_{nq}) - \bar{u}\chi^2(1+n\kappa\chi)\kappa_x + n\chi^3\bar{v}_x\kappa_x) + (r\bar{v}_n \\
&+ m(-\bar{v}\kappa\chi + \chi\bar{u}_x + \bar{w}_q))(f_T\tilde{T}_n + f_{TT}\tilde{T}\bar{T}_n) + (r\tilde{v}_n + m(-\tilde{v}\kappa\chi + \chi\tilde{u}_x + w_q))\bar{\mu}_n \\
&+ (\bar{v}_q + \bar{w}_n)f_T\tilde{T}_q + (\tilde{v}_q + w_n)\bar{\mu}_q + \chi(\bar{u}\kappa\chi + \bar{u}_n + \chi\bar{v}_x)(f_T\tilde{T}_x + f_{TT}\tilde{T}\bar{T}_x) \\
&+ \chi(\tilde{u}\kappa\chi + \tilde{u}_n + \chi\tilde{v}_x)\bar{\mu}_x = 0,
\end{aligned}
\tag{2.12b}
$$

q-momentum :

$$
\begin{aligned}
R_e\big[&- \tilde{p}_q - \bar{v}\bar{\rho}\tilde{w}_n - (\bar{v}\bar{\rho}(\frac{\tilde{p}}{\bar{p}} - \frac{\tilde{T}}{\bar{T}}) + \tilde{v}\bar{\rho})\bar{w}_n - \bar{\rho}\tilde{w}_t - \bar{w}\bar{\rho}\tilde{w}_q - (\bar{w}\bar{\rho}(\frac{\tilde{p}}{\bar{p}} - \frac{\tilde{T}}{\bar{T}}) \\
&+ \tilde{w}\bar{\rho})\bar{w}_q - \bar{u}\bar{\rho}\chi\tilde{w}_x - (\bar{u}\bar{\rho}(\frac{\tilde{p}}{\bar{p}} - \frac{\tilde{T}}{\bar{T}}) + \tilde{u}\bar{\rho})\chi\bar{w}_x\big] + \bar{\mu}(-\kappa\chi\tilde{w}_n \\
&+ \tilde{w}_{nn} + r\tilde{w}_{qq} + \chi^2\tilde{w}_{xx} + Q(\tilde{v}_{nq} + \chi(\tilde{u}_{qx} - \kappa\tilde{v}_q)) + n\chi^3\tilde{w}_x\kappa_x) \\
&+ f_T\tilde{T}(-\kappa\chi\bar{w}_n + \bar{w}_{nn} + r\bar{w}_{qq} + \chi^2\bar{w}_{xx} + Q(\bar{v}_{nq} + \chi(\bar{u}_{qx} - \kappa\bar{v}_q)) \\
&+ n\chi^3\bar{w}_x\kappa_x) + (\bar{v}_q + \bar{w}_n)(f_T\tilde{T}_n + f_{TT}\tilde{T}\bar{T}_n) + (\tilde{v}_q + w_n)\bar{\mu}_n \\
&+ (m(-\bar{v}\kappa\chi + \chi\bar{u}_x + \bar{v}_n) + r\bar{w}_q)f_T\tilde{T}_q + (m(-\tilde{v}\kappa\chi + \chi\tilde{u}_x + \tilde{v}_n) + r\tilde{w}_q)\bar{\mu}_q \\
&+ \chi(\bar{u}_q + \chi\bar{w}_x)(f_T\tilde{T}_x + f_{TT}\tilde{T}\bar{T}_x) + \chi(\tilde{u}_q + \chi\tilde{w}_x)\bar{\mu}_x = 0,
\end{aligned}
\tag{2.12c}
$$

Energy :

$$
\begin{aligned}
M^2(-1+\gamma)\bar{\mu}((2(\bar{u}\kappa\chi+\bar{u}_n))(\tilde{u}\kappa\chi+\tilde{u}_n)+2\bar{u}_q\tilde{u}_q-2m\bar{v}\kappa\chi\tilde{v}_n-2m\tilde{v}\kappa\chi\bar{v}_n+2\bar{v}_q\tilde{v}_q \\
+2\bar{u}\kappa\chi^2\tilde{v}_x+2\tilde{u}\kappa\chi^2\bar{v}_x+2\chi\bar{u}_n\tilde{v}_x+2\chi\tilde{u}_n\bar{v}_x+2\chi^2\bar{v}_x\tilde{v}_x+2\bar{v}_q\tilde{w}_n+2\tilde{v}_q\bar{w}_n \\
+2\bar{w}_n\tilde{w}_n+2m(\chi\bar{u}_x\tilde{v}_n+\chi\tilde{u}_x\bar{v}_n+\chi(-\bar{v}\kappa+\bar{u}_x)\tilde{w}_q+\chi(-\tilde{v}\kappa+\tilde{u}_x)\bar{w}_q+\bar{v}_n\tilde{w}_q \\
+\tilde{v}_n\bar{w}_q)+r(2\chi^2(-\bar{v}\kappa+\bar{u}_x)(-\tilde{v}\kappa+\tilde{u}_x)+2\bar{v}_n\tilde{v}_n+2\bar{w}_q\tilde{w}_q)+2\chi\bar{u}_q\tilde{w}_x \\
+2\chi\tilde{u}_q\bar{w}_x+2\chi^2\bar{w}_x\tilde{w}_x)+M^2(-1+\gamma)f_T\tilde{T}((\bar{u}\kappa\chi+\bar{u}_n)^2+\bar{u}_q^2-2m\bar{v}\kappa\chi\bar{v}_n \\
+\bar{v}_q^2+2\bar{u}\kappa\chi^2\bar{v}_x+2\chi\bar{u}_n\bar{v}_x+\chi^2\bar{v}_x^2+2\bar{v}_q\bar{w}_n+\bar{w}_n^2+2m(\chi\bar{u}_x\bar{v}_n \\
+\chi(-\bar{v}\kappa+\bar{u}_x)\bar{w}_q+\bar{v}_n\bar{w}_q)+r(\chi^2(-\bar{v}\kappa+\bar{u}_x)^2+\bar{v}_n^2+\bar{w}_q^2)+2\chi\bar{u}_q\bar{w}_x \\
+\chi^2\bar{w}_x^2)+M^2(-1+\gamma)R_e(\bar{v}\tilde{p}_n+\tilde{v}\bar{p}_n+\tilde{p}_t+\bar{w}\tilde{p}_q+\tilde{w}\bar{p}_q+\bar{u}\chi\tilde{p}_x \\
+\tilde{u}\chi\bar{p}_x)+R_e\bar{\rho}\sigma(-\bar{v}\tilde{T}_n-\tilde{v}\bar{T}_n-\tilde{T}_t-\bar{w}\tilde{T}_q-\tilde{w}\bar{T}_q \\
-\bar{u}\chi\tilde{T}_x-\tilde{u}\chi\bar{T}_x)+R_e\bar{\rho}(\frac{\tilde{p}}{\bar{p}}-\frac{\tilde{T}}{\bar{T}})\sigma(-\bar{v}\bar{T}_n-\bar{w}\bar{T}_q-\bar{u}\chi\bar{T}_x) \\
+\bar{\mu}(-\kappa\chi\tilde{T}_n+\tilde{T}_{nn}+\tilde{T}_{qq}+\chi^2\tilde{T}_{xx}+n\chi^3\tilde{T}_x\kappa_x)+f_T\tilde{T}(-\kappa\chi\bar{T}_n \\
+\bar{T}_{nn}+\bar{T}_{qq}+\chi^2\bar{T}_{xx}+n\chi^3\bar{T}_x\kappa_x)+\bar{T}_n(f_T\tilde{T}_n+f_{TT}\tilde{T}\bar{T}_n)+\tilde{T}_n\bar{\mu}_n \\
+\bar{T}_qf_T\tilde{T}_q+\tilde{T}_q\bar{\mu}_q+\chi^2\bar{T}_x(f_T\tilde{T}_x+f_{TT}\tilde{T}\bar{T}_x)+\chi^2\tilde{T}_x\bar{\mu}_x=0,
\end{aligned}
\tag{2.12d}
$$

Continuity :

$$
\begin{aligned}
-(\bar{\rho}\tilde{v}+\bar{\rho}(\frac{\tilde{p}}{\bar{p}}-\frac{\tilde{T}}{\bar{T}})\bar{v})\kappa\chi+\bar{\rho}\chi\tilde{u}_x+\bar{\rho}(\frac{\tilde{p}}{\bar{p}}-\frac{\tilde{T}}{\bar{T}})\chi\bar{u}_x+\bar{\rho}\tilde{v}_n+\bar{\rho}(\frac{\tilde{p}}{\bar{p}}-\frac{\tilde{T}}{\bar{T}})\bar{v}_n \\
+\bar{\rho}\tilde{w}_q+\bar{\rho}(\frac{\tilde{p}}{\bar{p}}-\frac{\tilde{T}}{\bar{T}})\bar{w}_q+\bar{v}\bar{\rho}(-\frac{\bar{T}_n\tilde{p}}{\bar{p}\bar{T}}-\frac{\tilde{T}\bar{\rho}_n}{\bar{T}\bar{\rho}}+\frac{\tilde{T}\bar{T}_n}{\bar{T}^2}+\frac{\tilde{p}_n}{\bar{p}}-\frac{\tilde{T}_n}{\bar{T}}) \\
+\tilde{v}\bar{\rho}_n+\bar{\rho}(-\frac{\bar{T}_t\tilde{p}}{\bar{p}\bar{T}}-\frac{\tilde{T}\bar{\rho}_t}{\bar{T}\bar{\rho}}+\frac{\tilde{T}\bar{T}_t}{\bar{T}^2}+\frac{\tilde{p}_t}{\bar{p}}-\frac{\tilde{T}_t}{\bar{T}})+\bar{\rho}(-\frac{\bar{T}_q\tilde{p}}{\bar{p}\bar{T}}-\frac{\tilde{T}\bar{\rho}_q}{\bar{T}\bar{\rho}}+\frac{\tilde{T}\bar{T}_q}{\bar{T}^2}+\frac{\tilde{p}_q}{\bar{p}}-\frac{\tilde{T}_q}{\bar{T}}) \\
+\tilde{w}\bar{\rho}_q+\bar{u}\chi\bar{\rho}(-\frac{\bar{T}_x\tilde{p}}{\bar{p}\bar{T}}-\frac{\tilde{T}\bar{\rho}_x}{\bar{T}\bar{\rho}}+\frac{\tilde{T}\bar{T}_x}{\bar{T}^2}+\frac{\tilde{p}_x}{\bar{p}}-\frac{\tilde{T}_x}{\bar{T}})+\tilde{u}\chi\bar{\rho}_x=0.
\end{aligned}
\tag{2.12e}
$$

2.1.2 Linear Stability Theory and e^N method

Linear stability theory (LST) is the oldest of the three models mentioned in this chapter and, coupled with the e^N method, is still the most widely used tool by industry to predict laminar to turbulent transition. The equations are derived by assuming that small fluctuations may be decomposed into Fourier modes, namely,

$$
\tilde{\phi}(x,n,q,t)=\hat{\phi}(n)e^{i(\alpha x+\beta q-\omega t)}. \tag{2.13}
$$

LST has many limitations, such as neglecting non-parallel effects and surface curvature, being unable to model non-linear mode interaction and completely omitting receptivity mechanisms. It does however, reduce to a nice eigenvalue problem, requiring the solution of a an eigenvalue based dispersion problem $\mathcal{D}(\alpha, \beta, \omega) = 0$, and is still today the single most practical method available for many industrial applications[45], particularly as a foundation for design processes. Essentially the e^N method correlates the transition location with the accumulated growth which is measured by the so-called N-factor. The N-factor is determined from experiments for different flow configurations and then used as a criterion in transition prediction methods based on LST.

The e^N method is directly related to the neutral stability curve of the problem at hand, and is governed by the precise nature of the background steady base state. For any given point x the spatial amplification, A, of the perturbation always relates to the amplitude, A_0, at the initial point of growth of the disturbance, x_0. As stated by Herbert[45], Liepmann's criterion is based on this relation between A and A_0 such that the amplitude ratio is given by,

$$\ln\left(\frac{A}{A_0}\right) = \int_{x_0}^{x} -\alpha_i dx, \tag{2.14}$$

where α_i is the complex part of the stream-wise wave number. By computing many frequencies and following the greatest $\ln(A/A_0)$ the N-factor envelope can be attained,

$$N = \max_f \left[\ln\left(\frac{A}{A_0}\right)\right]. \tag{2.15}$$

First found by Van Ingen[96] and Smith and Gamberoni[88] independently back in the 1950's. For an incompressible flow, with low disturbance environment, the N-factor reaches a critical value at around 7-9. This means transition will occur when the most locally unstable frequency is amplified by a factor e^7 to e^9 with respect to its initial amplitude A_0, ie. $\frac{A_{tr}}{A_0} \approx e^N$. Alternatively to evaluating spatial instability, where it is assumed the span-wise wave number β and the frequency ω are real, the temporal instability could be solved for. The temporal case assumes the stream-wise wave number is now real and instead the frequency is assumed complex, $\omega = \omega_r + i\omega_i$. Due to the non-linearities in α the temporal growth problem is much easier to solve although slightly less attractive since repeatable measurements can be more easily obtained with spatial theory.[45]

For compressible flows the problem becomes more extensive. The most unstable modes in compressible flows are oblique waves meaning the angle θ, between the wave number

vector and the x-axis, is required to satisfy a dispersion relation. Under the assumption that the growth only takes place in the stream-wise direction and that a spatial eigenvalue problem is solved given a fixed real frequency ω, $\beta_i = \theta_i = 0$ and β_r or θ_r is still required to be specified. Generally, the envelope method is followed for calculating the local amplification of a given, real only, frequency. For each x location the direction θ_M of the wave is sought to yield the maximum value $-\alpha_{iM}$ for all α_i. The N-factor envelope is then defined as follows.[5]

$$N = \max_f \int_{x_0}^{x} -\alpha_{iM} dx = \max_f \int_{x_0}^{x} \max_\theta(-\alpha_i) dx \tag{2.16}$$

The e^N method is widely considered a practical and efficient tool for predicting transition, particularly when the external environment disturbances are minimal. It is often able to predict the variation in transition location for a given test model and disturbance environment when varying a particular stability parameter. Due to the limitations of LST, the e^N method has now began to be coupled with more sophisticated methods, such as the Parabolised Stability Equations.

2.1.3 Parabolised Stability Equations (PSE)

The parabolised stability equations (PSE), contrary to LST, do take into account weakly non-linear disturbances, as well as wall curvature effects of the body surface. In this approach the perturbation is assumed to be nearly sinusoidal in the stream-wise direction and the original elliptic set of equations are forced to become parabolic in order to halt propagation of information upstream via acoustic waves or stream-wise viscous diffusive terms[108,14]. These parabolic equations are then solved by down stream marching along the free-stream direction, meaning the up stream history of the disturbance has an impact on the flow at any given position x. Free-stream turbulence or surface roughness forcing can not be modelled with the PSE, due to the formal parabolising procedure. This is usually modelled using receptivity modelling which retain stream-wise ellipticity and short-scale resolution required in the resonance stage of disturbance emergence.

Linear PSE

In classical stability analysis it is assumed that the basic steady state variations in the wall normal direction are large compared to variations in the stream-wise and span-wise directions, $\frac{\partial \bar{\phi}}{\partial x}, \frac{\partial \bar{\phi}}{\partial z} << \frac{\partial \bar{\phi}}{\partial y}$, meaning there is no dependence of the base flow on x or z. This is the so-called parallel flow assumption and is too restrictive for flows around

two dimensional bodies or complex vortical flows. The flow is instead assumed to be general in a two-dimensional plane, and mildly inhomogeneous in the third direction such that the following perturbation ansatz is introduced,

$$\tilde{\boldsymbol{\phi}}(x,n,q,t) = \hat{\boldsymbol{\phi}}(x,n)e^{i(\theta(x)+\beta q-\omega t)} + c.c.\ , \quad \text{where } \frac{d\theta}{dx} = \alpha(x), \tag{2.17}$$

where *c.c.* represents complex conjugate. The perturbation field is decomposed further into this shape, $\hat{\boldsymbol{\phi}}$, and phase function, $\int \alpha(x)dx + \beta q - \omega t$. Here α is complex and β and ω are real[45,12]. The amplitude functions (the so called slow variable) depend on n and x, and α depends on x, in contrast to the classical linear theory. Ellipticity is thereby retained for the wave function but the shape function is enforced to become parabolic through the application of a normalisation condition. This absorbs any rapid variations of $\hat{\boldsymbol{\phi}}$ into the phase function,

$$\frac{\int_0^\infty \tilde{u}^\dagger \frac{\partial \tilde{u}}{\partial x} + \tilde{v}^\dagger \frac{\partial \tilde{v}}{\partial x} + \tilde{w}^\dagger \frac{\partial \tilde{w}}{\partial x} dx^*}{\int_0^\infty \tilde{u}^\dagger \tilde{u} + \tilde{v}^\dagger \tilde{v} + \tilde{w}^\dagger \tilde{w}\ dx^*}. \tag{2.18}$$

Substituting 2.17 into 2.4 the set of equations can then be discretised and recast into

$$\big(\mathcal{L}_0 + \mathcal{L}_1\big)\hat{\boldsymbol{\phi}} + \mathcal{L}_2 \frac{\partial \hat{\boldsymbol{\phi}}}{\partial x} + \frac{d\alpha}{dx}\mathcal{L}_3 \hat{\boldsymbol{\phi}} = 0. \tag{2.19}$$

Here, $\mathcal{L}_0$, $\mathcal{L}_1$, $\mathcal{L}_2$ and $\mathcal{L}_3$ are all matrix operators in n which depend on (x,n) through the baseflow terms. $\mathcal{L}_0$ corresponds to the linear parallel terms, $\mathcal{L}_1$ contains non-parallel terms of the basic state, $\mathcal{L}_2$ encompasses non-parallel perturbation terms and last, but not least, $\mathcal{L}_3$ corresponds to wave number terms. The equations are then ready to be solved by downstream marching.[14,45,12,5]

Non-linear PSE

The non-linear PSE, although only capable of capturing weakly non-linear phenomena, are extremely attractive as they can tackle rather complex geometries and are computationally more efficient (cheaper) than DNS. Once again, the disturbance is assumed to be periodic in time and in the span-wise direction meaning the base flow is independent of t and q. Double Fourier expansions containing two- and three-dimensional discrete Fourier modes, (l,m) modes, are used to denote the disturbances,

$$\tilde{\phi} = \sum_{l=-\infty}^{\infty} \sum_{m=-\infty}^{\infty} \hat{\phi}_{l,m}(x,n) e^{i\left(\int_{x_0}^{x} \alpha_{l,m}(\xi)d\xi + m\beta q - l\omega t\right)}. \tag{2.20}$$

Where the Fourier mode (l,m) corresponds to the Fourier components, $\alpha_{l,m}$, the

stream-wise wave number, and $\hat{\phi}_{l,m}$, the shape function; $\alpha_{l,m}$ is complex whereas β and ω are real constants, chosen such that the longest wavelength and period are $\frac{2\pi}{\beta}$ and $\frac{2\pi}{\omega}$ respectively, in the span-wise and temporal domains. Negative values of l and m correspond to complex conjugates of the positive ones, i.e. we impose $\phi_{-l,-m} = \phi^{\dagger}_{l,m}$. These are imposed because we require the fluctuations we are considering to be real. Normalisation conditions are again required to ensure weak stream-wise variation of amplitude functions $\hat{\phi}_{l,m}$ with any rapid variations absorbed into the fast wave exponential component through $\alpha_{l,m}$.[14 5]

The mean flow distortion mode (0,0) in equation 2.20 is uniform in the q direction and independent of time. (0,m) modes do not depend on time but distort the basic flow periodically in the span-wise direction for a given position x. Analogously, the mode (l,0) is independent of the span-wise direction but is dependent on time. High harmonics of the fundamental mode correspond to large values of (l,m). In the linear regime they have very low amplitudes but in the non-linear regime they grow rapidly, causing the appearance of small wavelengths with high frequencies.[5]

For most stability problems the Fourier series can be truncated to a finite number of modes, N and M, such that,

$$\tilde{\phi} = \sum_{l=-N}^{\infty} \sum_{m=-M}^{\infty} \hat{\phi}_{l,m}(x,n) e^{i\left(\int_{x_0}^{x} \alpha_{l,m}(\xi) d\xi + m\beta q - l\omega t\right)}. \tag{2.21}$$

After substituting this into the linearised Navier-Stokes equations these can be reduced further though applying harmonic balancing and phase locking each non-linear mode to the real part of the fundamental wave number. Each mode will have its own growth rate, which is unlinked to the fundamental mode, and closure condition to be satisfied resulting with a system of coupled partial equations to be solved iteratively.

For the compressible non-linear PSE the problem becomes much more complex. Due to the arising of triple, and up to sextuple, summations after substitution of 2.21 into the linearised compressible Navier-Stokes equations, they are extremely difficult to solve with harmonic balancing. Instead, fast Fourier transforms are used to represent each perturbed variable and convolutions applied. These are then solved in the physical space and fast Fourier transformed back to the spectral space for solving of the systems of equations.

Limitations

The PSE, although capturing surface curvature, non-parallel effects and being able to model non-linear mode interaction, need to be given an initial amplitude to begin the computation, they can not model receptivity. The starting amplitude may be provided from a receptivity modelling tool such as the LHNS[71] or with analytical theory, such as triple deck. Triple deck theory involves breaking down the flow into a main deck, which is the basic boundary layer, a lower deck or viscous sub-layer, where instabilities generated within this layer cause a displacement in the streamlines. This displacement is then imparted on the upper deck, or ideal fluid layer. The modification of the streamlines, causes a variation in the pressure field which is then relayed back to the lower layer, resulting in a coupled system of equations.[79]

Another rather large limitation of the PSE is that they suffer a stream-wise step size restriction. Li and Malik[52] found that the point to point marching must be of a length scale Δx such that $\Delta x \geq \frac{1}{\alpha_r}$, where α_r is the real part of the wave number, in order to obtain a converged solution. This means that when introducing the roughness feature to the geometry, the roughness must be large enough to have a sufficient number of points describing the shape with large enough Δx to not violate the step size restriction.

Another potential limitation is whether the PSE can be used for flows with laminar separation present. Park and Park[64],[65] used the PSE for problems with and without separation bubbles present. They documented results using linear PSE, however when using non-linear PSE they only documented results for problems which maintained a favourable pressure gradient, i.e. no reverse flow. Perhaps the non-linear form used by Park and Park[64],[65] was unable to converge in the presence of locally reversed flow pockets within the laminar boundary layer, i.e in the presence of laminar separation bubbles.

Computational Framework

The linear or non-linear PSE are solved over a stretched grid in the wall normal direction. First an initial guess eigenvalue file is created, which is generated using a generalised eigenvalue solve step comprising the QZ algorithm[54,1], to compute the entire eigenvalue spectrum at the beginning of the space marching. From this computed spectrum the least stable eigenvalue is determined. The solver can then be re-ran using this initial guess eigenvalue to recompute the eigenvalue and corresponding eigenfunction using a considerably more efficient inverse Rayleigh iteration. This is then used as the initial condition, inflow state, for the space marching procedure. The equations

solved are touched on here for a TS wave in the (x, y) co-ordinate frame, corresponding to (stream-wise, wall normal) directions, but can be extended to include CFI also. The equations are parabolised with the assumptions mentioned in section 2.1.3 and a linear parabolic marching procedure solves the equations,

$$(\mathcal{L}_0 + \mathcal{L}_1)[\phi] + \mathcal{L}_2\Big[\frac{\partial \phi}{\partial x}\Big] = 0, \tag{2.22}$$

where $\mathcal{L}_0$, $\mathcal{L}_1$ and $\mathcal{L}_2$ are differential operators containing steady base flow terms and (ω, α). This is then discretised into a first order Euler scheme,

$$(\mathcal{L}_0 + \mathcal{L}_1)[\phi_j] + \mathcal{L}_2\Big[\frac{\phi_j - \phi_{j-1}}{\Delta x}\Big] = 0, \tag{2.23}$$

and solved for ϕ_j with boundary conditions,

$$[u, v, w, T](x, 0) = 0, \tag{2.24}$$

$$[u, w, T, p](x, y) = \frac{\partial [u, v, w, T, p](x, y)}{\partial y} = 0 \quad \text{as} \quad y \to \infty, \tag{2.25}$$

the pressure at the wall is found by solving the y-momentum with the continuity equation. The initial condition is provided at some starting point x_0 from the eigenvalue solution,

$$\phi(x_0, y) = f(y), \qquad \alpha(x_0) = \alpha_0. \tag{2.26}$$

The shape function is normalised with the closure condition in equation 2.18 which is discretised into,

$$\alpha_{n+1} = \alpha_n - \frac{i}{\Delta x} \frac{\int_0^\infty \phi_j^\dagger (\phi_j - \phi_{j-1}) dy}{\int_0^\infty \phi_j^\dagger \phi_j dy}. \tag{2.27}$$

Here n denotes the iteration number.

The solution is marched in a two stage process. First, the system of equations 2.23 is solved for ϕ_j with an initial guess α_j, which usually is just the value at the previous position α_{j-1}. Second, the new ϕ_j is used to compute 2.27 and provide a new value $\alpha_{n+1}^{(j)}$ which is then used in the reconstruction of $[\mathcal{L}_j]$. This two stage process repeats until alpha converges to some small prescribed convergence criterion. In the code this is based on no further changes in the number of significant figures in α, meeting a user specified criteria, typically 4 digits of $\alpha_{n+1}^{(j)}$. This ensures the transfer of the rapidly changing growth in amplitude of the disturbance into the phase function, or fast variable, thus maintaining the shape function with slow or weak variations in x.

A stretched grid is applied in the normal direction to recast $y \in [0, \infty]$ to the computational domain $\eta \in [0, 1]$ with the algebraic mapping $y = \frac{g\eta}{b-\eta}$. Here, g is a scaling parameter. The smaller this scaling parameter is, the finer the distribution of points at the wall. Also, $b = 1 + g/y_e$, where y_e is the location where the Dirichlet conditions are satisfied. Fourth order accurate central differencing is applied for the grid interior with second order accurate formulae used at the surface boundary point.

For the non-linear PSE, involving the purely two-dimensional TS interaction, we assume,

$$\tilde{q}(x, y, t) = \sum_{k=-\infty}^{\infty} \hat{q}^{(k)}(x, y) e^{i \int_{x_0}^{x} \alpha^{(k)}(s) ds - ik\omega t}. \tag{2.28}$$

The equations are formulated into the linear and non-linear parts for each mode of superscript k, such that,

$$(\mathcal{L}_0^{(k)} + \mathcal{L}_1^{(k)})[\phi^{(k)}] + \mathcal{L}_2^{(k)}\Big[\frac{\partial \phi^{(k)}}{\partial x}\Big] = \mathcal{N}^{(k)}, \tag{2.29}$$

for each k^{th} mode. Considering the two dimensional non-linear x-momentum equation,

$$\frac{\partial \tilde{u}}{\partial t} + \tilde{u}\frac{\partial \bar{u}}{\partial x} + \bar{u}\frac{\partial \tilde{u}}{\partial x} + \Psi = -\Big(\tilde{u}\frac{\partial \tilde{u}}{\partial x} + \tilde{v}\frac{\partial \tilde{u}}{\partial y}\Big), \tag{2.30}$$

where Ψ represents the remaining linear terms,

$$\Psi = \bar{v}\frac{\partial \tilde{u}}{\partial y} + \tilde{v}\frac{\partial \bar{u}}{\partial y} + \frac{\partial \tilde{p}}{\partial x} - \frac{1}{R}\Big(\frac{\partial^2 \tilde{u}}{\partial x^2} + \frac{\partial^2 \tilde{u}}{\partial y^2}\Big). \tag{2.31}$$

Upon substitution of the ansatz 2.28 the following is obtained,

$$\begin{aligned} \sum_{k=-\infty}^{\infty} \Big[(-ik\omega + i\alpha^{(k)}\bar{u})\hat{u}^{(k)} + \bar{u}\frac{\partial \hat{u}^{(k)}}{\partial x} + \Psi^{(k)}\Big] e^{i \int_{x_0}^{x} \alpha^{(k)}(s) ds - ik\omega t} \\ = -\sum_{p=-\infty}^{\infty}\sum_{m=-\infty}^{\infty} \Big[\hat{u}^{(p)}(i\alpha^{(m)}\hat{u}^{(m)} + \frac{\partial \hat{u}^{(m)}}{\partial x}) \\ + \hat{v}^{(p)}\frac{\partial \hat{u}^{(m)}}{\partial y}\Big] e^{i \int_{x_0}^{x} (\alpha^{(p)} + \alpha^{(m)}) ds - i(p+m)\omega t}, \end{aligned} \tag{2.32}$$

each k^{th} mode can be written,

$$\begin{aligned} (-ik\omega + i\alpha_k\bar{u})\hat{u}^k + \bar{u}\frac{\partial \hat{u}^k}{\partial x} + \Psi^k \\ = -\sum_{p=-\infty}^{\infty}\sum_{m=-\infty}^{\infty} \Big[\hat{u}^p(i\alpha_m\hat{u}^m + \frac{\partial \hat{u}^m}{\partial x}) + \hat{v}^p\frac{\partial \hat{u}^m}{\partial y}\Big] e^{i \int_{x_0}^{x} (\alpha^p ds + \alpha^m - \alpha^k) - i(p+m-k)\omega t}. \end{aligned} \tag{2.33}$$

The summation can be truncated to a bounded summation, $\pm K$ for example, and the complex conjugate relationships made use of to simplify and reduce equations, $\hat{q}^{-k} = \hat{q}^{k\dagger}$. Harmonic balancing is used to reduce the equations further with $p + m - k = 0$ giving $p = k - m$ to arrive at,

$$\begin{aligned}(-ik\omega + i\alpha^{(k)}\bar{u})\hat{u}^{(k)} + \bar{u}\frac{\partial \hat{u}^{(k)}}{\partial x} + \Psi^{(k)} \\ = \sum_{m=-M}^{\infty} \Big[\hat{u}^{(k-m)}(i\alpha^{(m)}\hat{u}^{(m)} + \frac{\partial \hat{u}^{(m)}}{\partial x}) \\ + \hat{v}^{(k-m)}\frac{\partial \hat{u}^{(m)}}{\partial y}\Big] e^{i\int_{x_0}^{x}(\alpha^{(k-m)}ds + \alpha^{(m)} - \alpha^{(k)})},\end{aligned} \tag{2.34}$$

for all $k \in [0, K]$. The code also assumes that all non-linear harmonics are phase-locked with the real part of the fundamental (k=1) wave number such that,

$$\mathcal{R}(\alpha_k) = k\mathcal{R}(\alpha_1). \tag{2.35}$$

The wave number is phase-locked but the imaginary part, of the growth rate, of each harmonic is free to change with no constriction to the fundamental forcing mode. There are then k+1 coupled system of equations which are solved iteratively at each j^{th} stream-wise position until convergence is obtained in the growth rate of each harmonic $\hat{\phi}_j^k$. Each harmonic has its own closure condition which needs to be satisfied in the marching process.

The same boundary and initial conditions are applied as in the linear case. However, special care needs to be paid to the mean flow distortion (0,0) mode. For the (0,0) mode the pressure gradient term $\frac{\partial \hat{p}}{\partial x}$ is set to zero to ensure full parabolicity of the equations. The boundary condition in the free-stream is modified to,

$$\hat{u}_{00} = \frac{\partial \hat{v}_{00}}{\partial y} = \hat{w}_{00} = \hat{T}_{00} = \hat{p}_{00} = 0 \quad \text{as} \quad y \to \infty, \tag{2.36}$$

allowing for growth in displacement thickness from the corrected mean flow profile $(\bar{u} + \hat{u}_{00})$ due to the non-linear interactions. This enables the mean flow from the boundary layer solution to adjust itself in order to maintain mass conservation[14].

2.1.4 Linearised Harmonic Navier-Stokes (LHNS)

The linearised harmonic Navier-Stokes (LHNS), although requiring slightly more computational resource than the PSE, provide much greater information about the growth of the instability. They also have the capability to model receptivity[71].

Linear

The LHNS equations, representing the BiGlobal problem, are derived by introducing the following ansatz

$$\tilde{\phi}(x,n,q,t) = \hat{\phi}(x,n)e^{i(\beta q - \omega t)} + c.c., \tag{2.37}$$

where β is the wave number and ω is the frequency, both are real quantities. The LHNS assume strict periodicity in the span-wise direction and are harmonic in time. They comprise of few assumptions and are a fully elliptic set of equations where, unlike the PSE formulation, all terms are retained including importantly the stream-wise pressure derivative term. The partial differential equations can then be recast upon numerical discretisation into a large matrix problem of unknown field state points, namely

$$\mathcal{L}\hat{\phi} = \hat{r}. \tag{2.38}$$

$\mathcal{L}$ is a matrix of known coefficients, $\hat{\boldsymbol{\phi}}$ is a vector of the unknown perturbation field and $\hat{\mathbf{r}}$ a forcing vector. The solution vector, $\hat{\boldsymbol{\phi}}$, is obtained directly by a lower-upper matrix decomposition method; the equations are not solved by time marching. The forcing vector, $\hat{\mathbf{r}}$, is composed of first order Taylor expansions which modify the wall boundary condition to generate the disturbance ahead of the step feature. The wall inhomogeneity may be either stationary (to generate zero frequency disturbances) or non-stationary to generate travelling disturbances, as denoted in figure 2.1.

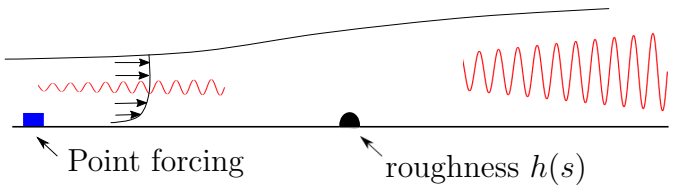

Figure 2.1: Depiction of the computational domain showing generation of the instability (red) within a fully developed laminar boundary layer and how this instability is modified when convecting over the roughness.

Non-linear

The non-linear harmonic Navier-Stokes (non-linear HNS) equations are capable of capturing weakly non-linear mode interaction and come at a fraction of the cost of DNS. In order to solve for the non-linear problem, the perturbation is assumed to take the following form,

$$\tilde{\phi} = \sum_{l=-\infty}^{\infty} \sum_{m=-\infty}^{\infty} \hat{\phi}_{l,m}(x,n) e^{i(m\beta q - l\omega t)}. \tag{2.39}$$

The Fourier series can be truncated to a finite number of modes though the application of complex conjugate applications, harmonic balancing applied. Contrary to the PSE, phase locking does not need to be assumed and enforced. It will arise naturally if indeed the phase locking mechanism is dominant. For the compressible non-linear problem these summations become extremely difficult to solve with harmonic balancing, meaning instead fast Fourier transforms are utilised as described in the non-linear PSE section. The numerical strategy is nearly identical to solving the non-linear PSE equations, and is in some way less complicated relative to the PSE.

Limitations

The limitations of this method are few. The LHNS require slightly more computational resource than the PSE, which is mainly due to requiring the direct inversion of a very large matrix through usage of a banded LU factorisation solver[61]. They also currently assume that the steady baseline stream-wise flow derivatives in the normal velocity component are zero[59]. Whilst this has been shown to have little impact in the analysis of smoothly varying aerofoil geometries, i.e. in clean computations, it is expected that in the presence of a step like feature, this quantity may no-longer be quite so negligible. This is applied due to the immense difficulty of computing these derivatives accurately, as opposed to any conceptual issue.

Computational Framework

The equations are discretised with a fourth order accurate central finite differencing scheme in the stream-wise direction and a pseudo-spectral approach is applied in the surface normal direction. This pseudo-spectral approach comprises of a Chebyshev collocation method using Gauss-Lobatto collocation points to evaluate the dependent variables. Gauss-Lobatto points are defined to include both ends of the domain and are given by,

$$\eta_i = cos\big(\frac{\pi * i}{N_y}\big), \quad i = 0, 1, ..., N_y, \tag{2.40}$$

where η_i is the Gauss-Lobatto point existing in $[-1, 1]$ and N_y is the order of the Chebyshev polynomial. The flow field can then be represented with a series of Chebyshev

polynomials at each of these points,

$$f(\eta_i) = \sum_{k=0}^{N_y} A_k T_k(\eta_i), \tag{2.41}$$

where A_k is the corresponding amplitude to the order k Chebychev polynomial, T_k,

$$T_k(\eta_i) = cos(kcos^{-1}(\eta_i)). \tag{2.42}$$

Knowing $T_0 = 1$ and $T_1 = \eta_i$ the Chebychev polynomials can also be derived recursively.

The inflow plane is situated sufficiently upstream of the actuation point such that perturbations can be considered negligible there. At the outflow boundary the PSE radiation condition is applied,

$$\frac{\partial \hat{\boldsymbol{\phi}}}{\partial x} = i\alpha\hat{\boldsymbol{\phi}}. \tag{2.43}$$

Here α is the stream-wise wave number estimated by a linear PSE computation. To introduce the disturbance to the domain the no-slip boundary conditions are relaxed at the required forcing location. This is generally dictated from experiments though it is well known from receptivity theory that forcing at the neutral point generally provides the most efficient means to generate disturbances. The wall conditions are relaxed near the location of the neutral point through application of Taylor expanded boundary conditions,

$$\begin{aligned}
\hat{\boldsymbol{u}}(x,0) &= -\epsilon\hat{H}(x)\frac{\partial\bar{\boldsymbol{u}}(x,0)}{\partial y},\\
\hat{\boldsymbol{v}}(x,0) &= -\epsilon\hat{H}(x)\Big(i\omega + \frac{\partial\bar{\boldsymbol{v}}(x,0)}{\partial y}\Big),\\
\hat{\boldsymbol{w}}(x,0) &= -\epsilon\hat{H}(x)\frac{\partial\bar{\boldsymbol{w}}(x,0)}{\partial y},
\end{aligned}$$

where $\epsilon << 1$ and $H(x,z)$ represents the roughness feature and $\hat{H}(x)e^{i\beta z}$ is the corresponding Fourier decomposition in the span-wise direction. The perturbation is assumed to be negligible in the far field. In order to solve the linear problem given by equation 2.38 a lower-upper factorisation is utilised. Further details may be found in[61] and[71].

Typically, 1800 points are used in the stream-wise direction, a more crucial criterion that we adhere to is having a minimum of 20 points per disturbance wavelength. In the wall-normal direction we typically use 51 Chebyshev polynomials for the no step cases. To resolve disturbance evolution over the very rapid changes in the BFS and

step induced boundary-layer flows as many as 10000 stream-wise and 90+ Chebyshev polynomials are subsequently utilised.

The non-linear HNS formulation is similar to that described in the PSE computational framework section, however this is much simpler as a normalisation condition does not have to be satisfied for each k^{th} mode. If we follow the same example as given in that earlier section 2.1.3 the ansatz would be,

$$\tilde{q}(x,y,t) = \sum_{k=-\infty}^{\infty} \hat{q}^k(x,y)e^{-ik\omega t}. \tag{2.44}$$

The equations are formulated into the linear and non-linear parts for each mode of superscript k, such that,

$$\mathcal{L}^k\phi^k = \mathcal{N}^k, \tag{2.45}$$

for each k^{th} mode. The non-linear matrix, $\mathcal{N}^k$, consists of the non-linear components and the wall forcing actuation. The Lower Upper block factorisation must be solved for each k^{th} mode. The $K+1$ system of coupled non-linear equations is solved in parallel and iteratively. The LU factorisation of the $\mathcal{L}^k$ factors remain unchanged with only the $\mathcal{N}^k$ forcing terms being updated throughout the iterations. The $\mathcal{N}^k$ variable comprises the nonlinear field source terms as well as any wall forced terms that are imposed as boundary conditions.

2.2 Roughness Transformation

The generation of a perturbation via a small surface actuation has been discussed; now consideration is needed for the relatively larger scale step feature and its incorporation into the modelling. It is important to note that for both PSE and LHNS codes, the solvers have visibility of the roughness though the base-flow profiles, but require an additional transformation to allow resolution of the step feature introduced. The original perturbed PSE[58] and LHNS[61] equations have been formulated based upon a body-fitted clean geometry coordinate system, without allowance for very rapid variations in surface topography such as those considered in this work.

In order to incorporate large scale roughness, an addition non-orthogonal coordinate system must be introduced and a parameter assigned to the roughness profile, $h(x)$, which is dependent on the stream-wise body fitted coordinate, x. The clean body fitted coordinate system (x,n,q) is transformed to the roughness incorporating coordinate system (s,Y,z) by application of the following transformation,

$$s = x, \qquad Y = n - h(x), \qquad z = q, \tag{2.46}$$

see figure 2.2 also. Transforming the variables with this implies that

$$\frac{\partial}{\partial n} = \frac{\partial}{\partial Y}, \qquad \frac{\partial^2}{\partial n^2} = \frac{\partial^2}{\partial Y^2}, \tag{2.47}$$

$$\frac{\partial}{\partial x} = \frac{\partial}{\partial s} - h'(s)\frac{\partial}{\partial Y}, \qquad \frac{\partial^2}{\partial x^2} = h'^2\frac{\partial^2}{\partial Y^2} - 2h'\frac{\partial^2}{\partial Y \partial s} - h''\frac{\partial}{\partial Y} + \frac{\partial^2}{\partial s^2}. \tag{2.48}$$

Since, upon substitution into the Navier-Stokes equations, the transformation is only introduced though the derivative terms, we can see that the roughness edges will cause the key difference between the original and transformed solutions, where dh/ds and d^2h/ds^2 hold non-zero values. If the newly introduced roughness feature shows streamwise invariance, i.e. with $dh/ds = d^2h/ds^2 = 0$, the equations will reduce to the original body-fitted equation set. The final transformed equation sets, which include the rapid geometrical step modelling, will from here on be referred to as the LHNSh and PSEh models.

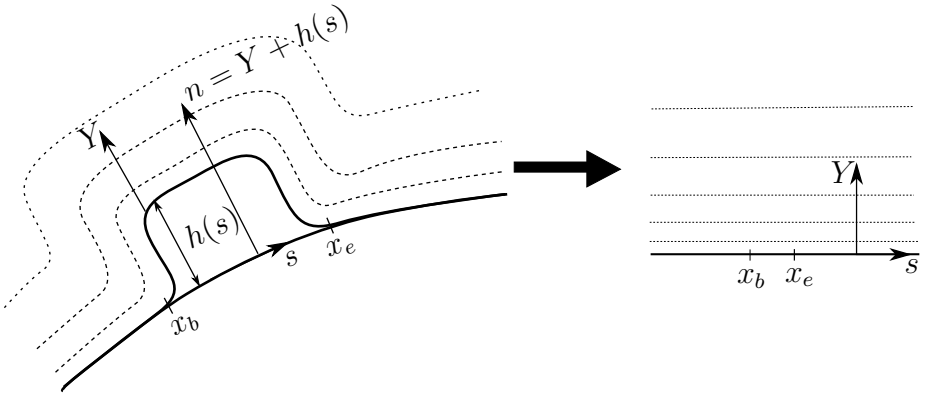

Figure 2.2: Depiction of coordinate transformation to decompose the roughness incorporating geometry, (x, n, q), to the body fitted clean surface, (s, Y, z), plus a separate h component. Computational domain is depicted on the right.

2.3 Linearised Harmonic Navier-Stokes with Roughness Correction (LHNSh)

2.3.1 Linear

We begin with the linearised incompressible body fitted Navier-Stokes equations 2.4 where an infinitely swept wing assumption is enforced, $\frac{\partial \bar{\phi}}{\partial q} = 0$. Upon substitution of the ansatz 2.37 we attain,

$$\begin{aligned} &R_e(\hat{u}\bar{v} + \bar{u}\hat{v})\kappa\chi - \hat{u}\kappa^2\chi^2 - R_e\chi\hat{p}_x - R_e\hat{v}\bar{u}_n - R_e\bar{v}\hat{u}_n - \kappa\chi\hat{u}_n + \hat{u}_{nn} \\ &\quad + R_e i\omega\hat{u} - R_e i\beta\bar{w}\hat{u} - \beta^2\hat{u} - R_e\hat{u}\chi\bar{u}_x - R_e\bar{u}\chi\hat{u}_x \\ &\quad + \chi^2\hat{u}_{xx} - 2\kappa\chi^2\hat{v}_x - \hat{v}\chi^2(1 + n\kappa\chi)\kappa_x + n\chi^3\hat{u}_x\kappa_x = 0, \end{aligned} \tag{2.49a}$$

$$
\begin{aligned}
-R_e 2\hat{u}\bar{u}\kappa\chi - \hat{v}\kappa^2\chi^2 - R_e\hat{p}_n + 2\kappa\chi^2\hat{u}_x - R_e\hat{v}\bar{v}_n - R_e\bar{v}\hat{v}_n - \kappa\chi\hat{v}_n + \hat{v}_{nn} \\
+ R_e i\omega\hat{v} - R_e i\beta\bar{w}\hat{v} - \beta^2\hat{v} - R_e\hat{u}\chi\bar{v}_x - R_e\bar{u}\chi\hat{v}_x \\
+ \chi^2\hat{v}_{xx} + \hat{u}\chi^2(1 + n\kappa\chi)\kappa_x + n\chi^3\hat{v}_x\kappa_x = 0,
\end{aligned} \tag{2.49b}
$$

$$
\begin{aligned}
-R_e i\beta\hat{p} - R_e\hat{v}\bar{w}_n - R_e\bar{v}\hat{w}_n - \kappa\chi\hat{w}_n + \hat{w}_{nn} + R_e i\omega\hat{w} - R_e i\beta\bar{w}\hat{w} - \beta^2\hat{w} \\
- R_e\hat{u}\chi\bar{w}_x - R_e\bar{u}\chi\hat{w}_x + \chi^2\hat{w}_{xx} + n\chi^3\hat{w}_x\kappa_x = 0,
\end{aligned} \tag{2.49c}
$$

$$
\chi\hat{u}_x + \hat{v}_n + i\beta\hat{w} - \hat{v}\kappa\chi = 0. \tag{2.49d}
$$

Now substituting the transformation in equation 2.46 into these equations 2.49 results with the Linearised Navier-Stokes Equations with transformation (LHNSh). Notice here that only the perturbation terms have had the transformation applied to them. This is due to the base flow, extracted from the Nektar++ solver, already having these extra h terms included within the base flow derivatives. This happens in the python script to be covered in chapter 3.

$$
\begin{aligned}
R_e(\hat{u}\bar{v} + \bar{u}\hat{v})\kappa\chi - \hat{u}\kappa^2\chi^2 - R_e\chi(\hat{p}_s - h'\hat{p}_Y) - R_e\hat{v}\bar{u}_Y - R_e\bar{v}\hat{u}_Y - \kappa\chi\hat{u}_Y + \hat{u}_{YY} \\
+ R_e i\omega\hat{u} - R_e i\beta\bar{w}\hat{u} - \beta^2\hat{u} - R_e\hat{u}\chi\bar{u}_s - R_e\bar{u}\chi(\hat{u}_s - h'\hat{u}_Y) \\
+ \chi^2(\hat{u}_{ss} - 2h'\hat{u}_{sY} - h''\hat{u}_Y + h'^2\hat{u}_{YY}) - 2\kappa\chi^2(\hat{v}_s - h'\hat{v}_Y) \\
- \hat{v}\chi^2(1 + (Y + h)\kappa\chi)\kappa_s + (Y + h)\chi^3(\hat{u}_s - h'\hat{u}_Y)\kappa_s = 0,
\end{aligned} \tag{2.50a}
$$

$$
\begin{aligned}
-R_e 2\hat{u}\bar{u}\kappa\chi - \hat{v}\kappa^2\chi^2 - R_e\hat{p}_Y + 2\kappa\chi^2(\hat{u}_s - h'\hat{u}_Y) - R_e\hat{v}\bar{v}_Y - R_e\bar{v}\hat{v}_Y - \kappa\chi\hat{v}_Y + \hat{v}_{YY} \\
+ R_e i\omega\hat{v} - R_e i\beta\bar{w}\hat{v} - \beta^2\hat{v} - R_e\hat{u}\chi\bar{v}_s - R_e\bar{u}\chi(\hat{v}_s - h'\hat{v}_Y) \\
+ \chi^2(\hat{v}_{ss} - 2h'\hat{v}_{sY} - h''\hat{v}_Y + h'^2\hat{v}_{YY}) + \hat{u}\chi^2(1 + (Y + h)\kappa\chi)\kappa_s \\
+ (Y + h)\chi^3(\hat{v}_s - h'\hat{v}_Y)\kappa_s = 0,
\end{aligned} \tag{2.50b}
$$

$$
\begin{aligned}
-R_e i\beta\hat{p} - R_e\hat{v}\bar{w}_Y - R_e\bar{v}\hat{w}_Y - \kappa\chi\hat{w}_Y + \hat{w}_{YY} + R_e i\omega\hat{w} - R_e i\beta\bar{w}\hat{w} + -\beta^2\hat{w} \\
- R_e\hat{u}\chi\bar{w}_s - R_e\bar{u}\chi(\hat{w}_s - h'\hat{w}_Y) + \chi^2(\hat{w}_{ss} - 2h'\hat{w}_{sY} - h''\hat{w}_Y + h'^2\hat{w}_{YY}) \\
+ (Y + h)\chi^3(\hat{w}_s - h'\hat{w}_Y)\kappa_s = 0,
\end{aligned} \tag{2.50c}
$$

$$
\chi(\hat{u}_s - h'\hat{u}_Y) + \hat{v}_Y + i\beta\hat{w} - \hat{v}\kappa\chi = 0. \tag{2.50d}
$$

To complete the problem, a boundary condition at the wall is also required. This is calculated by substituting the continuity and differential of the continuity, with respect to the normal component, into the normal-momentum equation to replace v_Y and v_{YY}. No slip is applied for u and w, but not for v to allow for the suction and blowing to initiate the perturbation.

In order to simulate this numerically, the physical space must then be transformed

once again to a bounded computational space. This is achieved with the mapping $Y = \frac{g\eta}{b-\eta}$ to move from $Y(0,\infty) \mapsto \eta(0,1)$, and an equivalent respective mapping for $s(0,\infty) \mapsto \xi(0,1)$, where g and b are constants. This type of mapping, taking the wall normal direction for example, ensures that the grid points are clustered abundantly close to the wall with cells gradually lengthening when traversing away from the wall. In the stream-wise direction this results with fine elements close to the leading edge of the geometry which become coarser when moving downstream. In this work we do not utilise a streamwise stretching, a uniform spacing is preferable, due to the short stream-wise length scales of the roughness.

The assumption $\bar{\phi}_{ss} = 0$ is also adopted since these terms are extremely difficult to compute accurately. This is reasonable for the clean boundary layer solutions but may become a limitation in the current framework since we expect these terms to play more of a role when a roughness is present. However, since the nature of our roughness are very localised and short-scale, contribution of the $\bar{\phi}_{ss}$ term to the overall disturbance modifications may well be relatively insignificant.

The compressible formulation of the problem is more extensive but follows the same principle. The final compressible LHNSh equation set is given by,

s-momentum :

$$
\begin{aligned}
&\Big[\frac{\chi\kappa\bar{\rho}R_e\bar{v} - iR_e\bar{w}\bar{\rho}\beta - \chi\bar{u}_sR_e\bar{\rho} + iR_e\bar{\rho}\omega + \bar{\mu}_Y\kappa\chi}{\bar{\mu}} - \beta^2 - \kappa^2\chi^2\Big]\hat{u} \\
&+ \Big[\frac{\chi\kappa\bar{\rho}R_e\bar{u} - \bar{\mu}_sr\chi^2\kappa - \bar{u}_YR_e\bar{\rho}}{\bar{\mu}} - r\chi^3\kappa_s\kappa Y - r\chi^3\kappa_s\kappa h - r\chi^2\kappa_s\Big]\hat{v} \\
&+ \frac{i\bar{\mu}_sm\chi\hat{w}\beta}{\bar{\mu}} + \Big[\frac{\chi R_e\bar{u}\bar{v}\kappa\bar{\rho} - \bar{u}_YR_e\bar{v}\bar{\rho} - \chi\bar{u}_sR_e\bar{u}\bar{\rho}}{\bar{\mu}\bar{p}}\Big]\hat{p} \\
&+ \Big[\big(\bar{u}\kappa\chi f_{TT}\bar{T}_Y + i\chi\bar{w}_sf_T\beta + r\chi^2\bar{u}_sf_{TT}\bar{T}_s + m\chi\bar{v}_Yf_{TT}\bar{T}_s - f_T\kappa\chi^2\bar{v}_sr \\
&- f_Tr\bar{v}\chi^3\kappa_s\kappa Y - f_Tr\bar{v}\chi^3\kappa_s\kappa h - f_Tr\bar{v}\chi^2\kappa_s - f_T\bar{u}\kappa^2\chi^2 - f_T\kappa\chi\bar{u}_Y \\
&- f_T\kappa\chi^2\bar{v}_s + f_Tr\chi^2\bar{u}_{ss} + f_TQ\chi\bar{v}_{sY} + \chi\bar{v}_sf_{TT}\bar{T}_Y + f_T\bar{u}_{YY} + f_Tr\chi^3\bar{u}_s\kappa_sh \\
&- r\chi^2\bar{v}\kappa f_{TT}\bar{T}_s + f_Tr\chi^3\bar{u}_s\kappa_sY + \bar{u}_Yf_{TT}\bar{T}_Y\big)\frac{1}{\bar{\mu}} + \frac{\bar{u}_YR_e\bar{v}\bar{\rho} - \chi R_e\bar{u}\bar{v}\kappa\bar{\rho} + \chi\bar{u}_sR_e\bar{u}\bar{\rho}}{\bar{\mu}\bar{T}}\Big]\hat{T} \\
&+ \Big[\frac{-R_e\bar{u}\bar{\rho}\chi + \bar{\mu}_sr\chi^2}{\bar{\mu}} + r\chi^3\kappa_sY + r\chi^3\kappa_sh\Big]\hat{u}_s \\
&+ \Big[\frac{-\bar{\mu}_sr\chi^2h_s - R_e\bar{v}\bar{\rho} + \bar{\mu}_Y + R_e\bar{u}\bar{\rho}\chi h_s}{\bar{\mu}} - r\chi^3\kappa_sYh_s - r\chi^3\kappa_shh_s - \kappa\chi - r\chi^2h_{ss}\Big]\hat{u}_Y \\
&+ \Big[-\kappa\chi^2 + \frac{\bar{\mu}_Y\chi}{\bar{\mu}} - \kappa\chi^2r\Big]\hat{v}_s + \Big[\frac{-\bar{\mu}_Y\chi h_s + \bar{\mu}_sm\chi}{\bar{\mu}} + \kappa\chi^2rh_s + \kappa\chi^2h_s\Big]\hat{v}_Y \\
&+ iQ\chi\beta\hat{w}_s - iQ\chi\beta h_s\hat{w}_Y - \frac{R_e\chi\hat{p}_s}{\bar{\mu}} + \frac{R_e\chi h_s\hat{p}_Y}{\bar{\mu}} + \Big[\frac{r\chi^2\bar{u}_sf_T + m\chi\bar{v}_Yf_T - r\chi^2\bar{v}\kappa f_T}{\bar{\mu}}\Big]\hat{T}_s \\
&+ \Big[\frac{\bar{u}\kappa\chi f_T + r\chi^2\bar{v}\kappa f_Th_s + \chi\bar{v}_sf_T - r\chi^2\bar{u}_sf_Th_s - m\chi\bar{v}_Yf_Th_s + \bar{u}_Yf_T}{\bar{\mu}}\Big]\hat{T}_Y \\
&+ r\chi^2h_s^2\hat{u}_{YY} - 2r\chi^2h_s\hat{u}_{sY} + r\chi^2\hat{u}_{ss} - Q\chi h_s\hat{v}_{YY} + Q\chi\hat{v}_{sY} + \hat{u}_{YY} = \mathcal{N}_1,
\end{aligned}
\tag{2.51a}
$$

Y-momentum :

$$
\begin{aligned}
&\Big[\frac{-\chi^2\kappa_s/r - 2\chi R_e\bar{u}\kappa\bar{\rho} - \chi\bar{v}_s R_e\bar{\rho} + \chi^2\bar{\mu}_s\kappa}{\bar{\mu}r} + \frac{-\chi^3\kappa_s\kappa Y - \chi^3\kappa_s\kappa h}{r}\Big]\hat{u}\\
&+\Big[\frac{-iR_e\bar{w}\bar{\rho}\beta + iR_e\bar{\rho}\omega - \bar{\mu}_Y m\kappa\chi - \bar{v}_Y R_e\bar{\rho}}{\bar{\mu}r} - \frac{\beta^2}{r} - \kappa^2\chi^2\Big]\hat{v}\\
&+\frac{i\bar{\mu}_Y m\hat{w}\beta}{\bar{\mu}r} + \Big[\frac{-\chi\bar{v}_s R_e\bar{u}\bar{\rho} - \chi R_e\bar{u}^2\kappa\bar{\rho} - \bar{v}_Y R_e\bar{v}\bar{\rho}}{\bar{\mu}r\bar{p}}\Big]\hat{p}\\
&+\Big[\big(-f_T\bar{u}\chi^3\kappa_s\kappa h - m\bar{v}\kappa\chi f_{TT}\bar{T}_Y - f_T\bar{u}\chi^3\kappa_s\kappa Y + f_T\chi^3\bar{v}_s\kappa_s h + f_T\chi^3\bar{v}_s\kappa_s Y\\
&+m\chi\bar{u}_s f_{TT}\bar{T}_Y + \bar{u}\kappa\chi^2 f_{TT}\bar{T}_s + f_T\kappa\chi^2\bar{u}_s + i\bar{w}_Y f_T\beta + f_T Q\chi\bar{u}_{Ys} - f_T\bar{u}\chi^2\kappa_s\\
&\chi\bar{u}_Y f_{TT}\bar{T}_s + \chi^2\bar{v}_s f_{TT}\bar{T}_s + f_T\chi^2\bar{v}_{ss}\big)\frac{1}{\bar{\mu}r} + \frac{\chi R_e\bar{u}^2\kappa\bar{\rho} + \chi\bar{v}_s R_e\bar{u}\bar{\rho} + \bar{v}_Y R_e\bar{v}\bar{\rho}}{\bar{\mu}r\bar{T}}\\
&+\frac{f_T\bar{v}_{YY} - f_T\bar{v}\kappa^2\chi^2 - f_T\kappa\chi\bar{v}_Y + f_T\kappa\chi^2\bar{u}_s + \bar{v}_Y f_{TT}\bar{T}_Y}{\bar{\mu}}\Big]\hat{T}\\
&+\Big[\frac{\kappa\chi^2 + \bar{\mu}_Y m\chi}{\bar{\mu}r} + \frac{\kappa\chi^2}{r}\Big]\hat{u}_s + \Big[\frac{-\bar{\mu}_Y m\chi h_s + \chi\bar{\mu}_s}{\bar{\mu}r} - \frac{\kappa\chi^2 h_s}{r} - \kappa\chi^2 h_s\Big]\hat{u}_Y\\
&+\Big[\frac{-R_e\bar{u}\bar{\rho}\chi + \chi^2\bar{\mu}_s}{\bar{\mu}r} + \frac{\chi^3\kappa_s Y + \chi^3\kappa_s h}{r}\Big]\hat{v}_s + \Big[-\kappa\chi + \frac{\bar{\mu}_Y}{\bar{\mu}} + \frac{R_e\bar{u}\bar{\rho}\chi h_s}{\bar{\mu}r}\\
&+\frac{-\chi^3\kappa_s h h_s - \chi^3\kappa_s Y h_s - \chi^2 h_{ss})}{r} + \frac{-\chi^2\bar{\mu}_s h_s - R_e\bar{v}\bar{\rho}}{\bar{\mu}r}\Big]\hat{v}_Y + \frac{iQ\chi\hat{w}_Y\beta}{r}\\
&+\frac{-R_e\hat{p}_Y}{\bar{\mu}r} + \Big[\frac{\bar{u}\kappa\chi^2 f_T + \chi\bar{u}_Y f_T + \chi^2\bar{v}_s f_T}{\bar{\mu}r}\Big]\hat{T}_s\\
&+\Big[\frac{-\bar{u}\kappa\chi^2 f_T h_s - m\bar{v}\kappa\chi f_T + m\chi\bar{u}_s f_T - \chi^2\bar{v}_s f_T h_s - \chi\bar{u}_Y f_T h_s}{\bar{\mu}r} + \frac{\bar{v}_Y f_T}{\bar{\mu}}\Big]\hat{T}_Y\\
&+\frac{\chi^2\hat{v}_{ss}}{r} + \hat{v}_{YY} + \frac{Q\chi\hat{u}_{Ys}}{r} - \frac{Q\chi h_s\hat{u}_{YY}}{r} - \frac{2\chi^2\hat{v}_{Ys}h_s}{r} + \frac{\chi^2 h_s^2\hat{v}_{YY}}{r} = \mathcal{N}_2,
\end{aligned}
\tag{2.51b}
$$

q-momentum :

$$
\begin{aligned}
&\big[\frac{-\chi\bar{w}_s R_e\bar{\rho}+i\chi\bar{\mu}_s\beta}{\bar{\mu}}\big]\hat{u}+\big[\frac{-iQ\chi\kappa\beta-\bar{w}_Y R_e\bar{\rho}+i\bar{\mu}_Y\beta}{\bar{\mu}}\big]\hat{v}\\
&+\big[\frac{iR_e\bar{\rho}\omega-iR_e\bar{w}\bar{\rho}\beta}{\bar{\mu}}-r\beta^2\big]\hat{w}+\big[\frac{-\bar{w}_Y R_e\bar{v}\bar{\rho}-\chi\bar{w}_s R_e\bar{u}\bar{\rho}}{\bar{\mu}\bar{p}}-\frac{iR_e\beta}{\bar{\mu}}\big]\hat{p}\\
&+\big[\big(-f_T\kappa\chi\bar{w}_Y+\chi^2\bar{w}_s f_{TT}\bar{T}_s-imf_T\beta\bar{v}\kappa\chi+f_T\chi^3\bar{w}_s\kappa_s Y+f_T\chi^3\bar{w}_s\kappa_s h\\
&+imf_T\beta\bar{v}_Y+imf_T\beta\chi\bar{u}_s+\bar{w}_Y f_{TT}\bar{T}_Y+f_T\chi^2\bar{w}_{ss}+f_T\bar{w}_{YY}\big)\frac{1}{\bar{\mu}}+\frac{\bar{w}_Y R_e\bar{v}\bar{\rho}+\chi\bar{w}_s R_e\bar{u}\bar{\rho}}{\bar{\mu}\bar{T}}\big]\hat{T}\\
&-iQ\chi\beta\hat{u}_Y h_s+iQ\hat{v}_Y\beta+iQ\chi\beta\hat{u}_s+\big[\frac{-R_e\bar{u}\bar{\rho}\chi+\chi^2\bar{\mu}_s}{\bar{\mu}}+\chi^3\kappa_s Y+\chi^3\kappa_s h\big]\hat{w}_s\\
&+\big[\frac{-\chi^2\bar{\mu}_s h_s-R_e\bar{v}\bar{\rho}+R_e\bar{u}\bar{\rho}\chi h_s+\bar{\mu}_Y}{\bar{\mu}}-\chi^3\kappa_s Y h_s-\chi^3\kappa_s h h_s-\chi^2 h_{ss}-\kappa\chi\big]\hat{w}_Y\\
&+\frac{\chi^2\bar{w}_s f_T\hat{T}_s}{\bar{\mu}}+\big[\frac{-\chi^2\bar{w}_s f_T h_s+\bar{w}_Y f_T}{\bar{\mu}}\big]\hat{T}_Y-2\chi^2\hat{w}_{Y s}h_s+\chi^2 h_s^2\hat{w}_{YY}+\chi^2\hat{w}_{ss}+\hat{w}_{YY}=\mathcal{N}_3,
\end{aligned}
\tag{2.51c}
$$

Energy :

$$
\begin{aligned}
&\big[M^2(-1+\gamma)\big(\frac{2\bar{u}_Y\kappa\chi+2\kappa\chi^2\bar{v}_s+2\bar{u}\kappa^2\chi^2+2i\chi\beta\bar{w}_s}{R_e}+\frac{\chi\bar{p}_s}{\bar{\mu}}\big)-\frac{\bar{\rho}\sigma\chi\bar{T}_s}{\bar{\mu}}\big]\hat{u}\\
&+\big[M^2(-1+\gamma)\big(\frac{2i\beta\bar{w}_Y-2m\kappa\chi\bar{v}_Y+2r\chi^2\bar{v}\kappa^2-2r\chi^2\bar{u}_s\kappa}{R_e}+\frac{\bar{p}_Y}{\bar{\mu}}\big)-\frac{\bar{\rho}\sigma\bar{T}_Y}{\bar{\mu}}\big]\hat{v}\\
&+\big[M^2(-1+\gamma)\big(\frac{2im\chi\beta\bar{u}_s-2im\chi\beta\bar{v}\kappa+2im\bar{v}_Y\beta}{R_e}\big)\big]\hat{w}\\
&+\big[M^2(-1+\gamma)\big(\frac{i\bar{w}\beta-iM^2(-1+\gamma)\omega}{\bar{\mu}}\big)+\frac{-\bar{\rho}\sigma\bar{u}\chi\bar{T}_s-\bar{\rho}\sigma\bar{v}\bar{T}_Y}{\bar{\mu}\bar{p}}\big]\hat{p}\\
&+\big[M^2(-1+\gamma)\big(2f_T\bar{u}\kappa\chi^2\bar{v}_s+2f_Tm\chi\bar{u}_s\bar{v}_Y+f_Tr\chi^2\bar{v}^2\kappa^2+2f_T\bar{u}\kappa\chi\bar{u}_Y\\
&-2f_Tm\bar{v}\kappa\chi\bar{v}_Y-2f_Tr\chi^2\bar{v}\kappa\bar{u}_s+f_T\bar{u}^2\kappa^2\chi^2+2f_T\chi\bar{u}_Y\bar{v}_s+f_Tr\chi^2\bar{u}_s^2+f_T\bar{u}_Y^2\\
&f_T\bar{w}_Y^2+f_T\chi^2\bar{v}_s^2+f_T\chi^2\bar{w}_s^2+f_Tr\bar{v}_Y^2\big)\frac{1}{\bar{\mu}R_e}+\frac{\bar{\rho}\sigma\bar{u}\chi\bar{T}_s+\bar{\rho}\sigma\bar{v}\bar{T}_Y}{\bar{\mu}\bar{T}}\\
&+\frac{f_T\chi^3\bar{T}_s\kappa_sY+f_T\chi^3\bar{T}_s\kappa_sh+f_T\chi^2\bar{T}_{ss}+\chi^2\bar{T}_s^2f_{TT}-f_T\kappa\chi\bar{T}_Y+f_T\bar{T}_{YY}+f_{TT}\bar{T}_Y^2}{\bar{\mu}R_e}\\
&+\frac{-\beta^2}{R_e}+\frac{i\bar{\rho}\sigma\omega-i\bar{\rho}\sigma\bar{w}\beta}{\bar{\mu}}\big]\hat{T}+\big[M^2(-1+\gamma)\big(\frac{-2r\chi^2\bar{v}\kappa+2m\chi\bar{v}_Y+2r\chi^2\bar{u}_s}{R_e}\big)\big]\hat{u}_s\\
&+\big[M^2(-1+\gamma)\big(\frac{2\chi\bar{v}_s-2m\chi\bar{v}_Yh_s-2r\chi^2\bar{u}_sh_s+2r\chi^2\bar{v}\kappa h_s+2\bar{u}_Y+2\bar{u}\kappa\chi}{R_e}\big)\big]\hat{u}_Y\\
&+\big[M^2(-1+\gamma)\big(\frac{2\chi\bar{u}_Y+2\chi^2\bar{v}_s+2\bar{u}\kappa\chi^2}{R_e}\big)\big]\hat{v}_s\\
&+\big[M^2(-1+\gamma)\big(\frac{2r\bar{v}_Y-2m\bar{v}\kappa\chi-2\bar{u}\kappa\chi^2h_s-2\chi\bar{u}_Yh_s-2\chi^2\bar{v}_sh_s+2m\chi\bar{u}_s}{R_e}\big)\big]\hat{v}_Y\\
&+\frac{2M^2(-1+\gamma)\chi^2\bar{w}_s\hat{w}_s}{R_e}+\big[M^2(-1+\gamma)\big(\frac{2\bar{w}_Y-2\chi^2\bar{w}_sh_s}{R_e}\big)\big]\hat{w}_Y\\
&+\frac{M^2(-1+\gamma)\bar{u}\chi\hat{p}_s}{\bar{\mu}}+\big[M^2(-1+\gamma)\big(\frac{\bar{v}-\bar{u}\chi h_s}{\bar{\mu}}\big)\big]\hat{p}_Y\\
&+\big[\frac{\chi^2\bar{\mu}_s+\chi^2\bar{T}_sf_T}{\bar{\mu}R_e}+\frac{\chi^3\kappa_sY+\chi^3\kappa_sh}{R_e}+\frac{-\bar{\rho}\sigma\bar{u}\chi}{\bar{\mu}}\big]\hat{T}_s\\
&+\big[\frac{\bar{T}_Yf_T-\chi^2\bar{T}_sf_Th_s+\bar{\mu}_Y-\chi^2\bar{\mu}_sh_s}{\bar{\mu}R_e}+\frac{-\bar{\rho}\sigma\bar{v}+\bar{\rho}\sigma\bar{u}\chi h_s}{\bar{\mu}}\\
&+\frac{-\chi^2h_{ss}-\kappa\chi-\chi^3\kappa_sYh_s-\chi^3\kappa_shh_s}{R_e}\big]\hat{T}_Y-\frac{2\chi^2\hat{T}_{Ys}h_s}{R_e}\\
&+\frac{\hat{T}_{YY}}{R_e}+\frac{\chi^2h_s^2\hat{T}_{YY}}{R_e}+\frac{\chi^2\hat{T}_{ss}}{R_e}=\mathcal{N}_4,
\end{aligned}
\tag{2.51d}
$$

Continuity :

$$\begin{aligned}
&\frac{\hat{u}\chi\bar{\rho}_s}{\bar{\rho}} + \big[\frac{\bar{\rho}_Y}{\bar{\rho}} - \kappa\chi\big]\hat{v} + i\hat{w}\beta + \big[\frac{\chi\bar{u}_s - i\omega + \bar{v}_Y + i\bar{w}\beta - \kappa\chi\bar{v}}{\bar{p}} \\
&\quad + \frac{-\bar{u}\chi\bar{T}_s - \bar{v}\bar{T}_Y}{\bar{p}\bar{T}}\big]\hat{p} + \big[\frac{\bar{v}\bar{T}_Y + \bar{u}\chi\bar{T}_s}{\bar{T}^2} + \frac{i\omega - \chi\bar{u}_s + \kappa\chi\bar{v} - i\bar{w}\beta - \bar{v}_Y}{\bar{T}} \\
&\quad + \frac{-\bar{u}\chi\bar{\rho}_s - \bar{v}\bar{\rho}_Y}{\bar{\rho}\bar{T}}\big]\hat{T} + \chi\hat{u}_s - \chi\hat{u}_Y h_s + \hat{v}_Y + \frac{\bar{u}\chi\hat{p}_s}{\bar{p}} \\
&\quad + \big[\frac{\bar{v} - \bar{u}\chi h_s}{\bar{p}}\big]\hat{p}_Y - \frac{\bar{u}\chi\hat{T}_s}{\bar{T}} + \big[\frac{-\bar{v}}{\bar{T}} + \frac{\bar{u}\chi h_s}{\bar{T}}\big]\hat{T}_Y = \mathcal{N}_5.
\end{aligned} \tag{2.51e}$$

For the linear problem all $\mathcal{N}_j$, where $j = 1:5$, are zero. The boundary condition at the wall is calculated in the same manner as for the incompressible problem and the same final transformation is applied to the whole equation set to bound the domain to the computational space.

2.3.2 Non-linear

The non-linear problem is more extensive once again. In addition to the terms stated in equations 2.51, the non-linear terms are obtained by retaining $\mathcal{O}(\epsilon^2)$ and $\mathcal{O}(\epsilon^3)$ during the linearising step, meaning there are extra inviscid and viscous terms to be included in the equations. The following equations now define the extra terms for $\mathcal{N}_j$, where $j = 1:5$, in equations 2.51 to complete the non-linear problem.

$$\begin{aligned}
&\big[\big((-\chi\tilde{u}_Y\tilde{u} - \tilde{u}_Y\bar{u}\chi + \tilde{T}_Y\chi\gamma M^2)\tilde{\rho} - \tilde{u}_Y\bar{\rho}\chi\tilde{u} - \tilde{T}\chi\tilde{\rho}_Y\gamma M^2\big)h_s \\
&+ \big((-\kappa\chi\tilde{v} - \bar{v}\kappa\chi - \chi\bar{u}_s - \chi\tilde{u}_s)\tilde{u} - (\bar{u}\kappa\chi - \tilde{u}_Y - \bar{u}_Y)\tilde{v} \\
&+ \tilde{u}_z\tilde{w} + \tilde{u}_Y\bar{v} + \bar{w}\tilde{u}_z + \tilde{u}_s\bar{u}\chi + \tilde{u}_t + \tilde{T}_s\chi\gamma M^2\big)\tilde{\rho} + (-\kappa\chi\bar{\rho}\tilde{v} + \tilde{u}_s\bar{\rho}\chi)\tilde{u} \\
&+ \tilde{u}_Y\bar{\rho}\tilde{v} + \tilde{u}_z\bar{\rho}\tilde{w} + \tilde{T}\chi\tilde{\rho}_s\gamma M^2\big]\frac{R_e}{\bar{\mu}} = -\mathcal{N}_1,
\end{aligned} \tag{2.52a}$$

$$\begin{aligned}
&\big[(-\chi\tilde{v}_Y\tilde{u} - \bar{u}\chi\tilde{v}_Y)\tilde{\rho} - \tilde{u}\bar{\rho}\chi\tilde{v}_Y\big)h_s + \big((\kappa\chi\tilde{u}^2 - (-2\bar{u}\kappa\chi - \chi\tilde{v}_s - \chi\bar{v}_s)\tilde{u} \\
&\quad - (-\tilde{v}_Y - \bar{v}_Y)\tilde{v} + \tilde{v}_z\tilde{w} + \bar{u}\chi\tilde{v}_s + \bar{v}\tilde{v}_Y + \bar{w}\tilde{v}_z + \tilde{v}_t + \tilde{T}_Y\gamma M^2\big)\tilde{\rho} \\
&\quad + \kappa\bar{\rho}\chi\tilde{u}^2 + \bar{\rho}\chi\tilde{v}_s\tilde{u} + \bar{\rho}\tilde{v}_Y\tilde{v} + \bar{\rho}\tilde{v}_z\tilde{w} + \tilde{\rho}_Y\tilde{T}\gamma M^2\big]\frac{R_e}{r\bar{\mu}} = -\mathcal{N}_2,
\end{aligned} \tag{2.52b}$$

$$\begin{aligned}
&\big[\big((-\tilde{w}_Y\chi\tilde{u} - \tilde{w}_Y\chi\bar{u})\tilde{\rho} - \bar{\rho}\tilde{u}\chi\tilde{w}_Y\big)h_s + \big(-(-\chi\bar{w}_s - \chi\tilde{w}_s)\tilde{u} - (-\bar{w}_Y - \tilde{w}_Y)\tilde{v} \\
&\quad + \tilde{w}_z\tilde{w} + \bar{v}\tilde{w}_Y + \bar{w}\tilde{w}_z + \tilde{w}_t + \tilde{T}_z\gamma M^2 + \bar{u}\chi\tilde{w}_s\big)\tilde{\rho} + \bar{\rho}\chi\tilde{w}_s\tilde{u} + \bar{\rho}\tilde{w}_Y\tilde{v} \\
&\quad + \bar{\rho}\tilde{w}_z\tilde{w} + \tilde{\rho}_z\tilde{T}\gamma M^2\big]\frac{R_e}{\bar{\mu}} = -\mathcal{N}_3,
\end{aligned} \tag{2.52c}$$

$$\Big[\big((-(\chi\tilde{T}_Y\sigma - M^2(-1+\gamma)\chi\tilde{T}_Y\gamma M^2)\tilde{u} - (\chi\bar{u}\tilde{T}_Y\sigma - M^2(-1+\gamma)\chi\bar{u}\tilde{T}_Y\gamma M^2))\tilde{\rho}$$
$$+ (M^2(-1+\gamma)\chi\tilde{\rho}_Y\tilde{T}\gamma M^2) - (\chi\bar{\rho}\tilde{T}_Y\sigma - M^2(-1+\gamma)(\chi\bar{T}\tilde{\rho}_Y + \chi\bar{\rho}\tilde{T}_Y)\gamma M^2))\tilde{u}$$
$$+ M^2(-1+\gamma)\chi\bar{u}\tilde{T}\tilde{\rho}_Y\gamma M^2)\big)h_s + \big(- (-\chi\bar{T}_s\sigma - \chi\tilde{T}_s\sigma$$
$$+ M^2(-1+\gamma)(\chi\bar{T}_s + \chi\tilde{T}_s)\gamma M^2)\tilde{u} - (-\tilde{T}_Y\sigma - \bar{T}_Y\sigma + M^2(-1+\gamma)(\tilde{T}_Y + \bar{T}_Y)\gamma M^2)\tilde{v}$$
$$- (-\tilde{T}_z\sigma + M^2(-1+\gamma)\tilde{T}_z\gamma M^2)\tilde{w} - (M^2(-1+\gamma)(\tilde{T}_t + \bar{v}\tilde{T}_Y + \bar{w}\tilde{T}_z + \chi\bar{u}\tilde{T}_s)\gamma M^2$$
$$- \bar{v}\tilde{T}_Y\sigma - \bar{w}\tilde{T}_z\sigma - \chi\bar{u}\tilde{T}_s\sigma - \tilde{T}_t\sigma))\tilde{\rho} + (-M^2(-1+\gamma)(\chi\bar{\rho}_s + \chi\tilde{\rho}_s)\gamma M^2\tilde{T}$$
$$- (M^2(-1+\gamma)(\chi\bar{T}\tilde{\rho}_s + \chi\bar{\rho}\tilde{T}_s)\gamma M^2 - \chi\bar{\rho}\tilde{T}_s\sigma))\tilde{u}$$
$$+ (-M^2(-1+\gamma)(\tilde{\rho}_Y + \bar{\rho}_Y)\gamma M^2\tilde{T} - (-\tilde{T}_Y\bar{\rho}\sigma + M^2(-1+\gamma)(\tilde{T}_Y\bar{\rho} + \tilde{\rho}_Y\bar{T})\gamma M^2))\tilde{v}$$
$$+ (-M^2(-1+\gamma)\tilde{\rho}_z\tilde{T}\gamma M^2 - (-\bar{\rho}\tilde{T}_z\sigma + M^2(-1+\gamma)(\bar{T}\tilde{\rho}_z + \bar{\rho}\tilde{T}_z)\gamma M^2))\tilde{w}$$
$$- M^2(-1+\gamma)(\tilde{\rho}_t + \bar{v}\tilde{\rho}_Y + \bar{w}\tilde{\rho}_z + \chi\bar{u}\tilde{\rho}_s)\gamma M^2\tilde{T}\Big]\frac{R_e}{\bar{\mu}} = -\mathcal{N}_4, \tag{2.52d}$$

$$\big[(\chi\tilde{u}_Y\tilde{\rho} + \tilde{u}\chi\tilde{\rho}_Y)h_s + (\kappa\chi\tilde{v} - (\chi\tilde{u}_s + \tilde{v}_Y + \tilde{w}_z))\tilde{\rho} - \chi\tilde{\rho}_s\tilde{u} - \tilde{\rho}_Y\tilde{v} - \tilde{w}\tilde{\rho}_z\big]\frac{1}{\bar{\rho}} = -\mathcal{N}_5. \tag{2.52e}$$

Upon substitution of the non-linear HNS ansatz 2.37 we obtain the extra non-linear terms. The boundary condition is formulated from the continuity equation and its derivatives to replace v_Y and v_{YY} in the non-linear y-momentum equation. In contrast to the PSE, we do not impose $p_x = 0$ in order to halt upstream propagation of information in the form of acoustic waves[104]. These are then transformed to the bounded computational domain as described in the linear section. The boundary condition is derived in the same way as for the LHNS. These equations are then mapped to the computational domain. The non-linear version of LHNSh has been implemented within the simpler original code by Dr. Mughal.

2.4 Parabolised Stability Equations with Roughness Correction (PSEh)

2.4.1 Linear

The PSE equations are only formulated in the compressible form but are, however, broken down into a surface curvature terms included code and a surface curvature terms excluded form. Both versions of the code have been derived with the h correction but only the more extensive curvature set will be covered here. The derivation begins much the same as with the Linearised Harmonic Navier-Stokes derivation, by taking the compressible equation set 2.12, linearising, applying the infinite sweep assumption and then substituting in the ansatz in equation 2.17. After substituting in the ansatz we must ensure the PSE assumptions are enforced, such as setting second stream-wise

derivatives, and products of stream-wise derivatives, to zero. Once this is achieved, the transformation in equation 2.46 can be applied to incorporate the roughness to the equations, resulting with,

s-momentum :

$$
\begin{aligned}
&\Big[\frac{\bar{\mu}_s r\chi^2\alpha + \chi\kappa\bar{\rho}R_e\bar{v} - iR_e\bar{w}\bar{\rho}\beta - R_e\bar{u}\bar{\rho}\chi\alpha + \bar{\mu}_Y\kappa\chi + iR_e\bar{\rho}\omega - \chi\bar{u}_s R_e\bar{\rho}}{\bar{\mu}} \\
&+ r\chi^2\alpha^2 - \beta^2 - \kappa^2\chi^2 + r\chi^3\kappa_s\alpha Y + r\chi^3\kappa_s\alpha h\Big]\hat{u} \\
&+ \Big[- \kappa\chi^2\alpha - r\chi^2\kappa_s - \kappa\chi^2 r\alpha - r\chi^3\kappa_s\kappa Y - r\chi^3\kappa_s\kappa h \\
&+ \frac{\chi\kappa\bar{\rho}R_e\bar{u} + \bar{\mu}_Y\chi\alpha - \bar{u}_Y R_e\bar{\rho} - \bar{\mu}_s r\chi^2\kappa}{\bar{\mu}}\Big]\hat{v} + \Big[\frac{i\bar{\mu}_s m\chi\beta}{\bar{\mu}} + iQ\chi\beta\alpha\Big]\hat{w} \\
&+ \Big[\frac{-R_e\chi\bar{T}\alpha - R_e\chi\bar{T}_s}{\bar{\mu}\gamma M^2} + \frac{\chi R_e\bar{u}\bar{v}\kappa - \bar{u}_Y R_e\bar{v} - \chi\bar{u}_s R_e\bar{u}}{\bar{\mu}}\Big]\hat{\rho} \\
&+ \Big[\big(f_T\bar{u}_{YY} - r\chi^2\bar{v}\kappa f_T\alpha/\bar{\mu} + f_T r\chi^3\bar{u}_s\kappa_s h - r\chi^2\bar{v}\kappa f_{TT}\bar{T}_s - f_T r\bar{v}\chi^3\kappa_s\kappa Y \\
&- f_T r\bar{v}\chi^3\kappa_s\kappa h + f_T r\chi^3\bar{u}_s\kappa_s Y + f_T Q\chi\bar{v}_{sY} + \chi\bar{v}_s f_{TT}\bar{T}_Y + r\chi^2\bar{u}_s f_T\alpha \\
&+ r\chi^2\bar{u}_s f_{TT}\bar{T}_s + m\chi\bar{v}_Y f_T\alpha + m\chi\bar{v}_Y f_{TT}\bar{T}_s + \bar{u}\kappa\chi f_{TT}\bar{T}_Y + i\chi\bar{w}_s f_T\beta \\
&- f_T\kappa\chi^2\bar{v}_s r - f_T r\bar{v}\chi^2\kappa_s + \bar{u}_Y f_{TT}\bar{T}_Y - f_T\kappa\chi^2\bar{v}_s - f_T\bar{u}\kappa^2\chi^2 - f_T\kappa\chi\bar{u}_Y\big)\frac{1}{\bar{\mu}} \\
&+ \frac{-R_e\chi\bar{\rho}\alpha - R_e\chi\bar{\rho}_s}{\bar{\mu}\gamma M^2}\Big]\hat{T} + \Big[2r\chi^2\alpha + r\chi^3\kappa_s Y + r\chi^3\kappa_s h + \frac{\bar{\mu}_s r\chi^2 - R_e\bar{u}\bar{\rho}\chi}{\bar{\mu}}\Big]\hat{u}_s \\
&+ \Big[\frac{\bar{\mu}_Y + R_e\bar{u}\bar{\rho}\chi h_s - \bar{\mu}_s r\chi^2 h_s - R_e\bar{v}\bar{\rho}}{\bar{\mu}} - \kappa\chi - r\chi^3\kappa_s Y h_s - r\chi^3\kappa_s h h_s - 2r\chi^2\alpha h_s\Big]\hat{u}_Y \\
&+ \Big[\frac{\bar{\mu}_Y\chi}{\bar{\mu}} - \kappa\chi^2 r - \kappa\chi^2\Big]\hat{v}_s + \Big[\frac{\bar{\mu}_s m\chi - \bar{\mu}_Y\chi h_s}{\bar{\mu}} + \kappa\chi^2 h_s + Q\chi\alpha + \kappa\chi^2 r h_s\Big]\hat{v}_Y \\
&+ iQ\chi\beta\hat{w}_s - iQ\chi\beta\hat{w}_Y h_s - \frac{R_e\chi\bar{T}\hat{\rho}_s}{\bar{\mu}\gamma M^2} + \frac{R_e\chi\bar{T}\hat{\rho}_Y h_s}{\bar{\mu}\gamma M^2} \\
&+ \Big[\frac{m\chi\bar{v}_Y f_T + r\chi^2\bar{u}_s f_T - r\chi^2\bar{v}\kappa f_T}{\bar{\mu}} - \frac{R_e\chi\bar{\rho}}{\bar{\mu}\gamma M^2}\Big]\hat{T}_s + \Big[\frac{R_e\chi\bar{\rho}h_s}{\bar{\mu}\gamma M^2} \\
&+ \frac{r\chi^2\bar{v}\kappa f_T h_s - r\chi^2\bar{u}_s f_T h_s - m\chi\bar{v}_Y f_T h_s + \chi\bar{v}_s f_T + \bar{u}\kappa\chi f_T + \bar{u}_Y f_T}{\bar{\mu}}\Big]\hat{T}_Y \\
&- Q\chi h_s\hat{v}_{YY} + Q\chi\hat{v}_{sY} + \hat{u}_{YY} = \mathcal{N}_1,
\end{aligned}
\tag{2.53a}
$$

Y-momentum :

$$
\begin{aligned}
&\Big[\frac{-\chi^2\kappa_s+\kappa\chi^2 r\alpha-\chi^3\kappa_s\kappa Y-\chi^3\kappa_s\kappa h+\kappa\chi^2\alpha}{r}\\
&+\frac{\chi^2\bar{\mu}_s\kappa+\bar{\mu}_Y m\chi\alpha-\chi\bar{v}_s R_e\bar{\rho}-2\chi R_e\bar{u}\kappa\bar{\rho}}{r\bar{\mu}}\Big]\hat{u}+\Big[\frac{\chi^2\alpha^2+\chi^3\kappa_s\alpha Y+\chi^3\kappa_s\alpha h-\beta^2}{r}\\
&+\big(\chi^2\bar{\mu}_s\alpha-\bar{v}_Y R_e\bar{\rho}+iR_e\bar{\rho}\omega-\bar{\mu}_Y m\kappa\chi-iR_e\bar{w}\bar{\rho}\beta-R_e\bar{u}\bar{\rho}\chi\alpha\big)\frac{1}{r\bar{\mu}}-\kappa^2\chi^2\Big]\hat{v}\\
&+\frac{i\bar{\mu}_Y m\hat{w}\beta}{r\bar{\mu}}+\Big[\frac{-\bar{v}_Y R_e\bar{v}-\chi\bar{v}_s R_e\bar{u}-\chi R_e\bar{u}^2\kappa}{\bar{\mu}r}-\frac{R_e\bar{T}_Y}{r\bar{\mu}\gamma M^2}\Big]\hat{\rho}\\
&+\Big[\big(f_T r\bar{v}_{YY}+r\bar{v}_Y f_{TT}\bar{T}_Y+i\bar{w}_Y f_T\beta+\chi^2\bar{v}_s f_{TT}\bar{T}_s+\chi\bar{u}_Y f_T\alpha+\chi\bar{u}_Y f_{TT}\bar{T}_s\\
&+\chi^2\bar{v}_s f_T\alpha+f_T\kappa\chi^2\bar{u}_s+f_T Q\chi\bar{u}_{sY}-f_T\bar{u}\chi^2\kappa_s-f_T\bar{u}\chi^3\kappa_s\kappa h\\
&-m\bar{v}\kappa\chi f_{TT}\bar{T}_Y-f_T\bar{u}\chi^3\kappa_s\kappa Y-f_T r\bar{v}\kappa^2\chi^2+m\chi\bar{u}_s f_{TT}\bar{T}_Y+\bar{u}\kappa\chi^2 f_T\alpha\\
&+f_T\chi^3\bar{v}_s\kappa_s h+f_T\kappa\chi^2\bar{u}_s r-f_T r\kappa\chi\bar{v}_Y+f_T\chi^3\bar{v}_s\kappa_s Y+\bar{u}\kappa\chi^2 f_{TT}\bar{T}_s\big)\frac{1}{r\bar{\mu}}-\frac{R_e\bar{\rho}_Y}{r\bar{\mu}\gamma M^2}\Big]\hat{T}\\
&+\Big[\frac{\kappa\chi^2}{r}+\frac{\bar{\mu}_Y m\chi}{r\bar{\mu}}+\kappa\chi^2\Big]\hat{u}_s+\Big[\frac{Q\chi\alpha-\kappa\chi^2 h_s}{r}+\frac{\chi\bar{\mu}_s-\bar{\mu}_Y m\chi h_s}{r\bar{\mu}}-\kappa\chi^2 h_s\Big]\hat{u}_Y\\
&+\Big[\frac{2\chi^2\alpha+\chi^3\kappa_s Y+\chi^3\kappa_s h}{r}+\frac{-R_e\bar{u}\bar{\rho}\chi+\chi^2\bar{\mu}_s}{r\bar{\mu}}\Big]\hat{v}_s\\
&+\Big[\frac{\bar{\mu}_Y}{\bar{\mu}}-\kappa\chi+\frac{-2\chi^2\alpha h_s-\chi^3\kappa_s Y h_s-\chi^3\kappa_s h h_s}{r}+\frac{-\chi^2\bar{\mu}_s h_s-R_e\bar{v}\bar{\rho}+R_e\bar{u}\bar{\rho}\chi h_s}{r\bar{\mu}}\Big]\hat{v}_Y\\
&+\frac{iQ\chi\hat{w}_Y\beta}{r}-\frac{R_e\hat{\rho}_Y\bar{T}}{r\bar{\mu}\gamma M^2}+\Big[\frac{\chi\bar{u}_Y f_T+\chi^2\bar{v}_s f_T+\bar{u}\kappa\chi^2 f_T}{r\bar{\mu}}\Big]\hat{T}_s\\
&+\Big[\frac{\bar{v}_Y f_T-\bar{u}\kappa\chi^2 f_T h_s-m\bar{v}\kappa\chi f_T-\chi\bar{u}_Y f_T h_s-\chi^2\bar{v}_s f_T h_s+m\chi\bar{u}_s f_T}{\bar{\mu}}-\frac{R_e\bar{\rho}}{r\bar{\mu}\gamma M^2}\Big]\hat{T}_Y\\
&-\frac{Q\chi h_s\hat{u}_{YY}}{r}+\frac{Q\chi\hat{u}_{sY}}{r}+\hat{v}_{YY}=\mathcal{N}_2,
\end{aligned}
\tag{2.53b}
$$

q-momentum :

$$
\begin{aligned}
&\big[\frac{i\chi\bar{\mu}_s\beta-\chi\bar{w}_sR_e\bar{\rho}}{\bar{\mu}}+iQ\chi\beta\alpha\big]\hat{u}+\big[\frac{-iQ\chi\kappa\beta+i\bar{\mu}_Y\beta-\bar{w}_YR_e\bar{\rho}}{\bar{\mu}}\big]\hat{v}\\
&+\big[\frac{iR_e\bar{\rho}\omega-R_e\bar{u}\bar{\rho}\chi\alpha-iR_e\bar{w}\bar{\rho}\beta+\chi^2\bar{\mu}_s\alpha}{\bar{\mu}}+\chi^3\kappa_s\alpha Y+\chi^3\kappa_s\alpha h+\chi^2\alpha^2-r\beta^2\big]\hat{w}\\
&+\big[\frac{-\chi\bar{w}_sR_e\bar{u}-\bar{w}_YR_e\bar{v}}{\bar{\mu}}+\frac{-iR_e\beta\bar{T}}{\bar{\mu}\gamma M^2}\big]\hat{\rho}+\big[\big(\chi^2\bar{w}_sf_T\alpha+\chi^2\bar{w}_sf_{TT}\bar{T}_s-f_T\kappa\chi\bar{w}_Y\\
&+imf_T\beta\bar{v}_Y+f_T\chi^3\bar{w}_s\kappa_sY+f_T\chi^3\bar{w}_s\kappa_sh+\bar{w}_Yf_{TT}\bar{T}_Y-imf_T\beta\bar{v}\kappa\chi\\
&+imf_T\beta\chi\bar{u}_s+f_T\bar{w}_{YY}\big)\frac{1}{\bar{\mu}}+\frac{-iR_e\beta\bar{\rho}}{\bar{\mu}\gamma M^2}\big]\hat{T}+iQ\chi\beta\hat{u}_s-iQ\chi\beta\hat{u}_Yh_s+iQ\hat{v}_Y\beta\\
&+\big[\frac{-R_e\bar{u}\bar{\rho}\chi+\chi^2\bar{\mu}_s}{\bar{\mu}}+2\chi^2\alpha+\chi^3\kappa_sY+\chi^3\kappa_sh\big]\hat{w}_s\\
&+\big[\frac{-\chi^2\bar{\mu}_sh_s-R_e\bar{v}\bar{\rho}+R_e\bar{u}\bar{\rho}\chi h_s+\bar{\mu}_Y}{\bar{\mu}}-\chi^3\kappa_sYh_s-\chi^3\kappa_shh_s-2\chi^2\alpha h_s-\kappa\chi\big]\hat{w}_Y\\
&+\frac{\chi^2\bar{w}_sf_T\hat{T}_s}{\bar{\mu}}+\big[\frac{-\chi^2\bar{w}_sf_Th_s+\bar{w}_Yf_T}{\bar{\mu}}\big]\hat{T}_Y+\hat{w}_{YY}=\mathcal{N}_3,
\end{aligned}
\tag{2.53c}
$$

Energy :

$$
\begin{aligned}
&\big[\frac{-R_e\bar{\rho}\sigma\chi\bar{T}_s + M^2(-1+\gamma)R_e\chi\bar{p}_s}{\bar{\mu}} + M^2(-1+\gamma)\big(- 2r\chi^2\bar{v}\kappa\alpha + 2m\chi\bar{v}_Y\alpha \\
&+ 2r\chi^2\bar{u}_s\alpha + 2i\chi\beta\bar{w}_s + 2\bar{u}\kappa^2\chi^2 + 2\bar{u}_Y\kappa\chi + 2\kappa\chi^2\bar{v}_s\big)\big]\hat{u} \\
&+ \big[\frac{-R_e\bar{\rho}\sigma\bar{T}_Y + M^2(-1+\gamma)R_e\bar{p}_Y}{\bar{\mu}} + M^2(-1+\gamma)\big(- 2m\kappa\chi\bar{v}_Y + 2\bar{u}\kappa\chi^2\alpha + 2r\chi^2\bar{v}\kappa^2 \\
&- 2r\chi^2\bar{u}_s\kappa + 2\chi\bar{u}_Y\alpha + 2\chi^2\bar{v}_s\alpha + 2i\beta\bar{w}_Y\big)\big]\hat{v} \\
&+ \big[M^2(-1+\gamma)\big(- 2im\chi\beta\bar{v}\kappa + 2im\chi\beta\bar{u}_s + 2\chi^2\bar{w}_s\alpha + 2im\bar{v}_Y\beta\big)\big]\hat{w} \\
&+ \big[\frac{-R_e\sigma\bar{u}\chi\bar{T}_s - R_e\sigma\bar{v}\bar{T}_Y}{\bar{\mu}} \\
&+ M^2(-1+\gamma)\frac{R_e\bar{u}\chi\bar{T}_s - iR_e\omega\bar{T} + iR_e\bar{w}\beta\bar{T} + R_e\bar{u}\chi\bar{T}\alpha + R_e\bar{v}\bar{T}_Y}{\bar{\mu}\gamma M^2}\big]\hat{\rho} \\
&+ \big[\big(\chi^2\bar{T}_s^2 f_{TT} + \chi^2\bar{\mu}_s\alpha - R_e\bar{\rho}\sigma\bar{u}\chi\alpha + f_{TT}\bar{T}_Y^2 - iR_e\bar{\rho}\sigma\bar{w}\beta + f_T\bar{T}_{YY} \\
&+ iR_e\bar{\rho}\sigma\omega + f_T\chi^3\bar{T}_s\kappa_s Y + f_T\chi^3\bar{T}_s\kappa_s h + \chi^2\bar{T}_s f_T\alpha - f_T\kappa\chi\bar{T}_Y\big)\frac{1}{\bar{\mu}} \\
&+ M^2(-1+\gamma)\big(f_T\bar{u}_Y^2 + f_T\bar{w}_Y^2 + f_T r\chi^2\bar{v}^2\kappa^2 + 2f_T m\chi\bar{u}_s\bar{v}_Y + 2f_T\bar{u}\kappa\chi\bar{u}_Y \\
&+ 2f_T/\bar{u}\kappa\chi^2\bar{v}_s + 2f_T\chi\bar{u}_Y\bar{v}_s - 2f_T r\chi^2\bar{v}\kappa\bar{u}_s - 2f_T m\bar{v}\kappa\chi\bar{v}_Y + f_T\bar{u}^2\kappa^2\chi^2 \\
&+ f_T r\chi^2\bar{u}_s^2 + f_T\chi^2\bar{v}_s^2 + f_T\chi^2\bar{w}_s^2 + f_T r\bar{v}_Y^2\big)\frac{1}{\bar{\mu}} \\
&+ M^2(-1+\gamma)\big(R_e\bar{u}\chi\bar{\rho}\alpha + iR_e\bar{w}\beta\bar{\rho} + R_e\bar{v}\bar{\rho}_Y + R_e\bar{u}\chi\bar{\rho}_s - iR_e\omega\bar{\rho}\big)\frac{1}{\bar{\mu}\gamma M^2} \\
&+ \chi^2\alpha^2 - \beta^2 + \chi^3\kappa_s\alpha Y + \chi^3\kappa_s\alpha h\big]\hat{T} + \big[M^2(-1+\gamma)\big(- 2r\chi^2\bar{v}\kappa + 2r\chi^2\bar{u}_s + 2m\chi\bar{v}_Y\big]\hat{u}_s \\
&+ \big[2M^2(-1+\gamma)\big(r\chi^2\bar{v}\kappa h_s - r\chi^2\bar{u}_s h_s - m\chi\bar{v}_Y h_s + \bar{u}\kappa\chi + \chi\bar{v}_s + \bar{u}_Y\big)\big]\hat{u}_Y \\
&+ \big[2M^2(-1+\gamma)\big(\bar{u}\kappa\chi^2 + \chi^2\bar{v}_s + \chi\bar{u}_Y\big)\big]\hat{v}_s \\
&+ \big[2M^2(-1+\gamma)\big(- \bar{u}\kappa\chi^2 h_s - m\bar{v}\kappa\chi - \chi^2\bar{v}_s h_s - \chi\bar{u}_Y h_s + m\chi\bar{u}_s + r\bar{v}_Y\big)\big]\hat{v}_Y \\
&+ 2M^2(-1+\gamma)\chi^2\bar{w}_s\hat{w}_s + \big[2M^2(-1+\gamma)\big(- \chi^2\bar{w}_s h_s + \bar{w}_Y\big)\big]\hat{w}_Y \\
&+ M^2(-1+\gamma)R_e\bar{u}\chi\bar{T}\hat{\rho}_s/(\bar{\mu}\gamma M^2) \\
&+ \big[- M^2(-1+\gamma)R_e\bar{u}\chi\bar{T}h_s/(\bar{\mu}\gamma M^2) + M^2(-1+\gamma)R_e\bar{v}\bar{T}/(\bar{\mu}\gamma M^2)\big]\hat{\rho}_Y \\
&+ \big[\frac{-R_e\bar{\rho}\sigma\bar{u}\chi + \chi^2\bar{\mu}_s + \chi^2\bar{T}_s f_T}{\bar{\mu}} + \chi^3\kappa_s Y + \chi^3\kappa_s h \\
&+ \frac{M^2(-1+\gamma)R_e\bar{u}\chi\bar{\rho}}{\bar{\mu}\gamma M^2} + 2\chi^2\alpha\big]\hat{T}_s \\
&+ \big[\frac{-R_e\bar{\rho}\sigma\bar{v} - \chi^2\bar{T}_s f_T h_s - \chi^2\bar{\mu}_s h_s + \bar{\mu}_Y + R_e\bar{\rho}\sigma\bar{u}\chi h_s + \bar{T}_Y f_T}{\bar{\mu}} \\
&- \chi^3\kappa_s Y h_s - \chi^3\kappa_s h h_s - 2\chi^2\alpha h_s - \kappa\chi - \frac{M^2(-1+\gamma)(R_e\bar{u}\chi\bar{\rho}h_s + R_e\bar{v}\bar{\rho})}{\bar{\mu}\gamma M^2}\big]\hat{T}_Y \\
&+ \hat{T}_{YY} = \mathcal{N}_4,
\end{aligned}
\tag{2.53d}
$$

Continuity :

$$\big[\chi\alpha + \frac{\chi\bar{\rho}_s}{\bar{\rho}}\big]\hat{u} + \big[-\kappa\chi + \frac{\bar{\rho}_Y}{\bar{\rho}}\big]\hat{v} + i\hat{w}\beta + \big[\frac{-\kappa\chi\bar{v} + \chi\bar{u}_s + \bar{v}_Y + i\bar{w}\beta - i\omega + \bar{u}\chi\alpha}{\bar{\rho}}\big]\hat{\rho} + \chi\hat{u}_s - \chi\hat{u}_Y h_s + \hat{v}_Y + \frac{\bar{u}\chi\hat{\rho}_s}{\bar{\rho}} + \big[\frac{\bar{v} - \bar{u}\chi h_s}{\bar{\rho}}\big]\hat{\rho}_Y = \mathcal{N}_5. \tag{2.53e}$$

For the linear problem all $\mathcal{N}_j$, where $j = 1:5$, are zero. A boundary condition at the wall is also required to complete the problem. This is calculated by substituting the continuity and differential of the continuity, with respect to the normal component, into the normal-momentum equation to replace $\tilde{v}_Y$ and $\tilde{v}_{YY}$. The enthalpy equation is also rearranged to substitute $\tilde{T}_{YY}$ into the normal-momentum equation. The physical space then needs to be transformed once again to a bounded computational space. This is achieved with the mapping $Y = \frac{g\eta}{b-\eta}$ to move from $Y(0,\infty) \mapsto \eta(0,1)$, where g and b are constants.

2.4.2 Non-linear

With the addition of non-linearity there inevitably comes complexity, as with the LHNSh. Again, $\mathcal{O}(\epsilon^2)$ and $\mathcal{O}(\epsilon^3)$ terms are additionally retained in the derivation to arrive at the additions stated in 2.52. Substituting in the ansatz from 2.21 arrives at the extra non-linear terms defining $\mathcal{N}_j$, where $j = 1:5$, in equations 2.53. The boundary condition in this case is formulated from the continuity and its derivation to replace v_Y and v_{YY} in the non-linear y-momentum equation. These are then transformed to the bounded computational domain as described in the linear section. The mean flow distortion (MFD) mode assumes $p_x = 0$ in order to halt upstream propagation of information in the form of acoustic waves[104]. The boundary condition is derived the same as for the linear PSE and these equations are then mapped to the computational domain.

2.5 Prandtl Boundary Layer Equation Solver

We will also make use of a Prandtl Boundary layer solver tool, CoBLc, to confirm we have obtained the correct boundary layer profiles from our more accurate steady DNS generated baseflows with no excrescence present. Unfortunately the CoBLc formulation cannot be used for cases when a roughness is present due to the presence of adverse pressure gradients and separated flow. The solution process is based on solving the parabolic boundary layer equations. It is well known that these governing equations fail on the emergence or onset of separated flow. The equations solved by

the CoBlc method are those satisfying a compressible boundary layer over an infinitely swept wing,

$$\frac{\partial}{\partial x}(\rho u) + \frac{\partial}{\partial y}(\rho v) = 0, \tag{2.54a}$$

$$\rho\Big(u\frac{\partial u}{\partial x} + v\frac{\partial u}{\partial y}\Big) = \rho_e u_e \frac{du_e}{dx} + \frac{\partial}{\partial y}\Big(\mu\frac{\partial u}{\partial y}\Big), \tag{2.54b}$$

$$\rho\Big(u\frac{\partial w}{\partial x} + v\frac{\partial w}{\partial y}\Big) = \frac{\partial}{\partial y}\Big(\mu\frac{\partial w}{\partial y}\Big), \tag{2.54c}$$

$$\rho\Big(u\frac{\partial T}{\partial x} + v\frac{\partial T}{\partial y}\Big) = \frac{1}{\sigma}\frac{\partial}{\partial y}\Big(\mu\frac{\partial T}{\partial y}\Big) - u\Big(\frac{\rho_e u_e}{c_p}\frac{du_e}{dx}\Big) + \frac{\mu}{c_p}\Big((\frac{\partial u}{\partial y})^2 + (\frac{\partial w}{\partial y})^2\Big). \tag{2.54d}$$

All variables here are dimensional and c_p is the specific heat at constant pressure. Values at the edge of the boundary layer are denoted with subscript e which are dependent on the stream-wise location. The equations are defined in the normal to leading edge co-ordinate frame. Similarity variables are then introduced through use of the Faulkner-Skan transformation,

$$\eta = \Big(\frac{\rho_e u_e}{\mu_e x}\Big)^{1/2}\int_0^y \frac{\rho(s)}{\rho_e}ds, \tag{2.55}$$

with the stream function,

$$\psi = \big(\rho_e \mu_e u_e x\big)^{1/2} f(\eta, x), \tag{2.56}$$

to reduce the equations to,

$$\frac{\partial}{\partial\eta}(\chi f'') + m_1(s - f'^2) + cff'' = x\Big(f'\frac{\partial f'}{\partial x} - f''\frac{\partial f}{\partial x}\Big), \tag{2.57a}$$

$$\frac{\partial}{\partial\eta}(\chi g') + cfg' = x\Big(f'\frac{\partial g}{\partial x} - g'\frac{\partial f}{\partial x}\Big), \tag{2.57b}$$

$$\frac{\partial}{\partial\eta}(\frac{\chi}{\sigma}s') + (\gamma-1)\chi(M_x^2 f''^2 + M_c^2 g'^2) + cfs' = x\Big(f'\frac{\partial s}{\partial x} - s'\frac{\partial f}{\partial x}\Big), \tag{2.57c}$$

where,

$$f' = \frac{u}{u_e}, \quad g' = \frac{w}{w_e}, \quad s = \frac{T}{T_e}, \quad \frac{\rho}{\rho_e} = \frac{1}{s}, \quad \chi = \frac{\mu\rho}{\mu_e\rho_e} \tag{2.58a}$$

$$m_1 = \frac{x}{u_e}\frac{du_e}{dx}, \quad c = \frac{1+m_1}{2} + \frac{1}{2}\frac{x}{\mu_e\rho_e}\frac{d}{dx}(\mu_e\rho_e) \tag{2.58b}$$

$$M_x^2 = \frac{u_e^2}{\gamma R^* T_e}, \quad M_c^2 = \frac{w_e^2}{\gamma R^* T_e}. \tag{2.58c}$$

Here f', g, s are all functions of η and x, M_x and M_c are stream-wise and crossflow edge Mach numbers and μ behaves under Sutherlands law. Far field boundary conditions

are,

$$f'(\eta \to \infty, x) = g(\eta \to \infty, x) = s(\eta \to \infty, x) = 1, \tag{2.59}$$

and wall conditions are,

$$f(0, x) = f_w(x), \quad f'(0, x) = g(0, x) = 0, \tag{2.60}$$

where subscript w refers the wall. The wall temperature,

$$s(0, x) = \frac{T_w(x)}{T_e(x)}, \tag{2.61}$$

or adiabatic wall condition

$$s'(0, x) = 0, \tag{2.62}$$

must also be satisfied. A fully implicit second-order accurate accurate three point backward differencing scheme is used in the stream-wise direction and a two point second order accurate scheme is used in the wall normal direction based on a Keller-Box scheme[50]. The equations can thus solve the development of non-similar boundary-layers over a general infinite swept aerofoil, given the slip velocities (i.e. u_e, w_e) or surface pressure variations computed by an inviscid flow solver.[60]

2.6 Pipeline of Tool Set

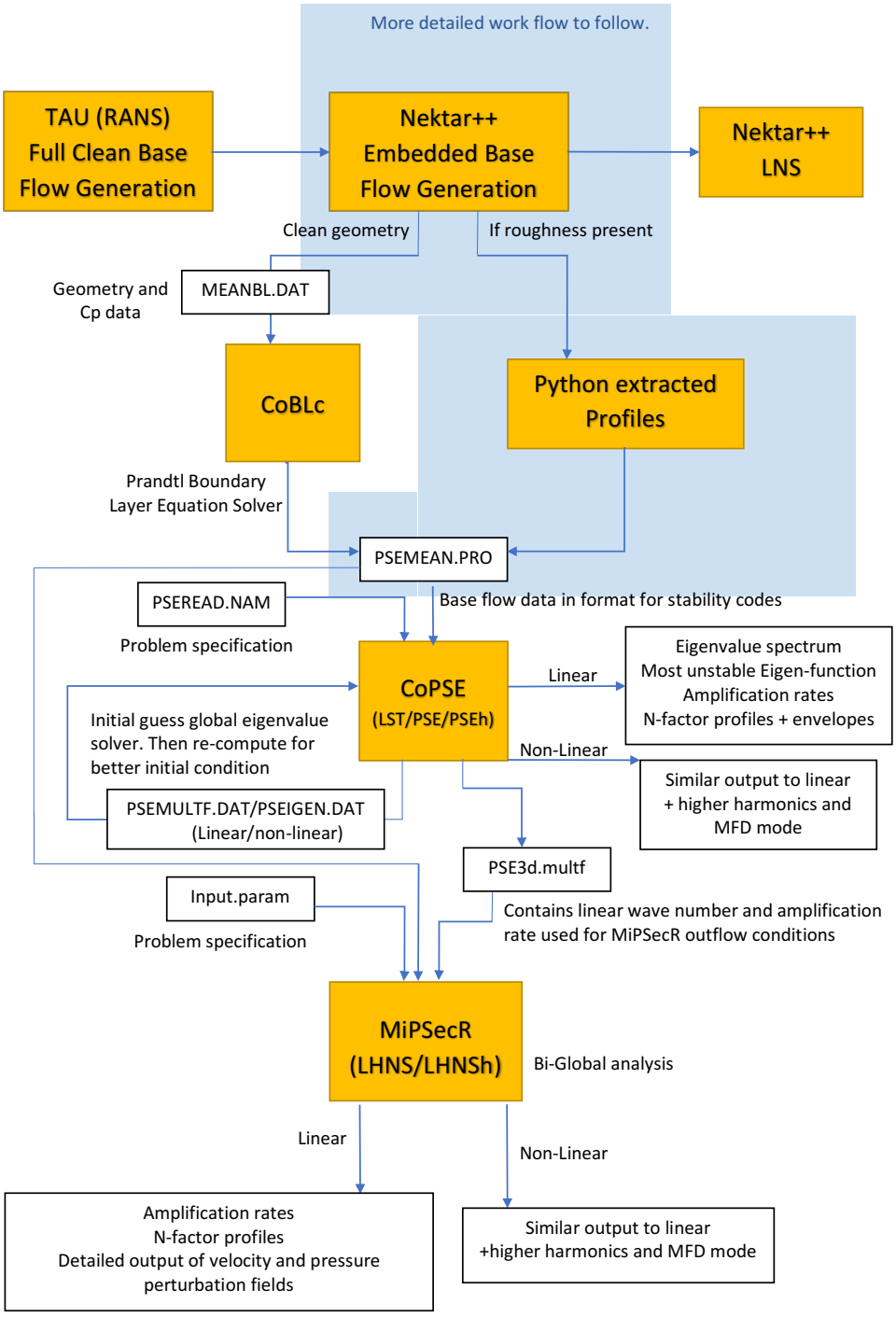

Figure 2.3: Pipeline for the stability tool sets.

CHAPTER 3

The Embedded Approach

The method generally adopted by industry for solving Partial Differential Equations (PDE's) is to use Computational Fluid Dynamics (CFD) models based on Reynolds-Averaged Navier-Stokes (RANS) equations using second order finite volume schemes. These produce satisfactory results but even state of the art schemes struggle to compute flows which are highly separated, vortex dominated or have complex geometries. Low order schemes, which generally encompass, at best, numerical methods that are second order accurate in space, traditionally struggle with high numerical dissipation and low accuracy when modelling transient or turbulent flow regimes in complex geometries.[42]

In contrast, high order methods such as spectral / hp element methods are very appealing as they have low numerical dissipation and dispersion. They also have the ability to increase accuracy in local regions and can, like low order methods, also use unstructured high order meshes to adapt to complex geometries. Unfortunately, high order methods suffer from a lack of robustness in terms of numerical stability. Although they are more computationally efficient at obtaining a smaller error value than a lower order method, they are not necessarily faster than a lower order method obtaining a larger error. There is also the issue of a lack in high order mesh generation software which is crucial for maximising the benefit of these high order methods. The robustness and mesh generation difficulties with high order methods hinders their use in industry, if they are used at all.[99]

One of the oldest and most commonly known method for solving PDE's is the Finite

Difference Method (FDM). FDM's usually begin with the conservative form of the governing equations and make use of Taylor expansions to approximate PDE's via structured grids. FDM's cope well with increasing order but have issues handling complex geometries due to the simplicity of the meshing[32]. Finite Volume Methods (FVM's) are based on the integral of the conservative form of the governing equations. The solution domain is split into a finite number of control volumes and the integral form of the equations are applied in each cell and solved for, about the centroid of the cell. FVM's are extremely good at dealing with complex geometries but are difficult to develop higher than second order accurate schemes for three dimensions.[99]

The Finite Element Method (FEM) discretises the domain into a finite number of elements to create a structured or unstructured mesh. These elements may be triangles or quadrilaterals in the 2D-case and tetrahedra, hexahedra, pyramids or prisms moving to the 3D-case. The governing equations are multiplied by a weight function and then integrated over the domain. The solution is approximated by trial functions, or shape functions, within each element ensuring continuity across the boundaries. The selected weight and trial functions are often the same, this is known as the Galerkin formulation.[99 32]

When the trial function spans the entire domain the FEM becomes a Spectral method. The spectral method provides superior convergence rates accompanied by extremely good error properties due to the exponential convergence achieved when increasing order, or increasing p-type refinement. However, since the trial functions span the entire domain, there comes the bottle neck of geometrical rigidity.

The spectral / hp element cherry picks the best aspects from FEM and Spectral methods to provide a high order solution for complex geometries. The domain is discretised into a set of finite elements and the solution is represented by a series of high order polynomials within each element, known as h and p type refinement respectively.

3.1 The High Order Spectral/HP Element Method

In order to describe the spectral / hp element method we must understand the application of the method of weighted residuals and the classical Galerkin formulation. The method of weighted residuals is used to identify convergence. Firstly, the governing system of equations for a problem are written in their strong form,

$$\mathcal{L}(u) = 0 \quad \in \Omega, \tag{3.1}$$

where $\mathcal{L}$ is a linear differential operator and $u(x,t)$ is a vector of unknowns defined within domain $\Omega = \{x,t : 0 \leq x \leq 1, 0 \leq t \leq T\}$. We assume that the exact solution, u, can be approximated by, u^δ, such that,

$$u^\delta(\mathbf{x},t) = u_0(\mathbf{x},t) + \sum_{i=1}^{N} u_i(t)\Phi_i(\mathbf{x}). \tag{3.2}$$

The set of functions $\Phi_i(\mathbf{x})$ are the expansion bases, or trial functions, $u_i(t)$ are unknown coefficients and u_0 is selected to satisfy the initial and boundary conditions. The set of points where $N_{i-1} \neq 0$ are defined as the support. Substituting equation (3.2) into equation (3.1) obtains a residual $\mathcal{R}$ which is non-zero,

$$\mathcal{L}(u^\delta) = \mathcal{R}(u^\delta). \tag{3.3}$$

The approximation is given by equation (3.2) but at this point we have not uniquely distinguished each $\hat{u}_i(t)$. In order to find each $\hat{u}_i(t)$ the residual $\mathcal{R}$ is placed under a restriction. The type of restriction that is imposed dictates the type of numerical scheme derived. In the method of weighted residuals a set of test, or weight, functions are introduced, $v_j(\mathbf{x})$, and an inner product between these and the residual $\mathcal{R}$ is computed. A requirement is placed to ensure the Legendre inner product, $(<,>)$, over the domain Ω must be zero,

$$< v_j(\mathbf{x}), R >= 0 \quad \text{for} \quad j = 1, ..., N. \tag{3.4}$$

At convergence the residual $\mathcal{R}$ tends to zero since, as $N \to \infty$ the approximated solution $u^\delta(\mathbf{x},t)$ approaches the exact solution $u(\mathbf{x},t)$. There are many different choices of expansion function $\Phi_i(\mathbf{x})$ and test function v_j each determining a different scheme. To name but a few of the most popular there is the collocation method, which uses the Dirac delta as a test function, $v_j(\mathbf{x}) = \delta(\mathbf{x} - \mathbf{x}_j)$, to define a set of collocation points $\mathbf{x}_j$ where the residual is zero, $\mathcal{R}(\mathbf{x}_j) = 0$. The differential equation is then exactly satisfied at these grid points and so this is the natural starting point for a finite difference method. The finite volume method, where the domain Ω is divided into non-overlapping sub domains, Ω^j, which take the value $v_j = 1$ inside Ω^j and $v_j = 0$ outside Ω^j. The least squares method, with the test function $v_j = \frac{\partial \mathcal{R}}{\partial \hat{u}_j}$, which determines the coefficients which minimise $< \mathcal{R}, \mathcal{R} >$. Finally, there is the Galerkin method, utilised by the Nektar++ Spectral / hp element method, which adopts the same test function as trial functions $v_j = \Phi_j$. For an example of the Galerkin formulation see appendix A.[66]

Each of the trial functions, Φ_i, are global expansion modes which will be zero over many of the h-type discretised $N-1$ elemental regions. Considering the expansion in

3.2 globally would be very inefficient. Instead they can be mapped to local elemental expansion functions, ϕ_p, for each element,

$$u^{\delta}(x,t) = u_0(\mathbf{x},t) + \sum_{i=0}^{N-1} \hat{u}_i(t)\Phi_i(x) = u_0(\mathbf{x},t) + \sum_{e=1}^{M}\sum_{p=0}^{P} \hat{u}_p^e(t)\phi_p^e(\xi), \tag{3.5}$$

where M is the total number of elements, p is the order of the local expansion. Reducing the element size, h-type refinement, causes the error in the numerical solution to decay achieving algebraic convergence.

Spectral methods are known for their advantageous convergence properties and high accuracy. If the support of the basis function does not just span an element, but spans the whole interval, then the method becomes a spectral method. A global discretisation of the domain is performed by using a single representation of function $u^{\delta}(x)$ throughout the domain. A linear combination of continuous functions represented with truncated series expansions are used for $u^{\delta}(x)$.[66]

$$u^{\delta}(x) \approx u_N(x) = \sum_{i=0}^{N} \hat{u}_i\phi_i \tag{3.6}$$

The expansion basis is composed of high order orthogonal polynomials from the Jacobi polynomial family, such as Chebyshev or Legendre, or trigonometric functions such as Fourier expansions. Increasing the order of the polynomial, P, or the basis functions, p-type refinement, leads to exponential convergence. The order of convergence of spectral methods is dictated by the regularity of the solution. Smooth solutions give better accuracy and convergence than finite element methods but this very quickly becomes untrue if the domain is irregular, hence their restriction to simple geometries. The spectral / hp element method is a combination of these two methods, where converged solutions can be obtained by refining the mesh or by increasing the polynomial order.

A local expansion is defined upon each standard element $\Omega_{st} = \xi : -1 \leq \xi \leq 1$ and can be mapped through the transformation $\chi^e(\xi)$ to any elemental domain Ω_e. The mapping χ expresses the global co-ordinate, x, to the local, ξ, co-ordinate[57]. Analogously, u_p^e are the local expansion coefficients. If the mapping is linear then the local expansion mode is a polynomial in x as well as in ξ, this also means the global expansion modes are also polynomials in x. However, curved elements require more complicated mappings meaning the global expansion may not remain a polynomial in x, even though by definition it is always a polynomial in ξ. Hence the necessity of a local expansion.

The choice of local expansion basis, $\phi_p^e(\xi)$ may be either nodal or modal. The case where solutions are approximated at a fixed set of nodes is called a nodal expansion,

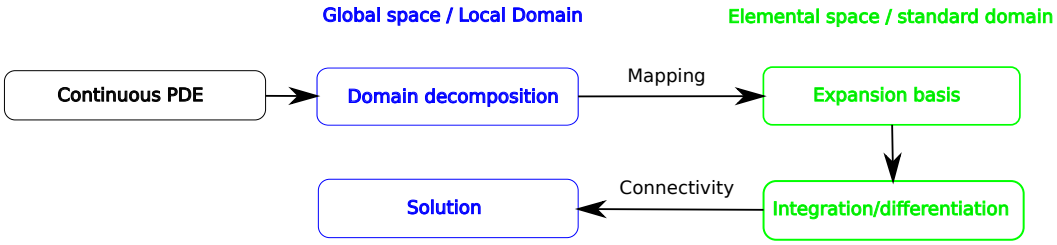

Figure 3.1: The main building blocks of the spectral / hp element method

and modal expansions apply lower order expansion basis within higher order modal expansions, more can be found on this in A. One way to ensure the scheme is well posed is to enforce C^0 continuity for the solution, u^δ, across the elements. This is a necessary condition for the continuous Galerkin method. By enforcing C^0 continuity in the global coefficients, $\hat{u}_i(t)$, the spectral/hp method can decompose these global expansions into local expansion coefficients, $u_p^e(t)$, with the same shape for efficient integration and differentiation.

The spectral / hp element method can be broken down into various building blocks in order to understand the entire process. First the domain is decomposed into non-overlapping elements, a local to standard element mapping is applied, and an expansion basis is described to define the solution within each element. Numerical integration and differentiation is then performed and the standard domain is then connected and transformed back to the global space. The pipeline is shown in figure 3.1.

3.1.1 Velocity Correction Scheme

A splitting scheme is applied for the use of the unsteady incompressible Navier-Stokes equations within Nektar++ which decouples the velocity fields from the pressure field. Application of splitting schemes improve numerical efficiency due to the independent handling of the velocity and pressure fields. A multi-step time integration which is

stiffly-stable is applied as follows[49,39],

$$\frac{\hat{\mathbf{u}} - \sum_{q=0}^{J-1} \alpha_q \hat{\mathbf{u}}^{n-q}}{\Delta t} = -\sum_{q=0}^{J-1} \beta_q (\hat{\mathbf{u}}.\nabla)\hat{\mathbf{u}}^{n-q} \quad \in \Omega, \tag{3.7}$$

$$\nabla^2 p^{n+1} = \nabla.\Big(\frac{\hat{\mathbf{u}}}{\Delta t}\Big) \quad \in \Omega, \tag{3.8}$$

$$\Big(\nabla^2 - \frac{\gamma_0}{\nu \Delta t}\Big)\hat{\mathbf{u}}^{n+1} = \nabla p^{n+1} - \frac{\hat{\mathbf{u}}}{\nu \Delta t} \quad \in \Omega, \tag{3.9}$$

$$\tag{3.10}$$

where Neumann boundary conditions are applied for the pressure,

$$\frac{\partial p^{n+1}}{\partial n} = -\mathbf{n}.\Big[\frac{\partial \mathbf{u}^{n+1}}{\partial t} + \nu \sum_{q=0}^{J-1} \beta_q (\nabla \times \omega)^{(n-q)} + \sum_{q=0}^{J-1} \beta_q (\partial \mathbf{u}^{n-q}.\nabla)^{(n-q)}\Big], \tag{3.11}$$

and $p^{n+1} = 0$ is enforced at the outflow. The velocity field is defined by $\mathbf{u}_n$, pressure by p_n and vorticity with ω_n at time t_n. δt denotes a time step, $t^{n+1} - t^n$. Integration weights for the explicit-implicit integration of the advection-diffusion equations are given by α_q, β_q and γ_0 and J is the order of integration. Non-linear advection terms in equations 3.7 are advanced explicitly in a first step, a second step solves the pressure Poisson problem and a third step enforces the elliptic viscous terms implicitly through application of a Helmholtz problem. The velocity boundary conditions are also enforced in this final step. An explicit advection scheme is chosen, since the advection terms are non-linear. The explicit treatment of these terms requires the Courant-Friedrichs-Lewy (CFL) condition to be satisfied to ensure the time-stepping remains stable. See Karniadakis and Sherwin[48] for further information.

3.1.2 High Order Outflow Condition

Due to the shape of the wing analysed and incidence applied in this work the flow can begin to separate from the aerofoil. These perturbations are usually managed by applying far away outflow boundaries from the geometry such that the separation has dissipated sufficiently upon exiting the domain. In order to obtain refinement over the excrescences in this work, an embedded approach is utilised, which will be expanded upon in the following section. This means the flow can separate and reverse at, or in very close vicinity of, the outflow boundaries. This influx of kinetic energy to the domain can cause the solution to become unstable at the boundary. In order to manage this separation a high order outflow boundary condition, introduced by Dong et al.[22], is applied.

Dong et al.[22] derived an outflow boundary condition which halts uncontrolled growth of energy flux into the domain via the outflow boundary,

$$p^{n+1} = \nu \sum_{q=0}^{J-1} \nabla \hat{\mathbf{u}}^{(n-q)}.\mathbf{n} - \frac{1}{2}\Big|\sum_{q=0}^{J-1} \hat{\mathbf{u}}^{(n-q)}\Big| S_0\Big(\mathbf{n}.\sum_{q=0}^{J-1} \hat{\mathbf{u}}^{(n-q)}\Big) - \mathbf{f}_b^{n+1}.\mathbf{n}, \tag{3.12}$$

where $S_0(\mathbf{n}.\mathbf{u}) = \frac{1}{2}(1 - tanh(\frac{\mathbf{n}.\mathbf{u}}{\mathbf{u}_0\delta}))$ is a step function. The characteristic velocity scale is given by u_0, δ is a non-dimensional sufficiently small positive constant and $\mathbf{f}_b$ is a forcing term. This forcing is set to zero for the aerofoil problem discussed in this thesis.

3.2 The Embedded Approach

A civil transport wing would have a boundary layer near the leading edge of the order of millimetres, a wing chord on the order of metres and a span of tens of metres. Computationally modelling a roughness of the order of microns on a geometry of this scale is very demanding with a single computation. To overcome such scale difficulties, in this work a hybrid approach is developed which combines the use of an industrial finite volume RANS solver to obtain the global flow regime with an embedded spectral / hp element approach to more efficiently resolve the fine detail in the laminar boundary layer and roughness. In order to produce the roughness base flow computations, firstly the clean geometry, steady base flow is computed using RANS solutions of the industrial flow solver TAU[21]. This consists of the full geometry prescribed in the line of flight direction. A new embedded mesh is constructed in the normal to leading edge direction, required for Nektar++, using AutoCAD Inventor. AutoCAD creates a smooth curvature spline CAD geometry consisting of 70% of the upper surface and truncated to 50% on the lower, in order to neglect the reverse flow on the suction side. Linear external boundaries are constructed to complete the domain. This is then exported and used as an input file for NekMesh. NekMesh is a mesh constructor creating curvilinear elements at the geometry surface. It places refinement in areas of higher curvature and uses smoothness algorithms to automatically set mesh sizings though application of the following formula,

$$\delta_e = 2R\sqrt{\epsilon(2-\epsilon)}\,. \tag{3.13}$$

Here ϵ is an element scaling parameter, R is the radius of curvature of the CAD geometry and δ_e is the element size. This is constrained between a maximum and minimum value prescribed by the user. Triangular elements are created unless additional parameters are prescribed to create a layer of quadrilateral elements in the domain. This

layer can be constructed cleverly by assigning the number of layers of quadrilateral elements, progression and thickness in order to construct a stream-wise growing layer of quadrilateral elements. Unfortunately this is not enough refinement alone. The meshing program also needs additional refinement lines over the upper surface which remains a heavily manual process. When the roughness is incorporated to the geometry, these additional refinement lines are absolutely essential. The generation of a well defined, robust mesh is in no way trivial. Once a valid mesh is created, a DNS simulation with the incompressible Navier-Stokes (ICNS) solver within Nektar++ can be computed. Although NekMesh offers Jacobian checking routines to highlight invalid elements introduced though the mapping defining the curvature, to ensure validity of the mesh, this does not ensure a robust mesh has been created. There may still be problems when running the ICNS, such as too severe element size changes between refinement lines, meaning the mesh generation must be returned to in order to try and resolve the problem. Inflow boundary conditions are extracted from the full TAU solution and high order outflow pressure conditions are applied at the outflow boundaries to enable converged solutions on the truncated domain[22], see figure 3.2. The angle of attack is fed in through the inflow velocities and the sweep is introduced through Fourier expansions along the span with periodic boundary conditions at inflow and outflow. This completes a 2.5 dimensional domain of one element thickness. The clean geometry is first simulated with low polynomial order and then ramped up to attain convergence. The solution is time marched to a steady state and then a time averaging filter is applied. The process is summarised in figure 3.4.

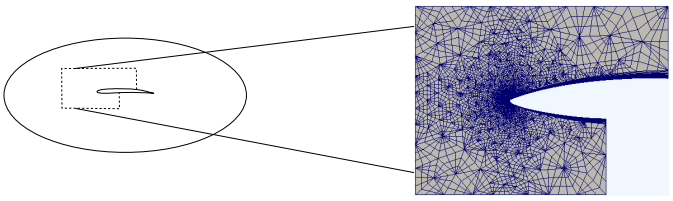

Figure 3.2: Left shows the full TAU solution, right shows the embedded Nektar++ domain.

3.3 Validation

Convergence studies of h and p type refinement are conducted to ensure no mesh dependence, see appendix B. Typically a seventh order polynomial approximation is required within the quadrilateral, near wall, layer and a lower order is sufficient within the external triangular elements. Usual roughness meshes contain 10,000 elements which are then expanded though the corresponding polynomial basis. Steady solutions are confirmed with an L^2 norm relative error of averaged velocity fields across the entire

domain such that,

$$\frac{c}{\bar{u}_\infty}\frac{\sum_{j=1}^{N}\left(\bar{\mathbf{q}}_t(j)-\bar{\mathbf{q}}_{t-1}(j)\right)^2}{\sum_{j=1}^{N}\left(\bar{\mathbf{q}}_t(j)\right)^2}\leq 10^{-5}, \tag{3.14}$$

where $\bar{\mathbf{q}}$ represents a vector of averaged velocity fields, subscripts denote the time position, j represents a point in the domain, c is the length scale of the chord and $\bar{u}_\infty$ the free stream velocity.

3.4 Extraction of Boundary Layer Profiles

Once the DNS has converged, the flow field needs to be converted into the correct format for input into the stability tool sets, the PSEMEAN.PRO file. Nektar++ simulations are computed in the Cartesian co-ordinate system, whereas the PSEMEAN file needs to be defined with respect to the h-incorporating body fitted system, the same as that described by the transformation equations 2.46.

First of all, the time averaged output file needs to be a 2D expansion, not a 2.5D. In order to do this a post processing routine within the FieldConvert library is applied (mean mode) in order to extract along the zero plane in Fourier space. This will then become the 2D file containing all information of the basic flow.

For the PSEMEAN file, only points within the boundary layer and just outside are required. As previously stated, these must be prescribed normal to the geometry surface which means the normal vector to the surface must be known. This is attained by using a wall extraction routine, wall shear stress, within the Nektar++ framework to provide all points over the geometry surface and a decomposition of the normal vector. This information can then be used within a python routine to generate a selection of points in the wall normal direction at each stream-wise wall point. Points are defined from the attachment line which is found by calculating the pressure coeffiecient maximum. Not all points along the surface are utilised as this would become too time consuming for the interpolations to follow. Each point along the surface, coordinate s, and all its corresponding normal points will now be referred to as a station. The selection of points prescribed in the wall normal direction are Chebyshev collocation points, leading to clustered points near the wall which are desired, and clustered points in the free stream which are undesired.

Once a points file has been constructed containing all the chosen coordinate points, these need to be probed in the averaged solution field. This is achieved through another FieldConvert option, interpolate points, to provide a data file of velocity components and pressure at the requested points. The PSEMEAN file not only requires the primitive variable, but also first and second derivatives with respect to the body fitted

system. Obtaining smooth second order derivatives is again not trivial, the task of finding a suitable interpolation process was achieved after a variety of attempts before finding the best way to proceed. Even now, there is still room for improvement which will be expanded upon later.

The velocities extracted from the probing routine are still prescribed in the Cartesian frame meaning these must first be transformed to the body fitted frame. The desire is then to have a set of points which are clustered at the wall, sparse in the free-stream and station profiles which are smooth for all derivatives. Although the primitive variables may look smooth to the eye, when taking derivatives to second order they can become rather noisy. This is because Nektar++ only enforces C^0 continuity of the variables. In order to smooth them, each station is cubic spline fitted to a set of equidistant points, every other point is then ignored and another cubic spline interpolation applied to obtain the original points profile and create smoother primitive variables. Derivatives of this smooth spline are then calculated with python inbuilt cubic spline interpolation with every other point of the equidistant distribution. The pressure field and its derivatives are obtained though the fitting of Chebyshev polynomials via other Python libraries and interpolated to equispaced points.

This has taken care of the wall normal derivatives, the next point to address is the stream-wise derivatives. Firstly, the body fitted coordinate system is still defined with respect to Cartesian coordinates. The wall normal direction is easy to assign since the points originate at zero, the wall, and are spaced as we prescribed. The stream-wise coordinate system begins at zero, from the attachment line, and points growing downstream are calculated using cumulated Pythagoras Theorem. Since the boundary layer points are more clustered near the leading edge of the geometry both in the stream-wise and normal direction, each row vector of points traversing away form the wall will be different. In order to take derivatives in the stream-wise direction, all stations need to have the same point distribution. This means, the entire domain of primitive velocity variables are again interpolated, via cubic splineing, along each station to a set of points defined by a geometric progression. The s-coordinate system is recalculated and a cubic spline fit can be applied in the stream-wise direction. Derivatives and cross derivatives can then be calculated and finally the whole flow field interpolated onto an equispaced grid.

The final task remains to non-dimensionalise the data. This is achieved with the boundary layer edge values which are determined by finding the point where the stream-wise velocity is 99.99% of the inviscid stream-wise velocity, such that $\bar{u_e} = 99.99\%\ \bar{u}_{inviscid}$. The boundary layer edge thickness can can be determined and these two quantities used in the scaling of the PSEMEAN file. This concludes the generation for the clean file.

If an excrescence is present there are some extra modification to be made to the process. Firstly, the roughness profile, $h(s)$, is required along with first and second derivatives. The first hurdle here is establishing $h(s)$ in the first place. This is because the roughness profile has been created in AutoCAD with a filleting procedure applied to curve the corners. Finding the distance, h, should be a simple task of finding the difference between the clean geometry and the roughness geometry. However, due to the wall surface distribution of points being different with each Nektar++ mesh generated, this does not become very straight forward. Essentially a triangle is constructed from the three nearest points, one from the roughness and two from the clean geometry. Two circles are then constructed between the excrescence point and each clean point and their location of intersection identified. This provides the normal to the clean surface, at the location of the roughness point. The tangent to the surface can be found from the negative inverse of this meaning equations of the lines governing the normal and tangent can be found. The intersection of these then gives the clean surface location of the roughness point, and so $h(s)$ can be finally found. Due to the steepness of the steps introduced, spline fitting of the profile to calculate derivatives obtains spurious overshoots. As a consequence of the non-equidistant grid points the usual central differencing stencil for the derivative is now only first order accurate. Instead a polynomial approximation is applied to retain second order accurate derivatives.

The other modification to the routine is for the stream-wise velocity derivatives. Due to the strong stream-wise gradient changes present in the neighbourhood of the roughness, a cubic spline fitting can no longer be applied here. Instead, a polynomial fitting is applied in the region of the roughness only and cubic spline interpolation is applied elsewhere in the domain, see figure 3.3. Stream-wise derivatives must also incorporate the transformation,

$$\bar{\mathbf{q}}_x = \bar{\mathbf{q}}_s - h'\bar{\mathbf{q}}_Y, \tag{3.15}$$

to ensure correct implementation of the roughness.

A summary of the process can be found in figure 3.4.

3.5 Nektar++ LNS

Nektar++ is also used to compute the unsteady linearized incompressible Navier-Stokes solutions (Nektar++ LNS) for comparison with the more efficient PSE and LNS stability codes. Contrary to the harmonic formulation of the LHNS equations, which provide the long time asymptotic solution, Nektar++ LNS applies a time marching procedure. The domain and method of solving is set up similarly to that of the baseflow cases[13] however, a finer mesh is required for the Nektar++ LNS in order to

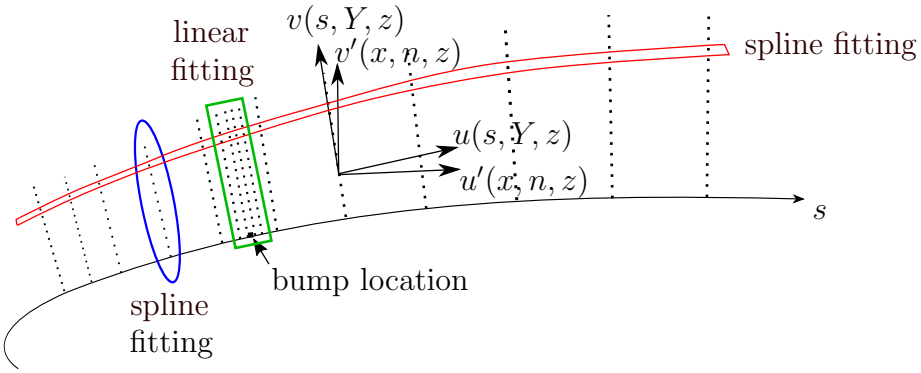

Figure 3.3: Transfomation of Cartesian velocity components to body fitted. Example of wall normal spline fitting denoted by the blue oval, stream-wise spline fitting points in red, and the green box denotes the region in which spline fitting is replaced with linear fitting.

obtain converged solutions. This results in using another embedded mesh consisting of only the upper surface geometry. The wall conditions are modified to provide suction / blowing across one Nektar++ surface element thickness to introduce the perturbation. The span-wise domain is configured such that it is the same length scale as the introduced CFI and periodic boundary conditions are then applied.

3.6 Pipeline of Tools

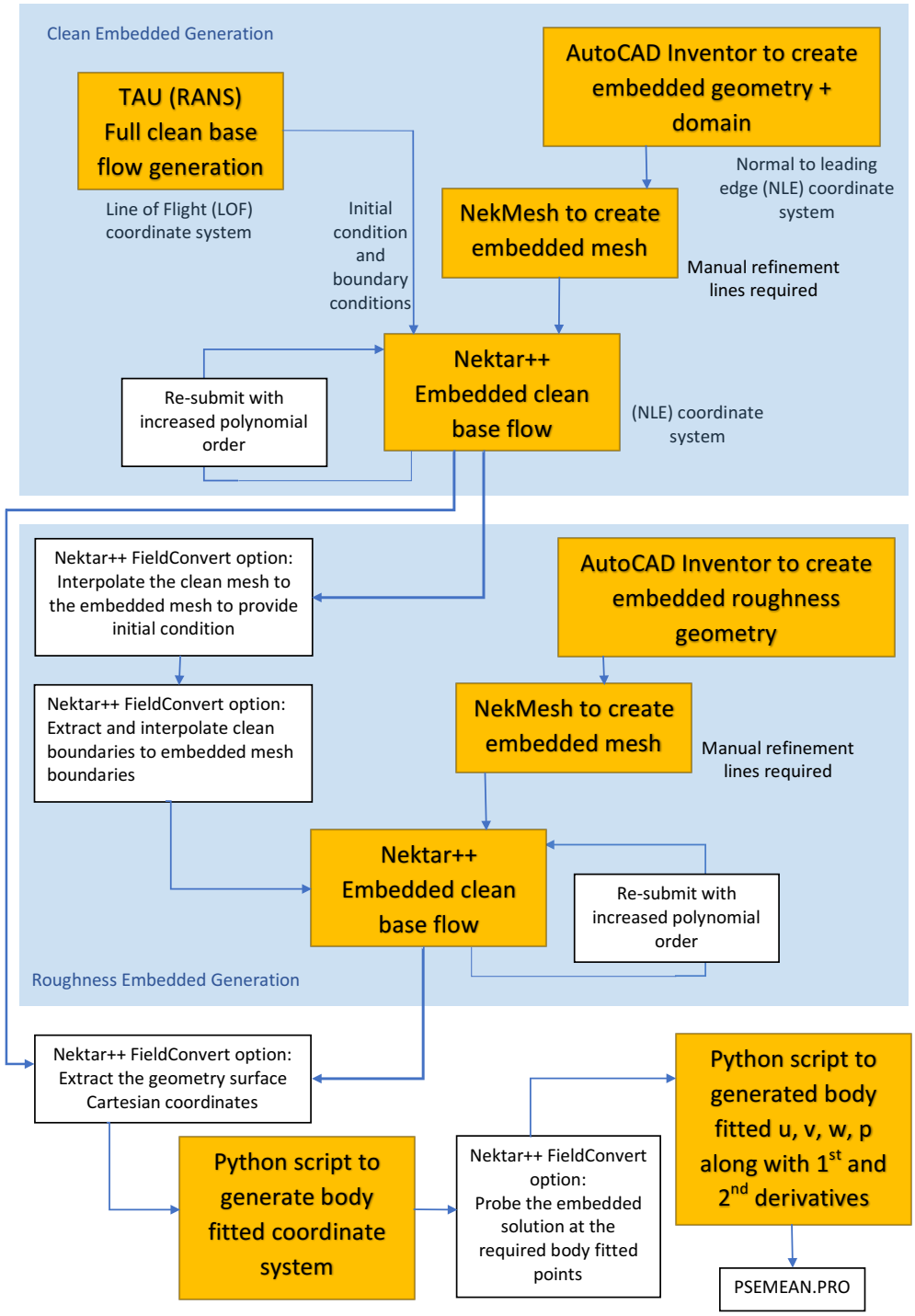

Figure 3.4: Pipeline for Nektar++.

CHAPTER 4

Two Dimensional Flow Problems

As a starting block for testing the new stability tools, PSEh and LHNSh, we began with flat plate un-swept cases. These consist of a dimple case, with a half cosine shaped indentation, and a randomly distributed roughness case, placed around the centre of the surface of the flat plate.

4.1 Dimple

The dimple case is based upon the work by Xu et al.[107] which features a surface indentation, of width either 11 (81mm) or 22 (162mm) times the boundary layer thickness, and height either 45% (0.81mm), 52% (1.62mm) or 60% (2.17mm) of the boundary layer thickness. There is a laminar separation bubble (LSB) confined within the dimple for some configurations. Two dimensional and three dimensional excrescences were considered; our analysis will focus on the two dimensional cases where the boundary layer profiles have been extracted through the mid-symmetry plane.

4.1.1 Nektar++ Base Flow Solution

Base flows were computed with Nektar++ incompressible Navier-Stokes solver. The flow configuration has a free stream velocity of 18 m/s and a Reynolds number of 1.2 million. The inflow domain is initiated at 0.2m where a Blasius flow, zero pressure gradient, is prescribed and the outflow is located at 1.2m. Computations typically

feature 4500 elements in the $x-y$ plane with a 5^{th} order polynomial expansion and the span is modelled with 120 Fourier expansions[107]. The dimple profile is described by a half cosine wave,

$$\xi = \frac{h}{2}\Big(cos\big(\frac{2\pi r}{\lambda}\big)\Big), \tag{4.1}$$

where h is the displacement from the clean surface, i.e. flat plate, λ is the width of the dimple and r is the radius. For the thinner width dimple there are recirculation bubbles present for the two deeper depths, but for the wider case, reverse flow is only just present in the deepest case. An example of a typical 2D baseflow is given in figure 4.1 along with typical dimple depth profiles. As expected, the boundary layer decelerates in the upstream part of the dimple and accelerates in the downstream part where the pressure gradient is adverse to favourable respectively. There is some asymmetry present in the pressure distribution and velocity profiles due to the displacement of the boundary layer. Example pressure gradients can be found in figure 3 of Gowree et al.[36].

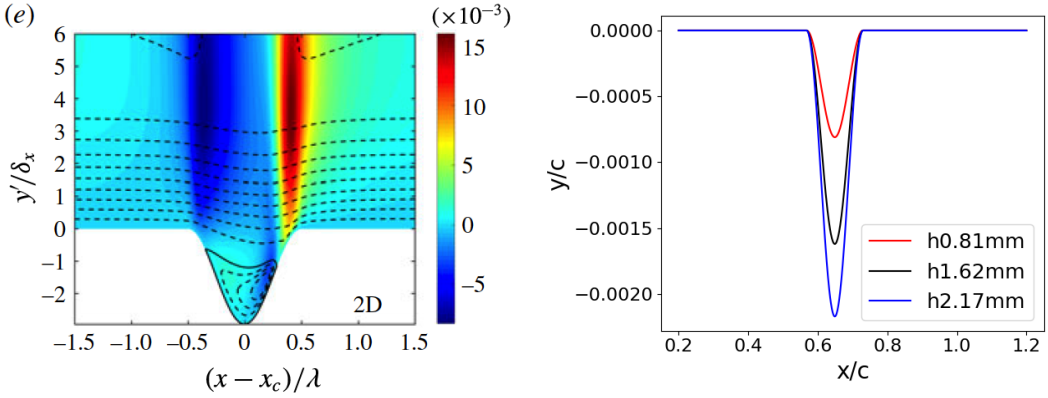

Figure 4.1: Left: Base flow for 2D dimple feature of 162mm width and maximum depth[107]. Right: Varying depth dimple $h(x)$ profiles.

Steady boundary layer profiles are extracted at 800 stream-wise equispaced positions for the stability analysis tools and then interpolated to the required grid with bi-cubic splines.

4.1.2 Linear Analysis

Tollmien Schlichting waves are generated at the neutral point to provide maximum growth, located at 0.375m from the leading edge of the flat plate. After sweeping though a range of frequencies, the most dangerous disturbance is identified as a 172Hz TS wave. This has a wavelength of around 34mm which is about 42% of the smaller width dimple and 21% of the wider dimple. Computations have been made using the PSE, PSEh, LHNS and LHNSh codes and are compared in figure 4.2. Generally

a grid size of 7500 stream-wise points and 57 wall normal polynomials are applied. The figure is constructed by taking the maximum absolute $\hat{u}$ perturbation at every stream-wise location and normalising with the local boundary layer edge velocity. First of all we can see that as the dimple depth increases the TS wave undergoes greater amplification. The smaller width dimple case at largest depth is the most dangerous, note the change in scale as this explosive growth is observed. The PSE is in line with predictions from the LHNS code and should be applauded for this, showing that even in the presence of a LSB, the PSE are able to converge to a reliable solution. It is only in the 81mm width dimple at 1.62mm depth that differences begin to become apparent and are exacerbated with clear visibility in the depth 2.17mm indentation. The deepest depth 81mm case features the largest reverse flow region causing more distortion to the basic flow and an inflectional detached shear layer. Amplitudes of the TS wave reach over 1% of the free-stream meaning non-linear interaction of modes is likely and mechanisms leading to break down play a role. The non-linearity is confirmed since in experiments higher harmonics are detected and a tripping or turbulence signal is also observed beyond the end of the indentation[36]. Although the PSE are not predicting the same as the LHNS, the LHNS result is likely to be unreliable as linear theory cannot model these features of the flow. The upstream noisiness that is observed from the dimple in the LHNS / LHNSh computations is probably due to generation of upstream propagating pressure waves, or acoustic waves, as discussed by Wu and Dong[104]. However, in our case the upstream propagation is very significant; Wu and Dong[104] looked at much weaker forms of scattering. To clarify, the LHNS are able to model the so-called scattering effect in its entirety, while the asymptotic framework developed by Wu and Dong[104] is an approximate form.

Comparing now the differences between the h corrected codes (PSEh, LHNSh) and original no-h corrected codes (PSE, LHNS) the change in TS growth over the dimple region is quite different. Both PSEh and LHNSh predict greater amplification within the dimple region than the PSE and LHNS, although all seem to converge to the same result upon exiting the dimple region, at least for the 162mm width case. The PSE / LHNS predict a short stabilisation upon entering the dimple whereas the PSEh / LHNSh predict a continuation of the growth, then an added destabilisation. They only predict a stabilisation near the end of the dimple. This is likely due to the scale of the favourable pressure gradient being much larger upon exiting the dimple than the scale of the adverse pressure gradient when entering the dimple, referring to figure 3 from Gowree et al.[36].

A comparison of these LHNSh results with the PSE3D and experimental results is shown in figure 4.3, courtesy of Gowree et al.[36]. The reader may refer to Paredes et al.[63], Ashworth and Mughal[6] and Gowree et al.[36] for information on the PSE3D.

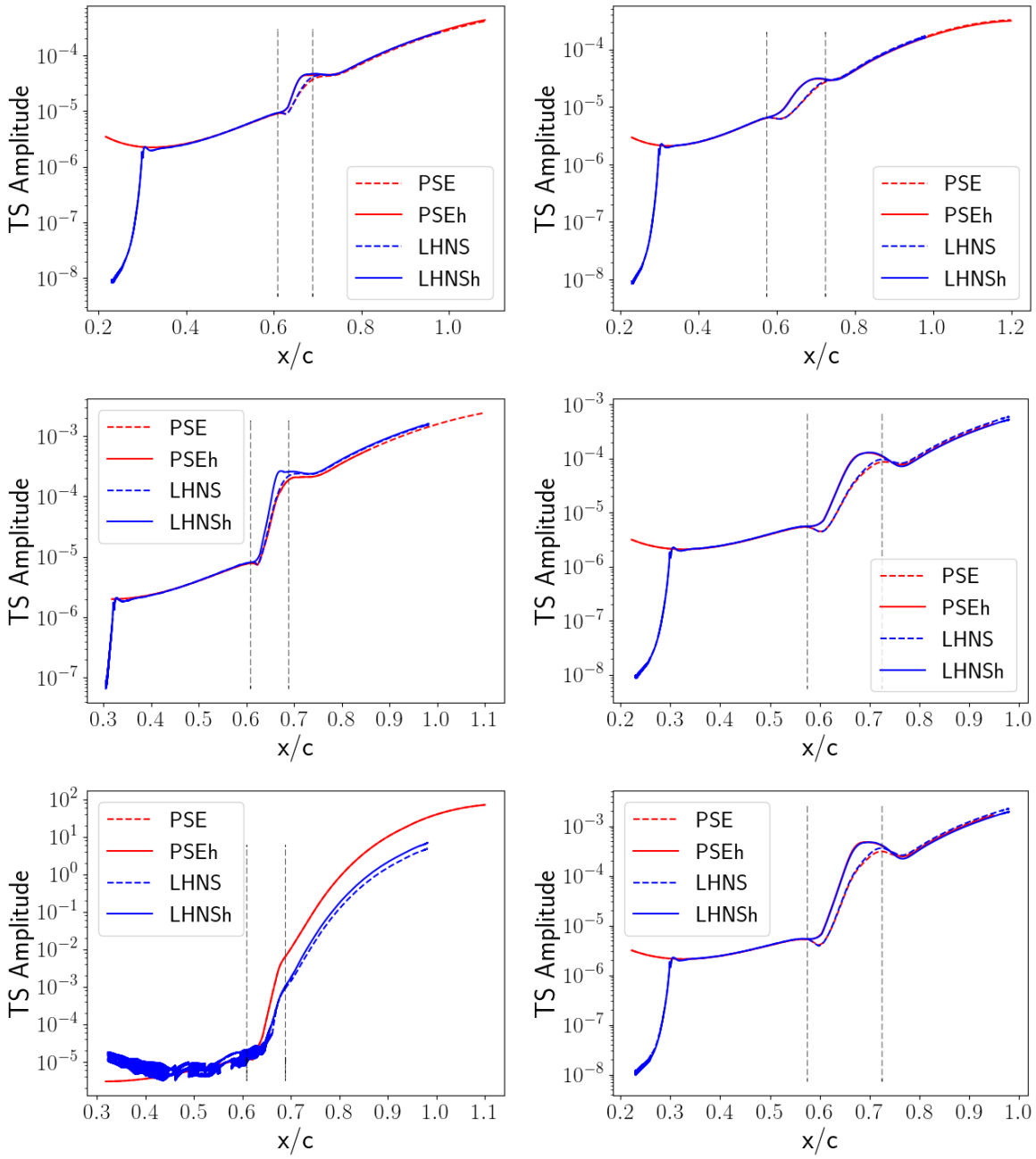

Figure 4.2: Amplitude growth of 172Hz TS wave as it convects over the dimple, marked out with vertical dashed black lines. Left: Dimple case 81mm wide. Right: Dimple case 162mm wide. Top to Bottom: 0.81mm, 1.62mm and 2.17mm depths.

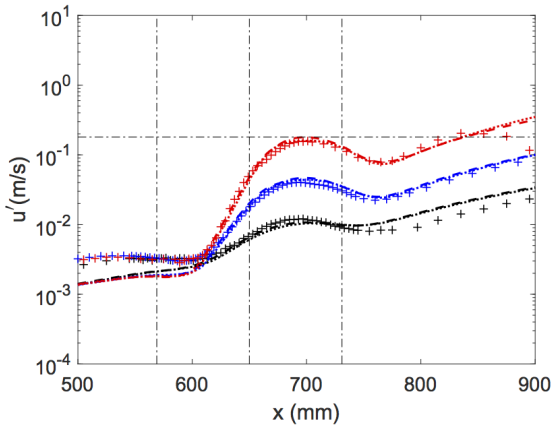

Figure 4.3: Amplitude of the maximum stream-wise fluctuating component, u', along the symmetry plane of the indentation for $h = 0.81$ mm (black), 1.62 mm (blue) and, 2.17 mm (red) for a constant $\lambda = 162$ mm. The experimental results are represented by the symbol '+'; the solid blue and dotted red lines represent the results from PSE3D and 2D LHNSh simulations. The positions of the beginning, centre and end of the indentation are represented by the vertical dotted-dashed lines and the horizontal dotted-dashed represents 1% of free-stream velocity.[36]

The disturbances $max(\hat{u})$, (or u'_{max} in the paper) evolution for varying depth dimples with constant widths of 162 mm, is shown. For the deeper cases, $h = 1.62$ and 2.17 mm, largest differences between the PSE3D and LHNSh (just visible in the plots) arise in the recovery region ($x \approx 700$ mm) in the latter half of the indentation and improves beyond $x \geq 780$ mm.

Looking now at the broader $\hat{u}$ flow field, normalised with the edge velocity at each station, over the dimple region and comparing the LHNS and LHNSh computations we can see that there are some slight differences in the perturbed field, see figures 4.4 and 4.5. Beginning with the 162mm width case, we can see that within the dimple the LHNSh predicts a more symmetrical $\hat{u}$ profile about the centre line, 0.65 x/c. Upon the TS wave exiting the dimple we can see that there are two maxima, when traversing away from the wall, predicted by the LHNS code. This is more clearly seen in the deepest case around 0.75 x/c. This second maxima is still present in the LHNSh case but it is much less pronounced. The 81mm width case exhibits rather different perturbed fields for the 1.62mm depth case; the LHNS tends to show the stabilisation to the left of the centreline whereas the LHNSh shows stabilisation to the right of the centreline. The 2.17mm depth case showcases the upstream wave fluctuations.

If we now take wall normal profiles from the centreline of the dimple, and examine $\hat{u}$ and $\hat{v}$ perturbations for the 162mm width dimple, we can see that there are two maxima, or lobes, for the shallowest dimple $\hat{u}$ perturbation and three for the two larger depths. See figure 4.6 for $\hat{u}$ perturbation profiles in the 162mm width dimple compared with experiments, extracted from Gowree et al.[36]. This shows a comparison of the theoretical results computed with the LHNSh formulation compared to experimental

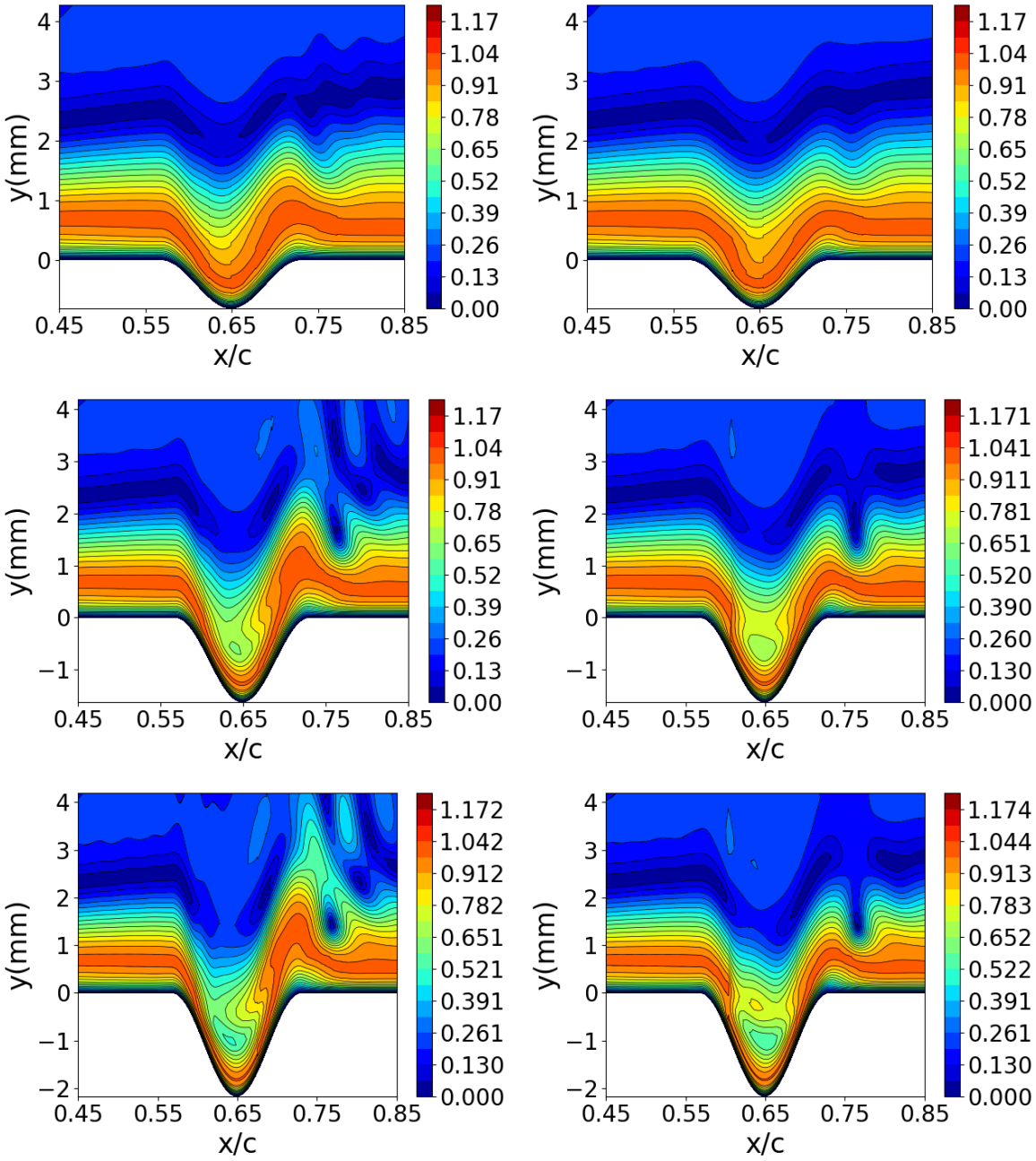

Figure 4.4: $\hat{u}$ contour plots of 162mm width dimple case. Left: Computed with LHNS. Right: Computed with LHNSh. Top to bottom: 0.81mm, 1.62mm and 2.17mm depths.

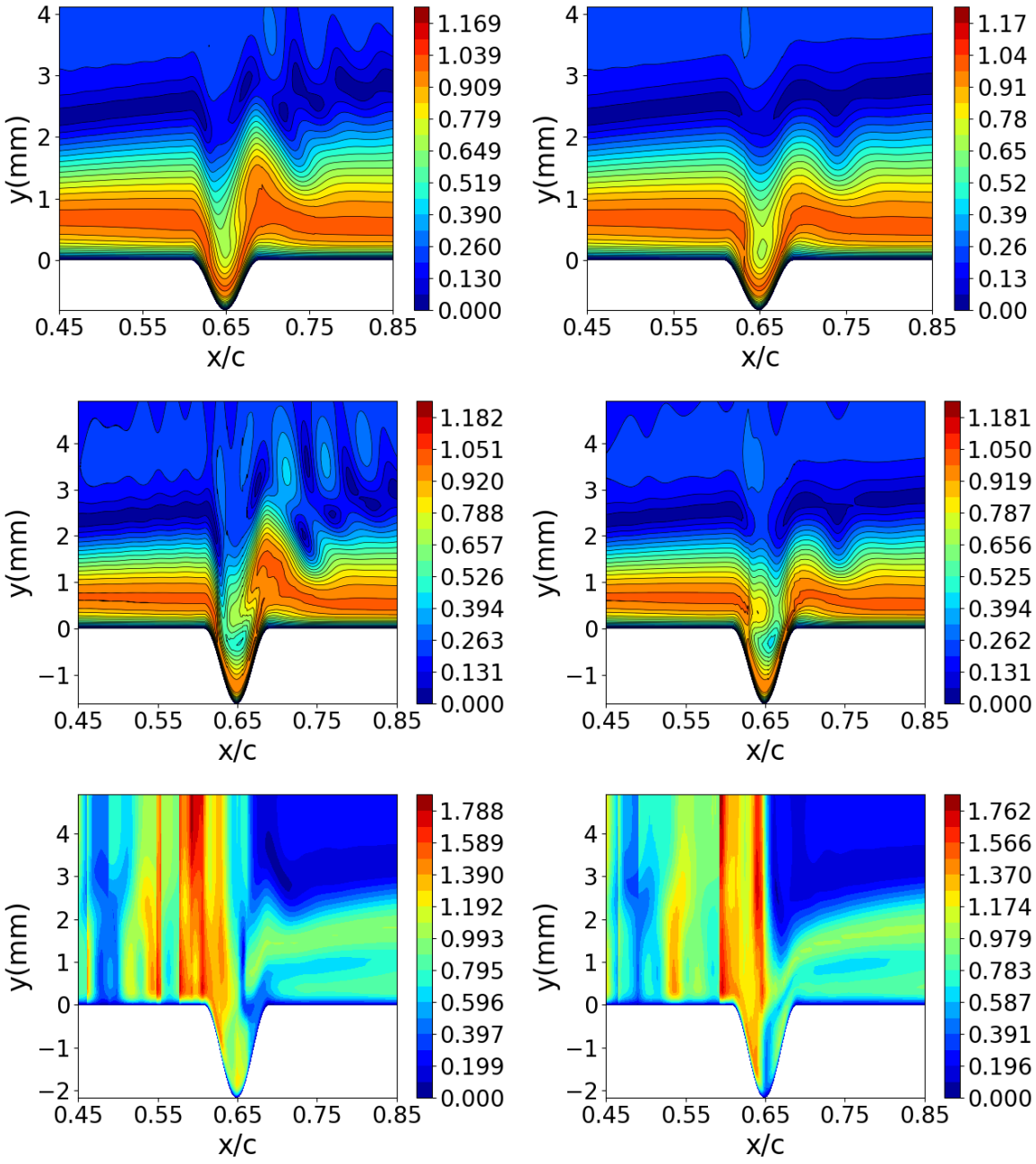

Figure 4.5: $\hat{u}$ contour plots of 81mm width dimple case. Left: Computed with LHNS. Right: Computed with LHNSh. Top to bottom: 0.81mm, 1.62mm and 2.17mm depths.

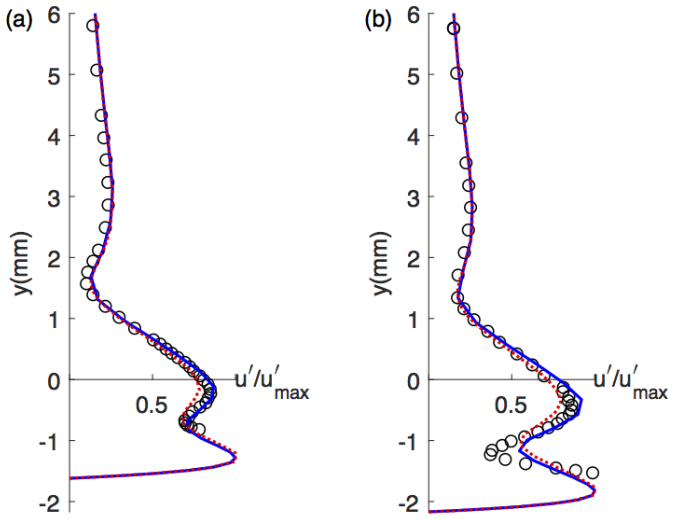

Figure 4.6: Profiles of the stream-wise fluctuating velocity component, u', normalised by the maximum amplitude along the centreline of the plate at $x = 650$ mm, (a), $h = 1.62$ mm and (b), $h = 2.17$ mm for $\lambda = 162$ mm. The experimental results are represented by '$\circ$'. The solid blue and dotted red lines represent the results from PSE3D and 2D LHNSh simulations respectively. Gowree et al. [36]

measurements and a fully PSE3D based simulation[6,63]. See figure 4.7 for $\hat{u}$ and $\hat{v}$ perturbation profiles for all cases. Such profiles have also been documented by Diwan and Ramesh[20] experimentally. As the dimple height increases we can see these maxima are lifted further away from the wall for both $\hat{u}$ and $\hat{v}$. We can also see that the three $max(\hat{u})$ predicted by the LHNSh are slightly larger than that of the LHNS code. This is similar for the minima, which are also more exaggerated in the LHNSh code. These features are also observed in the 81mm case, see figures 4.6 and 4.8.

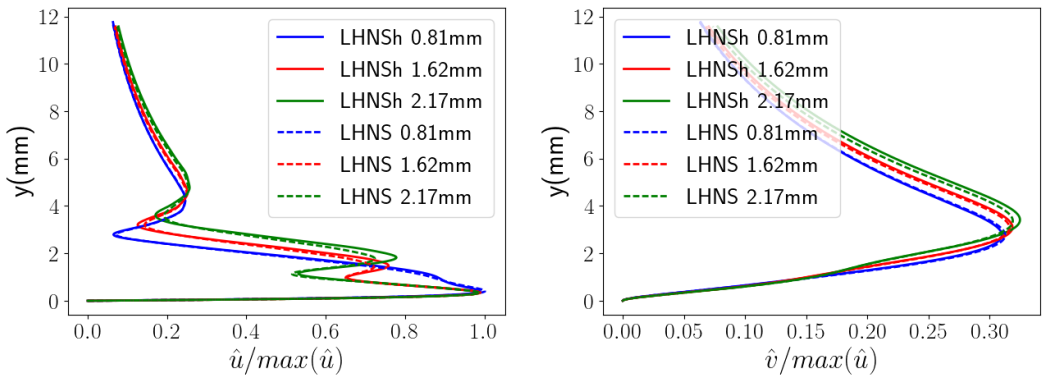

Figure 4.7: Perturbation profiles of 162mm width dimple case at the centre line location. Left: $\hat{u}$. Right: $\hat{v}$

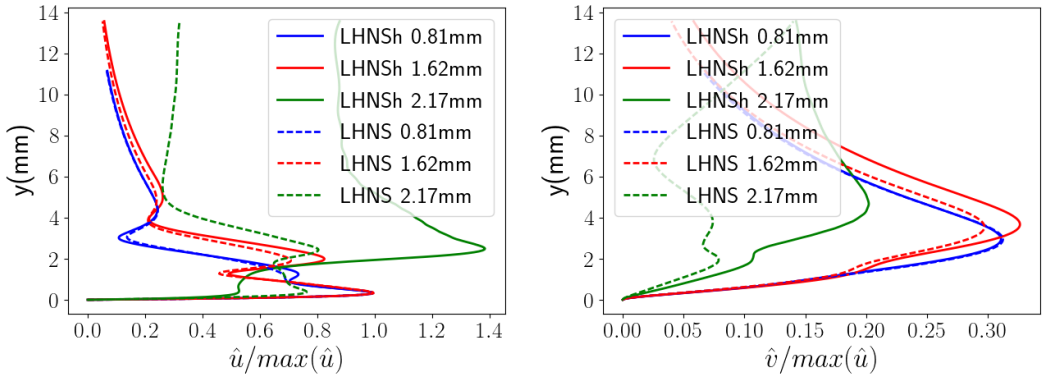

Figure 4.8: Perturbation profiles of 81mm width dimple case at the centre line location. Left: $\hat{u}$. Right: $\hat{v}$

4.1.3 Non-Linear Analysis

Non-linear analysis has also been conducted with all codes to see how well they perform in the presence of a LSB. First of all the LHNS and LHNSh are compared in figure 4.9. All computations converged except the largest depth 81mm case which features a LSB with a significantly larger peak reverse flow than the other bubbles, 8% of the free-stream, which accelerates the non-linear interactions. We can see that for the 81mm cases and the smallest depth 1.62mm case, all harmonics are very well agreed outside of the dimple. The mean flow distortion does however exhibit some differences outside of the dimple region, see figure 4.10. This is to be expected due to the $\frac{\partial p}{\partial x} = 0$ assumption applied in the derivation of the PSE / PSEh to halt upstream propagation of information. This is not enforced in the MFD for the LHNS / LHNSh which explains the differences. It is only in the larger two 162mm cases that we begin to see some differences between the amplitude growth after the dimple region for the second and third harmonics. This is likely due to the scattering effect, where the TS wave becomes abruptly distorted over the region of the bubble due to interaction with the MFD mode. The fundamental and higher harmonics then become scattered at this location, see Wu and Hogg [105]. When the fundamental reaches 1% of the mean flow, this is an indication the boundary layer will begin to distort. If the second and third harmonics reach 20% or 8% respectively of the fundamental mode then breakdown will occur, as stated by Klebanoff et al. [51]. This could be why there is no result for the largest depth, 81mm dimple case, and / or due to the possible existence of a bi-global absolute instability [4,93].

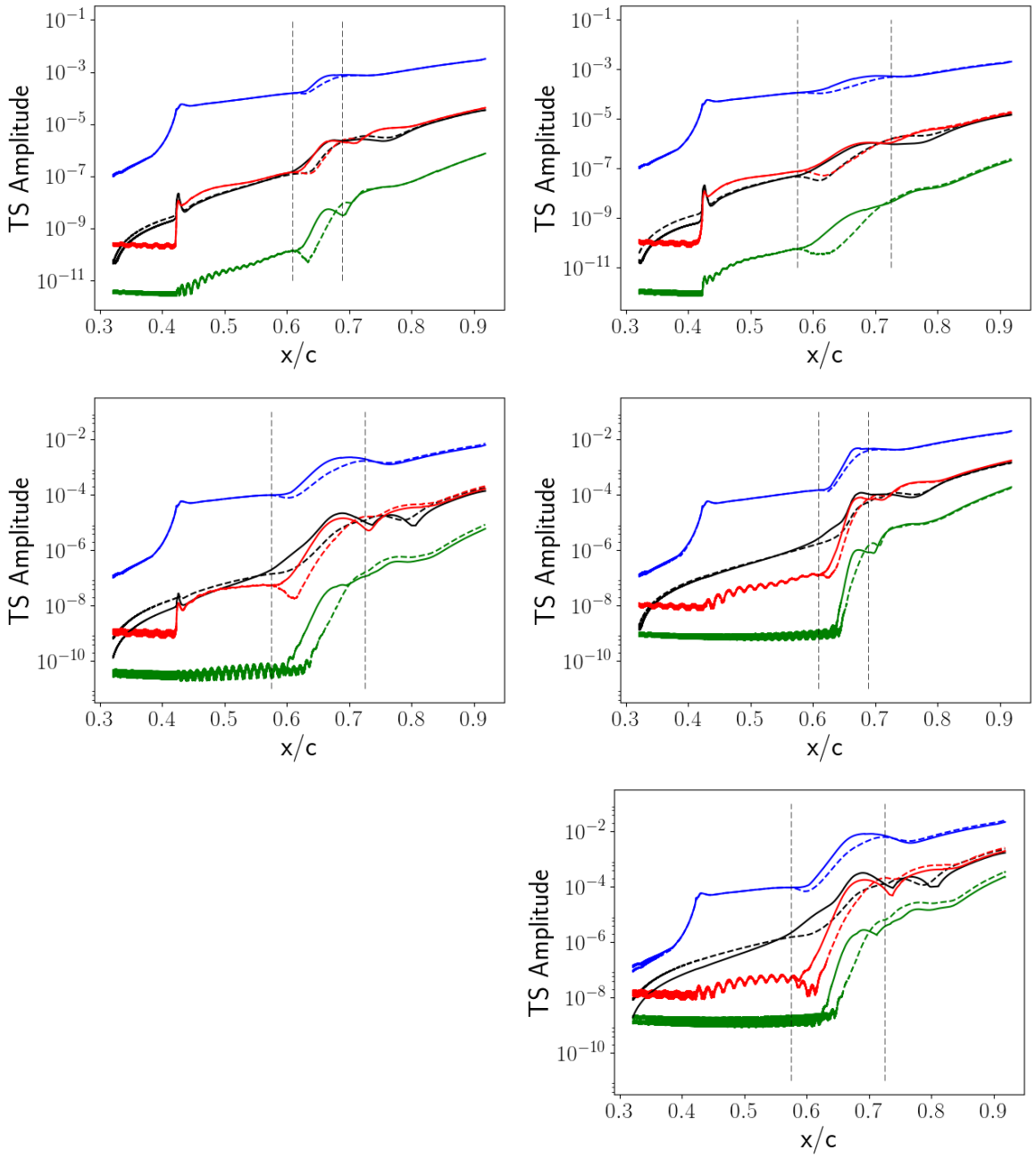

Figure 4.9: Non-linear HNS and HNSh comparison. Left: Dimple case 81mm wide. Right: Dimple case 162mm wide. Top to bottom: 0.81mm, 1.62mm and 2.17mm depths. Black for the mean mode, blue for the first harmonic, red second and green third harmonic. Dashed lines denote LHNS code, solid lines denote LHNSh code.

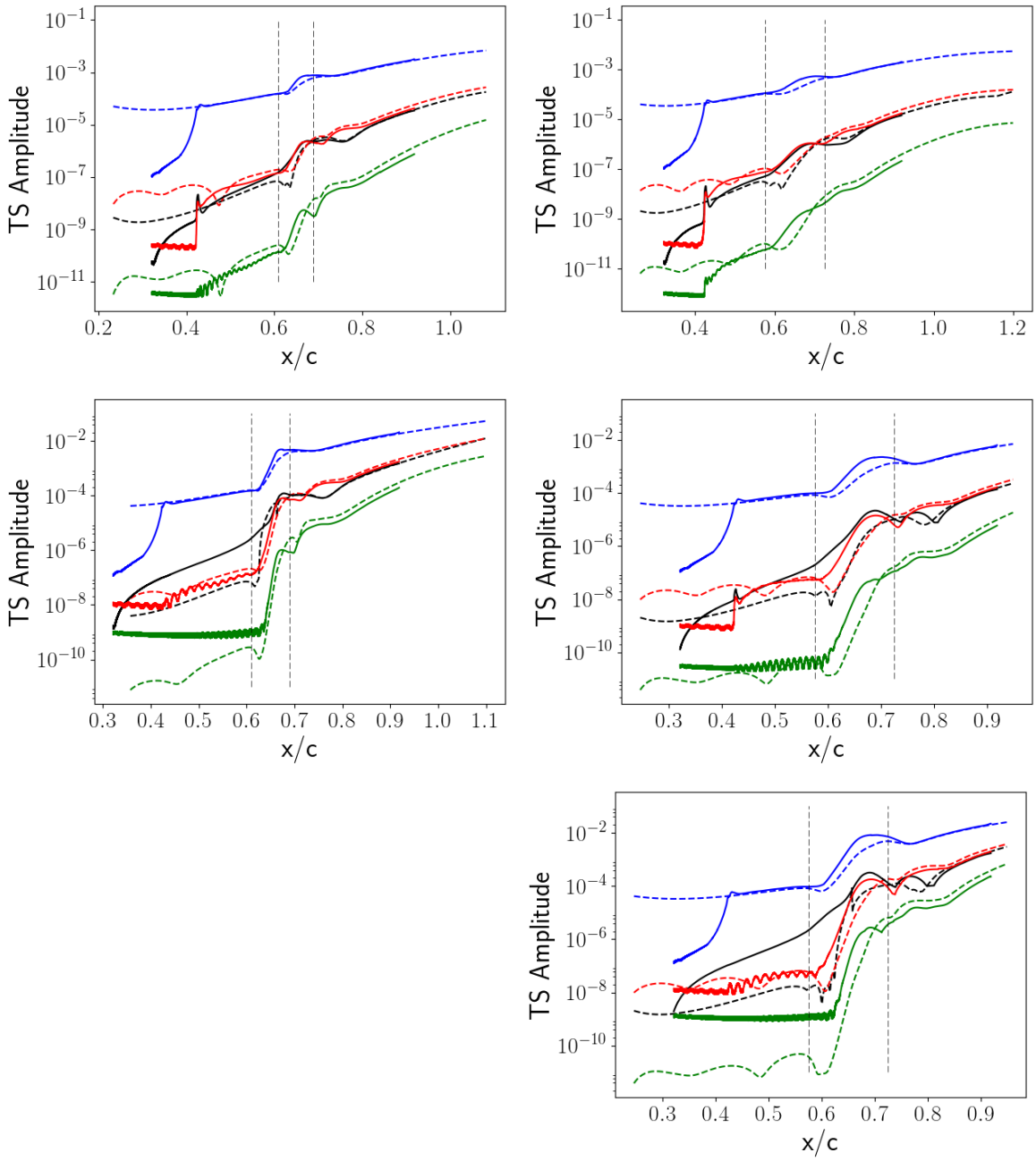

Figure 4.10: Non-linear PSEh and HNSh comparison. Left: Dimple case 81mm wide. Right: Dimple case 162mm wide. Top to bottom: 0.81mm, 1.62mm and 2.17mm depths. Black for the mean mode, blue for the first harmonic, red second and green third harmonic. Dashed lines denote PSEh code, solid lines denote LHNSh code.

4.2 Random Roughness

After the pleasing agreement of results obtained from the dimple case, we then progressed to a more complex excrescence, the random roughness. This random roughness work is based upon investigations by Xu et al.[107] who looked at a roughness of panel length 162mm over an un-swept flat plate of length 1.2m. A variety of roughness distributions were investigated by Xu et al.[107] but we shall only consider one distribution at three varying heights. These cases were investigated numerically only, for some initial insights of undertaking future experimental work on the effects of randomly distributed roughness on transition.

4.2.1 Nektar++ Base Flow Solution

The roughness distribution we consider is given by,

$$\xi = h \sum_{k=-N/2}^{k=N/2} \left(\sqrt{E(k)}\, e^{i(2\pi kx/\lambda + \theta_k)} \right) + c.c.\,, \tag{4.2}$$

where the power spectral density of the roughness is given by,

$$E(k) = e^{(k/k_{max})^2}, \tag{4.3}$$

and the root-mean-square of the roughness, R_q, is defined by,

$$R_q = \sqrt{\frac{1}{\lambda} \int^{\lambda} \xi^2 dx}\,. \tag{4.4}$$

Here k ranges from $k = 3 : 1000$ for three differing k_{max} values. We will only be investigating $k_{max} = 15$. Three roughness base flows are computed numerically with the incompressible Navier-Stokes Nektar++ solver corresponding to $R_q = 0.073$mm, 0.22mm and 0.37mm which equate to 2%, 6% and 10% respectively of the boundary layer thickness. The free-stream velocity for the base flows are 18ms^{-1} , Mach number 0.0527 and a temperature of 290.33K. The Reynolds number per meter is 1.2 million and the dynamic viscosity is $\mu = 1.8237 \times 10^{-}5 Ns/m^2$. Examples of the roughness profile $h(x)$ can be seen in figure 4.11.

4.2.2 Linear Analysis

The most destabilising Tollmien-Schlichting instability for this regime has a frequency of 172Hz and is investigated in the presence of three roughness heights. First, we

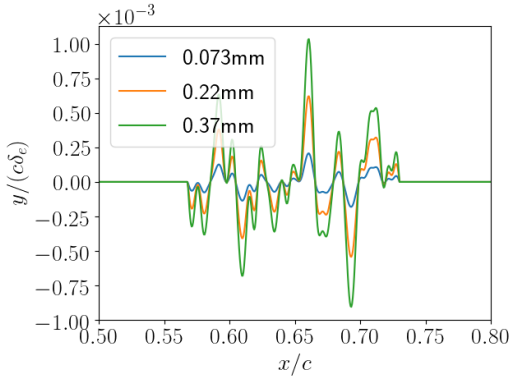

Figure 4.11: Right: Example roughness $h(x)$ profiles from the work of Xu et al.[107]. Both axes are made non-dimensional with the plate length, c. The y axis is also normalised with the boundary layer thickness at each x location.

begin with comparing linear computations of the modified PSE and LHNS codes. We can see that the smallest roughness height does not show much change exterior to the roughness region which is confined between the vertical dashed black lines, see figure 4.12. There appear to be some small changes between all codes within the roughness region. Increasing to the 0.22mm height case we can see that the differences between the codes become more apparent downstream of the roughness. The trends of the curves tend to follow the same shape when comparing the PSEh and LHNSh codes, and also for the PSE and LHNS codes, the differences seem to be slightly more amplified. Interestingly, here the LHNSh and PSEh (solid lines) seem to predict a slight stabilisation of the instability. The difference between the LHNSh and PSEh and then the LHNS and PSE seem to be around the same offset. This is likely to be due to the PSE and PSEh neglecting the small order terms, such as the second order stream-wise derivatives, which the LHNS and LHNSh do not. However, could also be due to the scattering effect caused by the many reverse flow regions situated in the troughs after large peaks in the roughness[105]. For the final plot, largest roughness case, we see a large difference between the PSEh and the other results. This is due to having to artificially skip over some boundary-layer profiles for the PSEh computation to converge, probably because of the many present LSBs and strong stream-wise gradients created in the velocity field, and also to meet the PSE numerical stability criterion of $\Delta x < 1/\alpha_r$, for a converged solution. If we take the example of a roughness peak, described by 6 stations (blue and orange markers in figure 4.13), each station on the positive gradient slope has a corresponding station on the negative gradient slope. This means that the h' values at these points are very similar, if not the same, and will have similar $\bar{u}$ components and similar opposite $\bar{v}$ components. If we now choose to ignore a (or multiple) station(s) to ensure the PSE will march to a solution for the full domain, this equal and opposite relationship is not retained. Through the act of ignoring stations it can mean that the derivative values

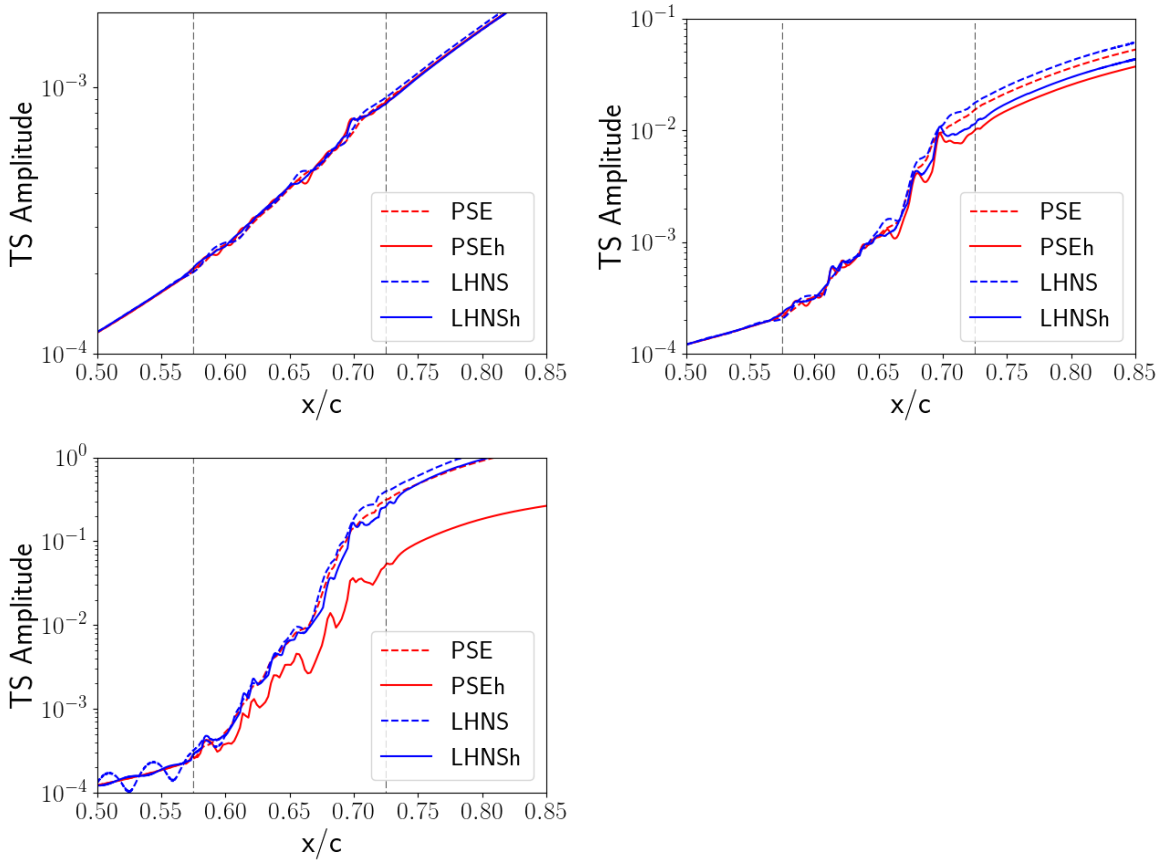

Figure 4.12: Amplitude growth of TS wave with frequency 172Hz as it convects over the roughness. Top left is for R_q= 0.073mm case, top right for 0.22mm case and bottom for 0.37mm case.

of h will no longer be of similar opposite weights, similarly for the $\hat{u}$ and $\hat{v}$ component of the velocity. We had to ignore more stations for the largest roughness height for the PSEh solution to converge. This explains why there is a larger difference between the PSEh and any other result in figure 4.12. This then leads us to the question, why did more stations have to be ignored for the PSEh computation than the PSE? This is likely to be due to the h'' derivative term, coupled with the $\hat{u}_{YY}$ viscous term in the x-momentum equations (amongst other contributing terms) which can both be large order quantities local to the roughness.

Contour plots of the $\hat{u}/\max(\bar{u}_e)$ perturbation become more and more distorted with increased roughness height, see figure 4.14.

4.2.3 Non-Linear Analysis

Non-linear analysis for these random roughness case is extremely difficult. We were only able to attain converged PSE and PSEh computations for the smaller two roughness cases. The non-linear analysis from the PSEh are shown in figure 4.15. We can

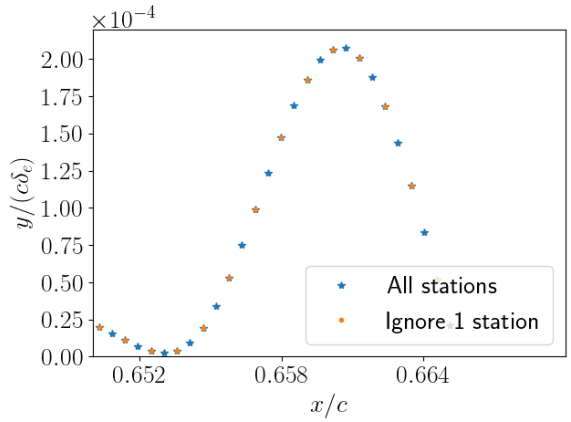

Figure 4.13: A zoomed in of section of roughness profile $h(s)$ to highlight consequence of ignoring stations in PSE/PSEh computations.

see from the second largest roughness height that the mean flow distortion effects all harmonics in the roughness region. Particularly halfway though the roughness region, where there is a large increase in the h profile. The growth of the harmonics undergo a greater change in amplitude with increasing order. We can see the MFD mode growth is not very smooth which provides an indication of why the largest roughness case did not converge. There is likely to be large upstream propagation of signals here that the PSE are inherently unable to capture. Converged non-linear HNS and HNSh results could only be obtained for the smallest height random roughness, the latter of which is shown in figure 4.15. This could be due to the sharp increase suggested by the medium roughness height PSEh computations. When the MFD mode is captured accurately, as in the non-linear HNSh code, the upstream modification may become too large for computations to converge, this should be further explored.

4.3 Concluding Remarks

Testing the new stability tools, PSEh and LHNSh, with the dimple and random roughness cases has highlighted their capabilities and limitations when in the presence of an excrescence. The dimple case has shown that deeper size roughness provide a greater destabilising effect on the convecting TS wave which is further exacerbated with a shorter width dimple. The linear PSEh have been shown to converge in the presence of a LSB, providing as good an overall growth prediction as the LHNSh. The LHNSh model, due to retention of all elliptic terms, is considered a more correct technique due to the existence of reversed flow in the LSB; one would imagine the reverse flow would invalidate usage of the PSEh model for such flow types. However, we see nearly identical results between the two fundamentally different flow physics models, with differences only becoming discernible for large LSBs. Differences between the h-

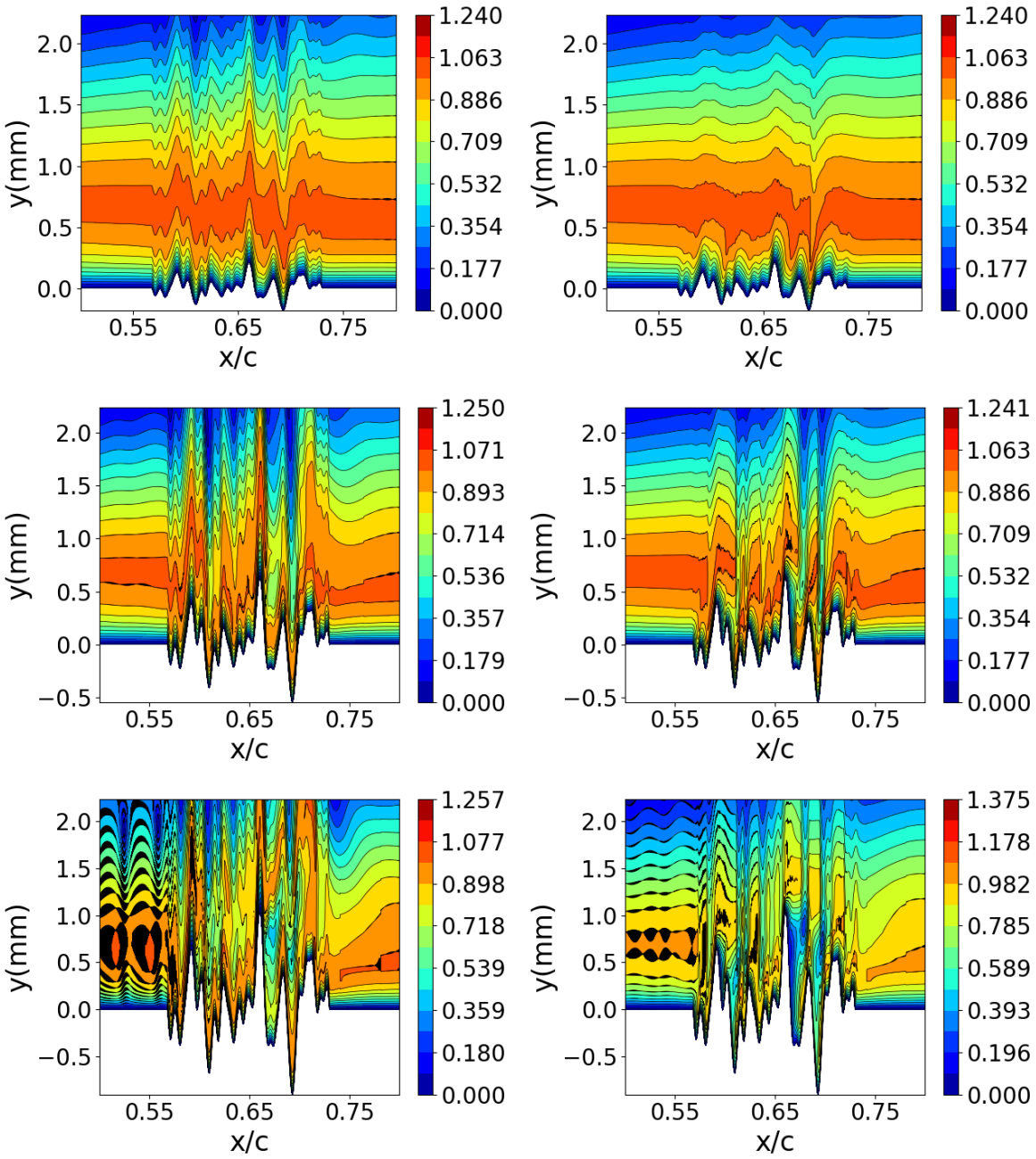

Figure 4.14: $\hat{u}$ contour plots of roughness case. Left: Computed with LHNS. Right: Computed with LHNSh. Top to bottom $R_q=$: 0.073mm, 0.22mm and 0.37mm depths.

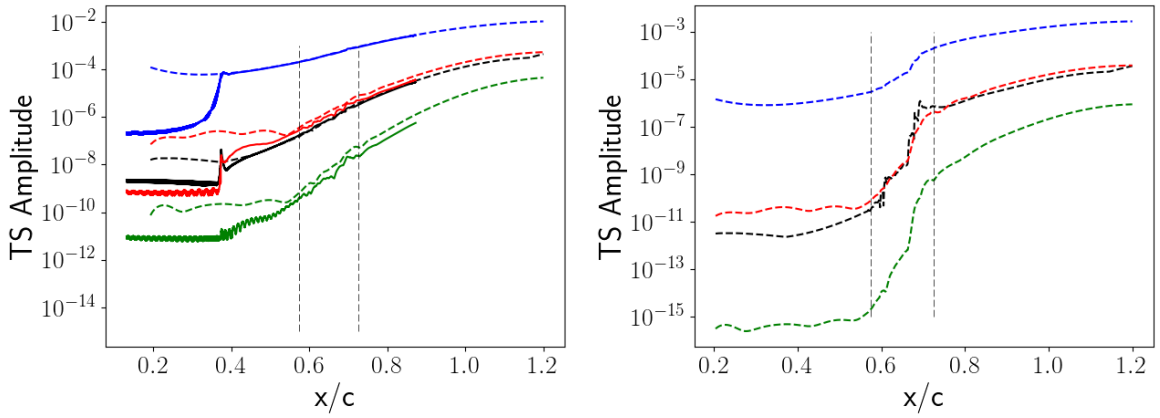

Figure 4.15: Non-linear PSEh and HNSh comparison. Left is for R_q = 0.073mm, right is for the 0.22mm case. Black for the mean mode, blue for the first harmonic, red second and green third harmonic. Dashed lines denote PSEh code, solid lines denote HNSh code.

transformed codes can be observed within the dimple itself, but these differences only impact the overall growth prediction for deeper cases. The PSEh only begins to break down in the most extreme of cases, the deepest 81mm width case. The non-linear computations also seem to cope well in the presence of a reverse flow region. It is only for the largest 162mm width case that we begin to observe some overall difference in the higher harmonic growth profiles. These are brought to light earlier for the 81mm case, exhibiting differences for the middle depth case. The mean flow distortion, (0,0) mode, does showcase some differences but we might expect this since the PSE / PSEh assume that the stream-wise pressure gradient is negligible. An assumption which is not adopted by the non-linear HNS / HNSh.

The roughness case has highlighted a few more limitations of the PSE / PSEh code, but we must bear in mind that this is a much more challenging problem with complex surface geometry featuring multiple LSBs. It must be stated that such a problem would even today pose a significant challenge using full state of the art DNS simulations, requiring significant HPC resources to resolve scales and complexity of the distributed and randomised roughness field. This could possibly be classed as an international first attempt, at modelling such complexity with PSE and LHNS. As shown above the PSE model is clearly unsuited, due to the very short-scales that require capturing. The results of all codes for the smallest random roughness case are very similar, it is only upon increasing to the 0.22mm case that differences begin to become apparent and the h' components begin to hold more weight. We could only achieve convergence of the linear PSEh result for the largest depth dimple by removing stations in the space marching. This has consequently impacted the PSEh result quite significantly and is likely to be due to an asymmetry in the h' and h'' derivatives over the peaks and troughs of the roughness profile. The reasoning behind having to ignore such stations

is likely to be due to the $h''\hat{u}_{YY}$ viscous term arising in the x-momentum equation, amongst other contributing terms.

Since the step like features we would like to investigate for the swept wing geometry only feature a singular reverse flow region, we hope that we do not run into these problems when undertaking the instability analysis. However, if we do, these two cases can help to gain a faster understanding and insight of why we might be seeing such results.

CHAPTER 5

Three Dimensional Infinitely Swept Wing Problems

Having shown the stability codes behave reliably for two dimensional problems, we next investigate a three dimensional problem, the swept wing. As can be expected, accompanying the more interesting problem of a three dimensional flow is the added complexity of modelling such a problem with the feature of localised steps or surface excrescences.

5.1 The Swept Wing

Motivation for this work arose from experiments undertaken by Saeed et al.[82] on the AERAST[61] swept wing geometry where movement of the laminar-turbulent transition front, with varying localised step heights, was observed with naphthalene. The AERAST geometry has a rather sharp leading edge and is designed to give favourable pressure gradients with negative incidence[91], see figure 5.3. Experiments were conducted within a $20ms^{-1}$ wind tunnel at a Reynolds number of one million. The geometry is positioned with a 40° sweep and a negative wing root incidence of 2.15° with a tip down linear twist of 1.5°[82]. Single, infinitely long, two dimensional steps were created with Kapton tape at varying heights to mimic steps, see figure 5.1. A key finding was that beyond a critical height, waviness and jaggedness in the transition front was observed, and travelling crossflow instability signals were measured in the hot-wire data. Further increments in step heights moved the transition front forward

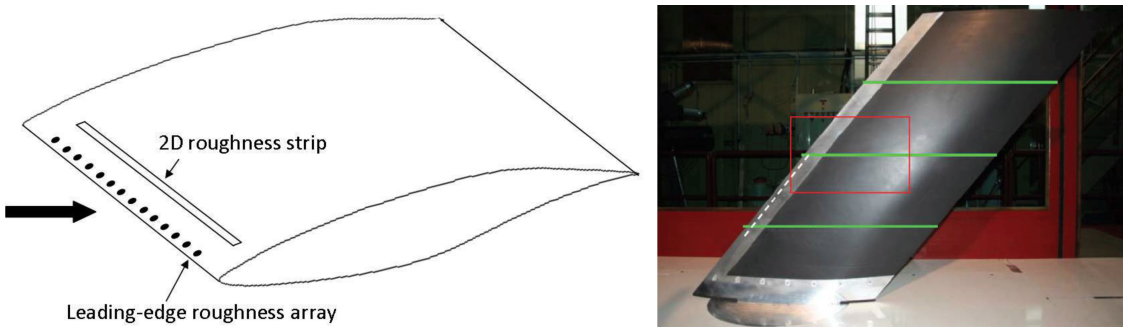

Figure 5.1: Schematic (left image) and experimental set-up (right image) of AERAST swept wing with bump profile from Saeed et al. [82]

towards the step. In recent more detailed experimental work Eppink et al. [31] found that the CFI destabilization that arises from backward facing steps (BFS's) is not straightforward. The movement of the transition front is insensitive to BFS's below a critical step height, once a threshold is crossed a rapid movement of the transition front to the step location is observed. These findings (together with findings of Saeed et al. [82]) suggest an altogether different mechanism in flow destabilisation arises in BFS based swept wing boundary layer flows.

Saeed et al. [82] looked at four different heights of bump profiles $330\mu m$, $495\mu m$, $660\mu m$ and $715\mu m$ located at three different locations over the wing (3%, 10% and 20% chord). The interest in the experiment was to observe how pre-existing stationary and travelling crossflow disturbances are affected by the localised step feature. In the experiment stationary crossflow disturbances were generated by the placement of periodically aligned leading edge distributed roughness elements, DREs, which were cylindrical in form[61]. Travelling crossflow signals were also observed in the experiment and were thought to have been generated by the wind-tunnel turbulence levels. In the work that follows, an attempt is made to replicate the experimental conditions and test matrix undertaken in the experiment. The experiment only looked at the effects of placing an infinitely long localised two dimensional roughness bump, figure 5.1, on crossflow disturbances. We replicate this but also then investigate decomposing the bump into a forward facing step and a backward facing step in the chapters that follow. This enables us to undertake a more comprehensive investigation of varying backward facing step, forward facing step and bump heights and locations on disturbance modification, as the pre-existing disturbances convect over the roughness feature. Before we can tackle these interesting configurations, we first need to compute the clean, step-free, case which serves as a benchmark and relative measure on the effects of excrescence placement.

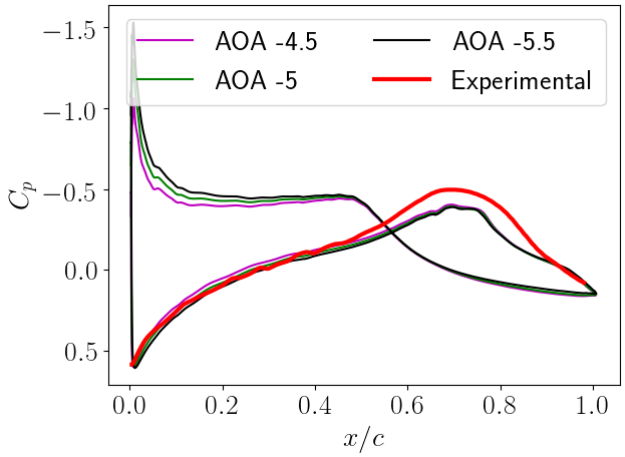

Figure 5.2: Full geometry coefficient of pressure (C_p) distribution for varying angles of attack compared with experimental C_p from Saeed et al. [82]

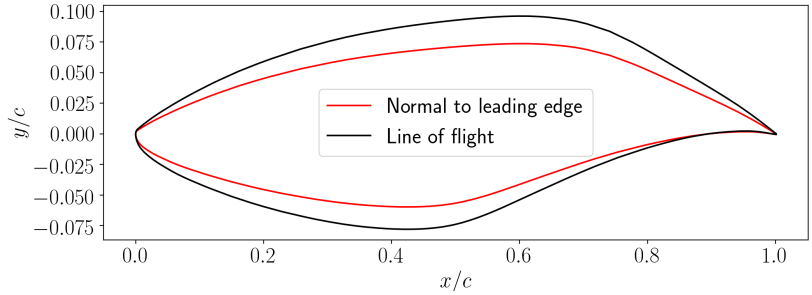

Figure 5.3: Aerast Geometry in line of light co-ordinate system for full RANS computation and normal to leading edge coordinate system for embedded DNS computation.

5.1.1 Validation of Clean Case

The full AERAST, clean, geometry is constructed with an Airbus meshing software, SOLAR, and then simulated with the Airbus RANS solver, TAU[21]. Flow conditions are designed to match the experimental regime as closely as possible. Inflow conditions are provided for a Mach 0.3 and Reynolds number 1 million case with a symmetry plane applied in the span-wise direction. A variety of incidences are computed to compare surface pressure distributions with the experimental data obtained by Saeed et al. [82]. An incidence of -4.5° was found to agree best with the experimental data in order to have closest agreement with the leading edge pressure profile, see figure 5.2. Various regression tests are completed to ensure time convergence along with mesh refinement studies to ensure grid convergence.

The embedded domain is then constructed using AutoCAD Inventor and Nekmesh, within the Nektar++ framework. The coordinate frame must be rotated from line of flight to normal to leading edge between the RANS computation and the DNS, see figure 5.3.

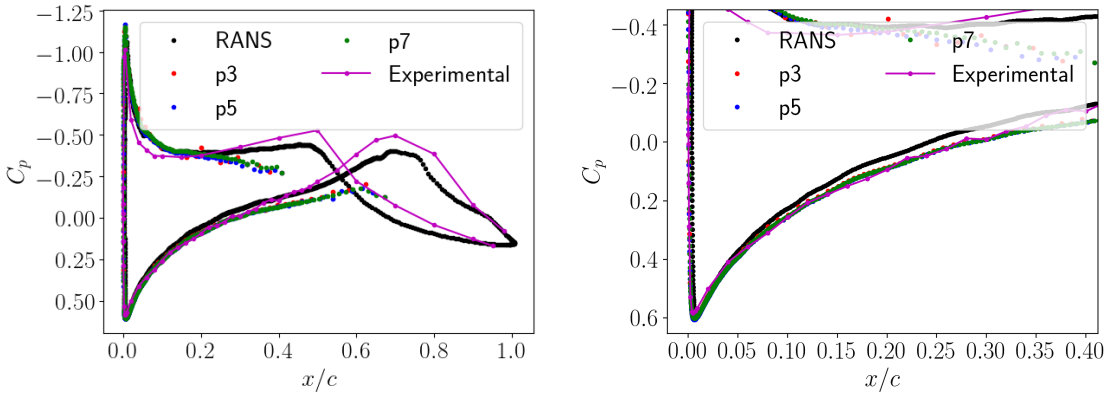

Figure 5.4: Cp distribution comparison between the full geometry RANS solution, Nektar++ at polynomial order 3 to 7 and experimentally measured data of Saeed et al.[82]. Right: Full geometry. Left: Zoom of attachment and upstream chord region.

The pressure side of the geometry is truncated to 70% chord and the suction side to 50% chord to avoid large separation at the outflow boundaries. Far field inflow boundaries are located 35% of a chord length above and below, and 40% of a chord length upstream, of the leading edge. Inflow boundary velocity components are interpolated from the full solution and applied in Dirichlet form, whilst the pressure adopts a Neumann condition. The lower vertical outflow utilises a high order outflow condition and an averaged pressure difference is applied at the upper outflow. No-slip conditions are applied at the wall. The embedded coefficient of pressure (C_p) solution is compared with the full geometry C_p to ensure the correct incidence is being enforced, see figure 5.4.

A polynomial expansion of order seven is required to obtain converged solutions, as determined from comparing C_p distributions, see figure 5.4, and boundary layer profiles, see appendix B. Polynomial convergence and mesh convergence studies can be found in Appendix B.

The Nektar++ extracted boundary layer profiles are compared with solutions from the Prandtl boundary layer equations to confirm the validity of the Nektar++ processed profiles. After ensuring good agreement between the two, see figures 5.5 and 5.6, this solution can then be used as an initial condition for the excrescence cases.

For the stability analysis, a range of CFI wave numbers and frequencies must be computed in order to find the most destabilizing CFI. When running the PSE solver on the clean geometry and sweeping through the wave numbers, the most destabilizing stationary CFI is found to be a wave number $\beta = 500m^{-1}$ for the stationary case and wave number-frequency combination of $\beta = 440m^{-1}, \omega = 420Hz$ for the travelling case. The amplitude growth predicted by the PSE and LHNS codes have been compared with the Nektar++ LNS computation. Both PSE and LHNS codes have

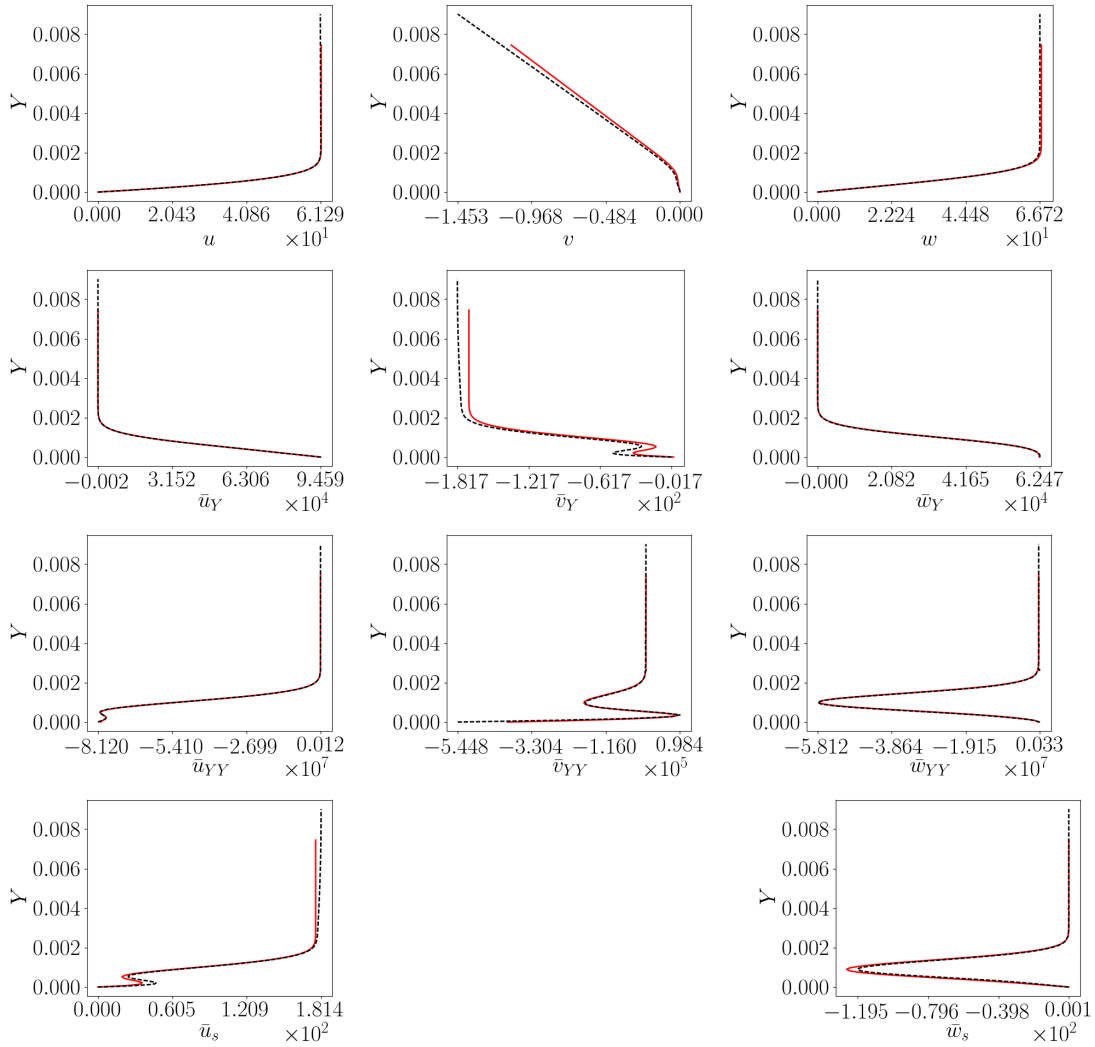

Figure 5.5: Clean: Comparison with Nektar++ extracted base flow profiles and the Prandtl boundary layer solver (CoBLc) generated profiles at 10% chord. All values are real physical quantities. Nektar++ solutions are represented with black, dashed, lines and CoBLc with red, solid, lines. Top row shows u, v and w, second and third rows show first and second derivatives, respectively, in the normal direction with respect to u, v and w and the last row is the first derivative in the stream-wise direction with respect to u, v and w. There is no $\bar{v}_s$ since this is not computed by CoBLc.

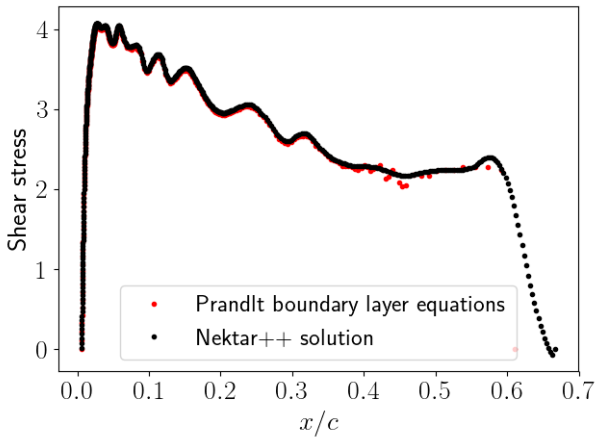

Figure 5.6: Shear stress comparison of Nektar++ solution with Prandlt boundary layer equations solution. (Computed with equation 6.3.)

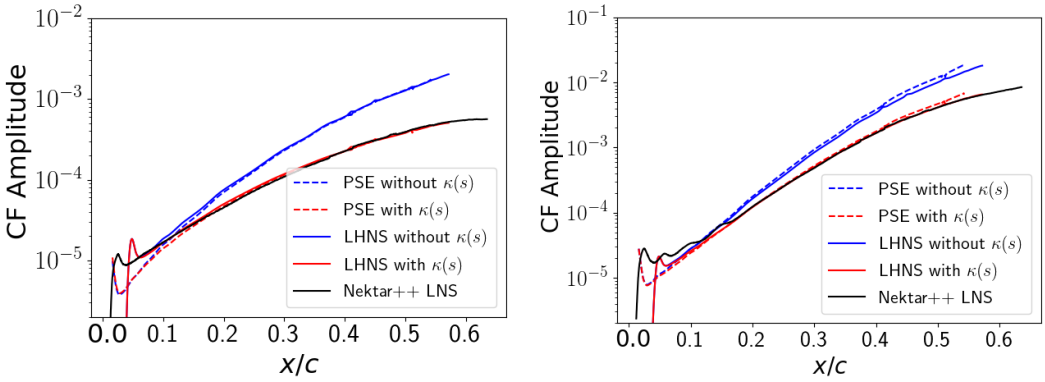

Figure 5.7: Clean AERAST geometry CFI amplitude growth comparison of LHNS and Nektar++ LNS, for including and excluding curvature, $\kappa(s)$. Left: Stationary CFI, $\beta = 500m^{-1}$. Right: Travelling CFI, $\beta = 440m^{-1}, \omega = 420Hz$

been computed including and excluding curvature terms, $\kappa(s)$. CFI amplitude plots are given by normalising the maximum of the steam-wise disturbance velocity with the boundary layer edge velocity at each stream-wise location. As expected, we see a stabilising effect from the inclusion of the curvature terms which is in good agreement with the Nektar++ LNS solution, see figure 5.7. There is a slight difference in the point of generating the instability, for Nektar++ this is slightly further upstream, due to the precision required in generating a perturbation which spans one element thickness. All analyses to follow will hence be computed with the inclusion of curvature. The PSE seems to be predicting the disturbance amplitudes very well in the absence of the roughness, and at the benefit of reduced computational cost. A clean PSE computation typically takes less than a second, the LHNS is around four minutes and the Nektar++ LNS solution requires around an hour using 24 nodes, 24 cores and a memory allocation of 60GB.

Since we have obtained good agreement between the stability codes and the Nektar++

LNS solution, we next introduce a roughness to the surface.

CHAPTER 6

Three Dimensional Ramp problem

A roughness case is constructed according to the experimental regime of Saeed et al. [82], however instead of having a vertical step bump feature, we first create ramped edges in order to create a slightly simpler problem for the stability tools to solve, see figure 6.1. Accompanying this ramped bump is the decomposition of this into a forward facing ramp and a backward facing ramp.

Figure 6.1: Schematic showing ramped edge bump compared to the vertical edge bump case, where l denotes the length of the bump and h the height.

6.1 Nektar++ Base Flow Computations for the Ramp

The three ramp cases are constructed at 10% chord of the AERAST geometry. The height and location are chosen corresponding to the maximum height case in the experimental work of Saeed et al. [82]: $715\mu m$. Roughness shape investigations consist of a forward facing ramp (FFR), a backward facing ramp (BFR) and a composition of the two named a bump ramp (BR). Nektar++ computations are constructed for a

non-dimensional co-ordinate frame meaning the height in the work of Saeed et al.[82] corresponds to $893\mu m$ and width of 3.75mm ($l = 3.75mm$ in figure 6.1) for a chord of length one meter. The roughness is added to the clean geometry surface through use of AutoCAD Inventor such that each ramp is at a 45° incline with the clean surface and corners are filleted with 0.0001m radii. Meshes are then constructed with NekMesh and used with the incompressible Navier Stokes solver within the Nektar++ framework, see figure 6.2. Computations are initialised from the converged steady clean solution and boundary conditions extracted from the full geometry solution.

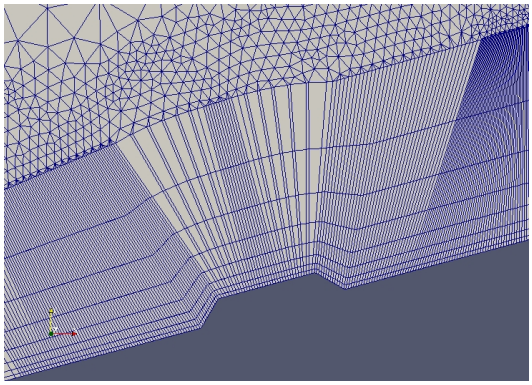

Figure 6.2: Localised view of the bump ramp mesh created with Nekmesh. Elements show h-type refinement only.

The flow conditions are the same as for the clean case: Reynolds number 1 million, Mach number 0.3 and the geometry is swept at 40°. The ramp height equates to 52.93% of the clean boundary layer thickness at 10% chord. The Nektar++ incompressible Navier-Stokes solver is used to generate steady base flows, see figure 6.3. Note that here velocities in Nektar++ are defined in the Cartesian co-ordinate frame, which is why we see a positive $\bar{v}$ field, this will become slightly negative when moving to the body fitted co-ordinate system. We can see that the FFR has virtually no LSB present whereas the BFR and BR do. Interestingly, the reverse flow region present for the bump case remains much further downstream than the BFR case; lengths of the LSBs are given in table 6.1. Here b_h is the length of the LSB, b_l, with respect to the ramp height, h, such that $b_h = b_l/h$. Analogously, b_w is the length of the bubble with respect to the width of the localised bump case, h_w such that $b_w = b_l/h_w$. The peak reverse flow within the bubble is, at maximum, 4.5 ms^{-1} which is under 5% of the free stream value. This means we do not expect to see absolute instability arising in the stability analysis[34]. However, these criteria are based on generally two dimensional highly idealised LSB analyses, whether such results carry over to the infinity swept 2.5D LSBs with a span-wise velocity component too, may be questionable. Some initial analysis of such flows were undertaken by Appel et al.[4]. The paper for the first time investigated the presence of bi-global instabilities where the LSB has an additional span-wise velocity component; this does not appear to have been investigated in the

literature prior to the work reported by Appel et al.[4].

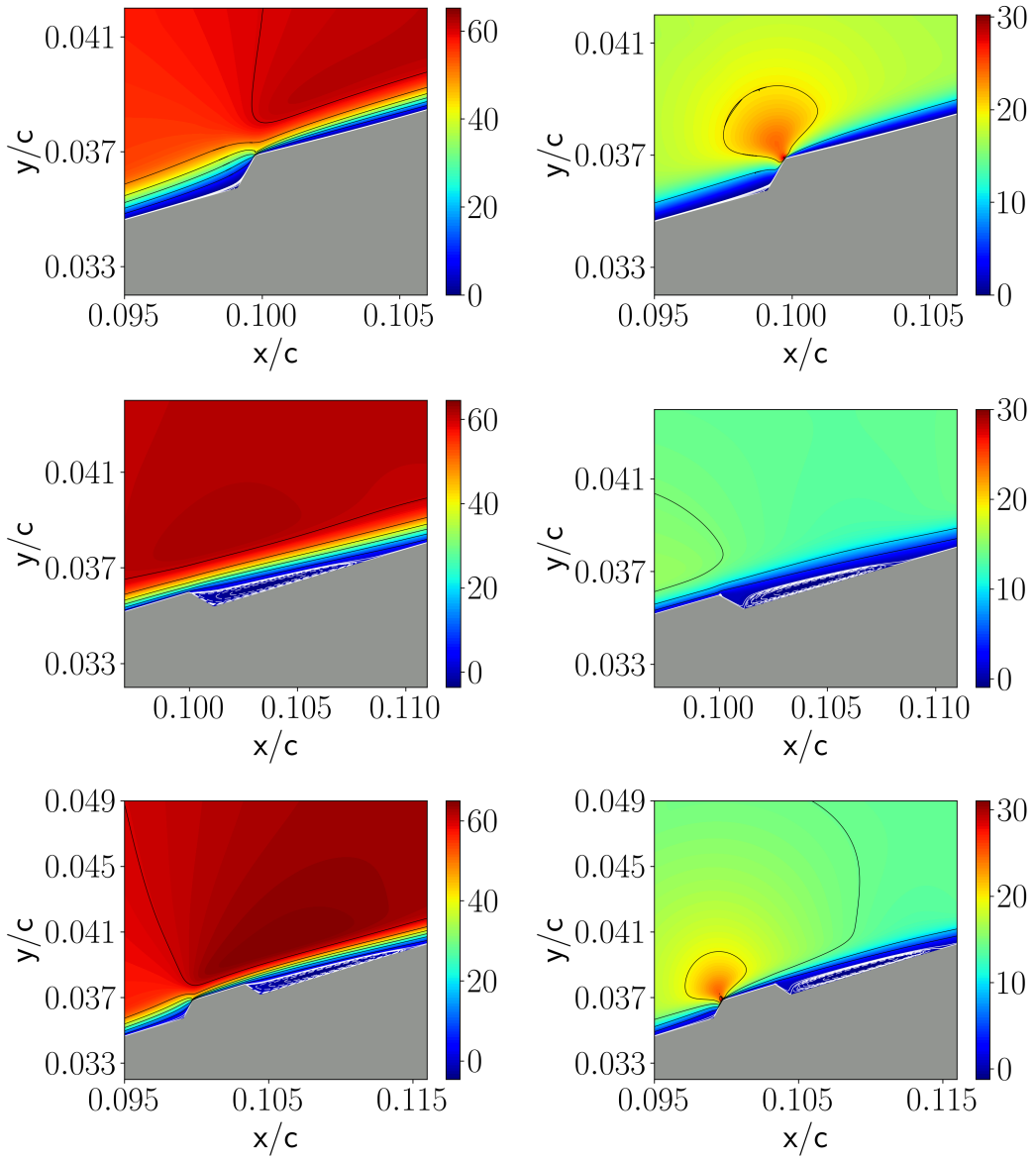

Figure 6.3: Nektar++ solutions at 10% chord, 893 microns for the FFR (top), BFR (middle) and bump ramp (bottom left). Contours show stream-wise velocity (left) and normal velocity (right), black lines show the outer boundary layer and free-stream flow. White lines show flow within the inner boundary layer and dashed white lines denote LSBs.

Boundary layer profiles and their derivatives are calculated at 6% chord length downstream of the ramp location, as depicted in figure 6.4 and 6.5. The profiles are made dimensionless with the free-stream edge velocity and boundary layer thickness. Comparing the BFR and bump ramp cases we can see that the stream-wise reverse flow is greater for the bump ramp, which is reasonable given that this location is much closer to the BFR component of the bump. This is also in line with the vertical component, which exhibits a clear inflection point within the boundary layer for the bump profile.

shape	height	forward b_w	forward b_h	backward b_w	backward b_h
Bump Ramp 10%	893	0.07	0.30	2.96	12.41
FFR 10%	893		0.31		
BFR 10%	893				8.84

Table 6.1: Bubble lengths for the ramped cases with relation to the roughness height, b_h. For the bump ramp case there are two separation regions, before (forward) and after (backward) the bump, which have been related to bump width, b_w, also.

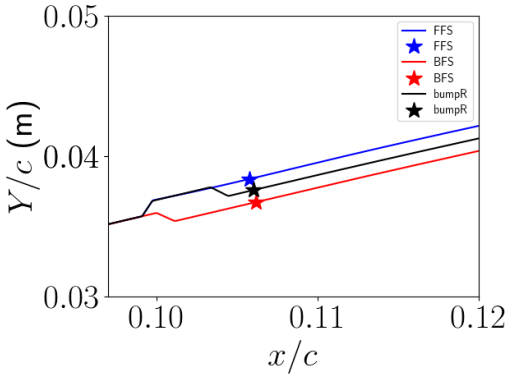

Figure 6.4: Location depiction of where boundary layer profiles are generated (6% of a chord length downstream of the ramp location). Blue, red, and black depict the FFS, BFS and bump ramp respectively.

The pressure coefficient (C_p) and skin friction coefficient (C_f) over the ramp region are shown in figure 6.6. Pressure coefficient is given by,

$$C_p = \frac{p - p_\infty}{0.5\rho_\infty V_\infty^2}, \tag{6.1}$$

and the skin friction coefficient by,

$$C_f = \frac{\tau_w}{0.5\rho_\infty V_\infty^2}, \tag{6.2}$$

where τ_w is the shear stress at the wall,

$$\tau_w = \mu \frac{\partial u(s,Y)}{\partial Y}\Big|_{Y=0}. \tag{6.3}$$

The C_p shows an increase leading up to the FFR, as the flow begins to decelerate, and a sharp decrease as the flow accelerates over the top of the ramp. We see the analogous result for the BFR where the velocity increases upon approaching the ramp, showing a decrease in C_p, and then we immediately enter the reverse flow region, where we can see an increase in the C_p denoting an adverse pressure gradient. The recovery of the pressure gradient takes much longer for the bump, which is why the bump ramp

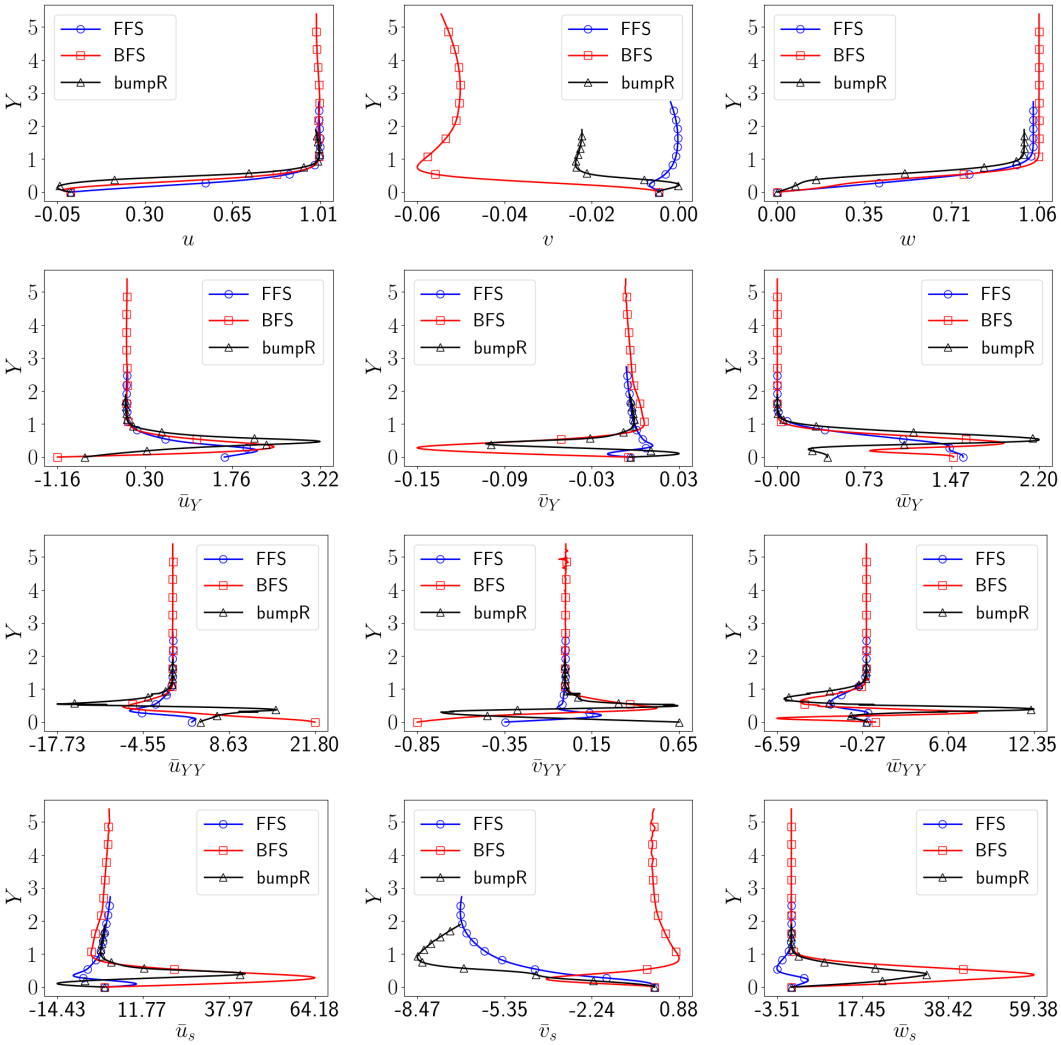

Figure 6.5: Ramp cases at 10% chord: Nektar++ generated base flow profiles generated at 10.6% chord. Non-dimensional values plotted: x-axis can be dimensionalised with the boundary layer edge velocity (and boundary layer thickness for higher derivatives) and the y-axis with the boundary layer thickness at that stream-wise location. Top row shows $\bar{u}$, $\bar{v}$ and $\bar{w}$, second and third rows show first derivative and second derivative respectively in the normal direction and the bottom row is the first derivative of $\bar{u}$, $\bar{v}$ and $\bar{w}$ with respect to the stream-wise direction.

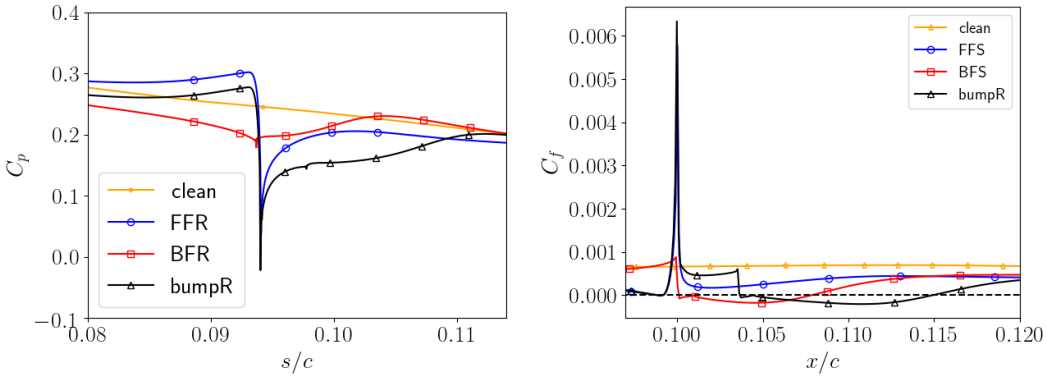

Figure 6.6: Ramp case pressure coefficient (C_p) and skin friction coefficient (C_f) comparison of all step heights. Left for C_p, right for C_f. Blue, red, and black depict the FFS, BFS and bump ramp respectively, the clean case is given in yellow. The dashed black line marks where skin friction coefficient is zero.

exhibits a longer LSB. From the C_f we can clearly identify reverse flow regions, where the C_f becomes negative, and see that the bump ramp has a much longer flow reversal than the BFR.

We know from the literature that ramped steps are less dangerous to the fluid flow than vertical step features. By rounding of the step feature the transition location can be delayed to further downstream and the step height which is deemed critical can be increased. In recent experiments, Eppink and Casper[28] looked at varying FFRs of varying degrees of steepness and their effect on stationary CFI. In their experiments the ramp height was 81% of the boundary layer thickness and had two differing incline degrees, 30° and 45° . Comparisons are drawn with their previous work for square forward facing steps[27]. They compare the shape factor, $H = \frac{\delta_1}{\delta_2}$, where δ_1 is the boundary layer displacement thickness and δ_2 is the boundary layer momentum thickness, to show that the square step exhibits the strongest adverse pressure gradient. This adverse pressure gradient decreases when moving to the 45° ramp and again to the 30° ramp. Sumariva et al.[90] have also looked at the effect of rounding indentations and humps, and obtain similar skin friction profiles to the ones shown in the present work.

6.2 Stability Analysis

As with any stability problem, we begin by exploring the parameter space. Neutral curves are constructed for all ramp cases using linear stability theory (LST) to identify crossflow wave-numbers (β) which are destabilised by the presence of the step, see figure 6.7. The ramp cases, given in black, are compared with the clean case, given in yellow, and the dashed vertical line denotes the ramp location. We can see

that the FFR case has the minimum impact on the parameter space, extending the range of destabilised wave numbers to β =1500m^{-1} just after the ramp location at $x/c = 0.1025m$, but soon returns to the same upper branch as the clean case at 0.14m. Interestingly, the unstable parameter space appears to be severed over the ramp region and becomes a stable space. We believe this region of stable space may not be completely stable due to being able to find a distinct upper branch point within this region, see just before 10% chord around $\beta = 1250m^{-1}$. The neutral curve in this region could have very small regions of instability which change rapidly in the streamwise direction making it extremely difficult to compute a solution along the branch. Equally, identifying an unstable mode in this region is extremely difficult.

From the BFR case we can see that the presence of the ramp destabilises the parameter space much more aggressively, sending the range of destabilised wave-numbers to as high as 2500 m^{-1} over the separation region. The LSB ends at around 10.7% chord which is where we see the upper and lower branches begin to converge to one another. Continuing traversing downstream we have now entered a short region of stability before another unstable parameter space begins again. The lower branch tends to recover to the clean branch curve almost immediately, whereas the upper branch does not recover back to the clean branch solution until just after 16% chord.

Moving now to the bump ramp case we can see a composition of the two FFR and BFR neutral curves. We observe the first unstable region, just prior to the FFR ramp, followed by a rapid expansion of the destabilised parameter space after the FFR to around $\beta = 1500m^{-1}$ just before the BFR. When reaching the BFR the parameter space is destabilised completely for the lower branch and reaching over β =2500 m^{-1} for the upper branch. Remembering that the LSB present in the bump ramp case is 33% larger than that of the BFR, the lower neutral branch does not begin to converge to the upper branch until 11.9% chord, and even so, never completely converges to the upper branch meaning that there is no severed parameter space at the end of the reverse flow region. The bump ramp lower branch then quickly converges to the clean lower branch and the upper branch does not meet the clean until 20% chord.

Now that we have explored the range of destabilised wave numbers the next step is to determine which is the most destabilising for each case. The PSE are used to scan through a range of wave numbers with the frequency fixed to zero for a stationary crossflow. N-factor curves are plotted to establish the CFI which is amplified the most, an example can be seen in figure 6.8 where we can see that the most destabilising mode here has wave number $\beta = 366m^{-1}$. Upon further refinement we find that the most dangerous wave number is β =350m^{-1}. These most destabilised wave numbers are identified for each of the ramp cases.

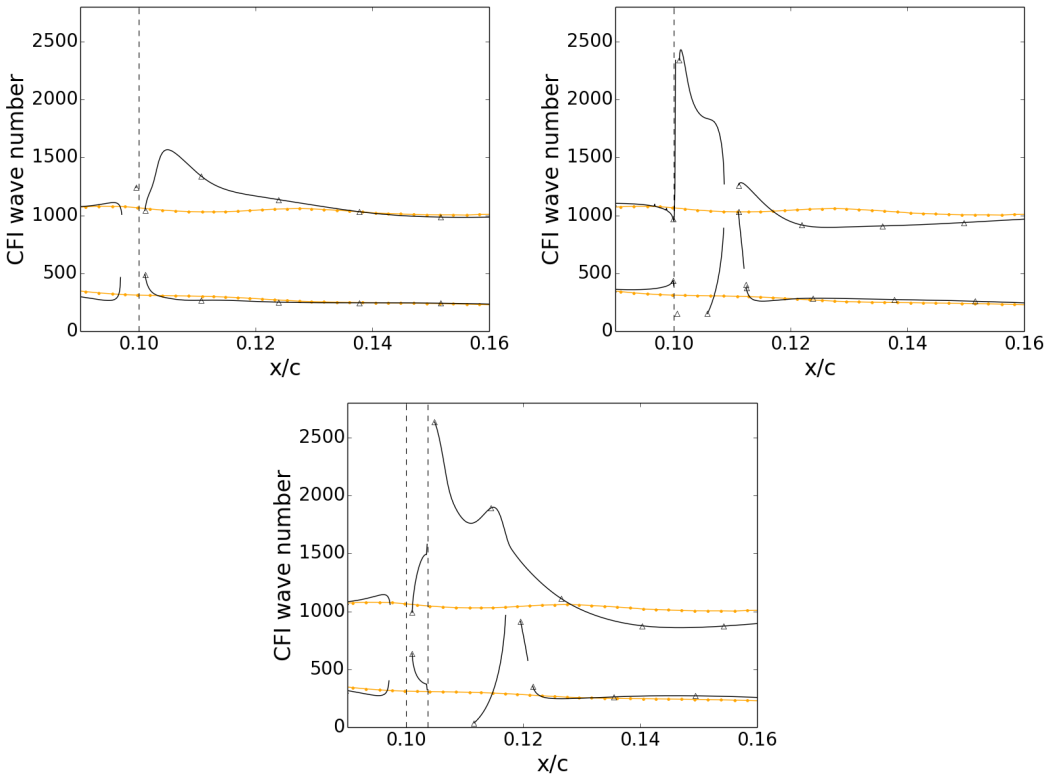

Figure 6.7: Stationary neutral stability curves, computed with LST, for the FFR (upper left), BFR (upper right) and bumpR (lower) each compared with the clean case. Black triangles depict neutral curves for the excrescence case and the clean is given in yellow points.

The PSE and PSEh codes are then compared with the clean case for the same wave number. Amplitude growths are compared and overlaid by scaling the initial amplitude to match downstream of the ramp location, see figure 6.9. All ramp cases predict a stabilisation compared to the clean case. This stabilisation is even more pronounced when solving with the PSEh code. The BFR shows the largest stabilisation, next being the bump ramp and the least stabilisation is shown from the FFR. These results are contrary to that of the literature which generally tend to show a destabilisation of the instability for similar CFI regimes and for two dimensional base flows.

The difference could be due to a few factors, the first being that many stream-wise station locations need to be neglected during the computation in order to attain a converging solution. We can see from figure 6.8 that the $\beta = 300m^{-1}$ case fails to continue the space marching past the ramp location. In order to enable the majority of these wave numbers to pass this point and converge to a solution, a number of station profiles are ignored, or 'stepped over'. This could be due to being on the cusp of the PSE numerical step size restriction although it is more likely due to the problem of having extremely rapid velocity gradient changes when traversing over the ramp. These are particularly large in the stream-wise direction which augments the need to ignore certain stations over the ramp region to enable the PSE to complete the space marching. This has also been observed by Sumariva and Hein [89]. The PSE concept is based on only weak variations in the basic flow stream-wise derivatives which is not true in the neighbourhood of the stepped features. However, even if these problems were not present and the PSE step size condition was satisfied, a major drawback of the PSE is that it will fail to compute a valid solution if the instability wavelength is greater than, or of the same length as, the roughness width [104]. In this case the ramp width is 0.893mm long for the FFR and BFS and 5.536mm for the bump ramp. The wavelength of the CFI is 11mm, meaning the PSE will fail to compute a valid solution for these configurations. With this in mind, we turned to the LHNS equations. The LHNS will not suffer a step-size restriction since all stream-wise derivative terms are retained; the equations are fully elliptic in character and as such with finer spatial discretisation we expect more accurate solutions. In principal the very rapid and short scale variations in the basic field should not pose any conceptual modelling or numerical issues, however the impact of these rapid stream-wise gradient fluctuations remains to be assessed.

All ramp cases are solved with the LHNS and LHNSh equations and compared with the Nektar++ time-stepping LHNS solution. The LHNS and LHNSh generates the CFI with a wall forcing placed at the clean neutral point (3% chord) and the ramp is located at 10% chord. The amplitude is plotted by taking the maximum $|\tilde{u}|$ at each stream wise location and normalising with the boundary layer edge velocity.

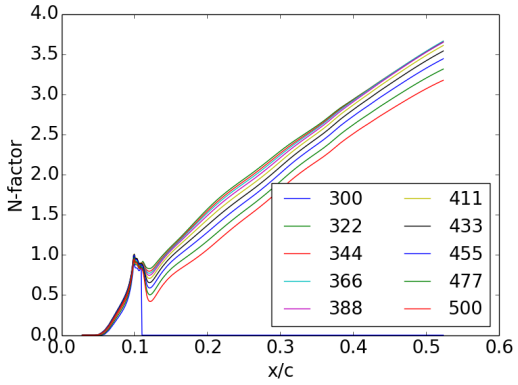

Figure 6.8: Sweeping though stationary CF wave numbers between $\beta = 300m^{-1}$ to $500m^{-1}$ for the bump ramp case.

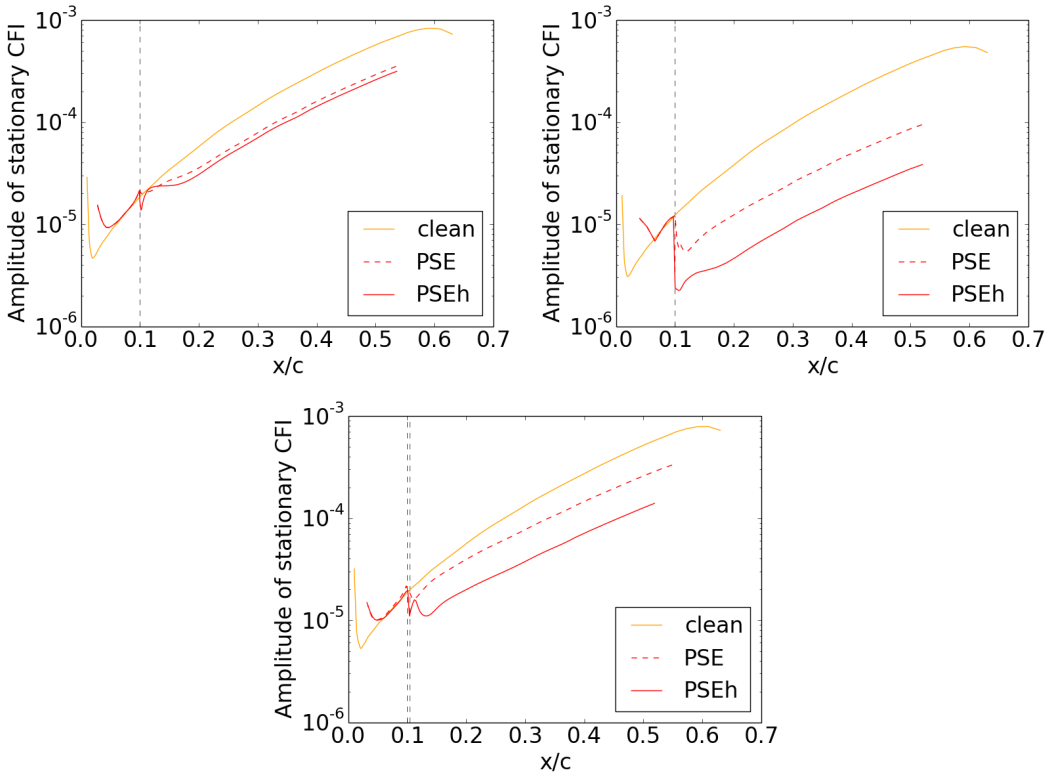

Figure 6.9: Stationary CFI PSEh and PSE comparison. Top left is FFR ($\beta = 450m^{-1}$), top right is BFR ($\beta = 460m^{-1}$) and bottom is the bump ramp roughness ($\beta = 380m^{-1}$) each located at 10% chord.

The results from these computations are very reassuring. We can see that when solving the LHNSh equations the amplitude growth follows that of the Nektar++ LNS solution very closely, see figure 6.10. Whereas the LHNS result either predicts very little change, in the case of the FFR, or predicts a reasonably large stabilisation, in the case of the bump ramp and BFR. If we look closer at the ramp location, the LHNSh solution also tends to follow the growth of the Nektar++ LNS solution very well, showing that the large changes in stream-wise gradients do not prove to be a

limitation for the LHNSh equations. Sumariva and Hein[89] generated similar growth profiles for the hump case they studied, although that was only for a two dimensional flow field with TS wave convecting over a flat plate. From the differences between the LHNS and LHNSh results and the similar agreement between the LHNSh and the Nektar++ time-stepping based LNS result, we can see that the h correction is crucial for capturing correct growth of the instability. We have scaled the Nektar++ derived result such that it agrees with the LHNS derived behaviour ahead of the ramp, and due to this a small difference appears between the two downstream of the ramp. We could equally have scaled the Nektar++ result such that it agreed with the LHNS amplitude variation downstream of the ramp, but then the small mis-match would have appeared ahead of the ramp. In a perfect setting we would expect the results between the two quite different techniques to be identical ahead, over and beyond the ramp. The small discrepancy is in all likelihood due to the difficulties of extracting the Nektar++ computed steady field derivatives for subsequent usage in the LHNS. The observed disturbance growth and evolution over the FFR, top right in figure 6.10, compares well with the experimental work of Eppink and Casper[28], figure 9a in their paper, although we tend to see a slightly earlier decrease and increase of the disturbance amplitude than observed by Eppink and Casper[28].

The presence of the FFR seems to be causing a larger amplification to the stationary CFI than the BFR, which is interesting since there is barely any reverse flow for the FFR case, whereas there is a large LSB present in the BFR. From the literature we know that LSBs can act as oscillators or amplifiers to TS waves, Sumariva and Hein[89] take their two dimensional flow regime with a smoothed hump on a flat plate and show that amplification of their TS wave is induced from the reattachment of the separated flow after the hump. Any inference from the Sumariva and Hein[89] simpler 2D flat plate findings are tentative at best since our base flows are three dimensional with a swept flow component, however in our simulations for CFI over the BFR we do not observe the reattachment induced growth meaning the mechanisms interacting with the CFI must be quite different to those interacting with the simpler two dimensional LSB TS wave findings, and needs further investigation. The stationary CFI amplitude growth curve behaviour is however consistent with the experimental work of Eppink et al.[31] who observed stationary CFI having little to no modification when convecting over a backward facing square step. Eppink et al.[31] argue that interaction of travelling modes with the stationary mode are responsible for the amplification of the convecting stationary CFI. Since we do not have a travelling component present in these computations, it can be reasonable to expect no growth from the BFR.

We can observe from the CFI amplification curves 6.10 that the FFR seems to provide a larger amplification compared to the bump ramp, which incorporates the same FFR

component. We must recall that these are computed with different wave numbers, FFR at $\beta = 450m^{-1}$ and bump ramp at $\beta = 380m^{-1}$ which were determined from the PSE/PSEh computations. Since we have deemed PSE growth prediction unreliable, the most unstable wave number we have identified may not truly be the most unstable wave-number. We consider this highly likely for the bump ramp case as it predicts less amplification than the clean case.

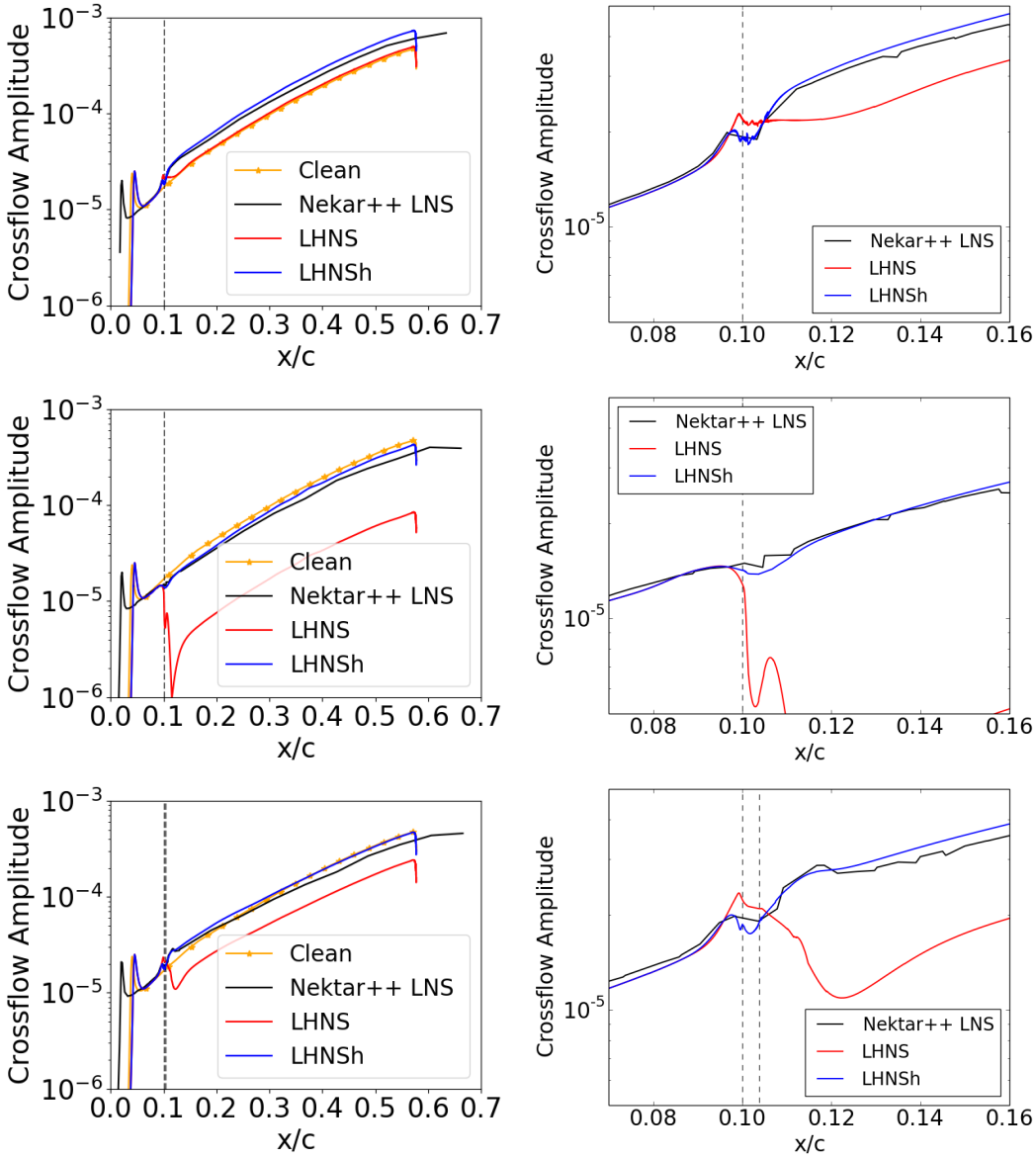

Figure 6.10: Stationary LHNSh and LHNS comparison with nektar++ time stepping LNS result, each located at 10% chord. All are compared with the most destabilised clean case, $\beta = 500m^{-1}$. Top is FFR ($\beta = 450m^{-1}$), middle is BFR ($\beta = 460m^{-1}$) and bottom is the bump ramp roughness ($\beta = 380m^{-1}$). Left shows the full embedded chord and right shows a zoom of the ramp location. Dashed vertical lined denote the ramp.

To try and establish what might be occurring in the vicinity of the ramp, contours of the $\hat{u}$ perturbation field normalised with the edge velocity at each station are created,

see figure 6.11. We can see that the FFR and bump ramp configurations cause the CFI to be modified and amplified further when convecting over the FFR upper corner. The $\hat{u}$ perturbation is lifted up from the upper corner of the ramp, following a rise in the unperturbed streamlines from the wall. This lift causes an amplification in the stationary crossflow which we observe in the amplitude plots 6.10. Comparing these contours to the experimental measurements of Eppink and Casper [28] we can see that they also observed this rise for the forward facing square step and also for the 45° ramp case, although not as pronounced. Comparison with Sumariva and Hein [89] 2D findings we note are tentative at best, however we will remark they observed this same modification of a TS instability, seeming to originate from the upper corner of their sharp hump case, although when looking at their smooth hump case this feature seems to disappear. They still however, observe a similar kick in their TS amplitude growth curves just after the forward facing component. We consider the upper corner for the ramp to be a key mechanism in the destabilisation of the stationary CFI.

Non-linear HNSh computations for all ramp cases are shown in figure 6.12. Since the computations require more extensive computational resource, the domain has been truncated in order to achieve good mesh refinement over the bump region. We do not see much change in growth for any of the modes for the FFR. However, for the BFR we do observe a change in the third harmonic, around 14% chord, and also in the bumpR third harmonic, further downstream at 17% chord, where the third harmonic begins to grow at a faster rate than the other modes. The change in growth however, does not seem substantial enough to surpass the other modes. The enforced fundamental mode amplitude in the simulations is small enough to elicit a weak linear response, with the higher forced modes essentially being tied to the fundamental driving mode evolution. If we were to undertake a more thorough investigation to see the effect of increasing the initial forcing magnitude of the fundamental driving disturbance, we may see some very different higher harmonic growth.

6.3 Concluding Remarks

We have successfully generated a baseflow for the largest bump height, $893\mu m$, in the work of Saeed et al. [82] but with ramped edges at a 45°incline with the Nektar++ incompressible solver. We have also simulated the decomposition of this into a forward facing ramp and a backward facing ramp. Each are located at 10% of the AERAST chord wing. We have found that the presence of the bump ramp causes a 25% more elongated LSB compared to the BFR.

Stationary CFI is imposed on the base flow and stability tools PSE, PSEh, LHNS, LHNSh and Nektar++ LNS are compared. We find that the stream-wise length scale

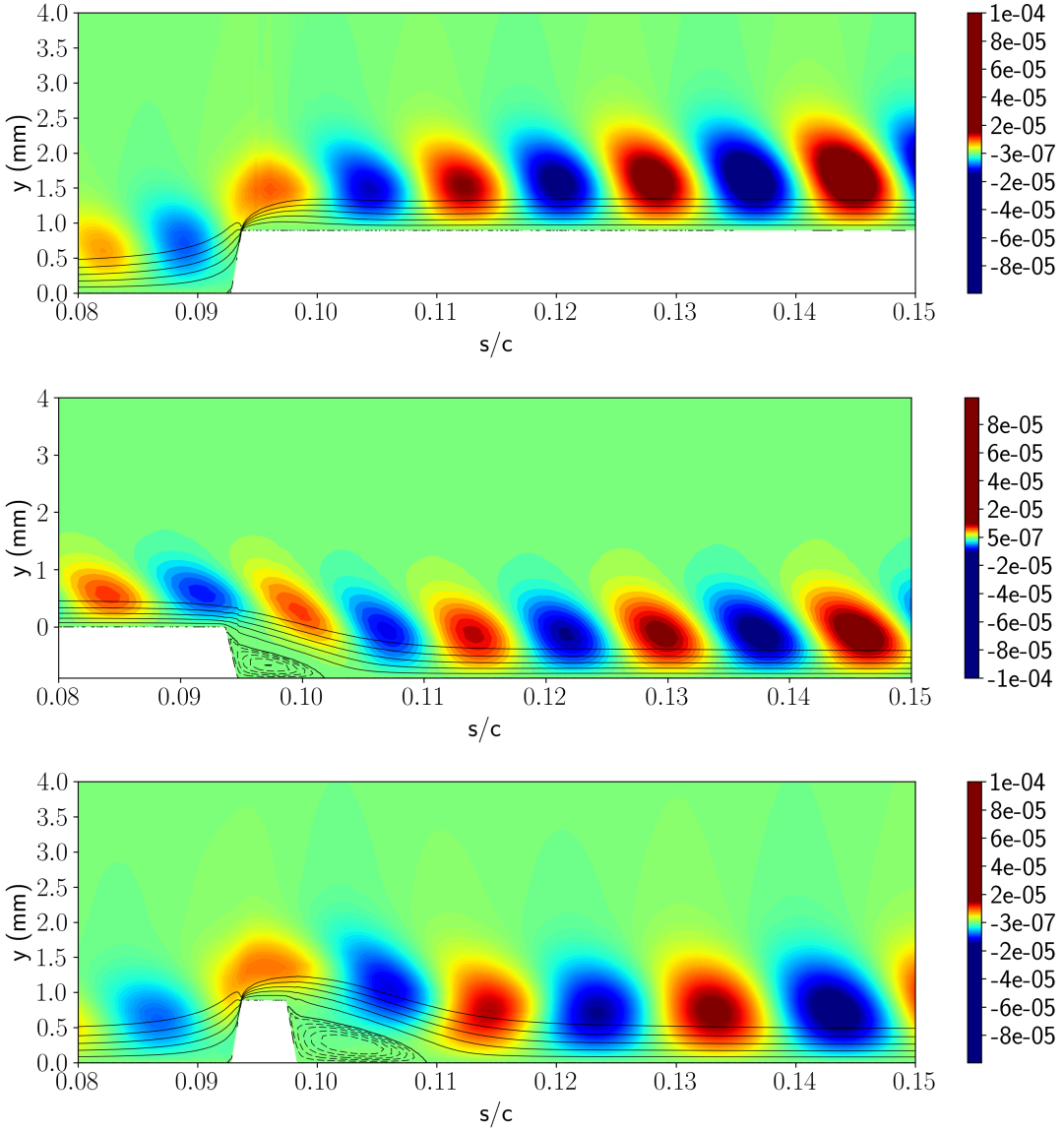

Figure 6.11: Stream-wise perturbation field, $\hat{u}$, for stationary CFI over FFR, BFR and bumpR at 10% chord. Upper left: FFR, ($\beta = 450m^{-1}$), upper right: BFR ($\beta = 460m^{-1}$) and lower: bump ramp ($\beta = 380m^{-1}$) Black lines denote constant valued $\bar{u}$ and dashed black lines denote flow within the LSB.

of the bump introduced in the experiments of Saeed et al.[82] is far too short relative to the most unstable stationary CFI wavelength, and also for many others wavelengths which are amplified[104]. However, we still see that the ramp, despite being quite short in the stream-wise extent, has a significant affect on the CF disturbance as it convects over the ramp. This comes about due the drastic modification of the steady local flow induced by the ramp. In order to undertake the PSE or PSEh space marching computations a number of stations need to be ignored which we ascertain is due to strong stream-wise velocity gradient changes meaning obtaining mesh independent results are unachievable. The LHNSh result, with the harmonic framework, compares remarkably well with the Nektar++ time stepping based LNS result which proves extremely

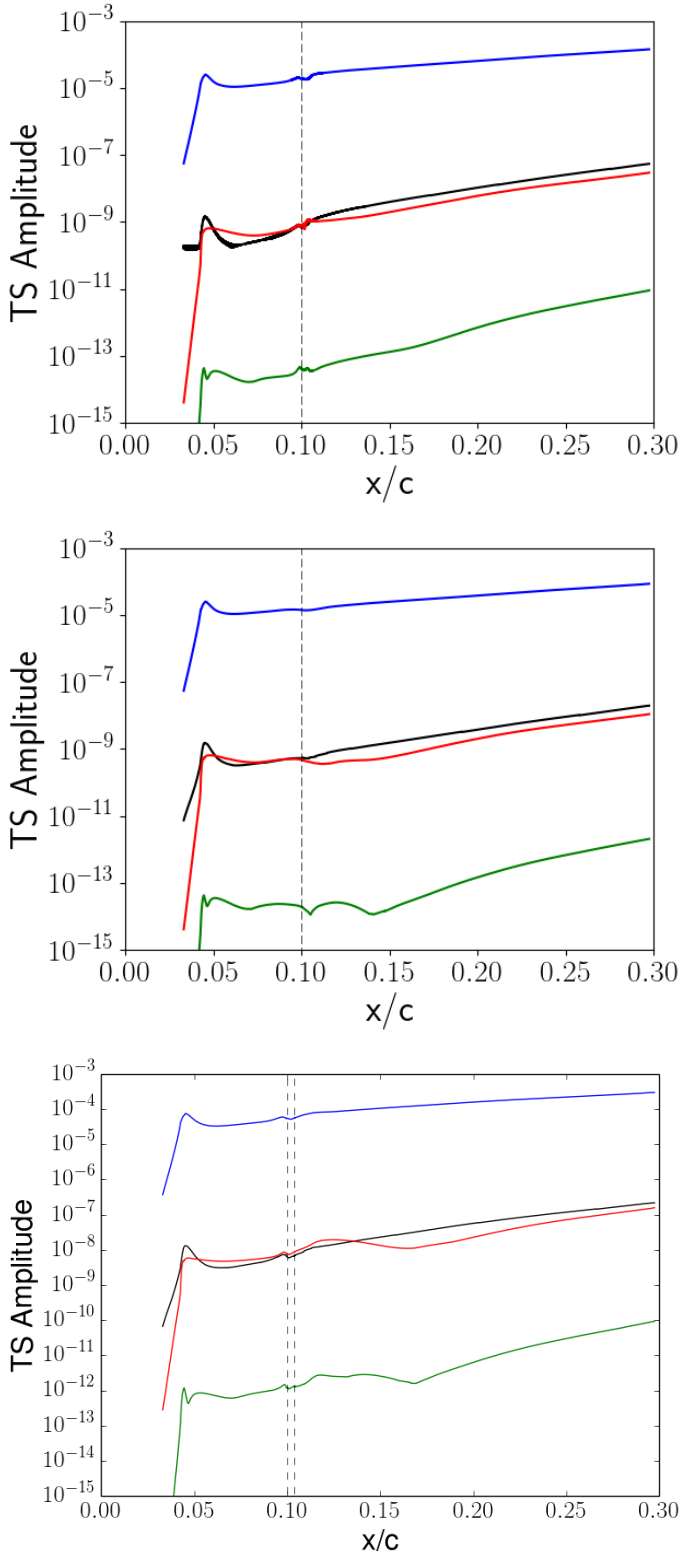

Figure 6.12: Stationary non-linear HNSh computations for all ramp cases located at 10% chord. Top is FFR ($\beta = 450m^{-1}$), middle is BFR ($\beta = 460m^{-1}$) and bottom is the bump ramp roughness ($\beta = 380m^{-1}$). Black denotes the (0,0) mode, blue the (0,1) mode, red for (0,2) and green for (0,3). Dashed vertical lined denote the ramp.

reassuring for tackling the true excrescence shape in the work of Saeed et al.[82]. The forward facing ramp component seems to provide a further amplification kick to the stationary CFI as it convects over the ramp, similar results have been observed by Sumariva and Hein[89] for flat plate TS propagation over a smooth hump and Eppink and Casper[28] for stationary CFI over a FFR. The BFR appears to modify the CFI growth only very slightly in the neighbourhood of the ramp before returning to the trend observed in the step free clean geometry analysis. This, somewhat counter intuitive, observation has also been observed in the work of Eppink et al.[31] who looked at stationary CFI introduced to a flat plate square backward facing step. All in all, the analysis for the ramp vindicates and provides confidence in the correct implementation of the modelling and numerical work undertaken in development of the LHNSh approach. We next investigate the more challenging case of introducing more extreme vertical step type configurations into the AERAST geometry in order to compare with the experimental work of Saeed et al.[82].

CHAPTER 7

Three Dimensional Vertical Step Problems

In the work of Saeed et al.[82] a vertical step is introduced to the geometry at 3%, 10% and 20% chord of the AERAST geometry. The steps were created by layering Kapton tape to create four varying step heights at each of these chord locations. Within this chapter we replicate this work numerically in order to gain greater understanding of the destabilisation mechanisms introduced by the roughness site. This work is extended to the decomposition of the bump into a forward facing step (FFS) and a backward facing step (BFS), incorporating and expanding upon the current work by Cooke et al.[15 16]. Due to the vast amount of cases considered in this chapter we shall first look at the generated baseflows as a whole and then break the stability analysis into the three different cases. Firstly only considering the FFS, followed by the BFS and concluding with the bump. There will be a final section to draw comparisons between the three cases.

7.1 Nektar++ Base Flow Computations for the vertical steps

Nektar++ computations are constructed for a non-dimensional co-ordinate frame meaning the heights of the bump roughness in the work of Saeed et al.[82] correspond to $412.5\mu m$, $618.7\mu m$, $825\mu m$ and $893\mu m$ for a chord length of one metre. The roughness is added to the clean geometry surface through use of AutoCAD Inventor such that each step is perpendicular to the surface and the corners are filleted with 0.0001m radii. Meshes are then constructed with NekMesh and used with the incompressible

Navier-Stokes solver within the Nektar++ framework, see figure 7.1. Computations are initialised from the converged clean solution and boundary conditions extracted from the full geometry solution.

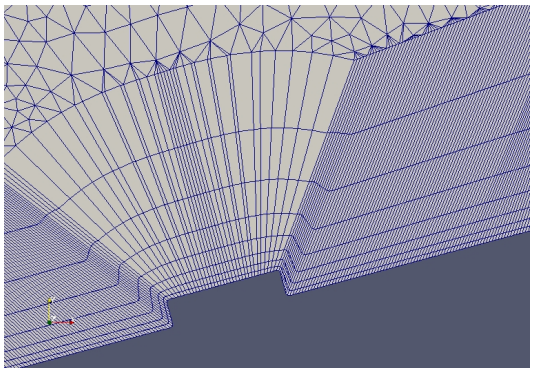

Figure 7.1: Localised view of the vertical edged bump mesh created with Nekmesh. Elements show h-type refinement only.

The height of these excrescences compared with the boundary layer of the clean geometry are shown in table 7.1. Nektar++ base flows with constant $\bar{u}$ velocity contours for the bump and step cases for the largest heights at 10% chord can be seen in figure 7.2. These have been compared with published similar configurations and are consistent[89,9,103,75,8]. Lengths of separation bubbles with respect to the roughness height, $b_h = b_l/h$, (and width, $b_w = b_l/h_w$, in the localized bump case) are listed in table 7.2 for the varying roughness shapes. We can see that the conjugation of the FFS and BFS in the bump case causes much more elongated bubbles for the downstream reverse flow, similar to what was observed from the ramp cases. At 3% chord a nearly blunt face is presented to the onwards flow, since the original clean step free boundary layer thickness at the 3% location is quite thin (82% as noted from 7.1). Introduction of the step at 3% chord gives rise to a major restructuring of the local field and this will inevitably change the development of and stability behaviour of the boundary layer as it develops further downstream. At 10% chord the difference between the ramp separation bubbles and the vertical step separation bubbles seems largely unchanged for the backward facing component, whereas the forward facing component reverse flow has tripled in length. Albeit, the forward facing separation is still extremely small compared to the backward facing separation bubble. As the steps are placed further downstream the upstream bubble (associated with the FFS) becomes slightly larger, then stays around the same size, whereas the downstream bubble (associated with the BFS) grows larger. The peak reverse flow within the bubble is, at maximum, 5 ms^{-1} which is under 7% of the edge velocity. From previous two dimensional LSB studies[76] this generally rules out the possibility of absolute instability. Since our work is 2.5D, the presence of absolute instability remains open. Indeed this topic, one would say, has not been given much attention until now, with the work of Appel et al.[4] possibly

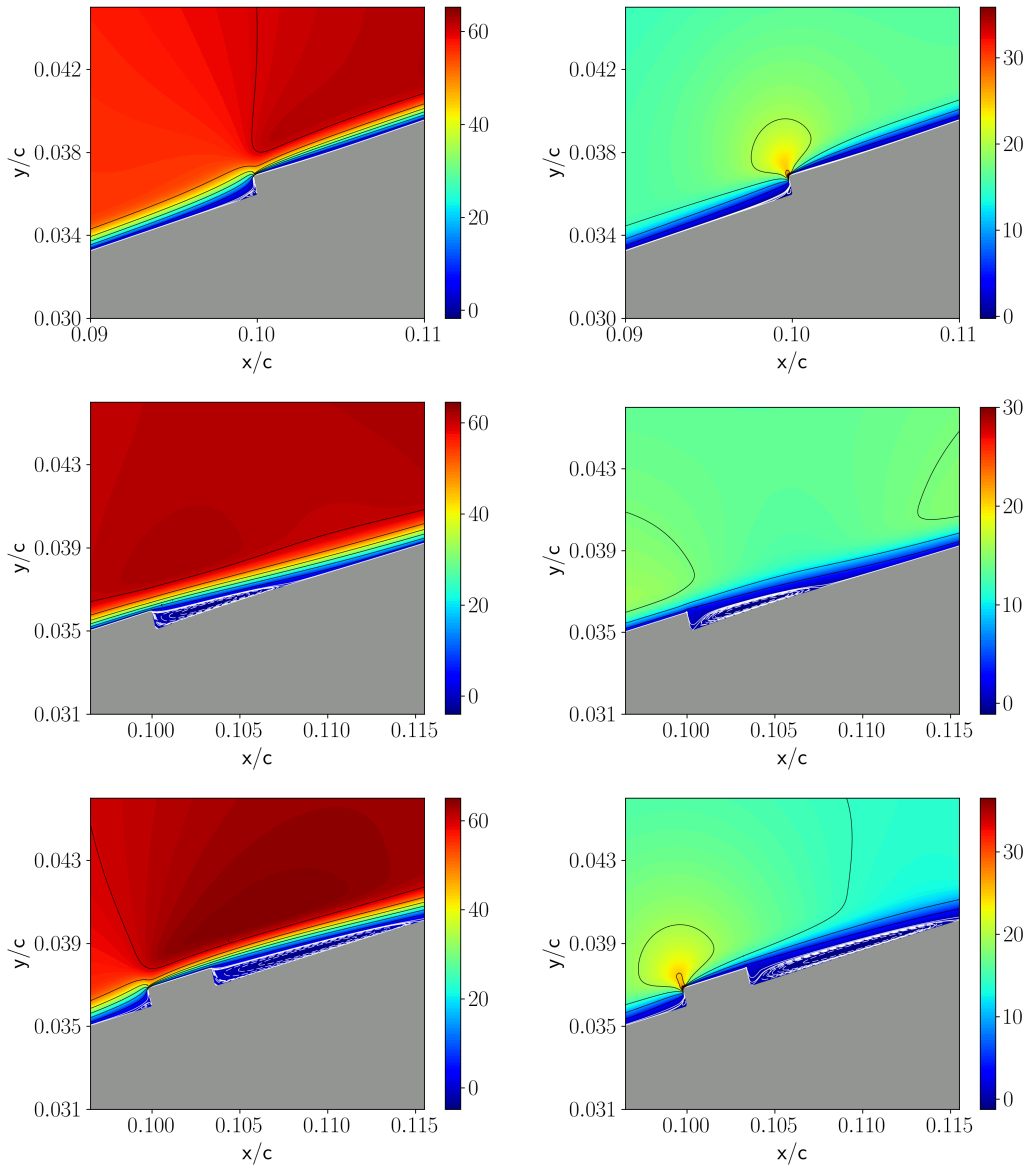

Figure 7.2: Nektar++ solutions at 10% chord, 893 microns for the forward step (top), backward step (middle) and bump (bottom). Contours show stream-wise velocity (left) and normal velocity (right), black lines show the outer boundary layer and free-stream flow. White lines show flow within the inner boundary layer and dashed white lines denote separation bubbles.

being amongst the first to investigate.

Table 7.1: Bump height as a percentage of boundary layer thickness of the clean geometry at each given location

	412.5μm	**618.7μm**	**825μm**	**893μm**
3% chord	38.00%	57.01%	76.01%	82.34%
10% chord	24.43%	36.65%	48.86%	52.93%
20% chord	18.49%	27.73%	36.98%	40.06%

Example non-dimensional baseflow boundary layer profiles for the FFS, extracted at

shape	height	forward b_w	forward b_h	backward b_w	backward b_h
bump 3%	413	0.02	0.15	0.41	3.74
bump 3%	618.7	0.06	0.38	0.84	5.09
bump 3%	825	0.14	0.63	1.34	6.13
bump 3%	893	0.16	0.69	1.49	6.24
FFS 3%	413		0.25		
FFS 3%	618.7		0.49		
FFS 3%	825		0.71		
FFS 3%	893		0.75		
BFS 3%	413				4.53
BFS 3%	618.7				4.99
BFS 3%	825				5.14
BFS 3%	893				5.11
bump 10%	413	0.03	0.25	0.87	7.98
bump 10%	618.7	0.09	0.56	1.74	10.57
bump 10%	825	0.20	0.91	2.69	12.22
bump 10%	893	0.25	1.04	3.06	12.83
FFS 10%	413		0.05		
FFS 10%	618.7		0.58		
FFS 10%	825		0.97		
FFS 10%	893		1.1		
BFS 10%	413				6.56
BFS 10%	618.7				7.59
BFS 10%	825				8.19
BFS 10%	893				8.35
bump 20%	413	0.03	0.26	1.12	10.22
bump 20%	618.7	0.08	0.49	2.42	14.69
bump 20%	825	0.19	0.84	3.98	18.08
bump 20%	893	0.23	0.99	4.50	18.88
FFS 20%	413		0.2		
FFS 20%	618.7		0.54		
FFS 20%	825		0.911		
FFS 20%	893		1.06		
BFS 20%	413				8.65
BFS 20%	618.7				10.96
BFS 20%	825				12.16
BFS 20%	893				12.41

Table 7.2: Bubble lengths with relation to the roughness height, b_h. For the bump case there are two separation regions, before (forward) and after (backward) the bump, which have been related to bump width, b_w, also.

2% of a chord length upstream of the step location, are given in figure 7.3. Most noticeable is the increase in the normal velocity component and corresponding derivatives as the step height is increased, resulting with an upstream lifting of the streamlines. Eppink[27] investigated FFSs experimentally, baseflow contours of the Nektar++ computed solutions compare extremely well to their experimentally obtained results in a qualitative manner. Their geometry was quite different to the AERAST model, a flat plate in the presence of a three dimensional pressure body to simulate an infinitely swept wing flow. The pressure coefficient (C_p) and skin friction coefficient (C_f) over the surface for all forward facing step heights, is given in figure 7.4. These are calculated with the formulas in equations 6.1 and 6.2. We can see from the skin friction coefficient there is a sudden increase in shear at the step location, this is due to the step inducing a sudden forcing of the boundary layer to halve in thickness. We can also see that there is barely any recirculation present for even the tallest FFS height but that as we increase the height of the FFS, there is greater deviation from the baseline case.

Steady baseflow boundary layer profile examples for the backward facing step are given in figure 7.5 along with the C_p and C_f variations over the surface for all step heights, figure 7.6. The drastic decrease in C_f after the BFS, entering negative values, indicates the presence of the separation bubble. The larger the step height the further downstream reverse flow is present. We can see that for 10% chord all BFS heights have returned to the baseline case by 12% chord, for the 20% chord cases it is only the lower two heights that have returned to the baseline by 22% chord.

Steady baseflow boundary layer profile examples for the bump case are very similar to those shown in the FFS and BFS sections so will not be presented here, they may however be found in appendix C. The C_p and C_f over the surface for all bump heights is shown in figure 7.7. We can clearly see that the bump results are a combination of features derived from the FFS and BFS with large similarity between these and the ramp case profiles. Profiles shown here are very similar to the work of Sumariva et al.[90] who exhibit skin friction plots for humps with varying degrees of steepness. Although they do not show an image of the skin friction for their steepest edge hump, we might expect to see something similar to our profile. We note that comparison may, again, be fortuitous since their investigations were for two dimensional flows.

7.2 Forward Facing Step (FFS) Stability Analysis

The natural place to begin is to gain a feel for how the wave number parameter space, from an instability viewpoint, is modified by the presence of the step. We achieve this though computing neutral curves with Linear Stability Theory (LST) for all locations

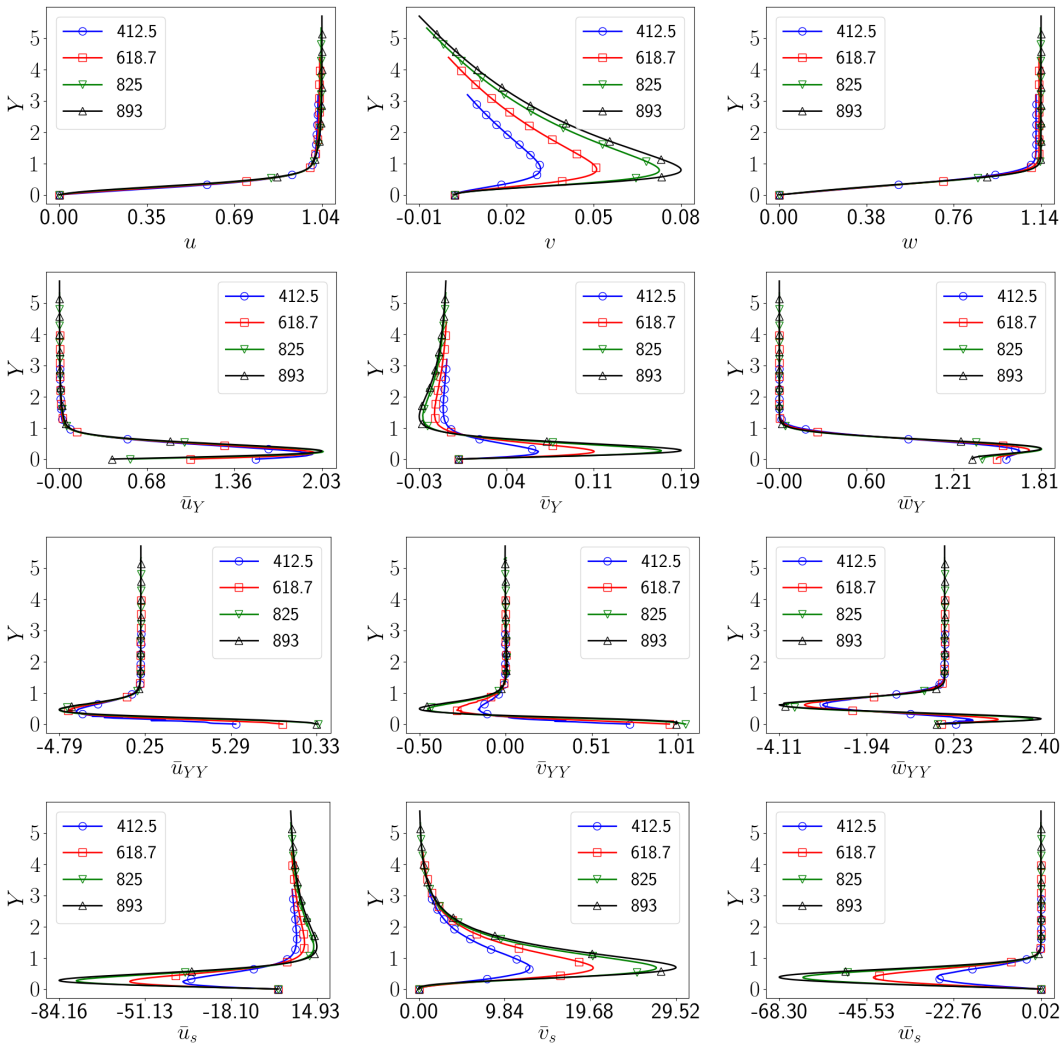

Figure 7.3: FFS case at 10% chord: Nektar++ generated base flow profiles generated at 9.8% chord, just before the bump. Non-dimensional values plotted; x-axis dimensionalised with the boundary layer edge velocity and y-axis is dimensionalised with the boundary layer thickness at that location. Blue, red, green and black depict bump height 412.5, 618.7, 825 and 893μm respectively. Top row shows $\bar{u}$, $\bar{v}$ and $\bar{w}$, second and thirds rows show first derivative and second derivative respectively in the normal direction with respect to $\bar{u}$, $\bar{v}$ and $\bar{w}$ and the bottom row is the first derivative in the stream wise direction with respect to $\bar{u}$, $\bar{v}$ and $\bar{w}$.

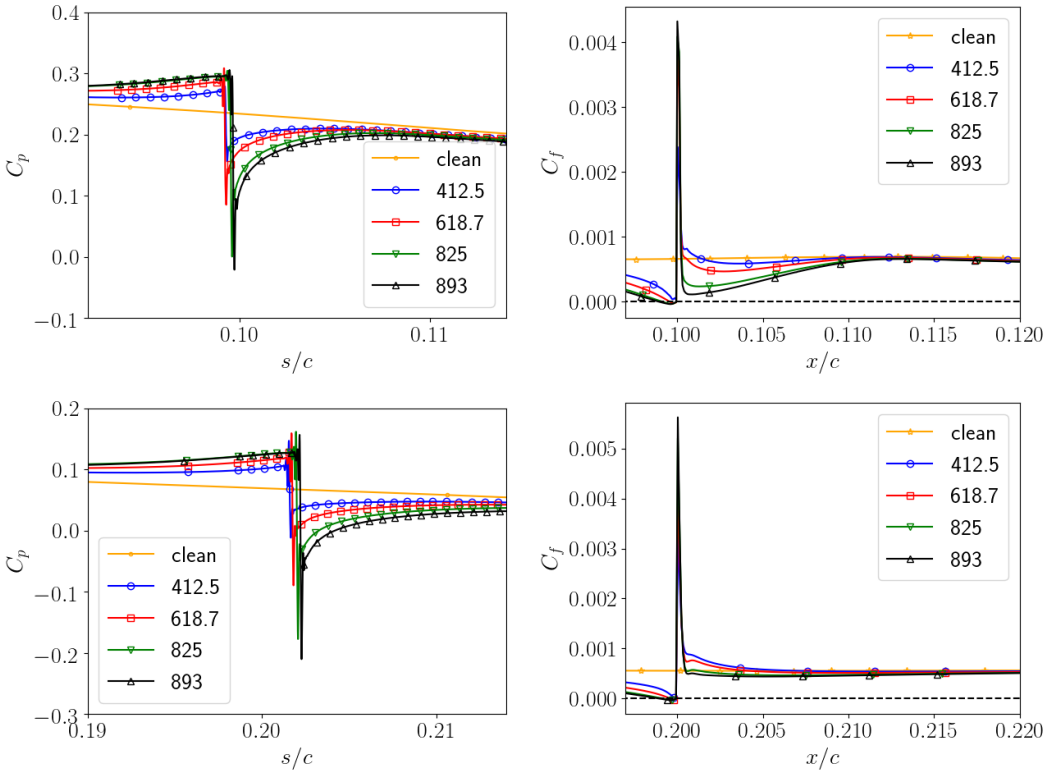

Figure 7.4: FFS case pressure coefficient (C_p) and skin friction coefficient (C_f) comparison of all step heights. Upper for 10% chord, lower for 20% chord. Blue, red, green and black depict bump height 412.5, 618.7, 825 and 893μm respectively, the clean case is given in yellow. The dashed black line marks where skin friction coefficient is zero.

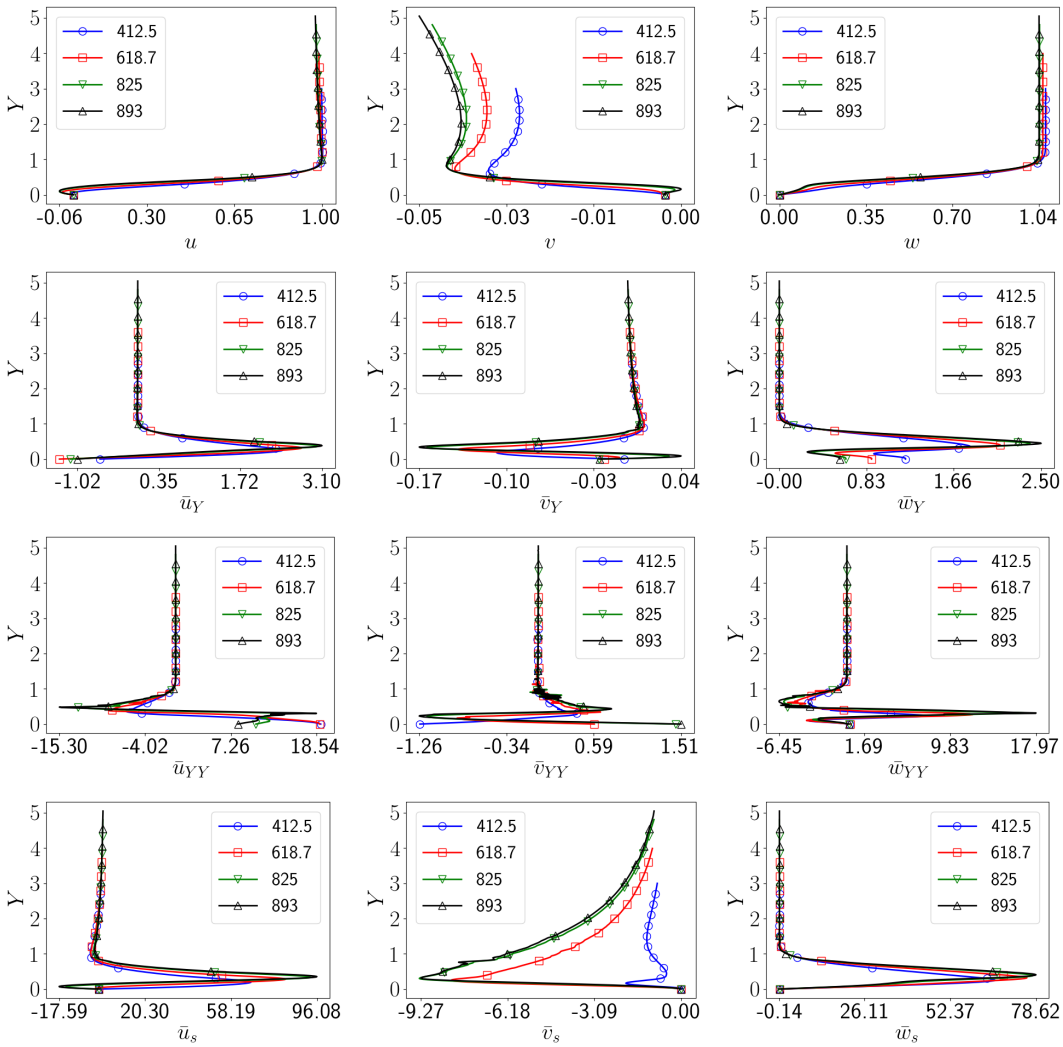

Figure 7.5: BFS case at 10% chord: Nektar++ generated base flow profiles generated at 10.2% chord, just before the bump. Non-dimensional values plotted; x-axis dimensionalised with the boundary layer edge velocity and y axis is dimensionalised with the boundary layer thickness at that location. Blue, red, green and black depict bump height 412.5, 618.7, 825 and 893 respectively. Top row shows $\bar{u}$, $\bar{v}$ and $\bar{w}$, second and thirds rows show first derivative and second derivative respectively in the normal direction with respect to $\bar{u}$, $\bar{v}$ and $\bar{w}$ and the bottom row is the first derivative in the stream wise direction with respect to $\bar{u}$, $\bar{v}$ and $\bar{w}$.

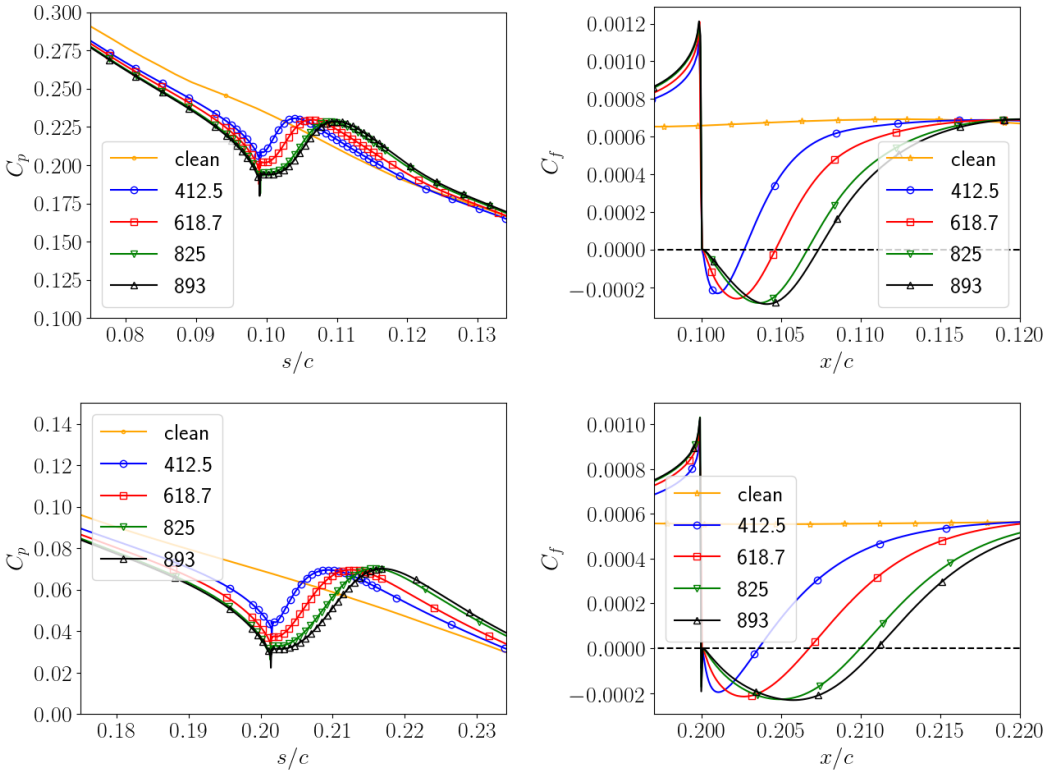

Figure 7.6: BFS case pressure coefficient (C_p) and skin friction coefficient (C_f) comparison of all step heights. Upper for 10% chord, lower for 20%chord. Blue, red, green and black depict bump height 412.5, 618.7, 825 and 893μm respectively, the clean case is given in yellow. The dashed black line marks where skin friction coefficient is zero.

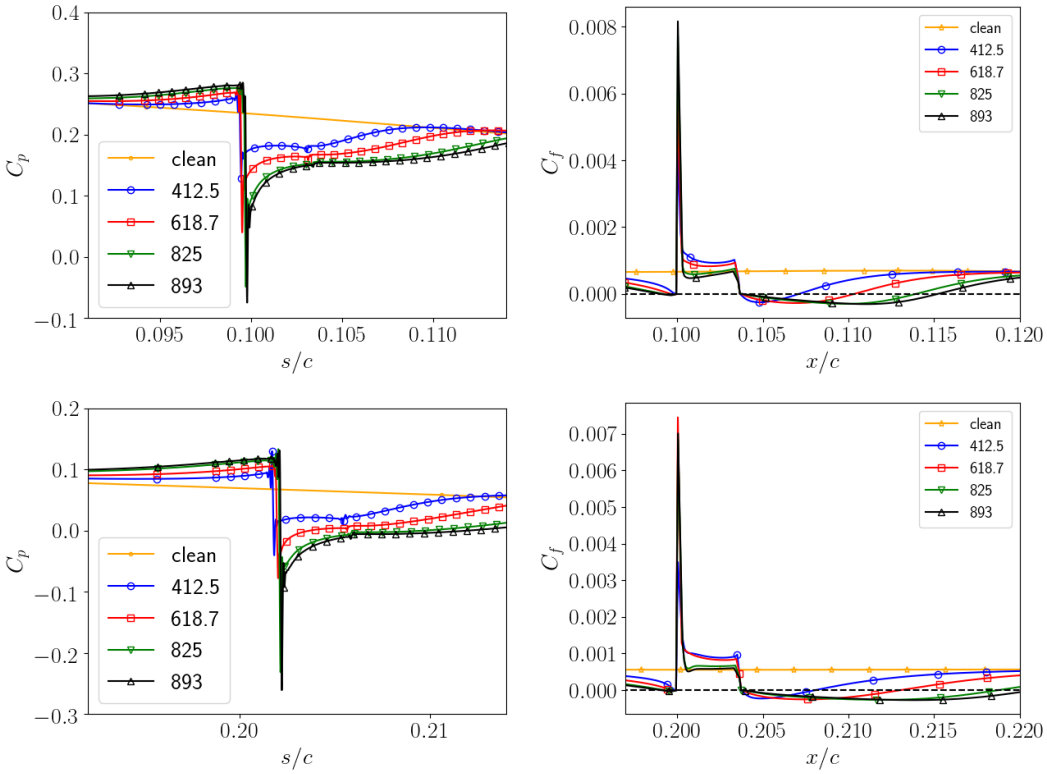

Figure 7.7: Bump case pressure coefficient (C_p) and skin friction coefficient (C_f) comparison of all step heights. Upper for 10% chord, lower for 20%chord. Blue, red, green and black depict bump height 412.5, 618.7, 825 and 893μm respectively, the clean case is given in yellow. The dashed black line marks where skin friction coefficient is zero.

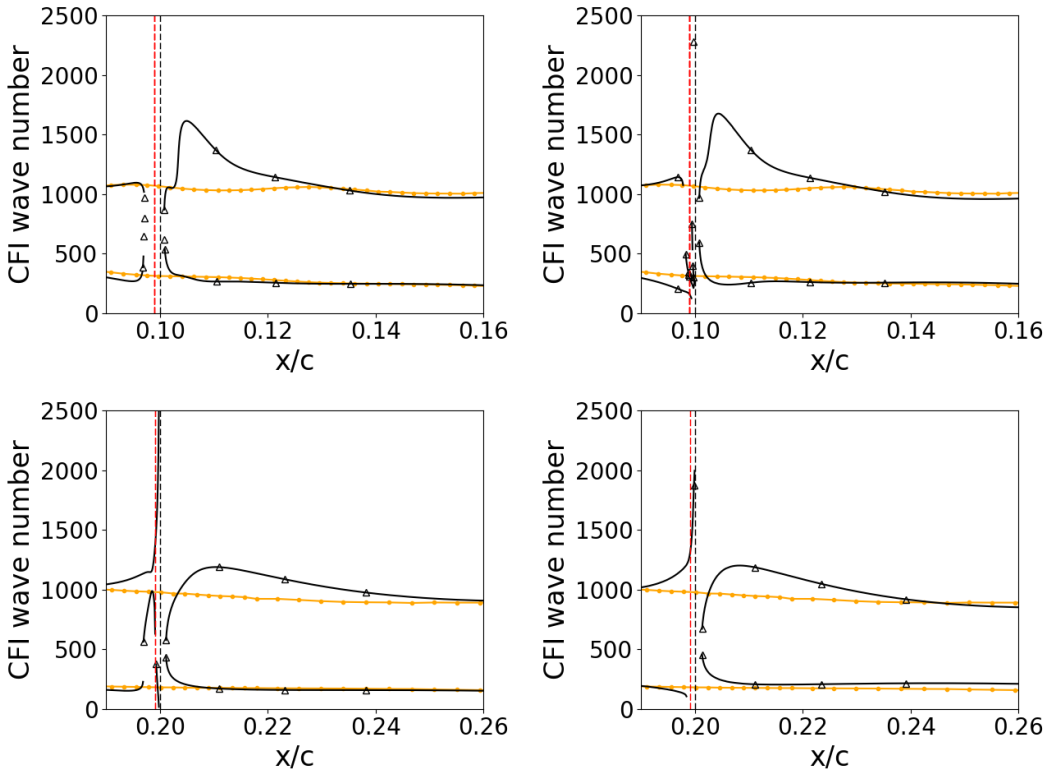

Figure 7.8: Neutral stability curves for the clean (yellow points) and FFS largest height step case (black triangles). Top row denotes the 10% chord location, bottom row denotes 20% chord location. Left for stationary crossflow, Right for travelling crossflow: clean frequency at 420Hz, 10% FFS at frequency 190Hz and 20% FFS at frequency 480Hz. The dashed red line denotes the start of the separation bubble and the dashed black line denotes the step location.

of roughness. LST estimates that the neutral point is located at around 5% chord, meaning the 3% chord roughness cases are located in a very stable region of the flow. This makes it extremely difficult for LST to find unstable eigenvalues. A large range of span-wise wave numbers and frequencies are explored in solution of the dispersion relationship, but no unstable (ω, β) combinations were found, even with the highest steps considered at 3% chord.

Comparing the largest step height with the clean case, see figure 7.8, we see the presence of the forward facing step increases the range of crossflow wave numbers that are destabilised from β =90-1100m^{-1} to β =0-2500m^{-1} in the most extreme case, at 20% chord. The 10% chord neutral curve, computed just for the stationary CFI, features two distinct unstable regions, just before the separation bubble and after the step. The presence of the FFS, or bubble, then expands the destabilised parameter space to extend the range of the upper branch beyond the step. Similarly to the ramp step case, we do not consider the stable space over the region of the separation bubble to be completely stable. There are probably very small areas of the parameter space that become briefly unstable. However, trying to identify these modes is extremely

difficult due to their brief spatial existence. The neutral curve we see here for the 10% stationary case is very similar to that of the FFR case, the main difference being that the FFS case exhibits a short lived convergence to the baseline, upper branch before the destabilised parameter range then shoots up to β =1600m^{-1}. For the ramp case this is more gradual.

When looking at the travelling crossflow case, in figure 7.8, there are no longer two clear unstable regions as there are in the stationary case. The downstream unstable region seems to be relatively unchanged except a smoother increase in the upper neutral branch just after the step, more similar to what we observe in the stationary ramp case. The upstream unstable region however, now seems to have opened up in the vicinity of the bubble and at the step location. It appears that just before the separation bubble the parameter space remains unstable in the lower wave number range, as we move towards the step location. Around the centre of the bubble the unstable wave number range shoots up to as high as β =2300m^{-1}. For the 20% chord stationary CFI we also observe an opening of the unstable region prior to the bubble, again adding to the suspicion that there may be some unstable region present in the 10% chord case that we are not able to detect with LST. Contrary to the 10% travelling case the opening of the first unstable region now appears to be in the higher wave number range, around β = 1000m^{-1}, and just as we reach the beginning of the separation bubble the two lower and upper branches diverge until the step location. The downstream unstable zone seems to have a much smaller range of destabilisation than the 10% chord case, only reaching around β=1250m^{-1} at 21% chord. The travelling CFI neutral curve seems to have a much larger region of destabilisation around the step location where both upper and lower branches tend to immediately diverge.

Now comparing all FFS height computed neutral stability curves we can see that with added height the range of destabilised wave numbers are increased, see figure 7.9.

All heights of FFS at 10% chord are computed with the PSE and PSEh codes for stationary and travelling CFI. Although we expect the PSE to fail to provide a valid solution for the instability growth, we computed these solutions to see if a result could even be obtained for such an extreme geometry change. The reason we expect this to fail is due to the length scale of the roughness being too short for the CFI introduced[104], as we found from the ramp study in chapter 6, and the presence of extremely strong stream-wise gradients causing the PSE not to converge[89]. The PSE are also required to provide the PSE radiation condition for the LHNS outflow boundary.

N-factor growth curves for the 10% chord located roughness are displayed in figure 7.10, the clean case has been added for reference. The general trend for both codes seems to be a stabilisation as the FFS height is increased, similarly to what was observed

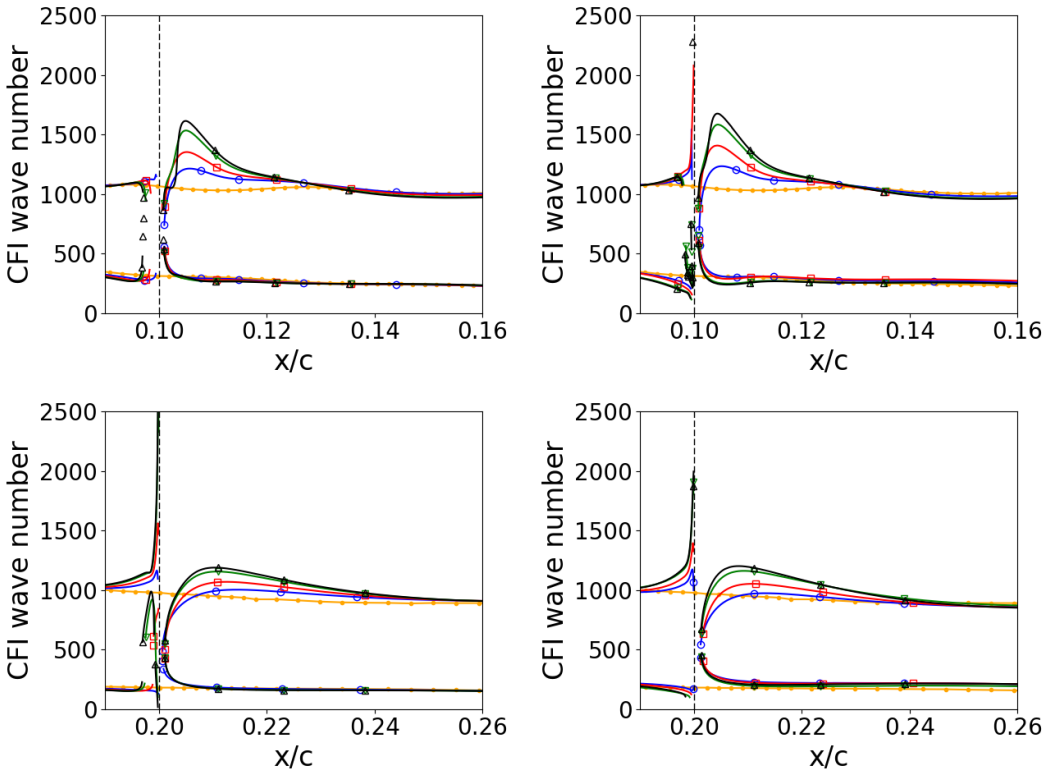

Figure 7.9: Neutral stability curves for all FFS heights. Yellow points denote the clean geometry, blue circles for 412.5 microns, red squares for 618.7, green downward pointing triangles for 825 and black upward pointing triangles for 893 microns. FFS largest height step case (black triangles). Top row denotes the 10% chord location, bottom row denotes 20% chord location. Left for stationary crossflow, Right for travelling crossflow: clean frequency at 420Hz, 10% FFS at frequency 470Hz, 480Hz, 460Hz and 480Hz for step heights 412.5, 618.7, 825 and 893μm respectively and 20% FFS at frequency 490Hz, 560Hz, 490Hz, 500Hz. The dashed black line denotes the step location.

in the ramp case but contrary to the general expectation and limited experimental evidence[27,31] that all steps will lead to a destabilisation of disturbances. As with the ramped case, many stream-wise station locations need to be neglected during the computation in order to attain a converged solution. This is due to the stream-wise derivative terms exhibiting very large gradient changes over the edges of the step, where there are rapid variations in geometry. The step, although considered large scale, is still very small meaning these neglected stations could be a necessary requirement for satisfying the PSE step size restriction. As a consequence of ignoring some stations, this can mean no profiles are selected over the edges of the FFS where the curvature of the roughness, dh/ds, holds a value. We can see this from heights 412.5, 618.7 and 825 microns, which give exactly the same predictions for PSE and PSEh computations. For the 893 micron case, which is the only case that selected a profile on the corner of the step, we do see a difference between the PSE and PSEh solutions. Similarly to the ramp case, the PSEh predicts a greater stabilisation than the PSE. All in all, we can confirm that the PSE fail, as predicted, to capture the presence of the step, largely due to vast variations in stream-wise gradients and the roughness being too small for the CFI introduced. Nevertheless, we did find that a PSE computation could be re-started beyond, and ahead of, the step, in which case the correct behaviour is computed with the PSE modelling. In the dimple case investigated, section 4.1, the stream-wise variations in the geometry were much smoother and gradual, and the PSE was able to capture this "kick" or amplitude jump, but in the present case the geometrical changes are of an extreme nature. In this situation only the LHNS approach is viable.

Since the PSE do not provide a reliable solution, we moved to LHNS and LHNSh computations. In order to resolve the step location a much finer mesh is required for LHNS and LHNSh computations than for the clean case. Typically we use around 8000 points in the stream-wise direction and 51 Chebyshev polynomials in the normal direction, whereas for the clean case we can obtain a mesh independent solution with as little as 1800 points in the stream-wise direction. CFI amplitude is constructed by taking the maximum $|\hat{u}|$ disturbance at each stream-wise location and normalising with the boundary layer edge velocity at that location. Plots for all FFS heights are shown in figures 7.11 and 7.12. The instability is generated by a wall forcing placed at the clean neutral point (3% chord) ahead of the step which is located at 10% chord. Both codes are generally consistent with the literature for CFI, where increased step height triggers greater amplification of instability and that travelling CFI is much more detrimental to the flow[27,95,69]. Notice that for the travelling cases the amplitude grows an order of magnitude larger than in the stationary case. Taking just the clean case we can see the peak of the travelling CFI reaches an amplitude of 5×10^{-2} whereas the stationary only reaches 5×10^{-3}. For the stationary CFI, the LHNS code predicts

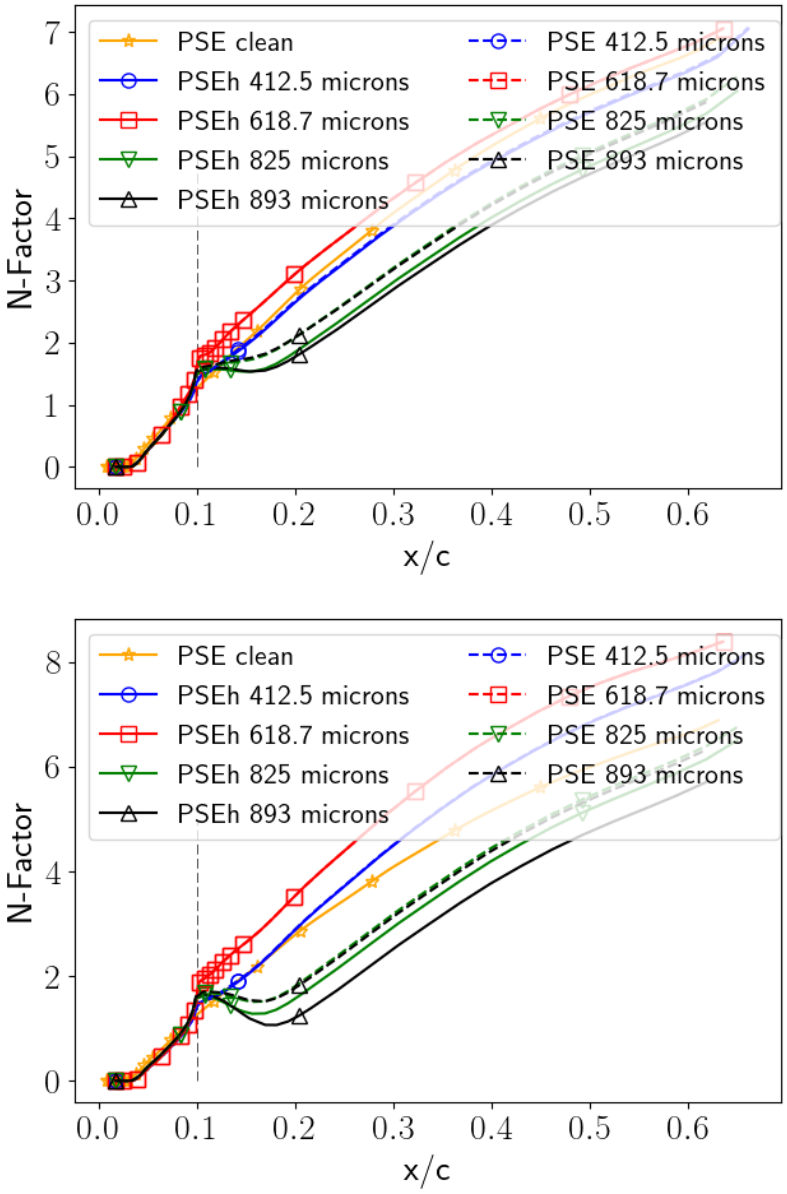

Figure 7.10: FFS at 10% chord: PSE calculation (dashed lines) and PSEh (solid lines) comparison of N-factor growth of most unstable CFI for all roughness heights. Blue for 412.5 microns, red for 618.7, green for 825 and black for 893 microns. Top: Stationary CFI. Bottom: Travelling CFI

an amplification in growth of the smallest bump case, compared with the clean and LHNSh code. This seems an unlikely prediction since there was no modification to the transition point in the experimental work of Saeed et al.[82], although their work did feature a bump roughness not a FFS. The growth predicted by the LHNSh code seems much more reliable due to a gradual increase in amplification with increased step height. It is clear that the relatively small correction to the LHNS equations, namely the LHNSh model, does capture the correct expected trend, whereas the LHNS without the h correction is clearly flawed. This is consistent with the literature, and is also in line with the findings of Saeed et al.[82]. They observed no change in the transition front for the smallest step height, although we should remember their work was for a bump shape roughness.

Looking now to the LHNS travelling CFI result, we would not expect the 825 micron case to move the transition front further forward than the 893 micron case. Again this merits the LHNSh code for providing a more reliable result. The difference in amplitude predicted by both codes is highlighted for the largest step height in figure 7.13.

If we compare a PSE result with the same corresponding LHNS result, matching the amplitudes prior to the roughness and after the roughness we can see that the PSE generally seems to predict the growth very well, however when reaching the roughness location the equations completely break down, thereby distorting the solution henceforth, see figure 7.14. The linear PSE solutions can be made to match, through a simple scaling, the LHNS result either ahead of the step or beyond the step feature, with the 'jump' not being modelled. This is precisely the so-called "scattering effect" that Wu and Dong[104] discuss, which we see the LHNS does capture. Sumariva and Hein[89] with their PSE composition with the LHNS equations, capture such jumps, but the approach undertaken in the present work is much simpler and more straightforward.

If we now look at the 20% chord cases, figures 7.15 and 7.16 we can see that for the LHNS stationary case, the trend for increased step height compared with amplitude of CFI growth seems to be true. However, there is a sharp decrease and then growth just after the step for the highest FFS at both 10% and 20% chord. Since this is present in both step cases, it could be that the velocity gradients are too large here without the presence of the $h-$correction in the equations to counteract for this. Looking at the travelling LHNS we can see that the second largest height seems to be becoming more stable than the clean case when convecting down-steam. We attribute this to not finding the truly, most unstable wave number. We can see the wave number for this case $\beta = 560m^{-1}$ is quite a lot higher than for the other cases, a consequence of using the PSE to rapidly search though the wave numbers and provide boundary conditions for the LHNS equations.

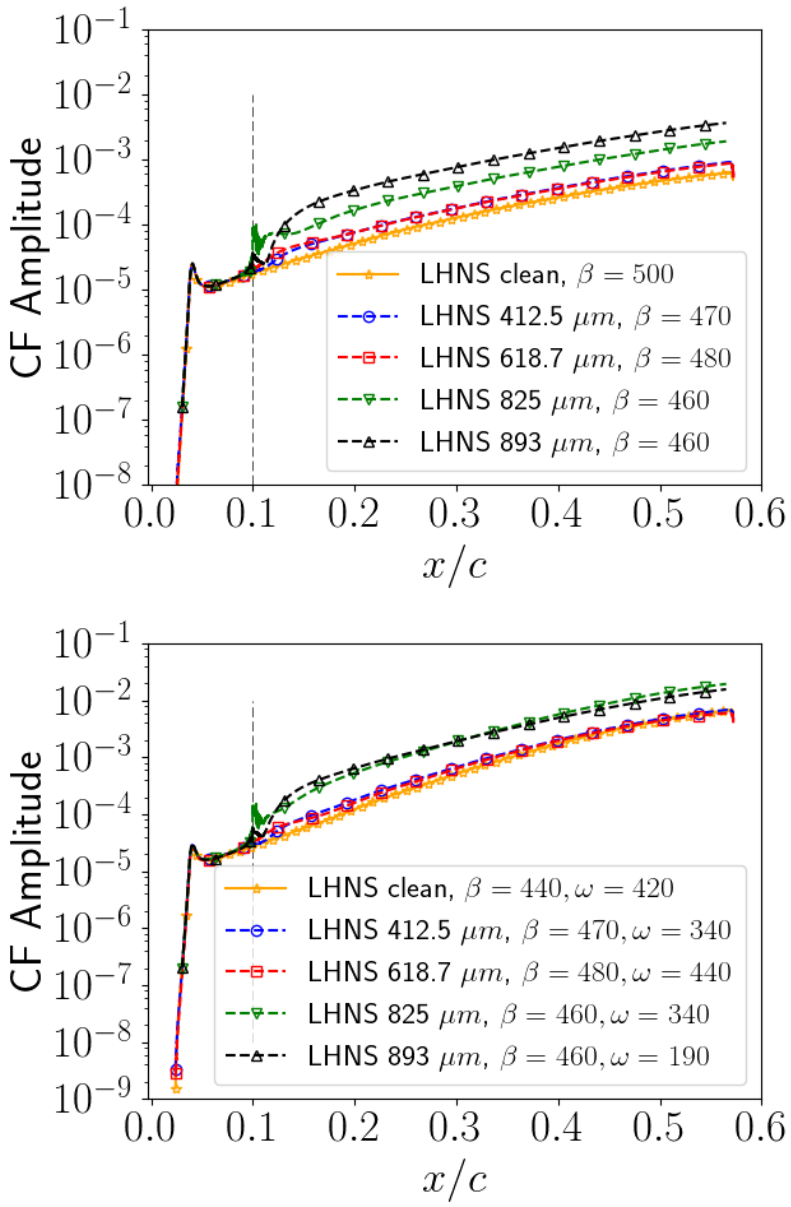

Figure 7.11: LHNS calculation for FFS at 10% chord: Comparison of most destabilizing CFIf for all roughness heights. Red for 412.5 microns, blue for 618.7, green for 825 and black for 893 microns. Top: Stationary CFI. Bottom: Travelling CFI. The dashed vertical line denotes the FFS location. Units of the span-wise wave number β are m^{-1} and the frequency ω is given in Hz.

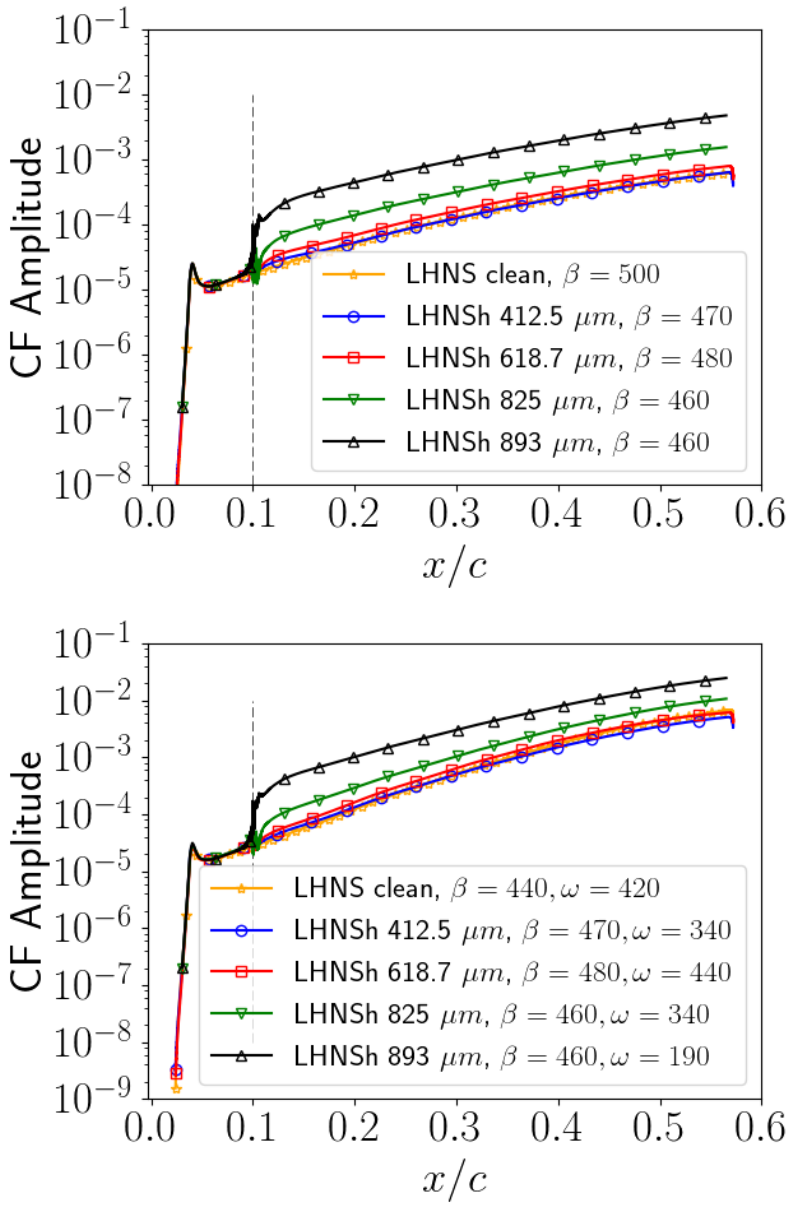

Figure 7.12: LHNSh calculation for FFS at 10% chord: Comparison of most destabilizing CFI for all roughness heights. Red for 412.5 microns, blue for 618.7, green for 825 and black for 893 microns. Top: Stationary CFI. Bottom: Travelling CFI. The dashed vertical line denotes the FFS location. Units of the span-wise wave number β are m^{-1} and the frequency ω is given in Hz.

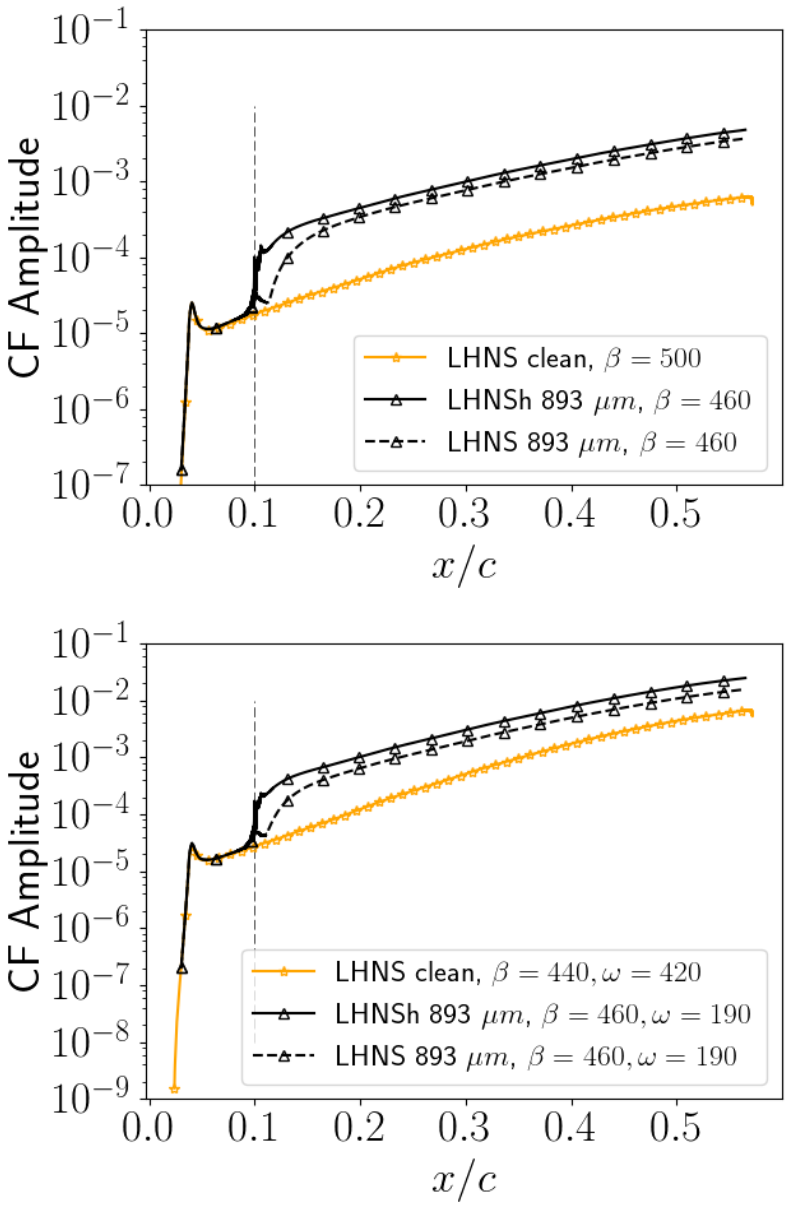

Figure 7.13: FFS at 10% chord with height of 893 microns: LHNSh (solid lines) and LHNS(dashed lines) comparison of crossflow instability. Top: Stationary CFI. Bottom: Travelling CFI. The dashed vertical line denotes the FFS location. Units of the span-wise wave number β are m^{-1} and the frequency ω is given in Hz.

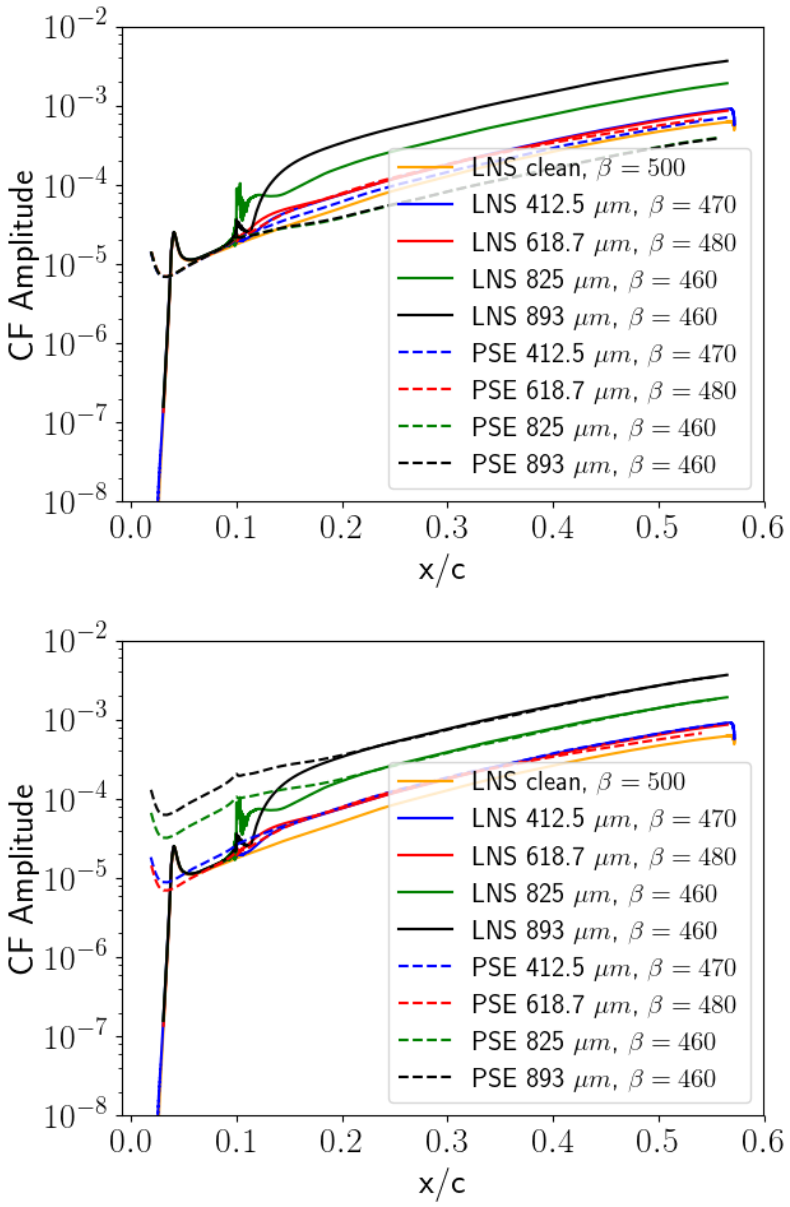

Figure 7.14: FFS at 10% chord: PSE calculation (dashed lines) and LNS (solid lines) comparison of amplitude growth of most unstable stationary CFI for all roughness heights. Blue for 412.5 microns, red for 618.7, green for 825 and black for 893 microns. Top: matching before the roughness location. Bottom: matching after the roughness location. Units of the span-wise wave number β are m^{-1}.

Looking now to the LHNSh solutions 7.16, again the general trend in amplification compared to step height is observed but there seems to be very little growth compared to the clean case. This could be due to the stream-wise gradient changes being of even greater magnitude at this further downstream position and these large numbers now beginning to effect the LHNSh computation. It could once again be due to the method of selecting the mode destabilised wave number or frequency. For example, 617.8 microns has a much higher wave number than any of the other cases and 825 microns has a much lower frequency than the other cases. Less amplified stationary CFI further downstream was also observed experimentally[81] for the bump case.

To compare LHNSh results with all step heights and both locations we have decided to take the growth from figure 7.11 and plot the amplitude of disturbance 10% after the location of the roughness. For the 10% roughness the reference point is 20% and for the 20% roughness the reference point is 30%. The $|\hat{u}|$ amplitude is scaled with the edge velocity at the measurement location (either 20% or 30% chord) and plotted against the height of the roughness, scaled with the boundary layer thickness at the excrescence location, as shown in table 7.1. The results can be seen in figure 7.17. Looking at the 10% located roughness cases it is clear to see the smallest step height has no effect on the stationary CFI growth but does for the travelling. As step heights are increased this growth is increased further and further, always with the travelling CFI being the more dangerous of the two. We observe similar trends for the 20% chord FFS but for the stationary case we do not see much change from the baseline when increasing the step height. For the AERAST bump model, similar plots have been created but evaluated at a fixed location of 25% chord for all of the bump heights[81]. It seems that when comparing the amplitude of CFI compared with the step height there is very little difference observed for the stationary CFI with bumps located at 10% and 20% chord, see figure 2a in work by Saeed and Morrison[81]. There is a slight change when reaching the equivalent height of our 618.8 micron case, but there is no data point for the 825 micron case at 10% chord, and the 20% chord case seems to decrease again. The authors mention that the bump provides less amplification to the CFI when placed further downstream along the chord, however, a downstream location does result in a decrease in the critical step height. Although we are not comparing like for like excrescences, it is encouraging that our linear analyses is in agreement with these experimental observations since we find more amplification from the 10% chord located FFS than the 20% chord.

Contour plots of the stream-wise perturbation field, normalised with the boundary layer edge velocity, for the largest step height are depicted in figure 7.18. Similarly to the FFR case, immediate growth of perturbation seems to be triggered by the step upper corner. This can be seen more clearly by looking at the travelling CFI 10%

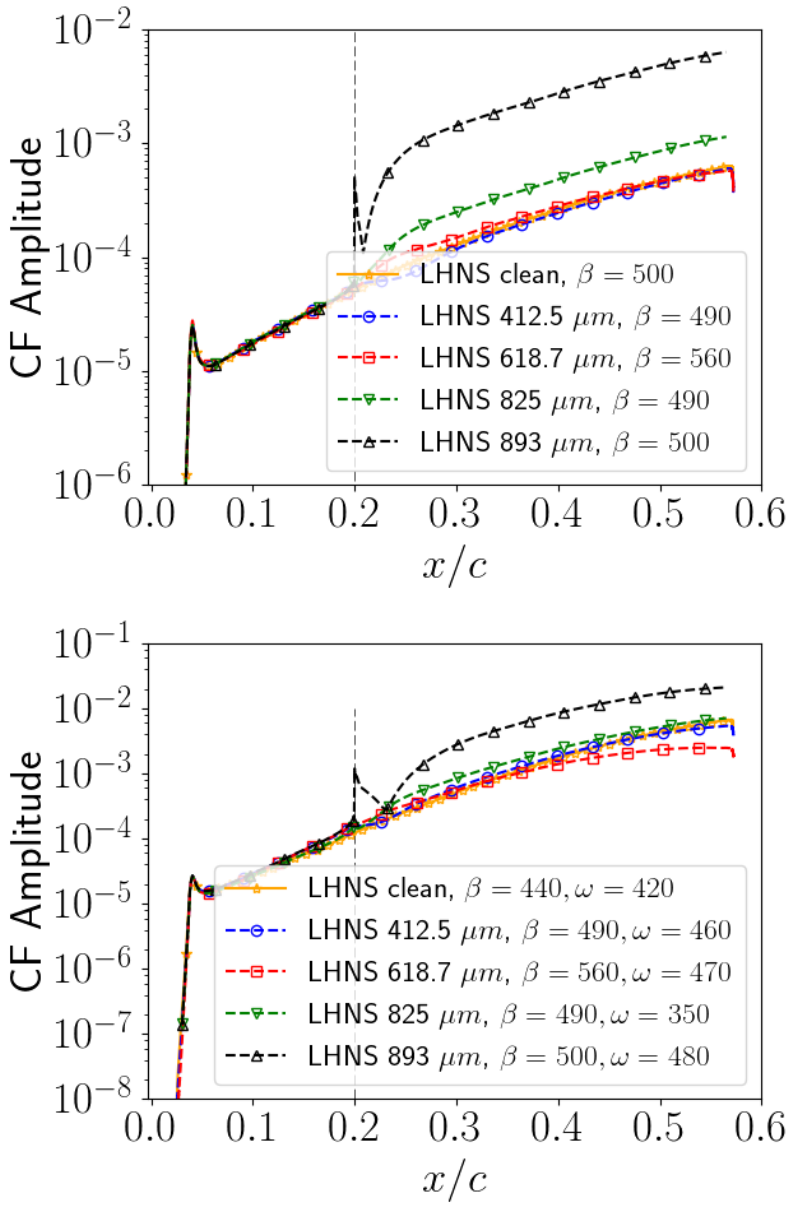

Figure 7.15: LHNS calculation for FFS at 20% chord: Comparison of most destabilizing CFI for all roughness heights. Red for 412.5 microns, blue for 618.7, green for 825 and black for 893 microns. Top: Stationary CFI. Bottom: Travelling CFI. The dashed vertical line denotes the FFS location. Units of the span-wise wave number β are m^{-1} and the frequency ω is given in Hz.

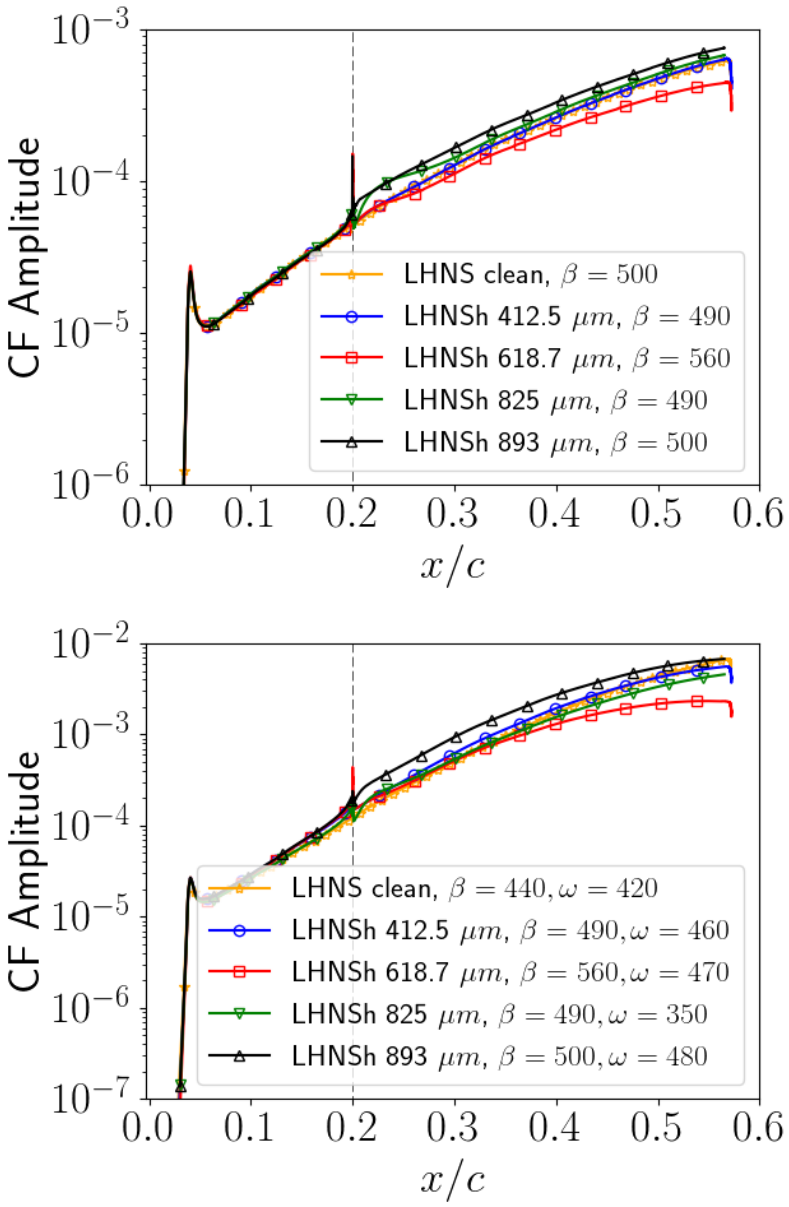

Figure 7.16: LHNSh calculation for FFS at 20% chord: Comparison of most destabilizing CFI for all roughness heights. Red for 412.5 microns, blue for 618.7, green for 825 and black for 893 microns. Top: Stationary CFI. Bottom: Travelling CFI. The dashed vertical line denotes the FFS location. Units of the span-wise wave number β are m^{-1} and the frequency ω is given in Hz.

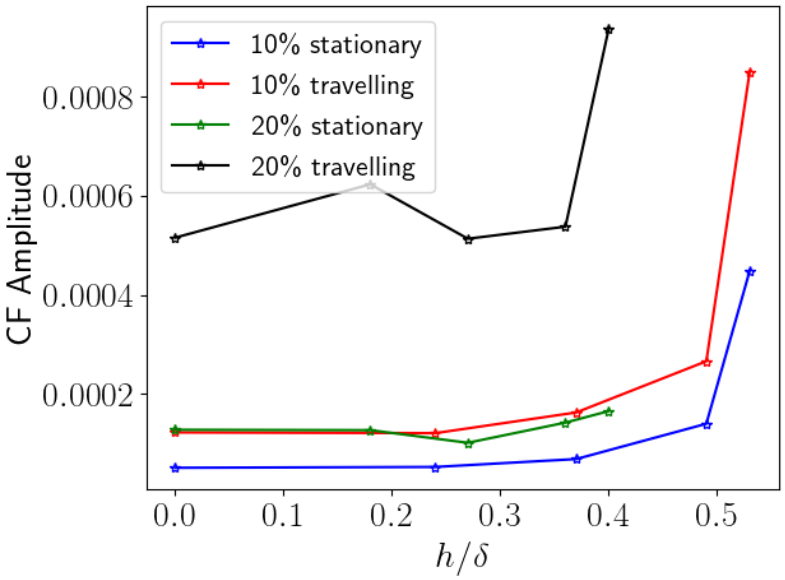

Figure 7.17: FFS LNSHh calculations for most destabilising stationary and travelling CFI for all step heights placed at 10% chord. Amplitude measurements are taken 10% after each respective roughness location (20% chord for the 10% chord FFS and 30% chord for the 20% chord FFS) and normalised with the edge velocity at the corresponding 10% downstream locations.

FFS case than in the FFR case, figure 6.10. As observed by Eppink and Casper[28], who looked at FFS and FFR impact on CFI over a flat plate, we see a lifting of the CFI from the wall following that of the constant $\bar{u}$ contours. Due to the sharpness of the step this uplift in the step corner is extremely clear. We can also see in the FFS 10% chord case, figure 7.18, a region of reversed $\hat{u}$ flow just above the step corner, sitting amongst the constant $\bar{u}$ velocity contours. Upstream of the step there is a region of crossflow reversal near to the separation bubble which we see clearly in figure 7.19. The sign of the vorticity at this inflection point is determined from the direction of the crossflow velocity in the boundary layer. A change in the sign of the crossflow $\hat{w}$ component can cause amplification of stationary CF vortices, rotating in the opposite direction to the primary vortices, leading to destabilisation of these primary vortices[28]. This strong kick that the step provides to the CFI is also observed in the work of Eppink and Casper[28], see figure 9a in their paper, where the sharp step peak amplitude immediately increases from 2 to 7. Sumariva and Hein[89], who looked at two dimensional flow with a convecting TS wave over a sharp bump on a flat plate, have also observed this jump in amplitude when reaching the step upper corner.

All velocity perturbation profiles are plotted at varying stream-wise locations in the neighbourhood of the step feature. Perturbation velocities are scaled with the free-stream velocity at that location. When examining $\hat{u}$ perturbation profiles we find that at the step region there are two peaks which form in the perturbation profile, the larger of which is closer to the wall. As we move downstream these peaks tend to

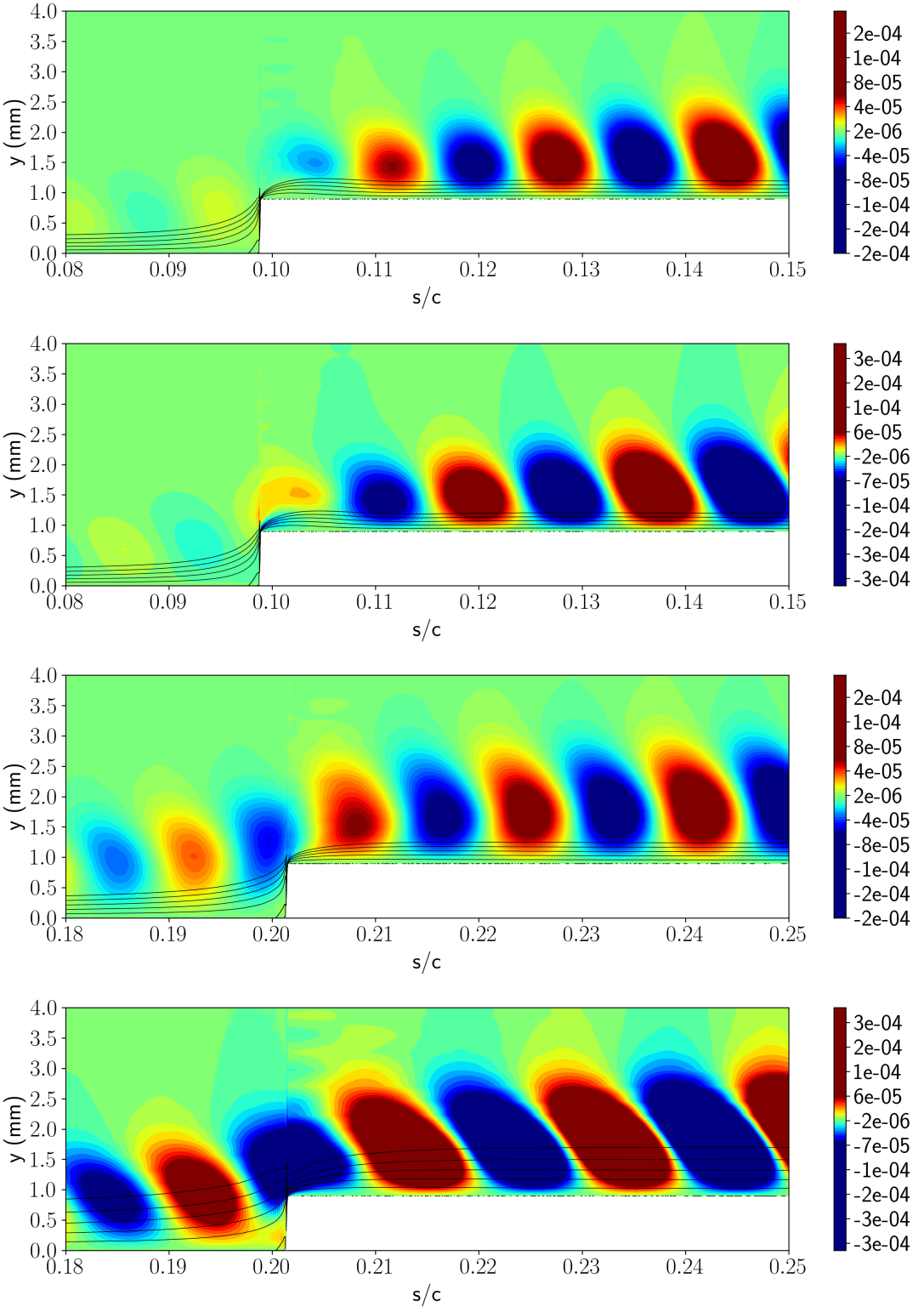

Figure 7.18: Stream-wise perturbation field, $|\hat{u}|$, for 893 micron FFS at 10% and 20% chord. Top: LHNSh 10% chord stationary case, $\beta = 460m^{-1}$. Second: LHNSh 10% chord travelling case, $\beta = 460m^{-1}$, $\omega = 190Hz$. Third: LHNSh 20% chord stationary case, $\beta = 500m^{-1}$. Bottom: LHNSh 20% chord travelling case, $\beta = 500m^{-1}$, $\omega = 480Hz$.

merge into one, see figure 7.19. Looking at the $\hat{w}$ component prior to the step at 9.6% chord, before we enter the small separation bubble, we can see the inflection profile typical of crossflow. Moving closer to the step to 9.8% chord, now much closer to the separation bubble location, we start to see a lifting of the upper peak and the lower peak has become further pronounced, indicating the presence of crossflow reversal[27]. These profiles are similar to those observed in experiments by Eppink[27].

Tufts et al.[95] have studied FFSs and BFSs experimentally and numerically on a swept wing, but their work features a separated flow region on the upper surface of the step as well as just prior to the step, which we do not find. Nonetheless, the height of the clean crossflow vortex (CFV) is compared with that of the height of the step to examine the postulation of Tufts et al.[95]. Tufts et al.[95] suggest that when the step height of a FFS, h, is larger than that of the clean case CFV height, y_c, there is a constructive interaction between the helical flow downstream of the FFS and the CFV. The height of the CFV varies with each wavelength of CFI introduced. This means the clean case needs to be evaluated for each of the corresponding most destabilising wavelengths for the FFS cases. When examining the perturbed velocity profiles, the height of the CFV is between 1463 microns for the stationary cases and 1417 microns for the travelling cases. These CFV heights are larger than any of the FFS heights, meaning the reasoning by Tufts et. al. is not appropriate for this FFS configuration. This suggests the amplification could be either due to the earlier helical flow before the step which the CFI is interacting with, the corner of the step itself or some other mechanism interacting with the stationary CFI. Since we do not have laminar separation bubble present above the step in our computations, this cannot be a key mechanism in our regimes.

From these observed stability results we can see that the FFS indeed works as a very clear amplifier to the convecting CFI.

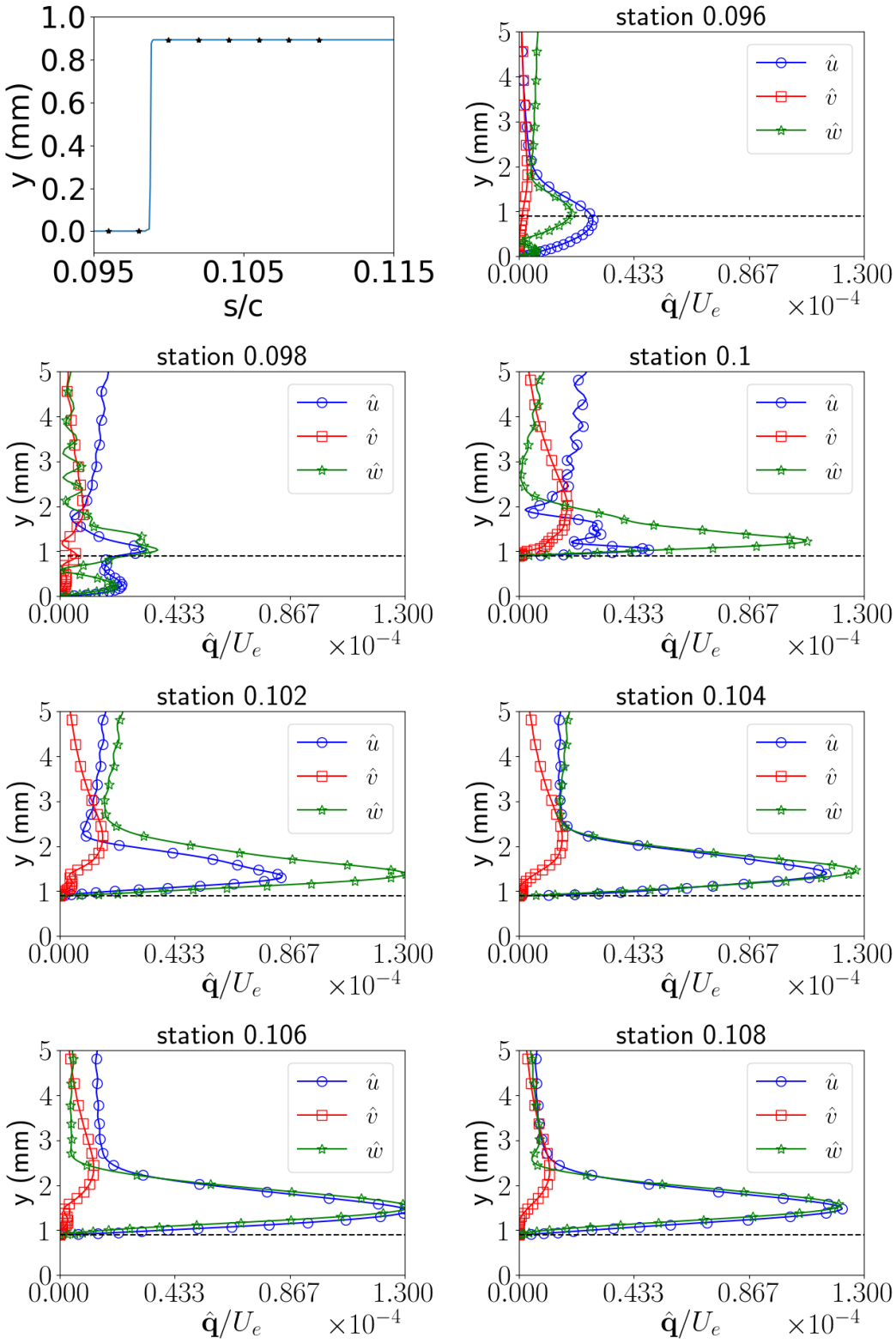

Figure 7.19: 10% chord largest FFS height with stationary CFI: LHNSh generated velocity profiles generated at a range of stations. The plot in the top left hand corner marks the stations at which the profiles are evaluated. The dashed horizontal line marks the step height.

7.3 Backward Facing Step (BFS) Stability Analysis

Neutral curves are computed with linear stability theory for the backward facing step. The largest step height is compared with the clean case for 10% and 20% chord, see figure 7.20. The neutral curves are a very different shape to those computed for the FFS. The BFS seems to have a more severe impact on the range of wave numbers which are destabilised. They also appear to remain unstable for a much further spatial extent than the FFS, the 2.5D separation bubble seems to be the main driver for this.

Beginning with the 10% chord stationary crossflow case, we can see there are now three unstable regions, instead of two as for the FFS. When the BFS is reached, marked with the dashed vertical black line, the parameter space is immediately completely destabilised up until $\beta = 2500m^{-1}$. The upper branch then seems to curve down to $\beta = 2000m^{-1}$ at around the midpoint of the separation bubble and the lower branch also begins again. The two branches then converge quite steeply to one another at the point of reattachment, denoted by the dashed red line. It is very shortly after this that the third unstable region begins. The lower branch almost immediately returns to the clean lower branch but the upper branch remains slightly higher at $\beta = 1300m^{-1}$. Until dropping lower than the clean upper branch to $\beta = 850m^{-1}$ and then slowly converging back to the clean upper branch around 18% chord.

Interestingly for the travelling crossflow case, the latter two unstable zones we see in the stationary case seem to have merged into one large unstable region. There is also the existence of a small, stable, boomerang shaped, isolated region. This short lived region of stabilisation is located in and slightly after the separation bubble, ranging from $\beta = 300m^{-1}$ to $\beta = 1300m^{-1}$. Similarly for the stationary case, as the upper neutral curve returns back towards the clean branch it over shoots to as low as $\beta = 700m^{-1}$ before starting to slowly increase back to the clean upper branch. We also observe a slight overshoot of the lower branch before returning to the clean case much further downstream.

For the stationary 20% chord case, again the largest range of destabilised wave numbers is in the region of chord where the reverse flow is. Unlike the 10% chord stationary case we now see a merging of the second and third unstable regions in the parameter space $\beta = 1000m^{-1}$ to $\beta = 1500m^{-1}$ at 21.5% chord. The lower neutral branch has attempted to converge to the upper branch here, reaching as high as the clean upper branch, before reversing back down and converging to the clean lower branch. The merging of the upper neutral branch to the clean case is much more gradual than the 10% case and seems to result in less of an overshoot.

The 20% travelling case has the largest unstable regions overall with the small stable

zone located within the recirculation region shrinking to a much smaller size than in the 10% chord case. It now only effects wave numbers between β =400m^{-1} to β =800m^{-1}. We do observe a downstream over-shooting of the neutral curves as they converge to the clean case, similar to the 10% travelling case. We also notice that the maximum range of destabilised wave numbers, around $\beta = 2250m^{-1}$, does not quite reach as high as the 10% case, $\beta = 2500m^{-1}$. This could be due to being in a thicker region of the boundary layer, since we are further downstream, meaning the step height is comparatively smaller when the step is scaled with the local boundary layer thickness.

Comparing through all backward facing step heights, figure 7.21, we can see that the point of separation between the second and third stable zones is dictated by the length of the laminar separation. When decreasing the backward facing step depth, the size of the separation bubble becomes shorter and so the end of the second unstable region moves further upstream, along with the beginning of the third region. This therefore may well be related to a Kelvin-Helmholtz type inviscid instability due to the inflectional nature of the boundary layer profile, existing as a consequence of the LSB. Most cases tend to behave similarly except for the smallest step height. For the stationary CFI 20% chord smallest step height we can observe an unstable region in the lower wave number range, $\beta = 100m^{-1}$ to $\beta = 500m^{-1}$ immediately after the step. This narrows to as little as 200 to 300 before the upper branch rapidly increases up to $\beta = 1250m^{-1}$. For both the 10 % and 20% travelling cases there is no small boomerang shaped stable region present in the reverse flow region for the smallest step height. The range of destabilised wave numbers is also much smaller after the step location.

We have already established that the PSE and PSEh will fail to capture the effect of the BFS, hence the PSE results will not be exhibited hereafter. Although it is pertinent to point out that the PSE results do not seem to be behaving outlandishly incorrectly since they are identifying the most unstable wave numbers to exist in the lower range. We expect lower wave numbers to become more amplified due to the thickening of the boundary layer caused by the BFS[67]. The PSE has still been used to identify dangerous modes to perform LHNS computations and supply the radiation conditions required in the LHNS outflow plane.

LHNS and LHNSh computations for stationary and travelling CFI are shown in figures 7.22 and 7.23 for all BFS heights. Typically we use around 9000 points in the stream-wise direction and 51 Chebyshev polynomials in the normal direction. Surprisingly, both codes seem to predict a stabilisation for the CFI compared with the clean case. Similar to the FFS, we see the travelling CFI is much more dangerous than the stationary, growing 10 times that of the equivalent stationary most amplified instabil-

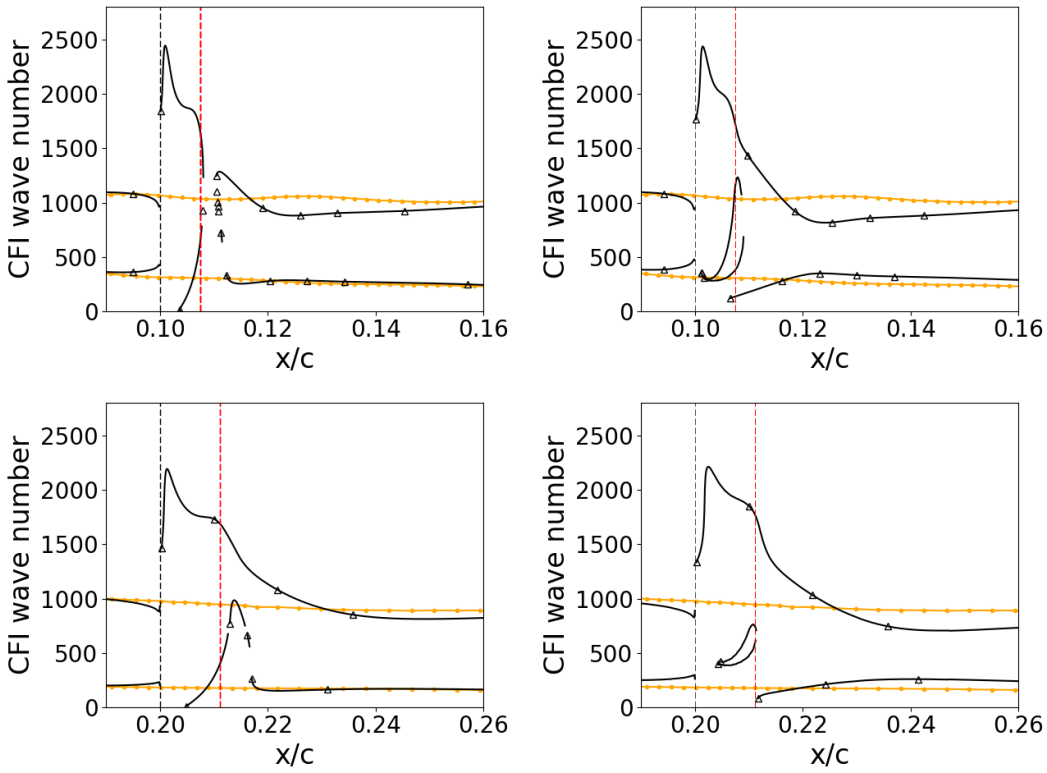

Figure 7.20: Neutral Stability Curves for the clean (yellow points) and BFS largest depth step case (black triangles). Top row denotes the 10% chord location, bottom row denotes 20% chord location. Left for stationary crossflow, Right for travelling crossflow: clean frequency at 420Hz, 10% BFS at frequency 360Hz and 20% BFS at frequency 450Hz. The dashed black line denotes the step location and the dashed red line denotes the start of the separation bubble.

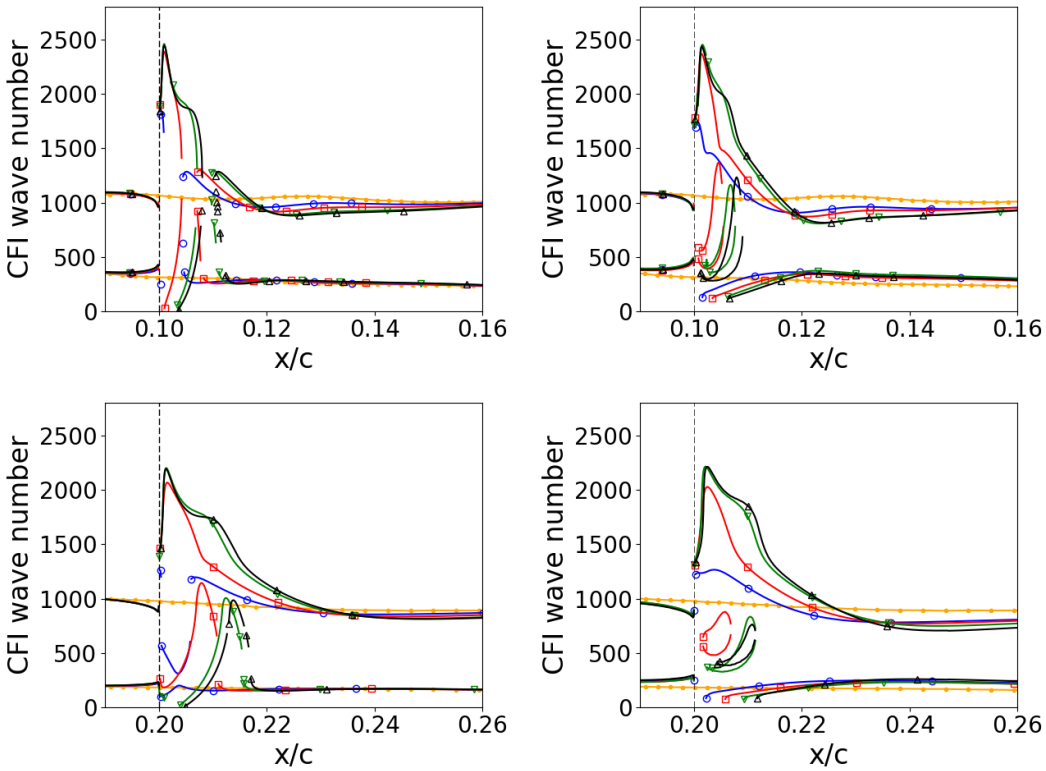

Figure 7.21: Neutral Stability Curves for all BFS heights. Yellow points denote the clean geometry, blue circles for 412.5 microns, red squares for 618.7, green downward pointing triangles for 825 and black upward pointing triangles for 893 microns. Top row denotes the 10% chord location, bottom row denotes 20% chord location. Left for stationary crossflow, Right for travelling crossflow: clean frequency at 420Hz, 10% BFS at frequency 490Hz, 360Hz, 470Hz and 360Hz for step heights 412.5, 618.7, 825 and 893 respectively and 20% BFS at frequency 440Hz, 350Hz, 510Hz and 450Hz. The dashed black line denotes the step location.

ity. The trend for the LHNS calculation is not clear. Some larger depth cases do not stabilise as much as some shorter depth cases and the growth predictions appear to be quite haphazard with how amplified the CFI becomes. This suggests the roughness height correction terms, which are missing from the LHNS equations, may hold quite some weight with respect to capturing the growth of the instability over this region. The largest step height seems to be the only case which doesn't show a stabilisation, which we also see in the LHNSh code. We initially thought this might be due to a noisy, inaccurately computed base flow profile, however we do not see the same trend in the travelling cases which utilise the same baseflow. As a result we do not yet have an explanation for this predicted result of amplitude growth.

From the LHNSh solutions, 7.23, we can see as the depth of the BFS is increased the stabilisation is increased, which seems contrary to the wider literature. The BFS has generally been shown to move the transition front forward in experimental works [67,95,25]. This is generally presumed as a consequence of 2D LSB analysis. It is clearly an open question, in view of the fact that few theoretical works have been undertaken on 2.5D swept wing boundary layers in the presence of LSBs, whether stabilisation may also be possible. In support to our findings, this stabilisation has been observed by Balakumar et al. [8] who conducted numerical investigations into FFSs and BFSs on a 30° swept wing. The heights of the steps varied between a third to a full boundary layer thickness and the flow regime was supersonic. They applied PSE to track the growth rates of CFI and found that all step heights provided a stabilising effect to both stationary and travelling waves, so much so that the amplitude of the CFI was decreased by 50% compared to the clean case at the transition location. They also observed increased stability with increased step depth, as we do in our simulations, and found that higher wave numbers were more stabilising than lower wave numbers. The use of the PSE in their case is somewhat more justified than in our computations since the PSE are able to resolve smaller stream-wise step sizes in supersonic flow. We are aware that the flow regime of Balakumar et al. [8] is very different to ours but it is reassuring that they have also observed a stabilisation. Eppink [25] ran extensive hot-wire investigations into backward facing steps placed on a swept flat plate. A pressure body is used to create a pressure field simulating an infinite swept wing. A delay in the transition location was observed for the smallest step height, suggesting a stabilisation. However, Eppink indicates this is contrary to other works and could be due to various other effects such as inconsistency in the naphthalene coating. Eppink et al. [31] exhibit amplitude and N-factor plots for the BFS with stationary CFI. For the large DREs case we can see a growth in amplitude over the reverse flow region followed a stabilisation upon one to two lengths of the reverse flow region downstream, around 20% of the plate. This occurs for all step heights with DREs present for the shorter

wavelength crossflow. Upon further private discussion with Eppink over these plots, it seems transition occurs shortly after the data points finish, which is attributed to the presence of travelling modes.

Turning now to the work of Saeed and Morrison[81], who looked at the effect of bumps on CFI and upon which this work is most similar to. Saeed and Morrison[81] observed that for their most upstream located bump profile, 3% chord, they could not detect a stationary CFI structure at 25% chord for bump heights larger than the second tallest bump. They do however, observe a sharp increase in unsteady disturbance amplitude after the second tallest bump. We suspect, from these results and the BFS work by Eppink et al.[31], that our 10% chord located BFS immediately initiates a highly non-linear mechanism for all step heights which cannot be captured by the linear analysis undertaken, and thus requires fully non-linear lines of enquiry. Should this theory be correct, then our results could be consistent with the wider literature, whereby the BFS initiates much more dangerous destabilisation mechanisms than the FFS.

The difference in amplitude predicted by both the LHNS and LHNSh are highlighted for the largest step height in figure 7.24. In the neighbourhood of the step we can see an opposite trajectory predicted by both codes. The LHNS predicts a short growth and then decay, whereas the LHNSh predicts a short decay and then growth. We know that the LHNSh models the step region more correctly, thus the LHNS result is clearly erroneous in the neighbourhood of the step. Beyond the step however, it is possible by a simple rescaling of the LHNS derived result, for it to be made to match precisely onto the LHNSh result downstream of the step.

Results for the 20% chord BFS are exhibited in figures 7.25 and 7.26. The general trend for the LHNS results, as step height is increased, is for further stabilisation to occur. For the LHNSh equations the stabilisation is still there but is much reduced, similar to what was observed for the 20% chord case. The trend in each scenario is not clear. This could be simply due to the variety in most unstable wave number and frequency combinations. In this case it would be worth while conducting comparisons with fixed wave number and frequency across all cases, even at the consequence of not remaining the most unstable mode for all cases.

To compare all step height configurations for travelling and stationary crossflow, the amplitude at 10% after the roughness location is plotted against the height of the non-dimensional roughness, as stated in table 7.1, see figure 7.27. For the 10% roughness the reference point is 20% and for the 20% roughness the reference point is 30%. The $|\hat{u}|$ amplitude is scaled with the edge velocity at the measurement location (either 20% or 30% chord). It is clear to see that the general trend is to predict a stabilisation of disturbances.

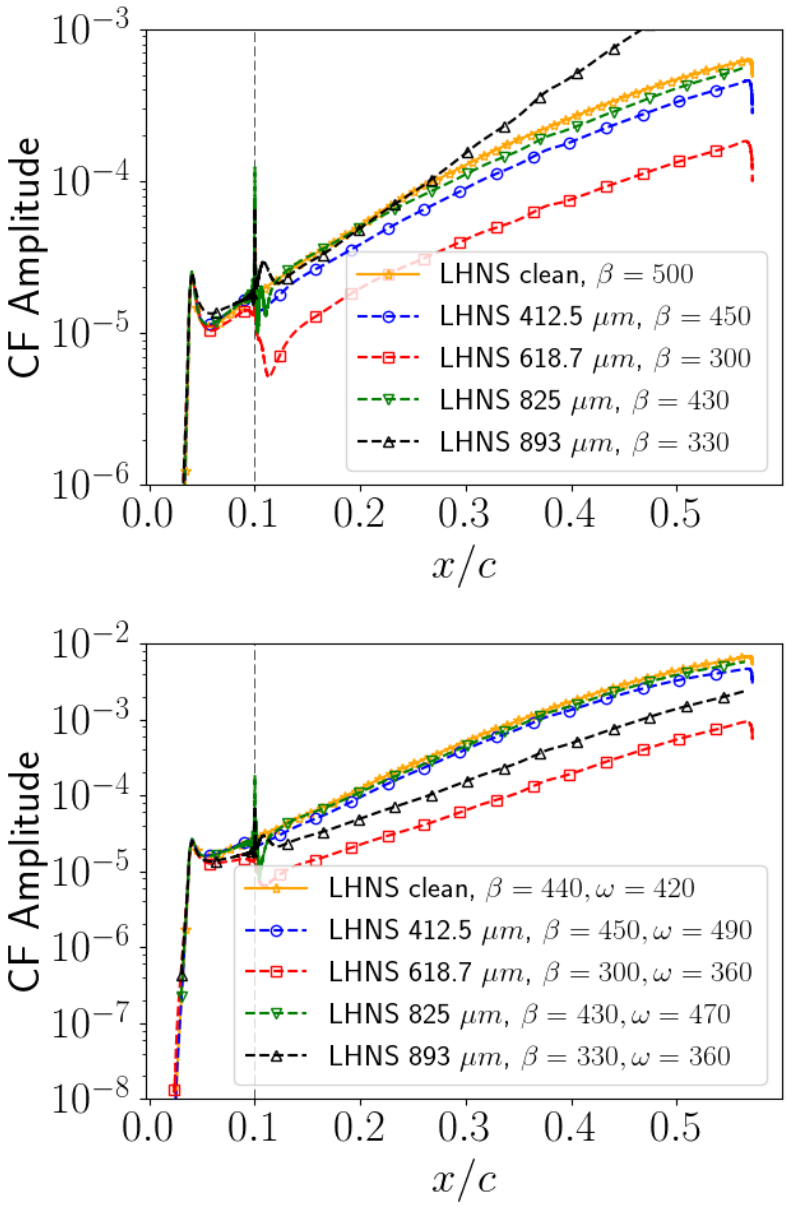

Figure 7.22: LHNS calculation for BFS at 10% chord: Comparison of most destabilizing CFI for all roughness heights. Red for 412.5 microns, blue for 618.7, green for 825 and black for 893 microns. Top: Stationary CFI. Bottom: Travelling CFI. The dashed vertical line denotes the BFS location. Units of the span-wise wave number β are m^{-1} and the frequency ω is given in Hz.

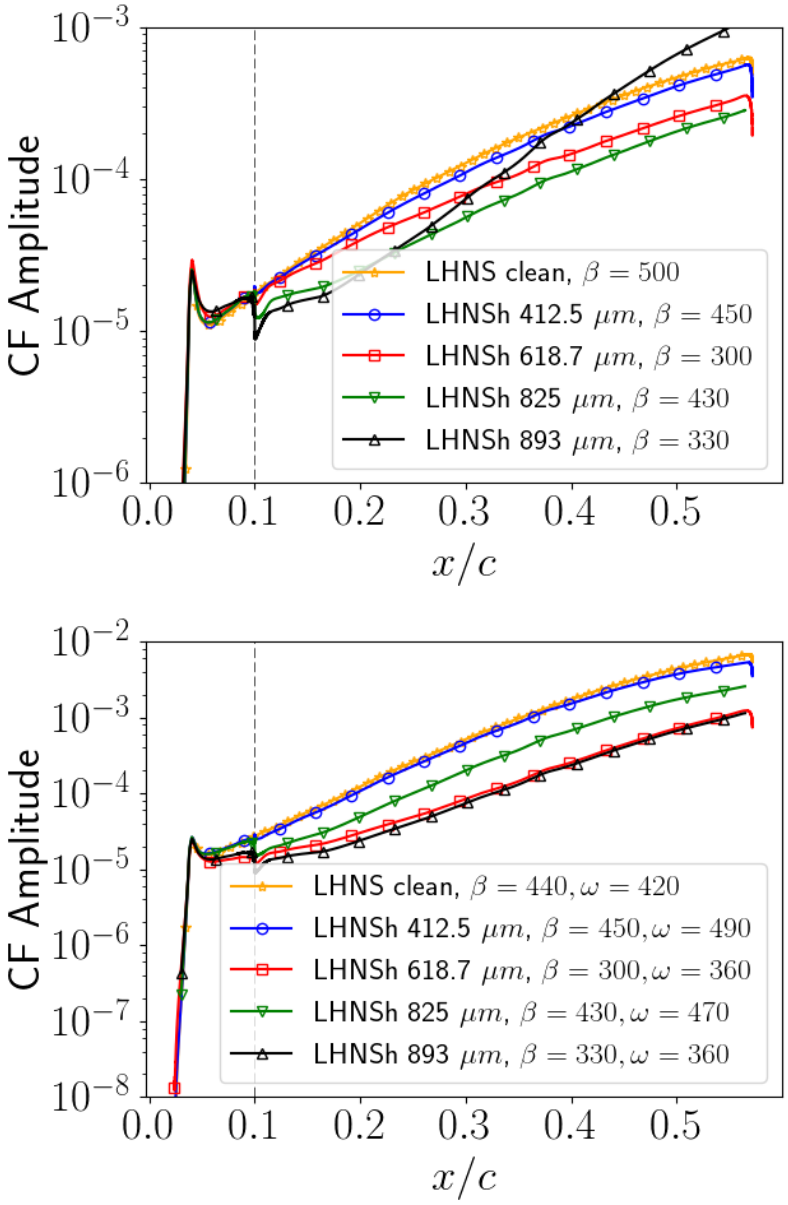

Figure 7.23: LHNSh calculation for BFS at 10% chord: Comparison of most destabilizing CFI for all roughness heights. Red for 412.5 microns, blue for 618.7, green for 825 and black for 893 microns. Top: Stationary CFI. Bottom: Travelling CFI. The dashed vertical line denotes the BFS location. Units of the span-wise wave number β are m^{-1} and the frequency ω is given in Hz.

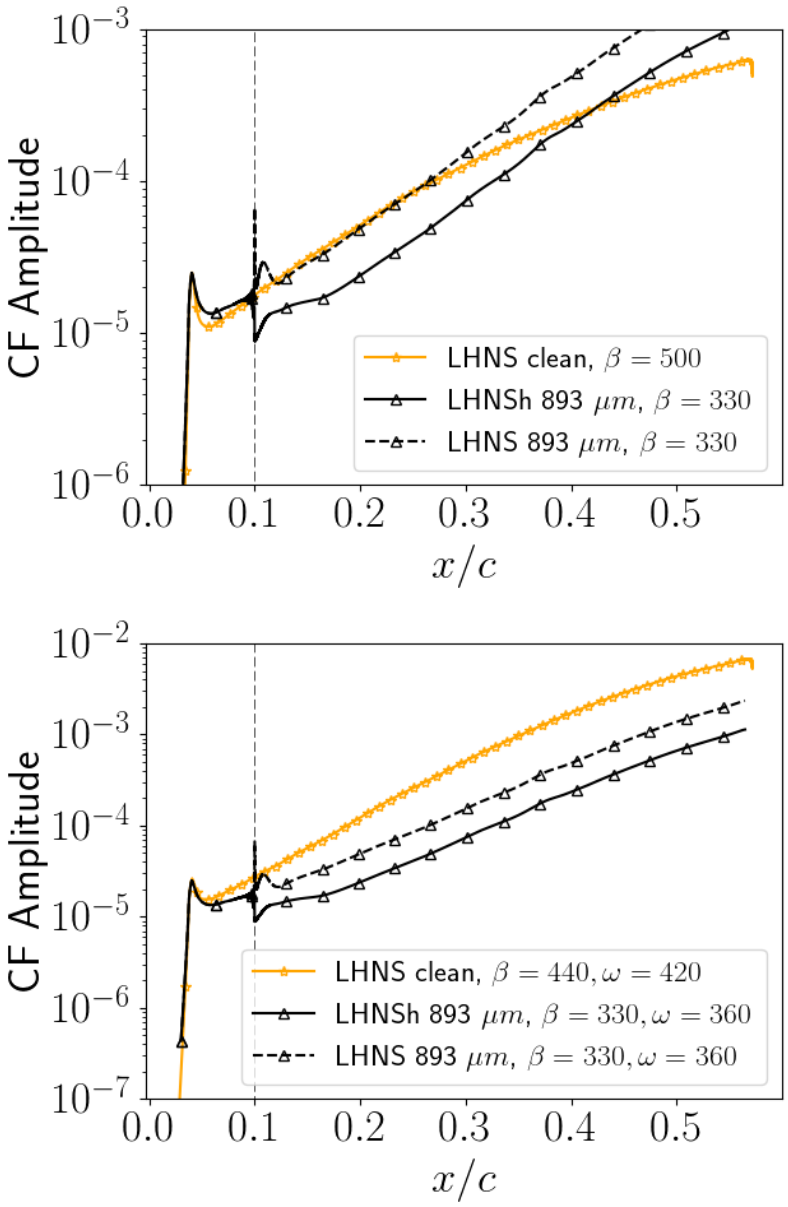

Figure 7.24: BFS at 10% chord with height of 893 microns: LNSh (solid lines) and LNS(dashed lines) comparison of crossflow instability. Top: Stationary CFI. Bottom: Travelling CFI. The dashed vertical line denotes the BFS location. Units of the span-wise wave number β are m^{-1} and the frequency ω is given in Hz.

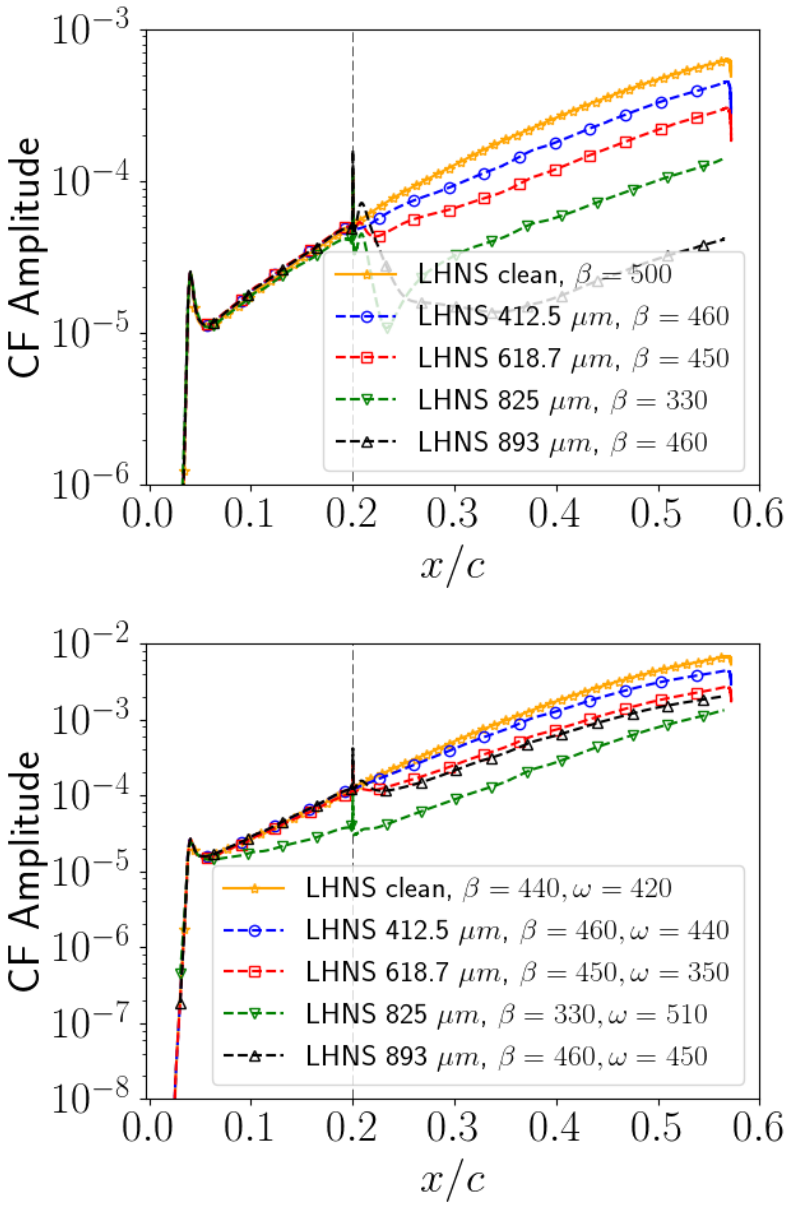

Figure 7.25: LHNS calculation for BFS at 10% chord: Comparison of most destabilizing CFI for all roughness heights. Red for 412.5 microns, blue for 618.7, green for 825 and black for 893 microns. Top: Stationary CFI. Bottom: Travelling CFI. The dashed vertical line denotes the BFS location. Units of the span-wise wave number β are m^{-1} and the frequency ω is given in Hz.

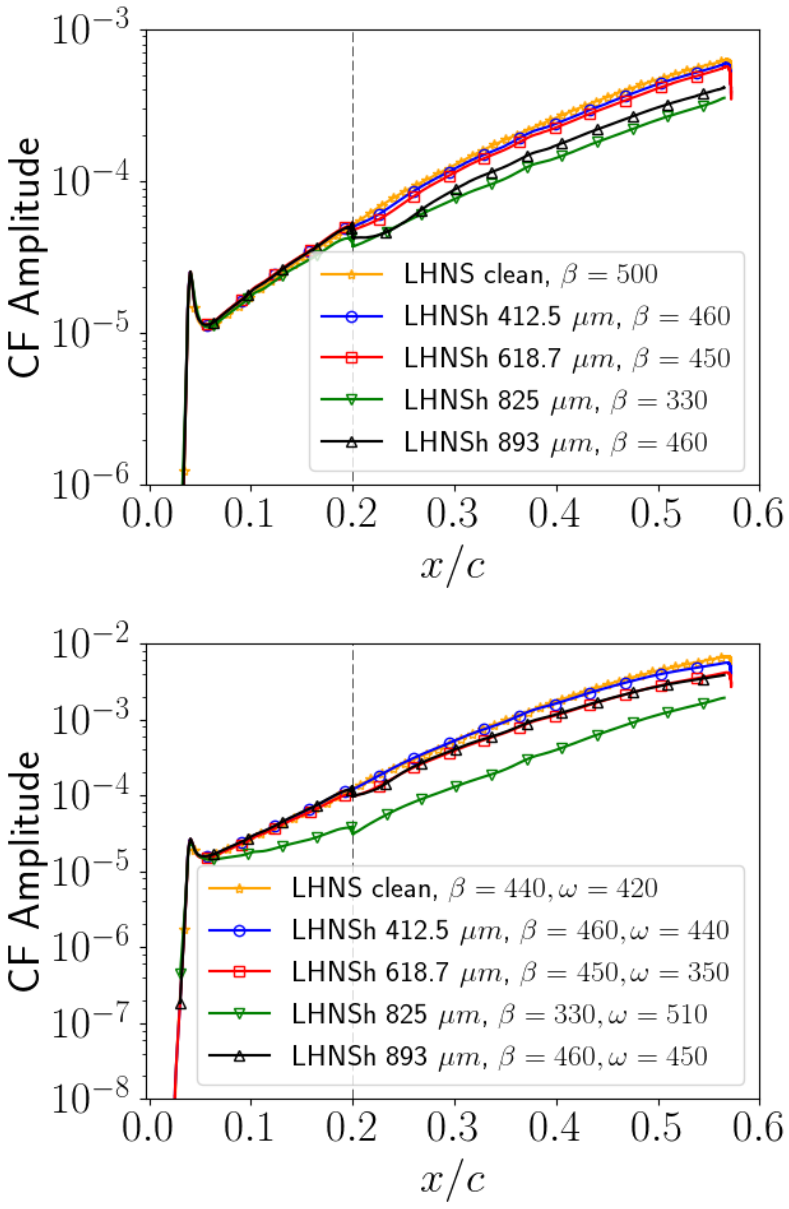

Figure 7.26: LHNSh calculation for BFS at 10% chord: Comparison of most destabilizing CFI for all roughness heights. Red for 412.5 microns, blue for 618.7, green for 825 and black for 893 microns. Top: Stationary CFI. Bottom: Travelling CFI. The dashed vertical line denotes the BFS location. Units of the span-wise wave number β are m^{-1} and the frequency ω is given in Hz.

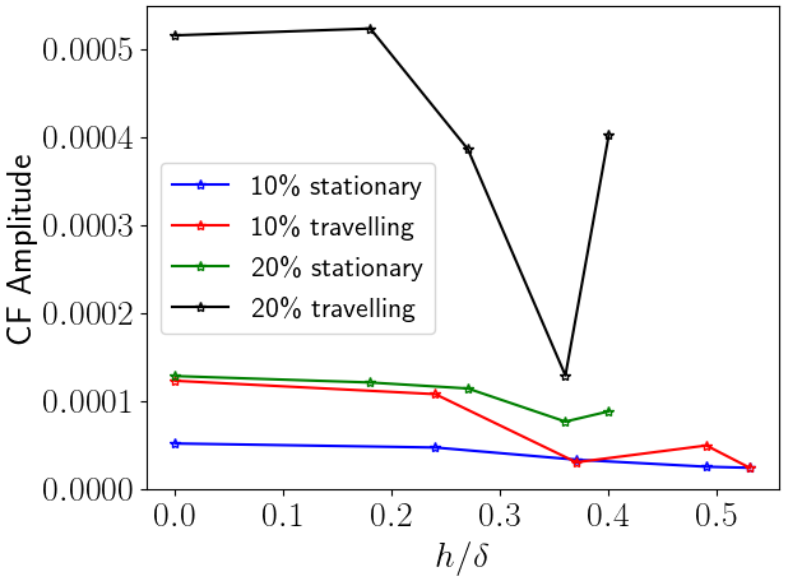

Figure 7.27: BFS LNSHh calculations for most destabilising stationary and travelling CFI for all step heights and locations. Amplitude measurements are taken 10% after each respective roughness location (20% chord for the 10% chord BFS and 30% chord for the 20% chord BFS) and normalised with the edge velocity at the corresponding 10% downstream locations.

Contour plots of the stream-wise perturbation field for the largest step height are depicted in figure 7.28. We can see the perturbation is clearly convecting over the separation bubble, never extending into it. The 10% chord cases seem to fold back to the wall quite rapidly, whereas the 20% cases remain lifted away from the wall for a longer distance downstream. If we adjust the velocity scale on the stationary 20% case we can see there exist multiple maxima and minima of $\hat{u}$ for some stations in the neighbourhood of the reverse flow region, see figure 7.29. Some noise within the contour field can be seen at the step location, giving an indication that the solutions are not resolved well enough, possibly due to noisiness in the extracted steady base flow field variables. Another aspect the reader should bear in mind, is that the plotting tool uses spline fitting, and due to the very rapid variations at the step junction interface, the slight jaggedness is most likely due to overshoots arising from splining in the contouring and colour shading algorithms (Python libraries).

Perturbed velocity profiles at locations close to and just downstream of the step are given in figure 7.30. From the two locations just after the step, we can see a small inflection point in the $\hat{w}$ profile and some similarity in the $\hat{v}$ perturbation field compared with the numerical and experimental study by Tufts et al.[95], who studied the effect of FFSs and BFSs on CFI.

Given the linear stability analysis undertaken in this section the results indicate that the BFS acts as a stabiliser. This is contrary to the literature of BFSs acting as an

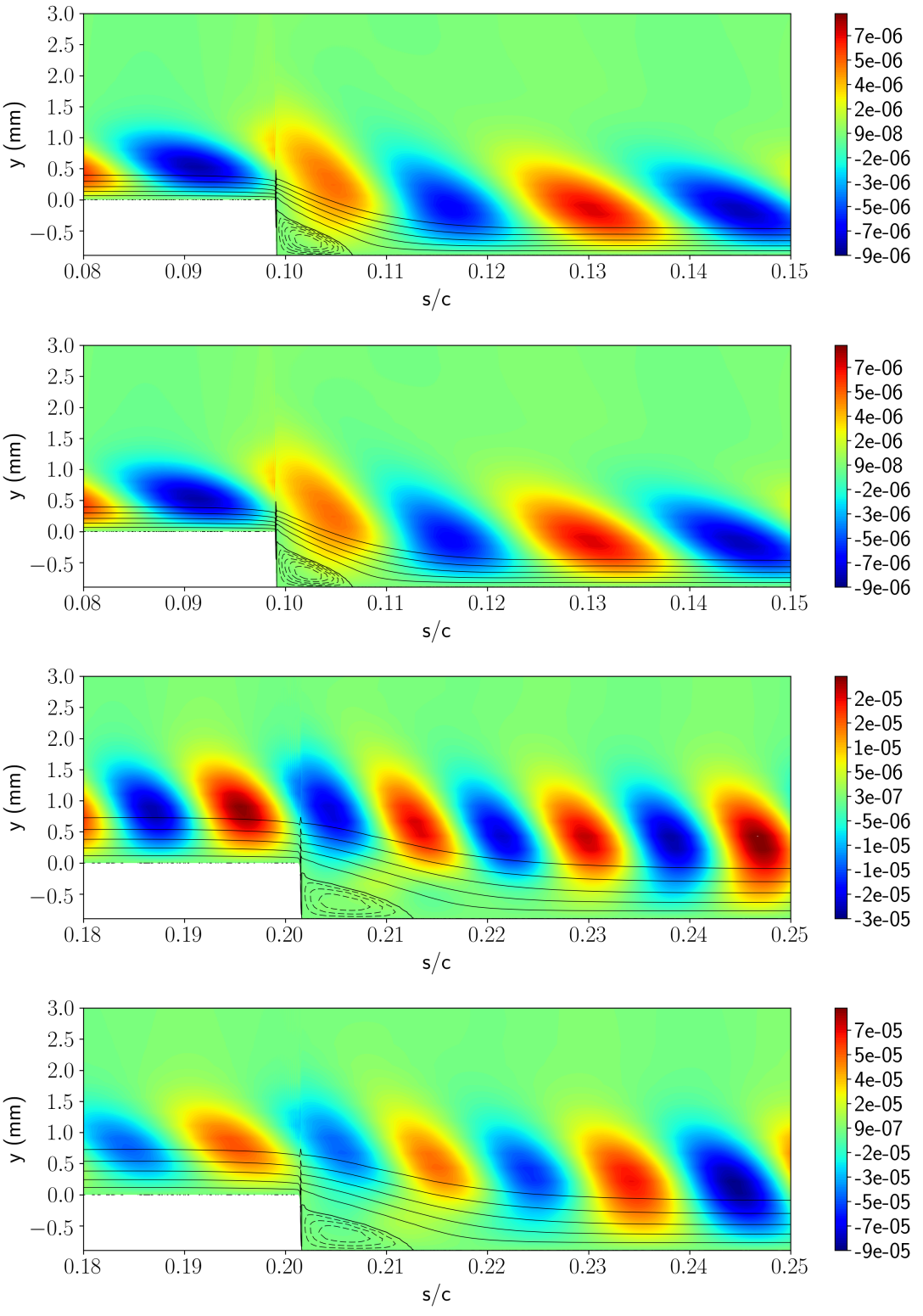

Figure 7.28: Stream-wise perturbation field, $|\hat{u}|$, for 893 micron BFS at 10% and 20% chord. Top: LHNSh 10% chord stationary case, $\beta = 330m^{-1}$. Second: LHNSh 10% chord travelling case, $\beta = 330m^{-1}$, $\omega = 360Hz$. Third: LHNSh 20% chord stationary case, $\beta = 460m^{-1}$. Bottom: LHNSh 20% chord travelling case, $\beta = 460m^{-1}$, $\omega = 450Hz$.

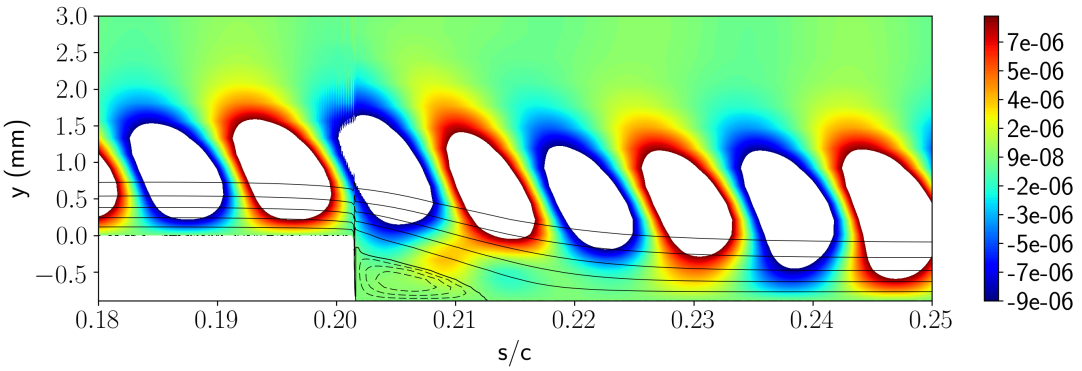

Figure 7.29: Stream-wise perturbation field, $|\hat{u}|$, for 893 micron BFS 20% chord with stationary cross-flow, $\beta = 460$. Scale is modified to see extra maxima/minima in $|\hat{u}|$.

amplifier mechanism through destabilising oscillator dynamics induced by the presence of LSBs. However much of these inferences have been drawn from detailed analysis of 2D LSBs. Destabilisation dynamics of 2.5D LSBs is as yet a topic not investigated in detail to our knowledge. In fact this was a reasoning for the research undertaken in this thesis. There is also the aspect that the observed experimental behaviour indicates that as the step height is increased the transition front does move towards the step location itself, once some step height amplitude threshold is reached. It could be, in all likelihood, that the processes involved are inherently non-linear. Certainly the present analysis, from this current limited study, suggests that a major flow destabilisation of BFSs does not arise through linear mechanisms.

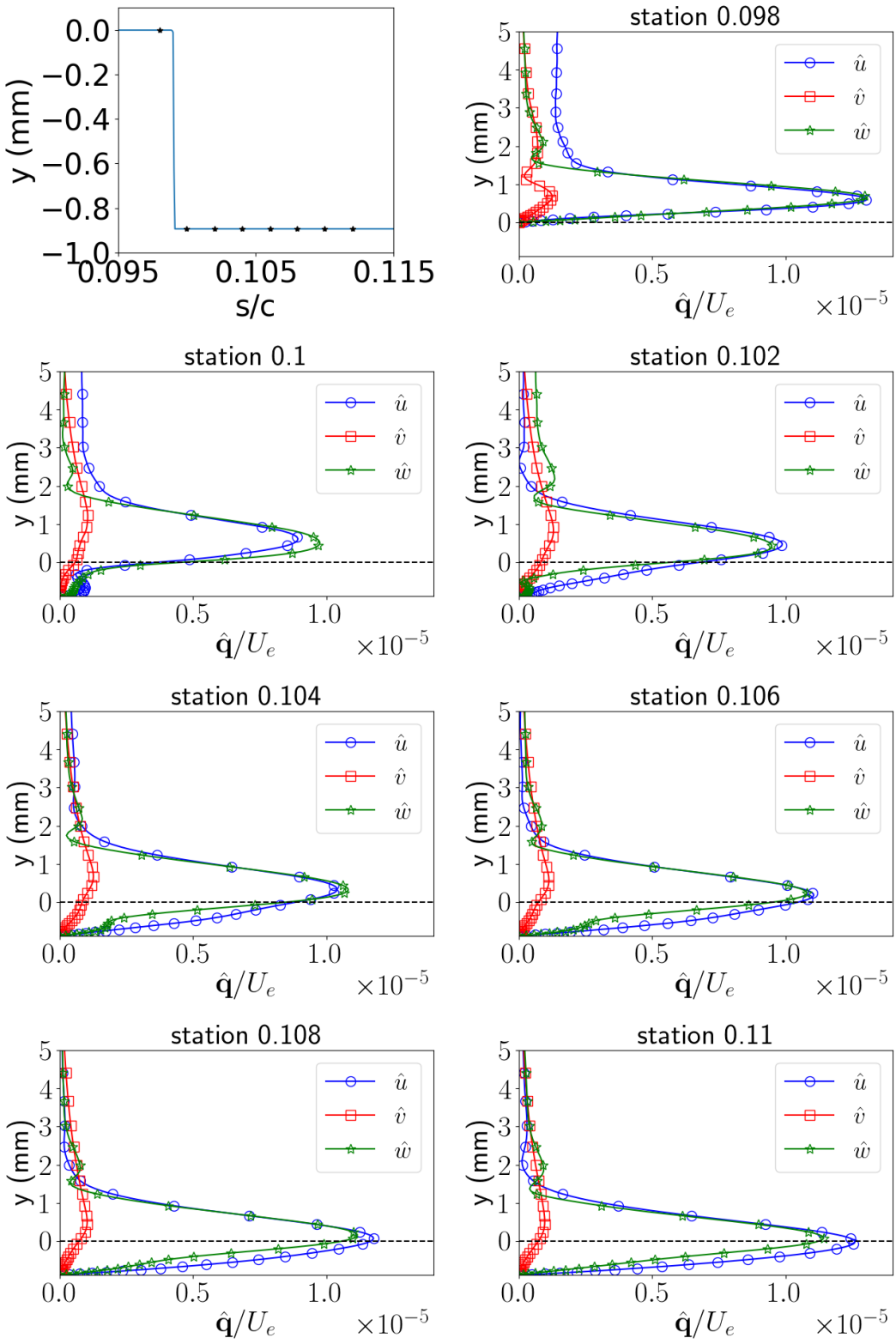

Figure 7.30: 10% chord largest BFS height with stationary CFI: LHNSh generated velocity profiles generated at a range of stations. The plot in the top left hand corner marks the stations at which the profiles are evaluated. The dashed horizontal line marks the step height.

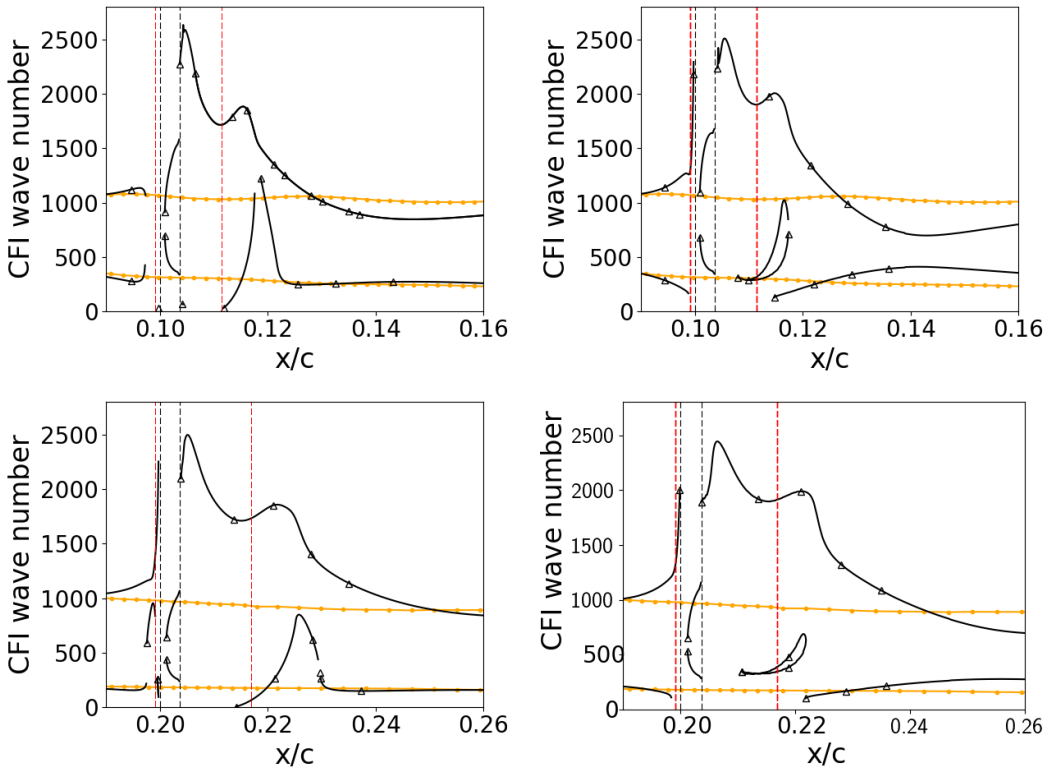

Figure 7.31: Neutral Stability Curves for the clean (yellow points) and bump largest height case (black triangles). Top row denotes the 10% chord location, bottom row denotes 20% chord location. Left for stationary crossflow, Right for travelling crossflow: clean frequency at 420Hz, 10% bump at frequency 550Hz and 20% bump at frequency 540Hz. The dashed red line denotes the start of the separation bubble and the dashed black line denotes the step location.

7.4 Bump Stability Analysis

Neutral curves are computed with linear stability theory for the largest bump height at 10% and 20% chord and compared with the clean, see figure 7.31. Features from both the FFS and BFS neutral curves can be clearly seen in the bump neutral curves. Once again the two reverse flow regions seem to be a trigger for destabilising a much larger range of wave numbers. Comparing this figure with the FFS largest bump height neutral curves, figure 7.8, we can see that the neutral curve looks identical upstream of the step for all cases except the travelling CF 10% chord case. For this particular case the upper branch drops down to the lower branch before dramatically increasing again to as high as β =2300m^{-1}. We do not observe this in the 10% bump travelling case where the upper branch immediately lifts up to β =2300 m^{-1}. Just after the FFS, now located at the top of the bump, the neutral curve begins to diverge again, as we saw for the FFS cases. However, in the bump case the upper branch moves straight up to β =1600. We do not observe any short convergence to the clean case and second rise as we did in the 10% FFS stationary case. When we reach 10.375% chord we hit the BFS component and the upper neutral curve immediately jumps up to around β =2500m^{-1}

for most cases, except the 10% chord stationary case which reaches β =2600m^{-1}. All of the bump case upper branches reach a higher range of unstable wave numbers arising from the BFS component relative to that observed in the pure BFS case, see figure 7.8. We also observe the lower neutral branch goes to zero number wave numbers. In the pure BFS stationary cases we observed the returning of the lower branch about midway though the separation bubble and either converging to the upper branch at reattachment, for the 10% case, or attempting to merge to the upper branch just after reattachment, for the 20% chord case. In the bump stationary case we do not see the lower branch reappear until further downstream at the reattachment point. The rise of the lower branch to upper branch is then also delayed by almost another separation bubble length. For the 10% bump stationary case we do not see a merging of the upper and lower branch as we did in the pure BFS case. Another observation is that an increase in the upper branch destabilised wave numbers is observed after reattachment in all bump cases, this feature is not present in the pure BFS case.

For the travelling CFI cases we can also see the presence of this small boomerang shaped stable region around $\beta = 500m^{-1}$, although it now seems to be located downstream of the separated region, contrary to the pure BFS case. For the travelling CF cases we also observe much more overshooting of the neutral curves relative to the clean case downstream. Their convergence to the clean neutral curve doesn't occur until much further downstream, about 10% of a chord length behind the step location. Generally, the conjugation of the FFS and BFS constructing the bump roughness appears to be more detrimental to the range of destabilised wave numbers downstream of the large recirculation reattachment.

All bump height neutral stability curves are compared in figure 7.32. Generally for all step heights the 10% chord case destabilises a larger range of wave numbers over the bump, between the solid dashed black lines, compared to the 20% chord case. As we walk down through the step heights we can see the larger two heights feature very similar neutral curve shapes. When we progress to the second smallest step height the main difference is that the upper branch second peak, located about 10% chord downstream of the bump, is no longer present and the shape looks more like that of the pure BFS case. As we move to the smallest height we see that the neutral curve has changed significantly. For the stationary 10% bump we see that immediately after the BFS component is an unstable region ranging from β =500m^{-1} to β =2400m^{-1}. The upper and lower branches merge about one bump length downstream, a brief moment of stability follows, before the fourth unstable region starts around 10.7% chord in the lower range parameter space, β =500m^{-1} to β =1500m^{-1}. The 20% chord case however, seems to have a small region of instability in the low wave number ranges, β =100m^{-1} to β =500m^{-1}, directly after the BFS component. The fourth unstable

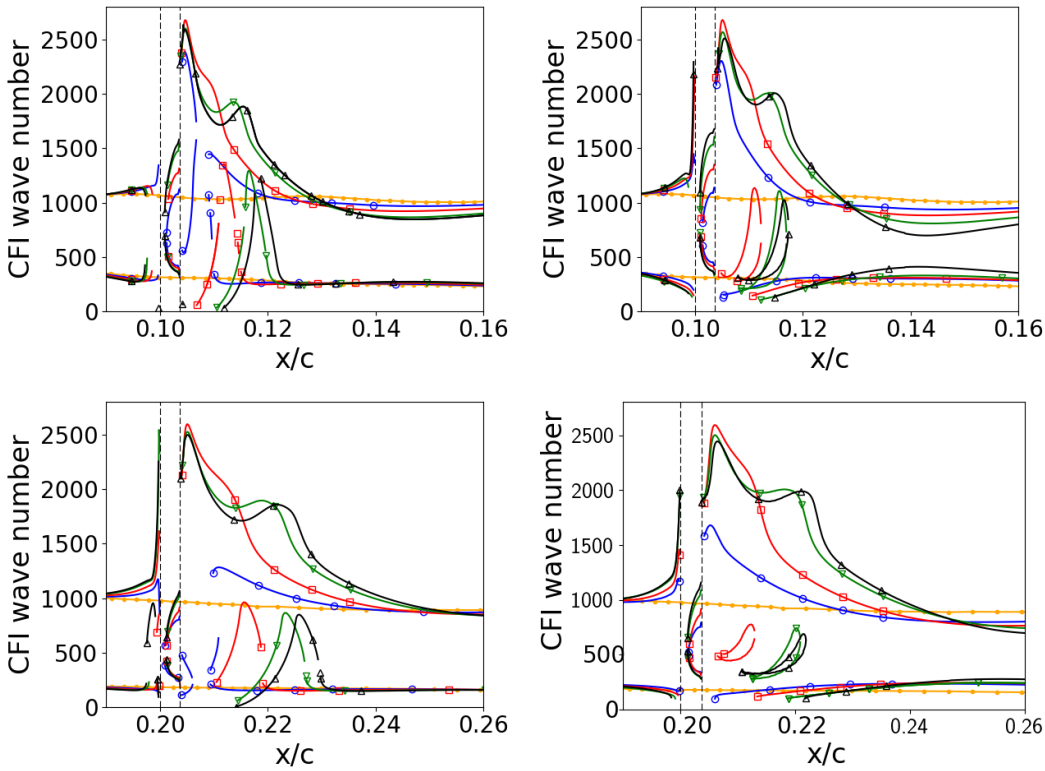

Figure 7.32: Neutral Stability Curves for all bump heights. Yellow points denote the clean geometry, blue circles for 412.5 microns, red squares for 618.7, green downward pointing triangles for 825 and black upward pointing triangles for 893 microns. Top row denotes the 10% chord location, bottom row denotes 20% chord location. Left for stationary crossflow, Right for travelling crossflow: clean frequency at 420Hz, 10% bump at frequency 380Hz, 340Hz, 330Hz and 550Hz for step heights 412.5, 618.7, 825 and 893 respectively and 20% bump at frequency 460Hz, 460Hz, 420Hz and 540Hz. The dashed black lines denote the bump beginning and end location.

region then begins shortly downstream. For the travelling cases, the 20% chord case only destabilised wave numbers as large as β =1700m^{-1} whereas the 10% chord case ranges up to $\beta = 2400m^{-1}$. There is also no brief boomerang shaped region of stability for both locations, or if there is, it is too short to be of relevance.

Once again the PSE and PSEh computations fail to capture the presence of the bump reliably due to the aforementioned reasons. The PSE is still utilised to find the most destabilising CFI wavelength and frequency to provide outflow boundary conditions to the LHNS and LHNSh equations. The problem of having to ignore stations with large stream-wise fluctuations is only exacerbated by the bump. Instead of there only being one vertical edge, as with the FFS and BFS, there are now two sides to the bump. This means we could have an event where a station along one edge of the bump is taken, but not its corresponding other edge, resulting in a positive dh/ds term in one instance but its corresponding negative contribution not being captured in the PSE computation. This should be kept in mind when evaluating wave numbers and frequencies identified as the most unstable for computation with the LHNS and

LHNSh equations.

LHNS and LHNSh computations for stationary and travelling CFI are shown in figures 7.33 and 7.34 for all bump heights at 10% chord. Typically we use around 8000 points in the stream-wise direction and 51 Chebyshev polynomials in the normal direction to achieve mesh independent solutions. Increasing the Chebyshev polynomials in the wall direction, did not alter the results to graphical accuracy. The LHNS solutions for the growth of shortest and tallest bump seem reasonable but the heights in between do not quite follow the trend of a taller bump causing more amplification to the CFI. The LHNSh solutions are generally consistent with the literature for stationary CFI, where increased step height triggers greater amplification of disturbances [27,95,69]. LHNSh predicts an even larger growth of disturbances for all bump heights larger than 618.7 microns, in comparison to the LHNS formulation. The 412.5 micron case gives a similar result to the clean case for both LHNS and LHNSh codes, showing the smallest bump height does not have any overall effect on the growth of the CFI, this is in agreement with observations in the experimental work of Saeed et al. [82]. According to the LHNSh, the next step height, 618.7 microns, also predicts no overall difference to the clean case. As the bump height increases further we begin to see an increased forward movement in transition. The LHNS model seems to predict more amplification of CFI for the 618.7 micron case than the 825 micron case, which seems very unlikely. Given the differences between the two LHNS / LHNSh solutions we are led to conclude that the LHNS formulation neglects some crucial role of the perturbed u_s field locally at the bump geometry change. Looking at the travelling CFI curves, there is a similar trend to the results as for the stationary case but the growth is amplified ten times that of the stationary crossflow. It is noticeable that the clean case is more amplified than the smaller bump heights in the LHNSh computations. We reason this is likely to be due to having used the PSE to find the most unstable CFI wave numbers. Since the PSE in unable to resolve the roughness region, the most unstable wave number it finds may not, truly, be the most unstable wave number. Our smallest bump height results compare well with the work of Saeed et al. [82] who found found that the smallest step height did not cause any forward movement of the transition front. We also however, observe that the second tallest height does not predict an increase in amplitude to the CFI, contrary to the experimental work. As the bump height increases we tend to see a decrease in the most unstable CFI wave number.

A direct comparison of the two codes for the largest bump case can be seen in figure 7.35. Here we can see the LHNSh code predicts a greater amplification of CFI than LHNS for both stationary and travelling CFI. Evaluating all heights, it would appear that if there was a critical bump height to cause transition, it must be located somewhere between 37% to 48% of the boundary layer thickness.

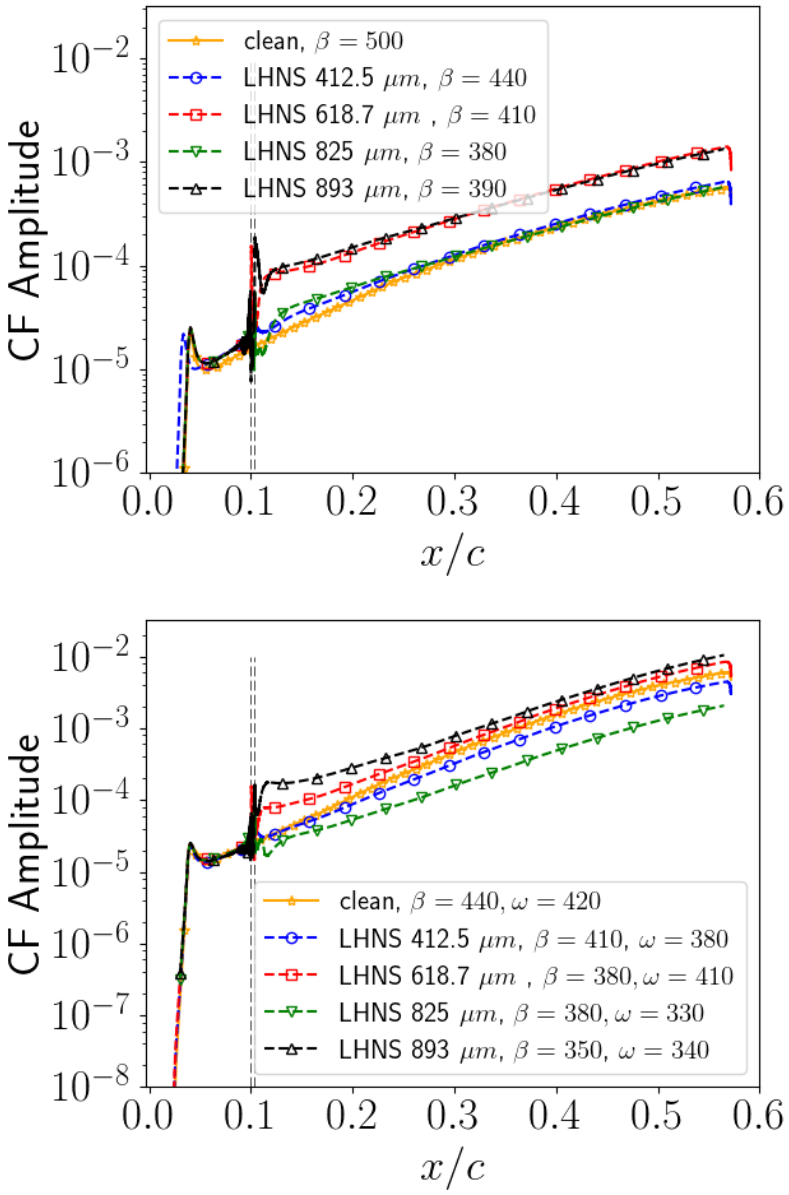

Figure 7.33: LHNS calculation for the bump at 10% chord: Comparison of most destabilizing CFI for all roughness heights. Red for 412.5 microns, blue for 618.7, green for 825 and black for 893 microns. Top: Stationary CFI. Bottom: Travelling CFI. Bump is located between the vertical dashed lines. Units of the span-wise wave number β are m^{-1} and the frequency ω is given in Hz.

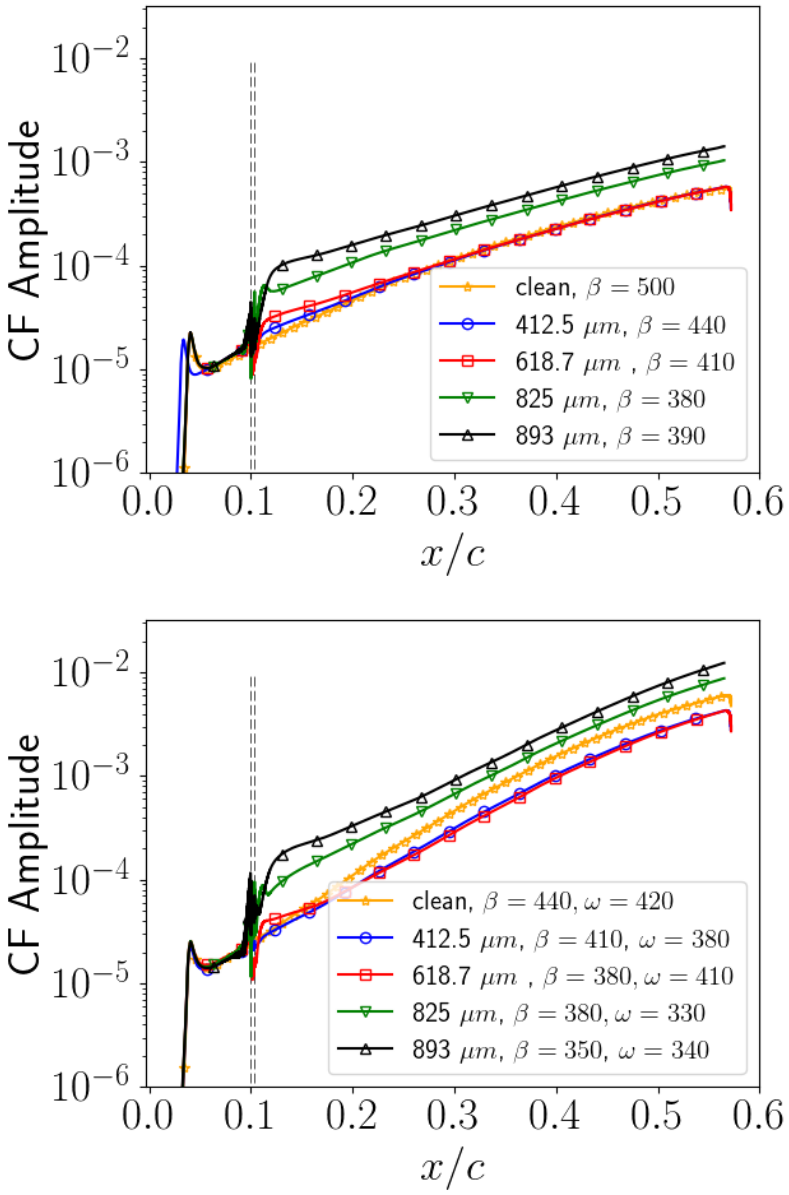

Figure 7.34: LHNSh calculation for the bump at 10% chord: Comparison of most destabilizing CFI for all roughness heights. Red for 412.5 microns, blue for 618.7, green for 825 and black for 893 microns. Top: Stationary CFI. Bottom: Travelling CFI. Bump is located between the vertical dashed lines. Units of the span-wise wave number β are m^{-1} and the frequency ω is given in Hz.

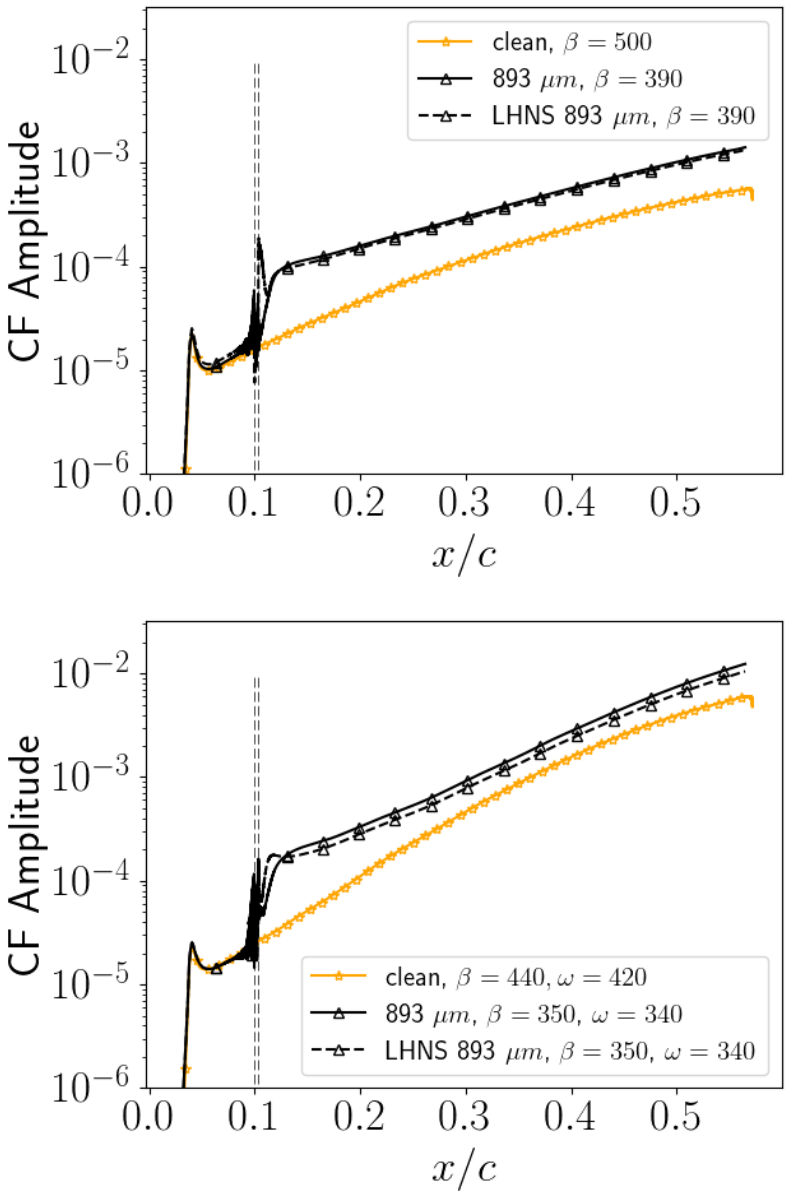

Figure 7.35: Bump at 10% chord with height of 893 microns: LHNSh (solid lines) and LHNS(dashed lines) comparison of crossflow instability. Top: Stationary CFI. Bottom: Traveling CFI. Units of the span-wise wave number β are m^{-1} and the frequency ω is given in Hz.

Looking at the 20% chord bump cases we can see that the LHNS code predicts a stabilisation to all bump heights, with increasing stability as the bump height is increased, see figures 7.36 and 7.37. This feature is very similar to what is observed in the BFS cases. However, when we solve the LHNSh equations the result is much more consistent with the literature. We see an increase in amplification to the CFI with increased bump height. The stationary CFI predicts a greater difference in amplitude growth for the largest bump case than for the travelling CFI, although the travelling case remains much more dangerous by an order of magnitude. The trend for the travelling case is slightly less clear but this could be attributed to utilising perhaps not the most dangerous wave number and frequency combination. We do observe that the most amplified modes, selected by the PSEh, at 20% chord have a longer wavelength than those at 10% chord, also observed by Saeed and Morrison [81]. Generally the results from the LHNSh code, predicting less amplification to the CFI when the step is placed further downstream, were observed in the experimental work [81]. Transition was observed by Saeed and Morrison [81] for lower step heights when the bump was placed further downstream, although the CFI underwent less amplification. They conclude that downstream located bumps have a lower critical height and that transition occurs though amplification of unsteady disturbances, also observed by Eppink et al. [31].

To compare all bump height configurations for travelling and stationary crossflow, the amplitude at 10% downstream of the roughness location is plotted against the height of the non-dimensional roughness, as stated in table 7.1, see figure 7.38. For the 10% roughness the reference point is 20% and for the 20% roughness the reference point is 30%. The $|\hat{u}|$ amplitude is scaled with the edge velocity at the measurement location (either 20% or 30% chord) and plotted against the height of the roughness, scaled with the boundary layer thickness at the excrescence location, as shown in table 7.1. We see that there is not much difference between the amplitude growth of the clean case and the first two bump heights, for the 10% chord. The larger two bump cases do cause an increased amplification to the CFI which is exacerbated with increased height. The 20% chord bumps do not show much growth from the clean case except for the largest bump case.

Saeed and Morrison [81] have constructed similar plots but all evaluated at 25% chord, for the 3%, 10% and 20% chord located bumps. We have also constructed a similar plot, see figure 7.39, where now we evaluate the disturbance amplitude at a 25% chord location for both 10% and 20% chord bump locations. Our stationary results compare relatively well with their experimental results, where there is no growth predicted for the first two bump heights, but we do see growth for the highest bump heights. Our travelling disturbance results do however, appear to be quite different. Saeed and Morrison [81] observe barely any change to any of the 10% chord placed bump heights

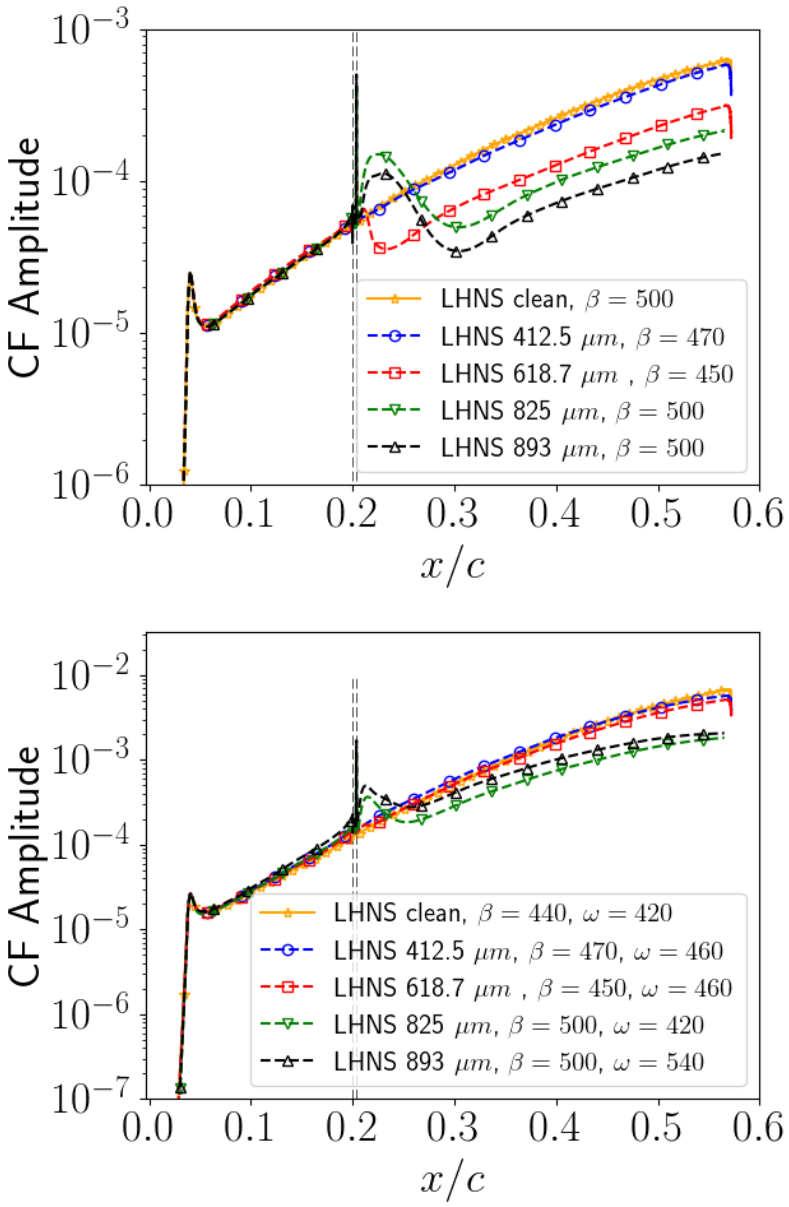

Figure 7.36: LHNS calculation for the bump at 20% chord: Comparison of most destabilizing CFI for all roughness heights. Red for 412.5 microns, blue for 618.7, green for 825 and black for 893 microns. Top: Stationary CFI. Bottom: Travelling CFI. Bump is located between the vertical dashed lines. Units of the span-wise wave number β are m^{-1} and the frequency ω is given in Hz.

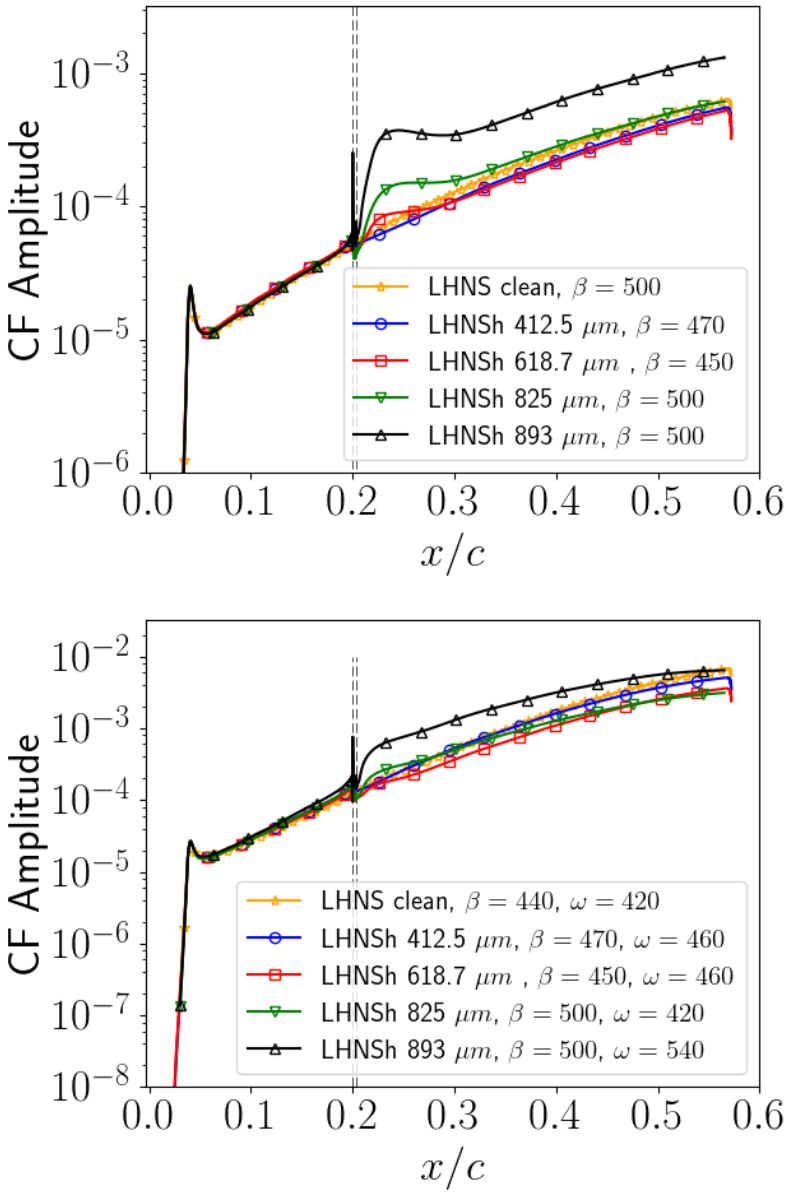

Figure 7.37: LHNSh calculation for the bump at 20% chord: Comparison of most destabilizing CFI for all roughness heights. Red for 412.5 microns, blue for 618.7, green for 825 and black for 893 microns. Top: Stationary CFI. Bottom: Travelling CFI. Bump is located between the vertical dashed lines. Units of the span-wise wave number β are m^{-1} and the frequency ω is given in Hz.

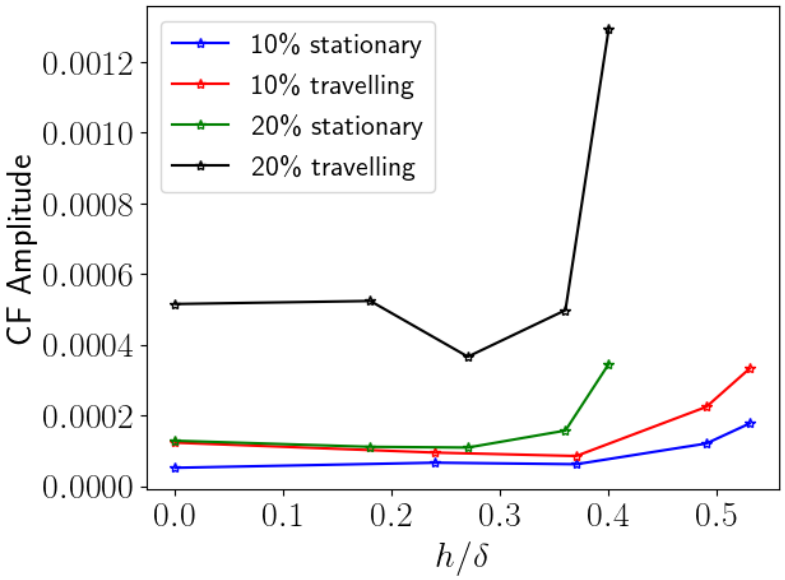

Figure 7.38: Bump LNSHh calculations for most destabilising stationary and travelling CFI for all step heights and locations. Amplitude measurements are taken 10% after each respective roughness location (20% chord for the 10% chord bump and 30% chord for the 20% chord bump) and normalised with the edge velocity at the corresponding 10% downstream locations.

and only in the 20% chord location do they see a slight rise in the unsteady amplitude caused by the taller two bump cases. We observe the same trend for the 20% chord case but the amplification is more significant and we also observe a significant increase in the 10% chord case, contrary to Saeed and Morrison [81]. Though it has to be remarked that the experimental findings may well have been clouded by the unknown free-stream tunnel environment. There is some uncertainty as to the precise nature of the unsteady forcing in the observed wind-tunnel measurements, whereas our LHNS simulations are of course modelled and forced by a precisely controllable theoretical scenario.

Contour plots of the stream-wise perturbation field for the largest bump height are depicted in figure 7.40. The 10% chord cases show the CFI clearly traversing over the separation bubble. Contrary to the BFS case the reverse flow region seems to be acting as a disturbance amplifier. Looking at the 20% chord cases the instability is much more amplified than the 10% cases. We can see the disturbance amplitude growing from the FFS corner of the bump. We see that the instability is no longer convecting over the laminar separation bubble but is also within it for the travelling 20% case. Also, just downstream of the upper corner, for the 20% chord cases, there is a region of reversed perturbation.

Perturbed velocity profiles are given in figure 7.41. For the $\hat{v}$ perturbation we observe a rise in the peak from the wall, station s/c =0.102, showing that the crossfow vortex has lifted up from the wall. Moving past the BFS, station s/c =0.104 and s/c =0.106,

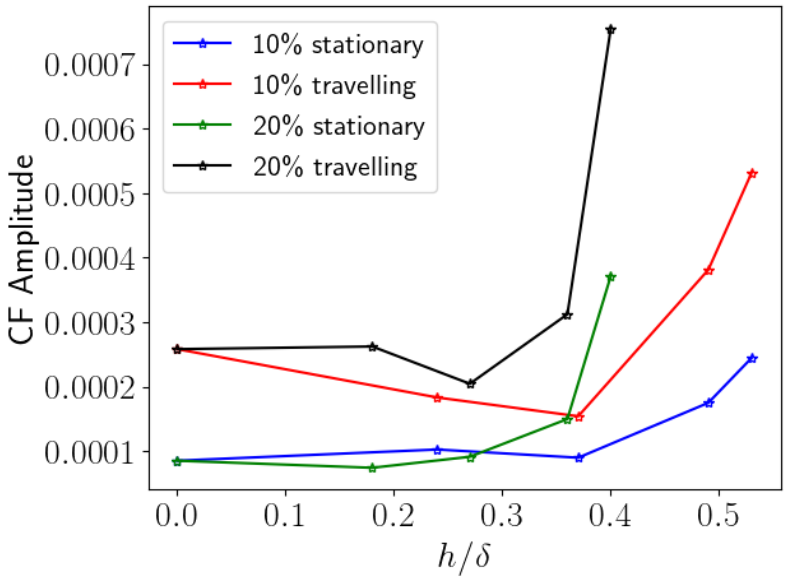

Figure 7.39: Bump LNSHh calculations for most destabilising stationary and travelling CFI for all step heights and locations. All amplitude measurements are taken at 25% chord and scaled with the edge velocity at this location.

we start to see a smaller maxima below the height of the bump, in the $\hat{w}$ component and also, although much smaller, in the $\hat{u}$ and $\hat{v}$ components. As we move further downstream this maxima, that is close to the wall, becomes larger. All of these CFV core heights are larger than any of the bump heights, meaning the Tufts et al.[95] criteria does not apply, although Tufts et al.[95] only looked at the singular component FFS for this criteria and had a helical flow on top of the step interacting with the CFI which we do not. When examining these instability velocity profiles, we have noticed $max(\sqrt{\hat{u}^2 + \hat{w}^2})$ seems to correlate with the bump height. The value of $max(\sqrt{\hat{u}^2 + \hat{w}^2})$ ranges from 646 to 692 microns in height, which is just higher than the second bump height.

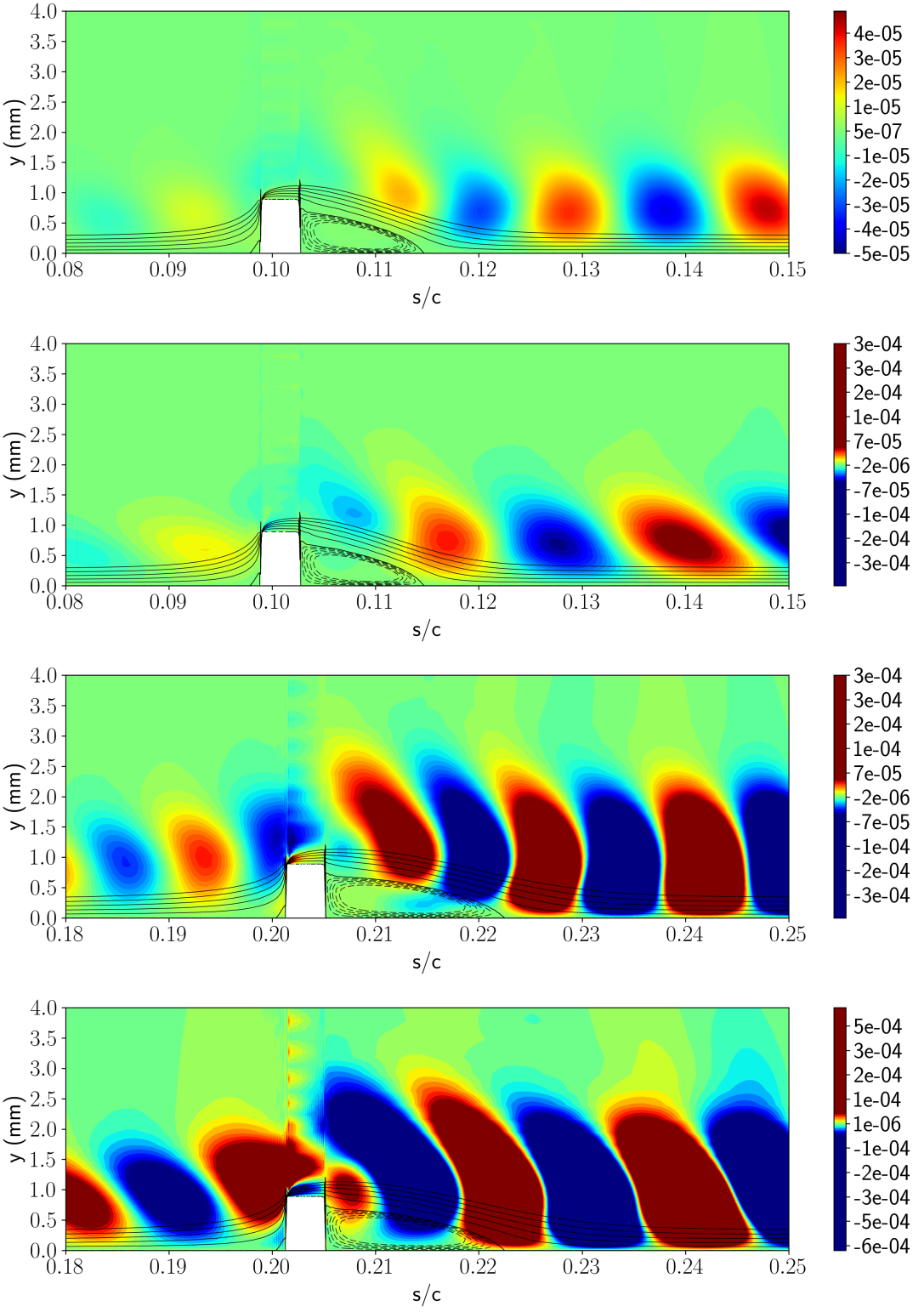

Figure 7.40: Stream-wise perturbation field, $|\hat{u}|$, for 893 micron bump at 10% and 20% chord. Top: LHNSh 10% chord stationary case, $\beta = 390m^{-1}$. Second: LHNSh 10% chord travelling case, $\beta = 350m^{-1}$, $\omega = 340Hz$. Third: LHNSh 20% chord stationary case, $\beta = 500m^{-1}$. Bottom: LHNSh 20% chord travelling case, $\beta = 500m^{-1}$, $\omega = 540Hz$.

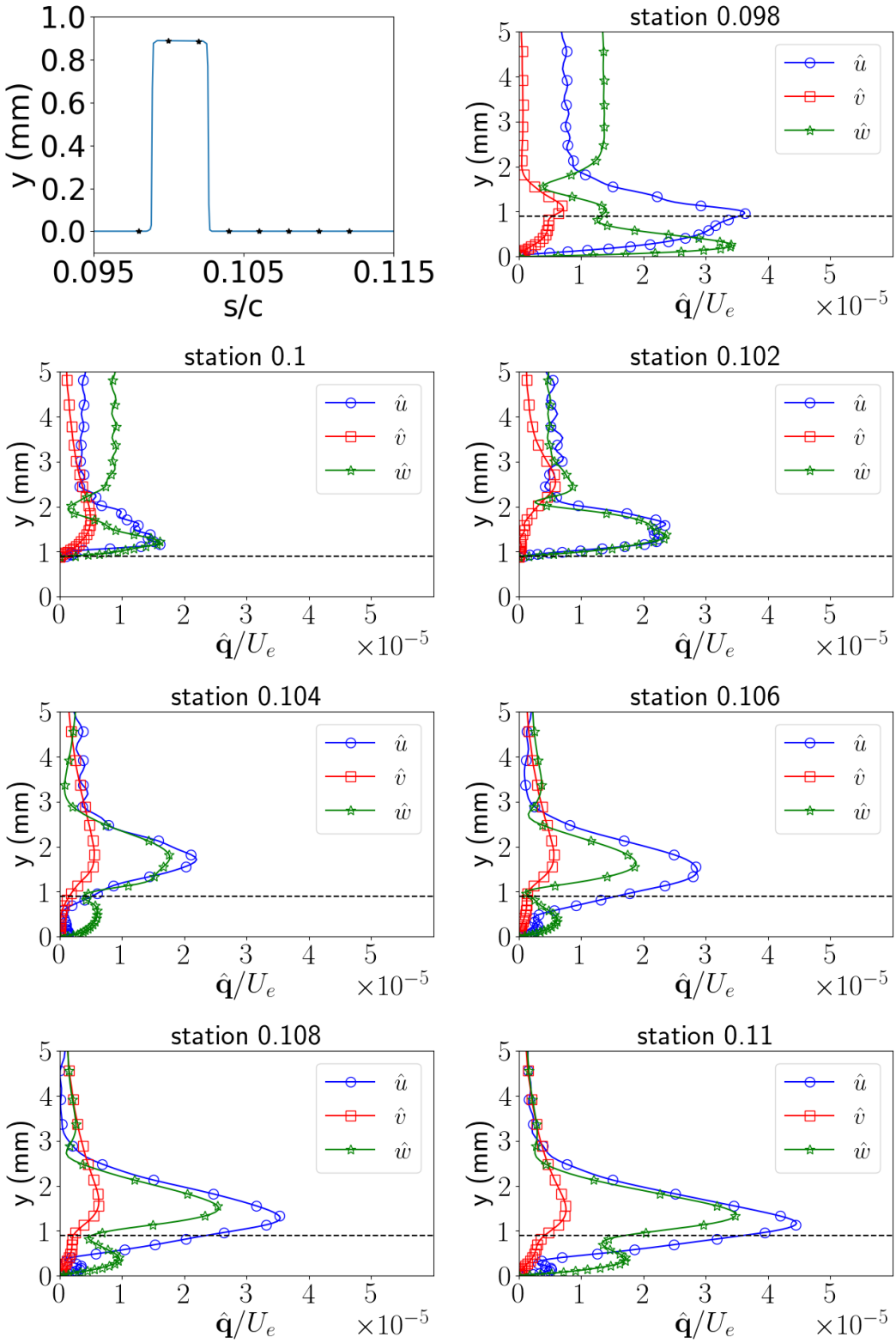

Figure 7.41: 10% chord largest bump height with stationary CFI: LHNSh generated velocity profiles generated at a range of stations. The plot in the top left hand corner marks the stations at which the profiles are evaluated. The dashed horizontal line marks the step height.

7.5 Comparison of all three cases

To compare the three different cases, FFS, BFS and the bump regime directly, we have compared the CFI amplitude versus the height of the roughness scaled with the boundary layer thickness, as shown in table 7.1. Comparisons are made for the 10% chord located roughness in figure 7.42. The $|\hat{u}|$ amplitude is scaled with the edge velocity at the measurement location (20% chord). We can see that the FFS appears to provide the most amplification to the CFI, and this is increased with increasing step height. The bump also causes an amplification with increasing step height but is not as substantial as the FFS. The BFS tends to predict a stabilisation with increasing step height. As stated previously, we think it is likely that there are highly non-linear mode interactions introduced by the BFS, and even the laminar separation bubble posterior to the step, which are not able to be captured with linear theory. Should this hypothesis be true, it likely applies to the bump case as well which is why we see a lesser destabilising impact on the CFI than the FFS.

7.6 Comparison with the Nektar++ time stepping LNS

To investigate the validity of the results, the time harmonic LHNSh code is compared with the Nektar++ LNS time marching solution, as we did for the ramped case where good agreement was found. In order to compute the incompressible LNS with Nektar++ a much finer mesh is required than for computing the baseflow solutions. Here we utilise a domain with around 1500 elements, the majority of which have been injected into the near wall quadrature layer, and a polynomial order of five is sufficient.

We do not see good agreement from any of the cases, contrary to that of the ramped cases, see figure 7.43. The forward and bump Nektar++ LNS (NekLNS) do show some increase in growth but it is nowhere near as amplified as that of the LHNSh results. For these two cases the growth in the region prior and after the bump location share very similar amplitude evolution. The bump does not seem to be providing as large a kick to amplification in the NekLNS solutions compared to the LHNSh solutions. Although, downstream of the bump the NekLNS and LHNSh solutions can be made to match by a simple scaling of one to the other. Mesh refinement studies with respect to h-type and p-type have been conducted with minimal change to the solutions. We were also not able to compute a solution for the BFS which did not decay along the chord. Upon reaching 65% chord the amplitude of CFI with NekLNS is 10^{-7}. The solution from Nektar++ for the BFS seems to agree qualitatively with the LHNSh code, that there is a stabilisation predicted for the CFI, but this claim is extremely tenuous. We would expect the NekLNS BFS result to agree beyond the step, at least

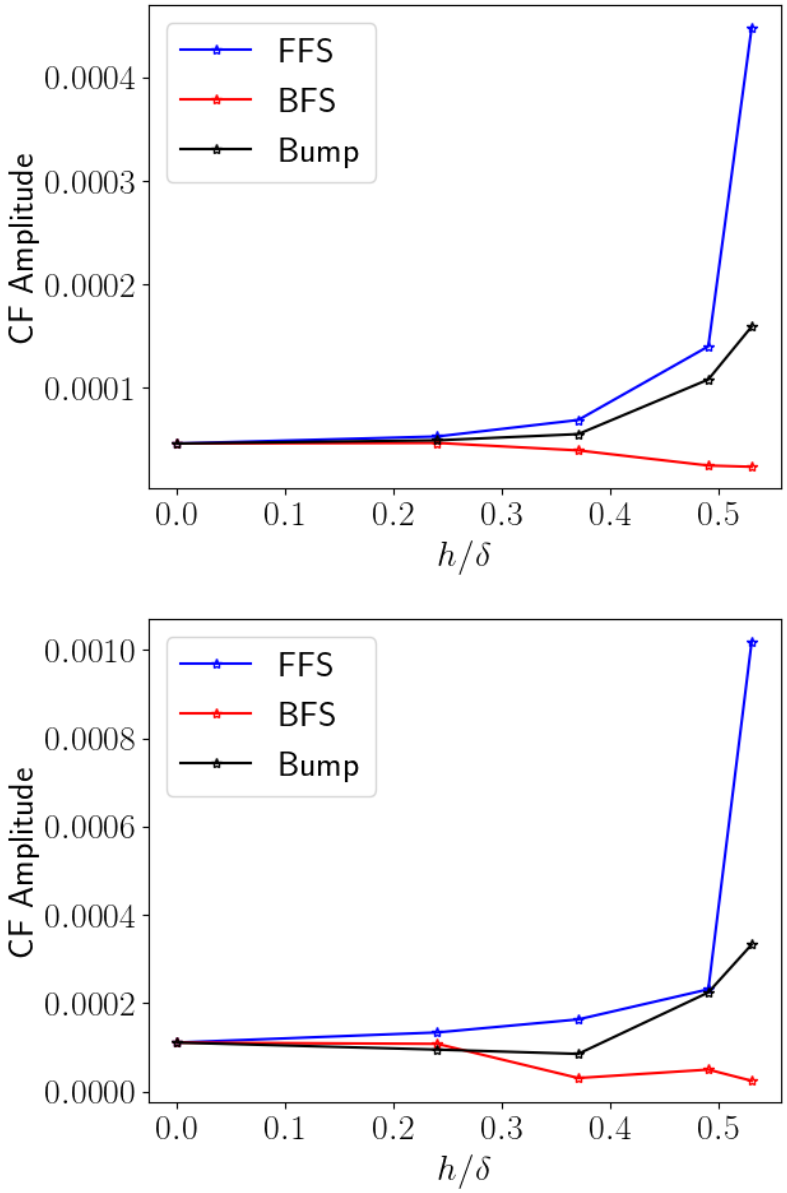

Figure 7.42: LNSHh calculations for most destabilising stationary (top) and travelling (bottom) CFI for all step heights and roughness shapes placed at 10% chord. Amplitude measurements are taken 10% after the roughness location (20% chord) and normalised with the edge velocity at each station location.

with similar evolution in amplitude as the FFS and bump do. Generally the NekLNS result requires much further investigation and this demonstrates the immense difficulty of solving such flows with time marching. A further point to consider here is that we are investigating spatial growth of convection instabilities. It could be that the reason forward movement of the transition front is observed in experiments could be due to temporal growth, an absolute instability or a non-linear interaction phenomenon. Appel et al.[4] numerically investigated temporal bi-global instability over steps and bumps on the AERAST geometry. They found that temporally unstable bi-global modes were present in configurations with BFSs present for heights exceeding 25% of the boundary layer thickness. No bi-global unstable modes were detected for the largest FFS heights, which may be due to these strong stream-wise gradient changes.

We have a number of considerations for the reader when evaluating these results. Firstly, we begin with regard to the NekLNS solution. We do not observe an increase in amplitude in figure 7.43 compared to the ramp cases in figure 6.10, which we find quite unlikely given the experimental work of Eppink and Casper[28], showing that FFRs are not as dangerous as sharp steps. Although, the reader should remember we are not comparing like for like wave numbers between our ramp cases and the vertical step cases here. The next point brings us to the mesh generation software within the Nektar++ framework. We are limited with the amount of points we can cluster over the vertical step geometry. This is due to a clustering of the normals far from the wall when reaching the triangular layer, not dissimilar to that of the action of a compression fan in compressible flow configurations. This can be seen in figure 7.1. As we increase the number of points over the step this causes the clustering of points near the triangular layer to become extremely fine. At some point we reach a limit where the mesh generation software will begin creating very poorly shaped elements in this region, elements with a negative Jacobian. Meshes with negative Jacobian elements will cause simulations to diverge. This puts quite a high constraint on the amount of refinement we can achieve over the bump region, although we do consider the refinement to be reasonably fine. Now considering the baseflow generation, the presence of the sharp step features introduce extremely large stream-size gradient changes. These could either be too noisy or be too severe, this becomes more exacerbated in the second order derivative terms, for even the NekLNS solution to provide a valid trajectory for correct modelling for these cases.

Secondly, we consider the LHNSh solutions. These are computed with baseflows extracted from the incompressible Navier-Stokes solver in Nektar++, which as just stated, is solving an extremely difficult problem arising from the rapid geometry changes the step features impose. We attempt to smooth these profiles over the bump region in the python script with finite differencing over the step region. However, even

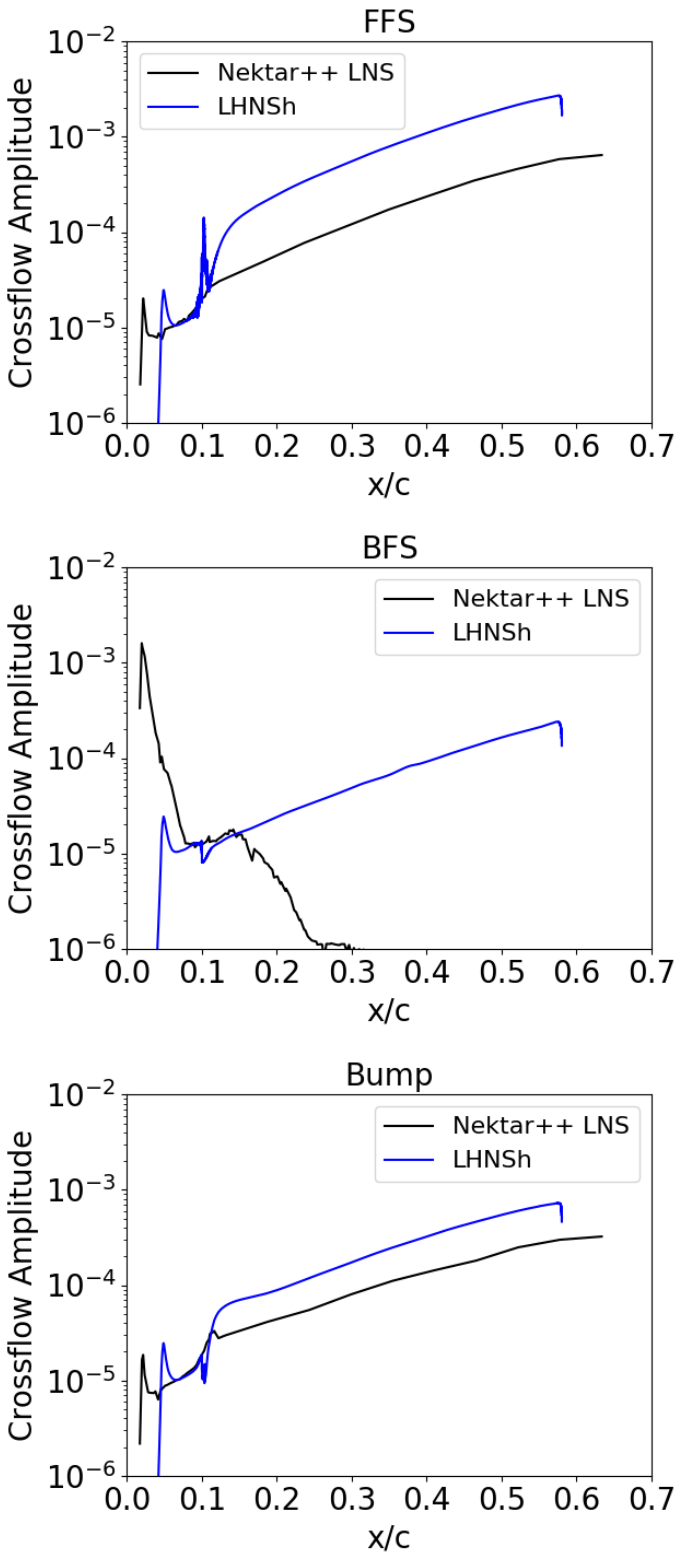

Figure 7.43: LHNSh comparison with nektar++ time stepping LNS result for stationary CFI. Top is for the FFS, β =460m^{-1}, middle for the BFS, β =330m^{-1} and bottom is the bump case, β =440m^{-1}, each located at 10% chord.

with this smoothing applied, we can still have some noise present in the second order derivative terms which can contain extremely large values. On top of this, when the baseflow is re-mapped to the LHNSh computational grid another linear spline is applied to the flow field and the step geometry, bi-cubic splining gave overshoots, hence linear splining was used to interpolate the Nektar++ boundary layer profiles onto the LHNS grid. This effectively causes a light stretching of the step in the stream-wise direction meaning that there are not multiple points along the normal axis which would cause infinitely large $\frac{dh}{ds}$ terms. Once again, these factors could all be affecting the solution when solving the LHNSh equations. Finally, there is always the slim chance, that we cannot entirely rule out, there has been a typo in the coding of these LHNSh equations when incorporating into the wider routine. These have been checked numerous times with the derived equations set but as the reader has seen, these are extremely extensive equations especially when considering the compressible formulation. However, we highly doubt this is the cause of the differences in solutions between the NekLNS and LHNSh formulations. Generally as shown in the earlier, relatively more benign, cases the LHNSh gives the expected results, the experimental verifications of the LHNSh (figures 4.3 and 4.6) are in some way a confirmation on the overall correctness of the model and coding.

7.7 Concluding Remarks

To summarise, we have numerically investigated the effect of FFSs, BFSs and bumps on stationary and travelling CFI. The roughness has been placed at 3%, 10% and 20% chord on the AERAST swept wing geometry, in correspondence with the experimental work of Saeed et al.[82]. Four different roughness heights have been simulated, also constructed around the work of Saeed et al.[82]. The Nektar++ incompressible Navier-Stokes solver has been used to generate steady baseflows. These have then been utilised in four different stability tool sets, LST, PSEh, LHNSh and the Nektar++ time marching LNS.

When simulating the 3% chord case we were unable to identify any unstable modes to begin computations with LST, PSE or LHNS. LST has been used to generate neutral curves which are of very different shapes depending on the shape of roughness. The presence of the roughness feature can destabilise the wave number parameter space from the range $\beta = 200m^{-1}$ to $\beta = 1000m^{-1}$, in the clean case, to $\beta = 0m^{-1}$ to $\beta = 2600m^{-1}$ for some roughness heights and locations. We have confirmed that the PSE and PSEh cannot be used to generate mesh independent results for any of the excrescence cases. Although, they have been used to identify the most destabilising wave number, or wave number - frequency combination, to provide outflow conditions

for the LHNS and LHNSh equations. This is due to the step being of a much smaller length scale than the CFI, the PSE numerical step size restriction must be respected for a converged solution[52]. Moreover, the large stream-wise gradient changes brought about by the roughness are also sources contributing to non-reliance of using the PSE for such problems.

Comparing the LHNS and LHNSh equations we can see that the incorporation of the h transformation is crucial to obtaining more accurate results, which thus computes results in qualitative agreement with literature findings. With the LHNSh equations, we generally see a large impact on CF disturbances convecting over steps placed at 10% chord, which is not as prominent with identical steps placed at 20% chord. We also see that the travelling CFI is much more dangerous than the stationary crossflow. The FFS cases produce a greater amplification than any of the other cases, confirming that it acts as a CFI amplifier. This amplification is increased with increasing step height. However, we can not associate this with a separated flow on top of the step, as Tufts et al.[95] did, due its non-existence in our step geometries. The BFS tends to predict a stabilisation. This is rather different from experimental results which tend to observe a forward movement in the transition front[81,31]. We attribute this difference to there being an extremely non-linear mechanism instantly present at the step location in experiments which we cannot capture with a linear growth mechanism. No added amplification in stationary CFI has been observed in similar experimental works of Eppink et al.[31] and Saeed and Morrison[81], they go on to note the non-linear mechanisms must be playing an important role in the amplification process. The bump cases generally predict a growth of CFI with increased step height but this is not as amplified as the FFS case. This is likely to be due to the presence of the BFS component providing a stabilisation.

We have not been able to validate these results with the Nektar++ time marching LNS computation. This may be due to the a restriction on how fine we can make the mesh in the roughness region. Essentially that the vertical step we have created is just too steep, which introduces extremely large gradient changes which can generate very noisy second derivative terms. It must be stated the modelling challenges posed by the extreme gradients and scales involved are formidable. This is, we believe, the prime reason for some of the inconsistent results that have arisen when comparing the direct time-marching Nektar++ and time harmonic LHNS derived solutions.

CHAPTER 8

Conclusions and Future Work

The aim of this work is to investigate how small roughness shapes interact with pre-existing instabilities within a laminar boundary layer. It is well understood that the presence of small roughness can cause a forward movement in the transition front. When considering these small imperfections over an aircraft wing, the turbulent flow causes an increase in shear stress on the surface, an increase in drag, and finally results in an increase in fuel consumption. These imperfections, or excrescences, on a wing could be anything from a rivet to the junction between materials, such as a leading edge to wing box junction, weather damage, such as hail stones, or even insect contamination. The roughness in question is usually of the order of 10 to 200 microns on a commercial aircraft wing that can be metres wide and tens of metres long. The understanding of the mechanisms behind what may stabilise or destabilise a convecting instability could help to understand how stringent requirements on manufacturing tolerances need to be for aircraft wings.

To solve this problem of a instability convecting over an aircraft wing numerically, industry tend to apply linear stability theory coupled with the e^N method to rapidly predict the growth and transition of an instability. The e^N method basically correlates the transition location with the accumulated growth of the instability. The problem with using LST is that essential geometry curvature information, growth of the boundary layer and non-linear effects are neglected in the computations. This type of information is vital for predicting instability growth accurately. At best, industry couple the e^N method with the PSE which do have the ability to encapsulate

curvature, boundary layer growth and non-linear effects in the transition prediction. However, the PSE are not derived to encapsulate a rapidly varying surface geometry introduced by such a feature as an excrescence. Now we could choose to pour extensive computational resource into the problem (evaluating the whole aircraft geometry instead of a partial wing slice), and gain vast amounts of information from the solution. However, this would take weeks of high computational power to compute just one solution and so really is not feasible for an industrial design process. This work seeks to gain greater understanding of the physical mechanisms at play in the step region and to achieve results within in a matter of minutes on a simple work station computational resource. We achieve this though modification and application of the PSE and LHNS equations.

Research is plentiful for roughness on unswept flat plates or aerofoil geometries which feature TS instability as the dominant perturbation[100,33,103,64,75,107,17,94,7]. The roughness can take the simplified shape of a dimple, hump, FFS or BFS and the variation between flow configurations is wide. There has been reasonable experimental and numerical research in this sector to try and quantify a critical step height, which brings about the forward movement of the transition front. Although, there has been no wide spread agreement on this criterion, there are some which are more widely used in industry than others, such as the Re_h criterion[62]. The difficulty in finding a general criterion, if one exists, is the wide variety of flow regimes which may change the mechanisms involved in the destabilisation. The general finding, whether the research is experimental or numerical, is that increasing the height, or depth, of the roughness causes earlier transition onset. This is exacerbated if the roughness is a BFS[100,64].

On swept wing flows, the dominant instability becomes CFI which, contrary to TS modes, can be destabilised by adverse or favourable pressure gradients. The characteristic that defines CFI is a velocity profile featuring an inflection point within the boundary layer due to some wall-normal local maximum. Research is far less rich in the area of CFI on a flat plate with a roughness and becomes extremely sparse for three dimensional flows, specifically for CFI over a swept wing. This very sparsity is what instigated the present work. Recent studies[31,95,89,81] which have revealed new insight into these regimes are referenced and compared with regularly. The general idea remains that BFSs are more destabilising to the CFI than FFSs due to the oscillation induced from the laminar separation bubble.

An extensive numerical study is conducted into the effects of these small scale roughness elements on convecting instabilities within the boundary layer, via development of rapid perturbation prediction tools. We aim to numerically recreate the experimental work of Saeed et al.[82] who investigated bump shaped steps on the AERAST swept wing geometry[91]. We apply the PSE and LHNS equations to solve for the excrescence

region. However, before this can correctly be applied, both equation sets require an adjustment to capture the rapidly varying surface topography introduced by the excrescence. We successfully introduced a non-orthoganal transformation to incorporate the roughness region to the clean geometry. The introduction of this transformation means that any regions of curvature along the roughness will be introduced though h' and h'' terms.

Firstly, we apply these equation sets to a flat plate case with a dimple, in order to observe how a TS mode is modified when convecting over the region. This work utilises baseflows generated by Xu et al.[107] where the depth and width of the dimple is varied between cases which contain a laminar separation bubble, located inside the dimple, and those that remain fully attached. For the dimple case we observe that the growth difference between the PSE and PSEh or LHNS and LHNSh seem to remain unchanged before and after the dimple region, however we observe quite a different growth within the depression. We also see extremely good agreement with the non-linear computations outside of the dimple region, only starting to observe a difference in the third harmonic. Linear results are exhibited from the work of Gowree et al.[36] that show extremely good agreement of our LHNSh solutions with experimental results. We have shown that the linear and non-linear PSE / PSEh are able to converge to accurate solutions when subjected to flows with the presence of a laminar separation bubble. A random roughness case was also simulated on a flat plate. However it is much more difficult to obtain converged solutions for these cases. The smallest random roughness height gave little difference between the codes but anything larger than that produced visible differences between all codes. We attribute this to there being extremely large velocity fluctuations over the roughness region and the presence of multiple small separation bubbles, making this an extremely difficult problem for the PSEh and LHNSh to solve.

With the encouraging results obtained in the flat plate cases, we moved on to tackling the problem of a swept wing case. The experimental work of Saeed et al.[82], whom looked at varying height bump roughness on the AERAST swept wing, is the work we chose to construct our numerical investigation around. We have successfully simulated the AERAST infinitely swept wing using a three stage process. Firstly the full geometry is simulated with a RANS solver to generate a steady clean baseflow of the full wing. Secondly, an embedded mesh is then created using the high order spectral / hp element solver, Nektar++. Boundary and initial conditions from the full solution are provided to the embedded domain circumference and interior. An embedded domain is necessary in order to capture the magnitude of mesh scale refinement required around any roughness we chose to place on the wing. Thirdly, these steady baseflows are then extracted and utilised in varying stability tool sets. Remarkably good agreement is

obtained between the PSE, LHNS and Nektar++ LNS time-stepping solution.

With the clean AERAST geometry simulated, we then imposed the largest height roughness from the work of Saeed et al.[82] on the AERAST geometry at 10% chord. Instead of imposing a vertical bump case, we decided to slope the edges of the bump in order to create a ramp shape profile and provide a simpler roughness element for the stability tools to simulate. The ramp shape, chosen with an incline of 45° , also encapsulates a longer stream-wise region where the h component plays a role. To accompany the bump ramp case, we decomposed this structure into its FFR and BFR components to gain insight into which may be triggering certain growth mechanisms. We establish that the PSE and PSEh cannot be used to provide an accurate solution for any of the ramp cases due to a few contributing factors. One being that a number of stream-wise stations need to be stepped-over in order for the computation to converge at the full length of the chord. This, we attribute to there being extremely large stream-wise gradient changes locally to the ramp. Another factor is that the stream-wise length scale of the ramp is much shorter than that of the convecting CFI. This means the PSE will be unable to accurately capture the growth mechanism[104]. When applying the LHNSh equations to these cases we see extremely good agreement with the Nektar++ time-stepping LNS solution, emphasising the importance of solving the LHNSh equations as opposed to the LHNS. The FFR case tends to provide a large kick to the amplification growth which seems to originate from the upper ramp corner. Similar observations were made by Eppink and Casper[28] for convecting stationary CFI over a FFR, and by Sumariva and Hein[89] numerically for a TS wave over a flat plate, although we do note that the Sumariva and Hein[89] study was two dimensional and comparisons may be tenuous. The BFR interestingly appears to modify the stationary CFI only very slightly after the step location and the growth tends to then follow that of the clean case. Eppink et al.[31] also observed this in their experimental investigations for stationary CFI over a BFS.

With these very encouraging results we then moved on to investigating the true problem we sought to solve, the vertical bump roughness as considered by Saeed et al.[82]. We applied our embedded mesh approach to construct the four varying vertical bump heights at the three chord locations considered by Saeed et al.[82]. We also extended this to pure vertical FFS and pure vertical BFS roughness in order to conduct a thorough investigation on the roughness impact. We were unable to identify unstable modes at the 3% chord location with LST, PSE or LHNS for any of the step heights. Instead our analyses focused on the 10% and 20% chord locations. Neutral curves were constructed using LST. We can see that the presence of the roughness can cause the range of destabilised wave numbers to grow from β =200m^{-1} to β =1000m^{-1}, in the clean case, to β =0m^{-1} to β =2600m^{-1} in the most severe case. We observe slightly differ-

ent shaped curves between stationary and travelling CFI, with the latter causing more prolonged stream-wise destabilisation. Again, the PSE and PSEh cannot be used for these cases due to the large stream-wise gradient terms and the fact that the bump or step feature is much too short for the CFI length scale[104]. The PSEh is used, however, to provide boundary conditions for the LHNS and LHNSh equations and are thereby used to determine the most unstable wave numbers. Generally we see that the FFS and bump predict a destabilisation which is exacerbated with increased step height and the travelling CFI seems to be much more dangerous than the stationary. We were not able to correlate the results with some of the aforementioned step height criteria, such as the Tufts et al.[95] criteria, due to the lack of separation bubble present on top of the step. Tufts et al.[95] attribute this separation bubble to be the main destabilising mechanism, however, we still observe a destabilisation with no bubble, meaning this cannot be the mechanism behind our destabilisation. We believe our mechanism lies heavily in the top corner of the FFS or bump. This theory is supported by the experimental work of Eppink and Casper[28] due to the similarities in observations.

The BFS tends to predict a stabilisation with increased step height which is contrary to much of the literature but is observed in the work of Balakumar et al.[8]. We attribute this feature to there being a highly non-linear mechanism instantly brought about by the presence of the step. Trying to capture this non-linear interaction with linear theory is just not possible. Further investigation would need to be carried out with the non-linear code set to confirm if this is the case. We suspect this is true since there has been high levels of non-linear mode interaction observed in the experimental work[82,31], where the stationary CFI has been shown to have no growth and even to have decayed, or not be detected down-stream.

Our bump results tend to correlate with the experimental work of Saeed et al.[82] whereby there was no amplification observed to the CFI from the smallest bump height. However, we also observed that there was no overall growth for the second largest bump height, contrary to that of Saeed et al.[82]. After this, we do observe a more exaggerated growth with increased bump height. Although, these never become as amplified as in the pure FFS cases. We think this due to the composition with the BFS, which by our equations are predicting a stabilisation.

When comparing all of these cases with the Nektar++ time stepping LNS we were not able to gain good agreement, unlike the ramp cases, and observe that the ramp cases predict a larger amplification of CFI growth compared to the step. Although, we add the caveat that these are not compared with like for like wave numbers. We would believe this is due to either the restriction on how fine we can make the mesh locally to the roughness and possibly that the gradient changes induced from the geometry of the vertical step are just too large.

All in all, we have added essential corrections to the PSE and LHNS equations (PSEh and LHNSh) to enable accurate modelling of the effect of a small roughness on a pre-existing instability within the boundary layer. We set out to investigate vertical step features, typical to those found on aircraft wings, and have found that the challenges in modelling such features are formidable. However, the models perform remarkably well compared to experiments when not considering a vertical feature.

Going forward, we would suggest that a study is performed varying the angle of the 45° ramp to a vertical step with NekLNS. The stationary CFI and roughness height should remain the same to gauge at what point the solution begins to predict less amplified growth with a steeper ramp. This can also be conducted with the LHNSh equations for comparison. We could also extend this in the other direction to lower the angle of the ramp in order to establish at which point the PSEh begin to break down. Although, perhaps the ramp angle would be too shallow, in order to make the ramp longer than the CFI wavelength, to add much insight.

Secondly, we would suggest returning to the ramp cases and solving for the varying heights at both 10% and 20% chord to gain more insight into what is occurring locally to the ramp, that we could not achieve with the vertical step cases.

Thirdly, we have began investigations into applying this process to the BLADE natural laminar flow wing. This is a fully three-dimensional flow problem. The BLADE wing is swept, tapered and dihedral, adding even further complexity to this already complex problem. The aim here is to compare the stability tool solutions to in-flight test data obtained by Airbus. Due to the confidentiality of the geometry and data we do not discuss this in this thesis.

Our final suggestions relate to the solution pipeline itself. An alternative form of mesh generation could be investigated, software that allows partitioning of the domain. This would mean that locally to the step the mesh could be partitioned into different sections allowing increased refinement to be added, although the corners of the step would have to be made sharp and un-filleted. This in itself is a hard task. The current high order meshing software available, that can generate a curve-linear element for the wall of the aerofoil, is scarce. To the authors knowledge there is GMSH and NekMesh, within the Nektar++ framework, neither of which support segmented domains. Having curve-linear wall elements is an important feature for gaining optimal solutions from the spectral / hp element solver. Improvement could also be made to the python routine for extracting smooth baseflows from the Nektar++ baseflow solution. Although there was a lot of time spent on generating these smooth profiles, there still remains some noise in the second derivative terms around the step located profiles. Perhaps this problem would solve itself with partitioned mesh generation.

APPENDIX A

Further Methodology

A.1 The Galerkin Method

The Galerkin method used in FEM assigns the trial functions to the test functions so that both are equal, $v_j = \Phi_j$. Beginning with the one-dimensional elliptic equation, $\mathcal{L}(u) = u_{xx} = s(x)$ with boundary conditions $u(0) = g_{\mathcal{D}}$ and $u_x = g_{\mathcal{N}}$. Integrating gives

$$\int_0^1 v(x)u_{xx}dx = \int_0^1 v(x)s(x)dx \tag{A.1}$$

integrating by parts to the left hand side attains the weak form

$$-\int_0^1 v_x u_x dx + v(1)u_x(1) - v(0)u_x(0) = \int_0^1 v(x)s(x)dx \tag{A.2}$$

For two or three dimensions Gauss divergence Theorem would be applied. Obtaining the equation in the weak form makes the matrix of the discretized system symmetric and reduced the smoothness requirements on u. The weight functions $v(x)$ are zero at Dirichlet boundaries, $v(0) = 0$. The Dirichlet boundary condition can be applied by imposing $u_0 = 0$ since the weight functions are zero at this boundary. Next u and v are replaced by their corresponding trial functions $u^{\delta}(x)$, given in equation (3.2), and

test functions $v^\delta(x)$, where $v(x) = \Phi_i(x)$. Applying these gives

$$-\int_0^1 \left(v_x^\delta u_x^\delta dx + v^\delta(1) g_\mathcal{N} = \int_0^1 v^\delta s(x) dx \right. \tag{A.3}$$

for $i = 1, ..., N-1$. This has directly implemented the Neumann boundary condition but the Dirichlet still remains to be fully dealt with. The approximation for $u(x)$ is recomposed into a known function, $u^\mathcal{D}$, which satisfies the Dirichlet conditions and an unknown homogeneous function, $u^\mathcal{H}$, which is zero on the Dirichlet boundaries, such that

$$u^\delta(x) = u^\mathcal{D} + u^\mathcal{H} \quad \text{where} \quad u^\mathcal{D}(\partial\Omega_\mathcal{D}) = g_\mathcal{D}, \quad u^\mathcal{H}(\partial\Omega_\mathcal{D}) = 0 \tag{A.4}$$

substituting this into equation (A.3) and re-arranging gives

$$-\int_0^1 v_x^\delta u_x^\mathcal{H} dx = -v^\delta(1) g_\mathcal{N} - \int_0^1 v^\delta s(x) dx + \int_0^1 v_x^\delta u_x^\mathcal{D} dx \tag{A.5}$$

all of the terms on the right hand side are known meaning the differential problem has been reduced to a finite linear algebraic system which may now be solved numerically. This method for applying the Dirichlet boundary condition is known as the lifting method.[66]

A.2 Domain Decomposition

The domain Ω is divided into N non-overlapping sub-domains, elements, Ω_n.

$$\Omega = \bigcup_{i=0}^{N-1} \Omega_n, \quad \bigcap_{n=0}^{N-1} \Omega_n = 0. \tag{A.6}$$

It is common to associate each elemental shape a reference element called the standard domain or element denoted as Ω_s, see figure (A.1) from the PhD thesis of De Grazia[18]. The expansion basis, integration and differentiation are then defined on each of these standard elements.

For line segments the definition is

$$\Omega_s = (\xi) \in [-1, 1] \tag{A.7}$$

where ξ is the one dimensional co-ordinate associated with Ω_s. The parametric map-

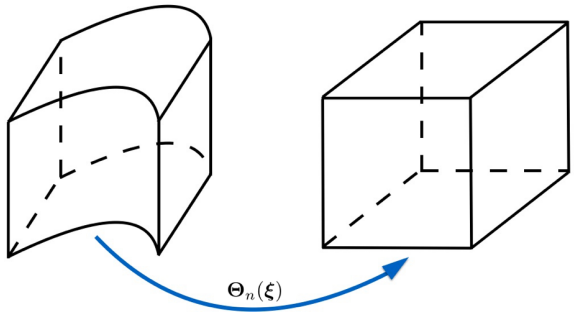

Figure A.1: The Mapping $\Theta(\xi)$ from the physical to the standard domain[18]

ping $\Theta(\xi)$ defining the transformation is then

$$x = \Theta_n(\xi) = \phi_0(\xi)x_{n-1} + \phi(\xi)x_n \qquad \forall \quad \xi \in \Omega_s \tag{A.8}$$

where ϕ_0 and ϕ_1 are general expansions for the mapping and $\Theta(\xi)$ is the mapping between the local element and the standard element. For the straight segment the mapping becomes

$$x = \Theta_n(\xi) = \frac{1-\xi}{2}x_{n-1} + \frac{1+\xi}{2}x_n \qquad \forall \quad \xi \in \Omega_s \tag{A.9}$$

Extending this to two-dimensions, the standard quadrilateral is

$$\Omega_s = (\xi_1, \xi_2) \in [-1, 1] \times [-1, 1] \tag{A.10}$$

where ξ_i are orthogonal co-ordinates in Ω_s, Cartesian say. Representing the Cartesian co-ordinates x_1 and x_2 as

$$x_1 = \Theta_{n,1}(\xi_1, \xi_2) \quad x_2 = \Theta_{n,2}(\xi_1, \xi_2) \tag{A.11}$$

the mapping for a straight edged quadrilateral with vertexes A,B,C,D, see figure(A.2) can be written as

$$\mathbf{x} = \mathbf{\Theta}(\xi_1, \xi_2) = \mathbf{x}^A \frac{1-\xi_1}{2}\frac{1-\xi_2}{2} + \mathbf{x}^B \frac{1+\xi_1}{2}\frac{1-\xi_2}{2} + \mathbf{x}^D \frac{1-\xi_1}{2}\frac{1+\xi_2}{2} + \mathbf{x}^C \frac{1+\xi_1}{2}\frac{1+\xi_2}{2} \tag{A.12}$$

For curve-linear edges of a quadrilateral the following mapping may be used

$$\mathbf{x} = (x_1, x_2)^T = \mathbf{\Theta}(\xi_1, \xi_2) = \sum_{p=0}^{Q_1}\sum_{q=0}^{Q_2} \hat{\mathbf{x}}_{pq}\phi_p(\xi_1)\phi_q(\xi_2) \tag{A.13}$$

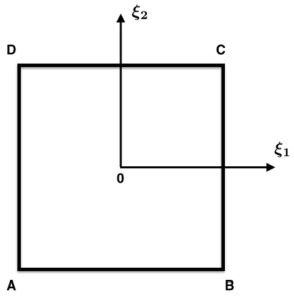

Figure A.2: Vertex labels for quadrilateral element[18]

where ϕ_p and ϕ_q are the same basis functions used for representing the solution. If $\mathbf{x}$ is a polynomial of order P and $P < Q_1, Q_2$ then the mapping is sub-parametric, and if $P > Q_1, Q_2$ the mapping is super-parametric. These mappings may then be used to determine the geometric terms needed for transforming back and forth between the physical and the standard space. The deformation gradient, $\mathbf{G}$, and the determinant of this, the Jacobian J, for the quadrilateral is given by

$$\mathbf{G}_n = \begin{bmatrix} \frac{\partial x_1}{\partial \xi_1} & \frac{\partial x_1}{\partial \xi_2} \\ \frac{\partial x_2}{\partial \xi_1} & \frac{\partial x_2}{\partial \xi_2} \end{bmatrix} = \frac{1}{J_n} \begin{bmatrix} \frac{\partial x_2}{\partial \xi_2} & -\frac{\partial x_2}{\partial \xi_1} \\ -\frac{\partial x_1}{\partial \xi_2} & \frac{\partial x_1}{\partial \xi_1} \end{bmatrix} \quad , \quad J = |\mathbf{G}| \tag{A.14}$$

A.3 Expansion Bases

The choice of local expansion bases functions is very important as it has a large influence over the efficiency and numerical accuracy of the code. The ability to exploit particular structure of the matrices is integral. In spectral h/p element methods nodal or modal polynomials are usually implemented for the expansion bases in each standard element. To distinguish between modal and nodal basis functions two examples will be introduced for two sets of polynomials up to order P.

$$\phi_p^M(\xi) = \xi^p, \qquad p = 0, \ldots, P \tag{A.15}$$

$$\phi_p^N(\xi) = \frac{\prod_{q=0, q\neq p}^{P} (\xi - \xi_q)}{\prod_{q=0, q\neq p}^{P} (\xi_p - \xi_q)}, \qquad p = 0, \ldots, P \tag{A.16}$$

$$\tag{A.17}$$

Equation (A.15) is a modal expansion because the order P-1 expansion set is contained within the order P expansion set, therefore satisfying

$$\chi_{P-1}^{\delta} \subset \chi_P^{\delta} \tag{A.18}$$

Usually all the modes, or polynomials, influence the boundary points of a given element in simple modal bases. This can be extremely inefficient when applying connectivity rules between the various elements in the spatial discretisation. To increase the efficiency of the connectivity process these expansions can be redefined within a boundary - interior decomposition. Here only two nodes are defined as non-zero at the boundaries whilst all other boundary nodes are zero. Nodes at interior points are assumed non-zero. The most adopted modal basis using boundary - interior decomposition for spectral h/p element methods is

$$\phi_p(\xi) = \begin{cases} \psi_0^a(\xi) = \frac{1-\xi}{2}, & p = 0 \\ \psi_p^a(\xi) = \left(\frac{1-\xi}{2}\right)\left(\frac{1+\xi}{2}\right)P_{p-1}^{1,1}, & 0 < p < P \\ \psi_P^a(\xi) = \frac{1+\xi}{2}, & p = P \end{cases} \tag{A.19}$$

where $P_{p-1}^{1,1}$ represents Jacobi polynomials. Jacobi polynomials are a class of orthogonal polynomials with respect to the weight $(1-x)^\alpha(1+x)^\beta$ on the interval $[-1, 1]$.

Equation (A.16) is a Lagrange polynomial defined on a set of P+1 nodal points ξ_q. It consists of P+1 polynomials of order P meaning

$$\chi_{P-1}^\delta \not\subset \chi_P^\delta \tag{A.20}$$

The Lagrange polynomials also have the property $\phi_p^N = \delta_{pq}$, where δ is the Kronecker delta, leading to

$$u^\delta(\xi_q) = \sum_{p=0}^{P} u_p \phi_p^N(\xi_q) = \sum_{p=0}^{P} u_p \delta_{pq} = u_q \tag{A.21}$$

which says that the physical values of the discrete solution u^δ at the nodal points ξ_q are the coefficients of the Lagrange expansion basis. The boundary interior decomposition is no longer necessary as it already fulfilled, provided that the nodal points include element boundaries. Both nodal and modal expansion bases described can be written as one dimensional tensors. This can be extended to quadrilateral elements through the product of two of these tensors

$$\phi_{pq}(\xi_1, \xi_2) = \phi_p(\xi_1)\phi_q(\xi_2), \qquad 0 \le p, q; \quad p \le P, \quad q \le P_2 \tag{A.22}$$

In general the polynomials are allowed to be different in each co-ordinate direction. The differences between standard modal and nodal expansion bases are well displayed by Moxey[57] in figure (A.3).

The matrix form of the expansion bases will no be introduced. The equations will be evaluated on a set of nodal points. For the one-dimensional case $u(\xi_q)$ on the set of Q

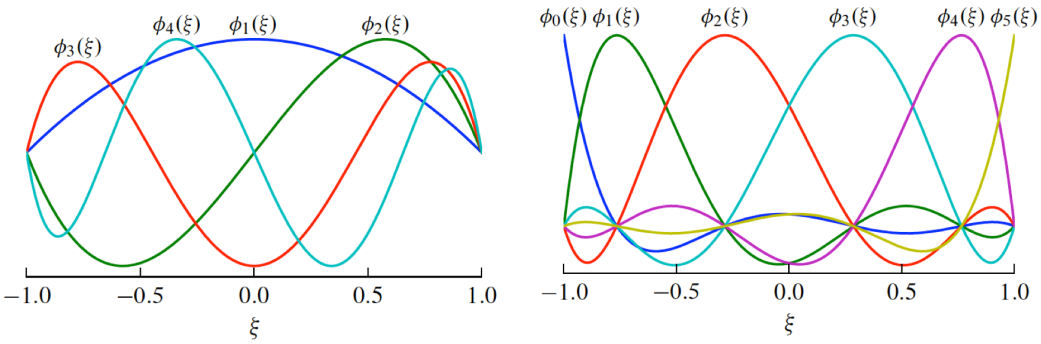

Figure A.3: Left: Modal expansion bases. Right: Nodal Lagrange expansion bases
Both images from the thesis of Moxey 2011,[57]

nodal points $\xi = [\xi_0, \xi_1, \ldots, \xi_{Q-1}]^T$,

$$\mathbf{u} = [u(\xi_0), u(\xi_1), \ldots, u(\xi_{Q-1})]^T \tag{A.23}$$

The matrix form for the expansion basis of the one -dimensional case is

$$\mathbf{B} = \begin{bmatrix} \phi_0(\xi_0) & \ldots & \phi_p(\xi_0) & \ldots & \phi_P(\xi_0) \\ \vdots & \ddots & \ddots & \ddots & \vdots \\ \phi_0(\xi_{Q-1}) & \ldots & \phi_p(\xi_{Q-1}) & \ldots & \phi_P(\xi_{Q-1}) \end{bmatrix} \tag{A.24}$$

P is the order of the expansion and $\mathbf{B}$ is the basis matrix.

For the two-dimensional case there is also the following, for Q_i where $i = 1, 2$ are points in the orthogonal directions.

$$\mathbf{u} = [u(\xi_{1,0}, \xi_{2,0}), \ldots, u(\xi_{1,Q-1}, \xi_{2,0}), \ldots, u(\xi_{1,0}, \xi_{2,1}), \ldots, u(\xi_{1,Q_1-1}, \xi_{2,Q_2-1})]^T \tag{A.25}$$

with the basis matrix

$$\mathbf{B} = \begin{bmatrix} \phi_{0,0}(\xi_{1,0}, \xi_{2,0}) & \ldots & \phi_{p,q}(\xi_{1,0}, \xi_{2,0}) & \ldots & \phi_{P_1,P_2}(\xi_{1,0}, \xi_{2,0}) \\ \vdots & \ddots & \ddots & \ddots & \vdots \\ \phi_{0,0}(\xi_{1,Q_1-1}, \xi_{2,0}) & \ldots & \phi_{p,q}(\xi_{1,Q_1-1}, \xi_{2,0}) & \ldots & \phi_{P_1,P_2}(\xi_{1,Q_1-1}, \xi_{2,0}) \\ \vdots & \ddots & \ddots & \ddots & \vdots \\ \phi_{0,0}(\xi_{1,Q_1-1}, \xi_{2,Q_2-1}) & \ldots & \phi_{p,q}(\xi_{1,Q_1-1}, \xi_{2,Q_2-1}) & \ldots & \phi_{P_1,P_2}(\xi_{1,Q_1-1}, \xi_{2,Q_2-1}) \end{bmatrix} \tag{A.26}$$

APPENDIX B

Clean AERAST geometry convergence studies

A comparison for increased polynomial order Nektar++ solutions are shown in figure B.1. Comparison between the currently used mesh and a twice finer mesh is given in figure B.2. There is some difference between the v_s derivative terms but since this is generally small and ignored in the stability codes currently.

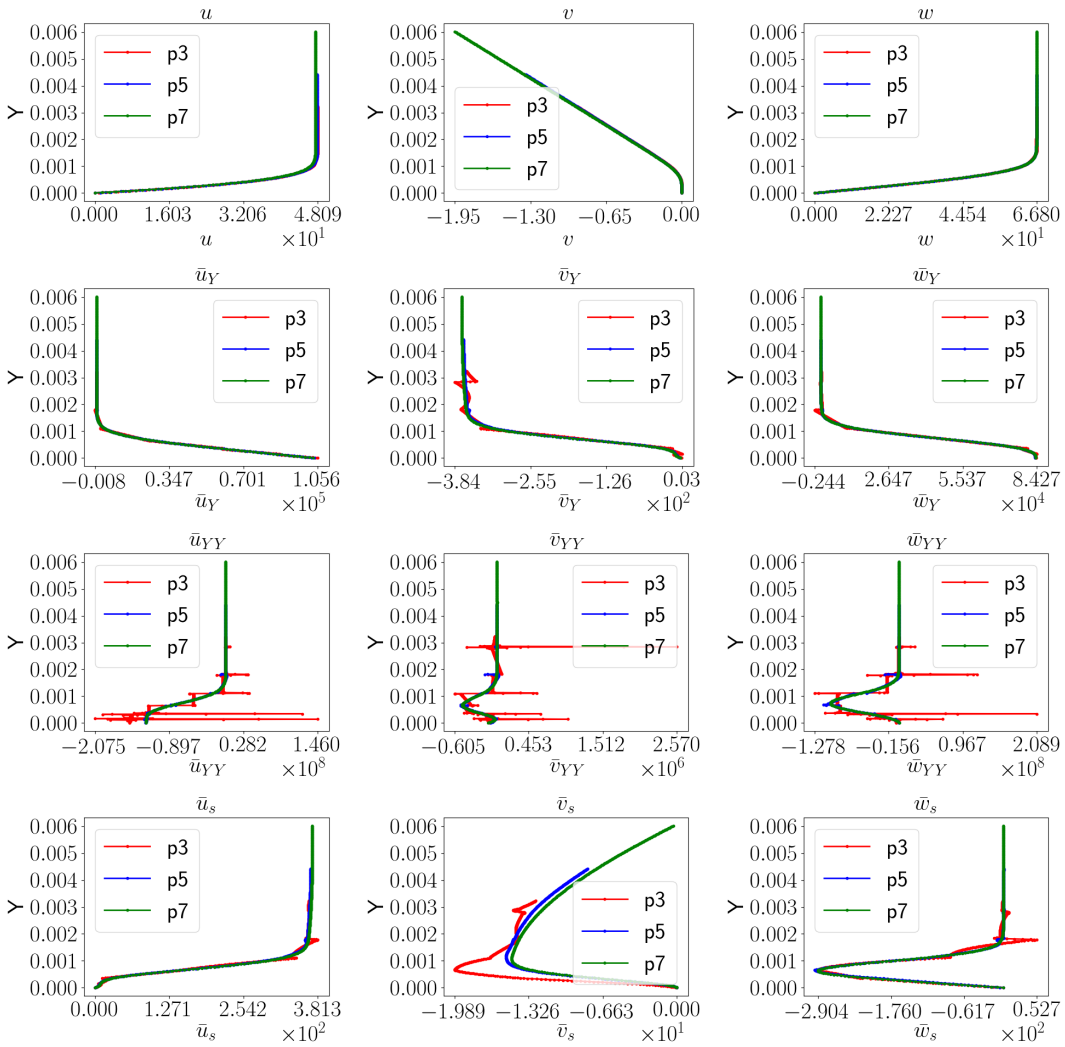

Figure B.1: Clean: Nektar++ generated base flow profiles at 5% chord with increasing polynomial order. Red is for p3, blue for p5 and green for p7.
Top row shows $\bar{u}$, $\bar{v}$ and $\bar{w}$, middle row shows first derivative in the normal direction with respect to $\bar{u}$, $\bar{v}$ and $\bar{w}$ and the bottom row is the first derivative in the stream wise direction with respect to $\bar{u}$, $\bar{v}$ and $\bar{w}$.

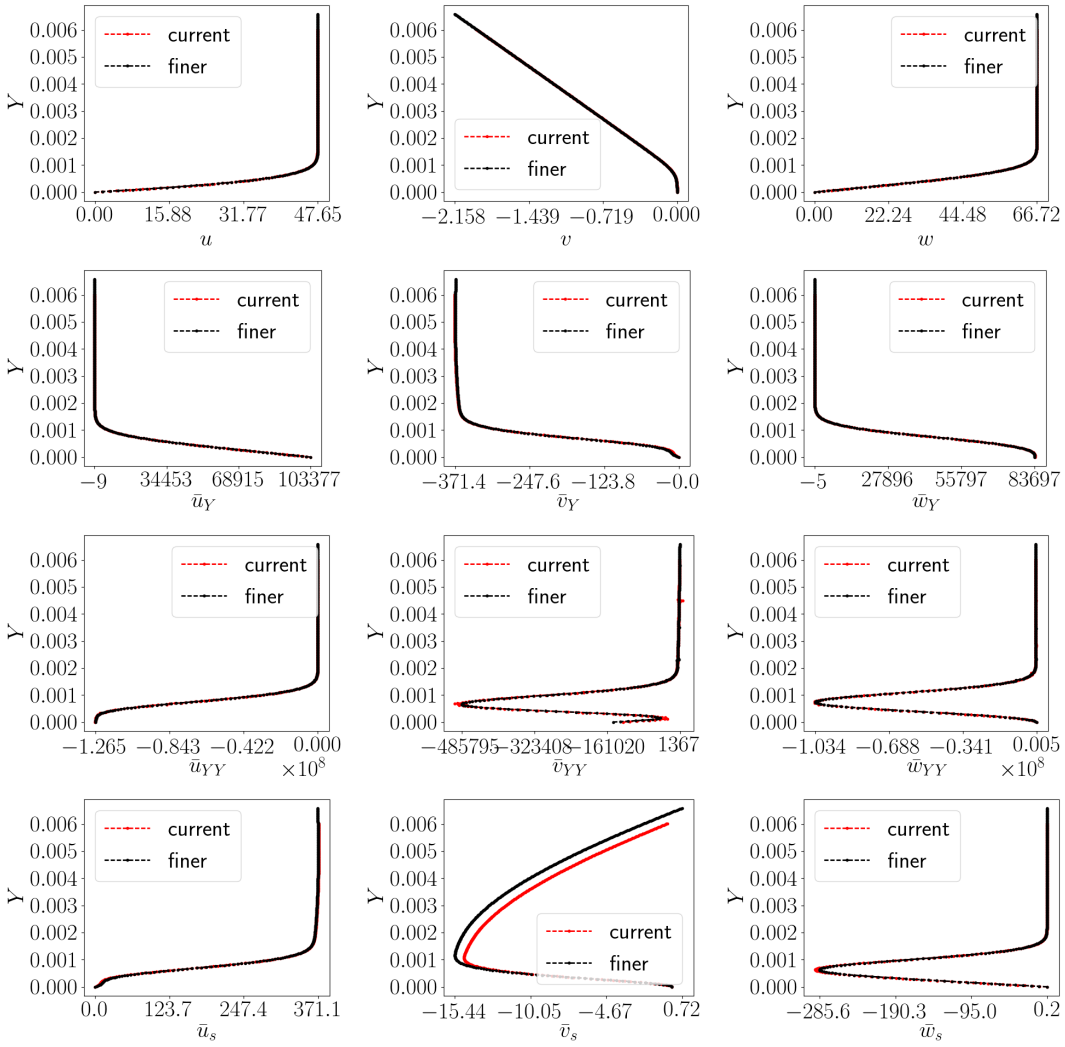

Figure B.2: Clean: Nektar++ generated base flow profiles at 5% chord with red for the coarser (current) mesh and black for the finer mesh.
Top row shows $\bar{u}$, $\bar{v}$ and $\bar{w}$, middle row shows first derivative in the normal direction with respect to $\bar{u}$, $\bar{v}$ and $\bar{w}$ and the bottom row is the first derivative in the stream wise direction with respect to $\bar{u}$, $\bar{v}$ and $\bar{w}$.

APPENDIX C

Bump baseflow profiles.

Base flow profiles extracted at 0.098 x/c, before the beginning of the bump, see figure C.1, and profiles extracted at 0.106 after the bump, see figure C.2

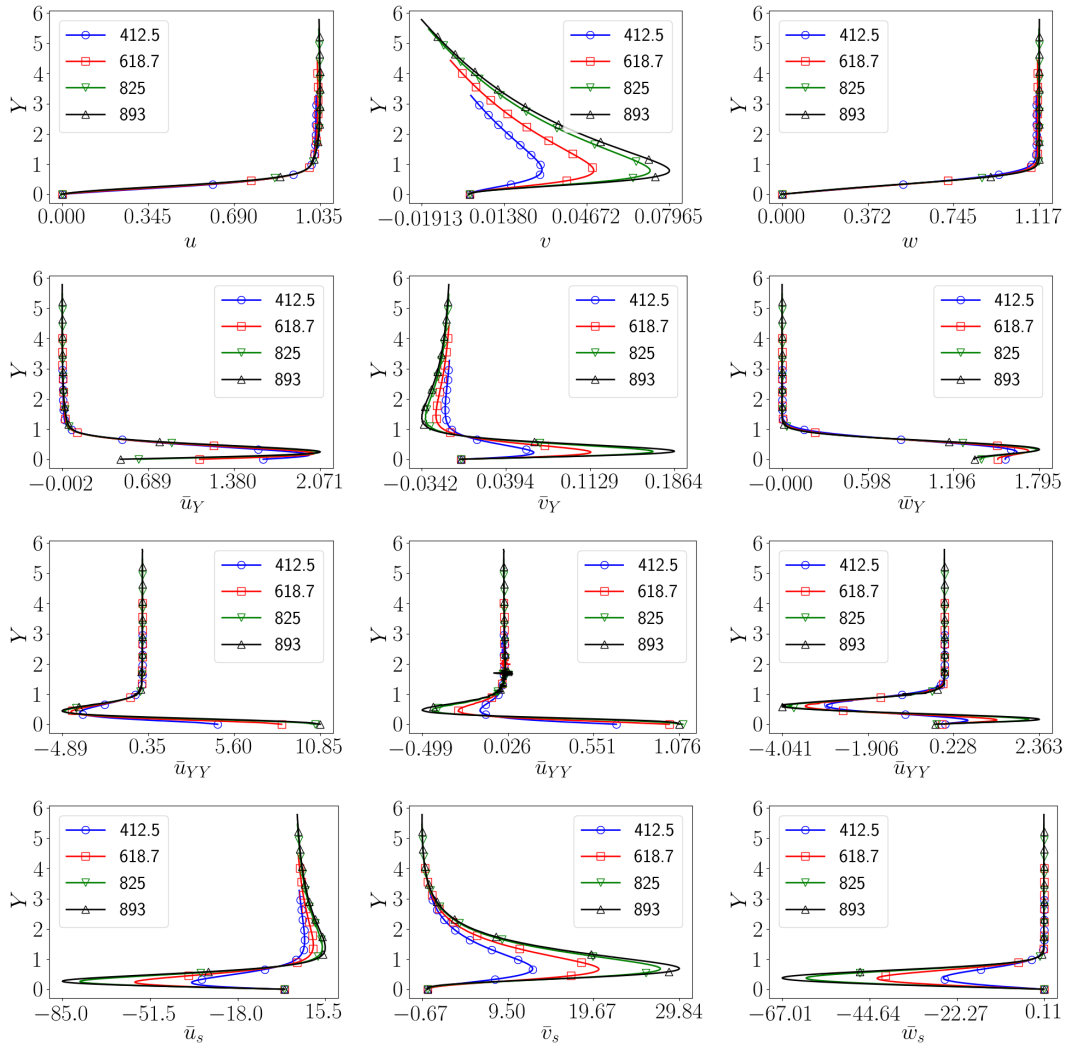

Figure C.1: Bump case at 10% chord: Nektar++ generated base flow profiles generated at 9.8% chord, just before the bump. Non-dimensional values plotted; x axis dimensionalised with the boundary layer edge velocity and y axis is dimensionalised with the boundary layer thickness at that location. Blue, orange, green and red depict bump height 412.5, 618.7, 825 and 893 respectively. Top row shows u, v and w, middle row shows first derivative in the normal direction with respect to u, v and w and the bottom row is the first derivative in the stream wise direction with respect to u, v and w.

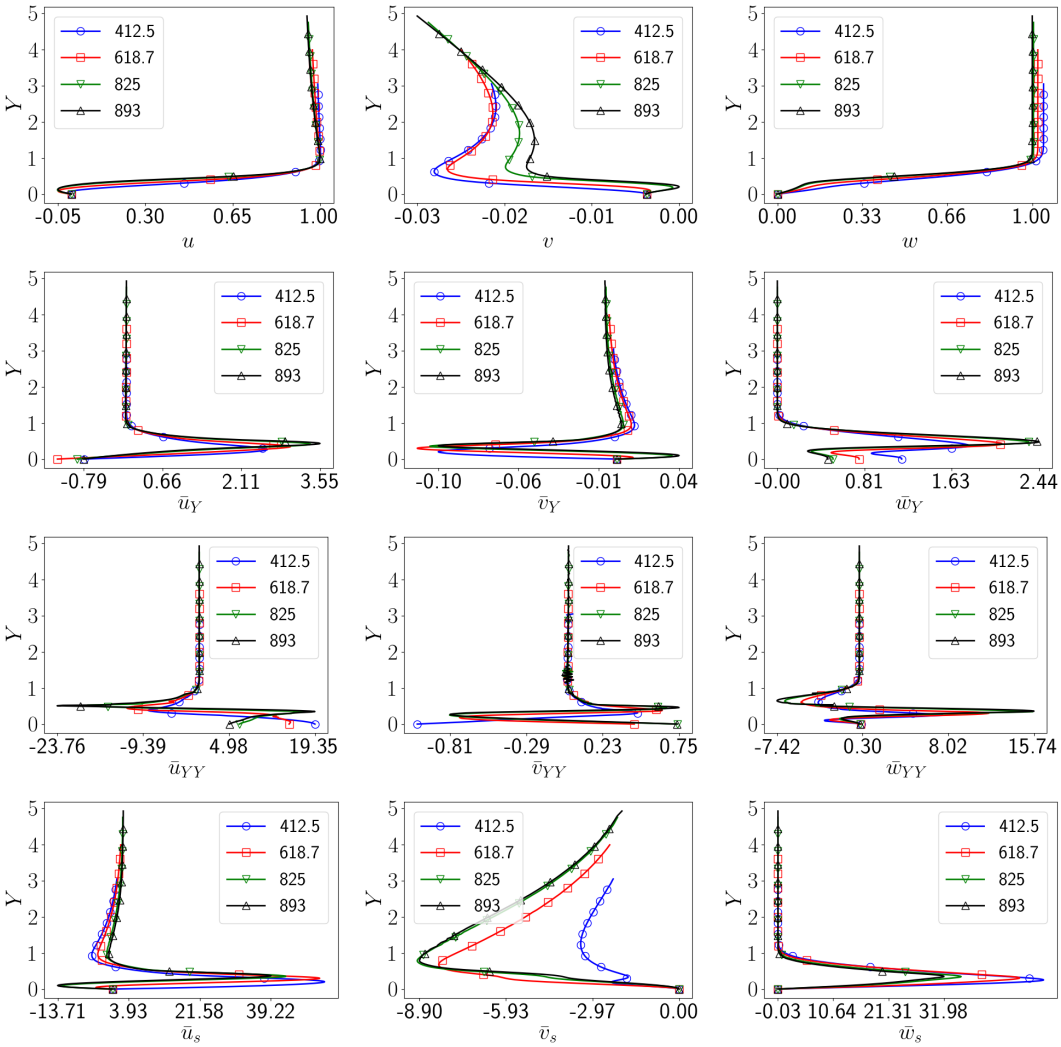

Figure C.2: Bump case at 10% chord: Nektar++ generated base flow profiles generated at 10.2% chord, in the centre of the bump. Non-dimensional values plotted; x axis dimensionalised with the boundary layer edge velocity and y axis is dimensionalised with the boundary layer thickness at that location. Blue, orange, green and red depict bump height 412.5, 618.7, 825 and 893 respectively. Top row shows u, v and w, middle row shows first derivative in the normal direction with respect to u, v and w and the bottom row is the first derivative in the stream wise direction with respect to u, v and w.

References

[1] *Numerical Methods for General and Structured Eigenvalue Problems*, volume 46, chapter The QZ Algorithm. Springer, Berlin, Heidelberg, 2005.

[2] M. Alam and N. D. Sandham. Direct numerical simulation of short laminar separation bubbles with turbulent reattachment. *JFM*, 410:1–28, DOI: https://doi.org/10.1017/S0022112099008976, 2000.

[3] J. D. Jr. Anderson. Ludwig prandtl's boundary layer. *American Institute of Physics Journal*, 58(12):42, DOI: https://doi.org/10.1063/1.2169443, 2005.

[4] T. Appel, E. Cooke, S. Mughal, and R. Ashworth. Biglobal stability analysis of swept-wing boundary layers with forward and backward facing steps. *IUTAM Paper (in review)*, 2020.

[5] D. Arnal and C. Casalis. Laminar-turbulent transition prediction in three-dimensional flows. *Progress in Aerospace Sciences Journal*, 36(2):173–191, DOI: https://doi.org/10.1016/S0376–0421(00)00002–6, 2002.

[6] R. Ashworth and S. Mughal. Modeling three dimensional effects on cross flow instability from leading edge dimples. *ScienceDirect Journal*, 14:201–210. DOI: https://doi.org/10.1016/j.piutam.2015.03.041, 2015.

[7] R. Ashworth, S. Lawson, R. Lowry, A. Martinez-Cava, S. Mughal, H. Roland, and C. Thomas. Numerical and experimental study of the tolerance of natural laminar flow on a wing to ts destabilisation at the leading edge /wing-box junction. *Royal Aeronautical Society Applied Aerodynamics Paper*, pages 336–349, July 2016.

[8] P. Balakumar, R. A. King, and J. Eppink. Effects of forward- and backward-facing steps on the crossflow receptivity and stability in supersonic boundary layers. *AIAA Paper*, 2639:DOI: https://doi.org/10.2514/6.2014–2639, 2014.

[9] D. Barkley, M. G. M. Gnomes, and R. D. Henderson. Three-dimensional instability in flow over a backward-facing step. *JFM*, 473:167–190, DOI: https://doi.org/10.1017/S002211200200232X, 2002.

[10] N. Beck, T. Landa, A. Seitz, L. Boermans, Y. Liu, and R. Radespiel. Drag reduction by laminar flow control. *Energies Journal*, 11(252):DOI: 10.3390/en11010252, 2018.

[11] H. Bippes. Basic experiments on transition in three-dimensional boundary layers dominated by crossflow instability. *Progress in Aerospace Sciences Journal*, 35 (4):363–412, DOI: https://doi.org/10.1016/S0376–0421(99)00002–0, 1999.

[12] M. S. Broadhurst and S. J. Sherwin. The parabolised stability equations for 3d-flows: Implementation and numerical stability. *Applied Numerical Mathematics*, 58(7):DOI: https://doi.org/10.1016/j.apnum.2007.04.016, 2008.

[13] C. D. Cantwell, D. Moxey, A. Comerford, A. Bolis, G. Rocco, G. Mengaldo, D. De Grazia, S. Yakovlev, J.-E. Lombard, D. Ekelschot, B. Jordi, H. Xu, Y. Mohamied, C. Eskilsson, B. Nelson, P. Vos, C. Biotto, R. M. Kirby, and S. J. Sherwin. Nektar++: An open-source spectral/hp element framework. *Computer Physics Communications*, 192:205–219, DOI: https://doi.org/10.1016/j.cpc.2015.02.008, 2015.

[14] C. Chang, M. R. Malik, G. Erlebacher, and M. Y. Hussaini. Linear and nonlinear pse for compressible boundary layers. Technical Report 93-70, NASA, 1993.

[15] E. E. Cooke, M. S. Mughal, S. J Sherwin, R. Ashworth, and S. Rolston. Destabilization of stationary and traveling crossflow disturbances due to steps over a swept wing. *AIAA Paper*, (3533):DOI: https://doi.org/10.2514/6.2019–3533, 2019.

[16] E. E. Cooke, M.S. Mughal, S. J Sherwin, R. Ashworth, and S. Rolston. Destabilisation of stationary and travelling crossflow disturbances due to forward and backward facing steps over a swept wing. *IUTAM Paper (in review)*, 2019.

[17] M. Costantini, S. Risius, and C. Klein. Experimental investigation of the effect of forward-facing steps on boundary layer transition. *IUTAM Paper*, 14:152–162, DOI: https://doi.org/10.1016/j.piutam.2015.03.036, 2015.

[18] D. DeGrazia. *Three-dimensional discontinuous spectral/hp element methods for compressible flows*. PhD thesis, Imperial College London, 2016.

[19] H. Deyhle and H. Bippes. Disturbance growth in an unstable three-dimensional boundary layer and its dependence on environmental conditions. *JFM*, 316(73): 114, DOI: https://doi.org/10.1017/S0022112096000456, 1996.

[20] S. S. Diwan and O. N. Ramesh. On the origin of the inflectional instability of a laminar separation bubble. *JFM*, 629:263–298, DOI: https://doi.org/10.1017/S002211200900634X, 2009.

[21] DLR. *TAU-Technical documentation of the DLR TAU-code*. Institute of Aerodynamics and Flow Technology, Braunshweig, 2011.2.0. edition, 2011.

[22] S. Dong, G. Karniadakis, and C. Chryssostomidis. A robust and accurate outflow boundary condition for incompressible flow simulations on severely-truncated unbounded domains. *Journal of Computational Physics*, 216:83–105, DOI: 10.1016/j.jcp.2013.12.042, 2013.

[23] P. W. Duck, A. Ruban, and C. N. Zhikharev. The generation of tollmien-schlichting waves by free-stream turbulence. *J. Fluid Mechanics*, 312:341–371, DOI: https://doi.org/10.1017/S0022112096002042, 1996.

[24] G. T. Duncan Jr., B. K. Crawford, M. W. Tufts, W. S. Saric, and H. L. Reed. Effects of step excrescences on a swept wing in a low-disturbance wind tunnel. *AIAA Paper*, (0910):DOI: https://doi.org/10.2514/6.2014–0910, 2014.

[25] J. Eppink. *THE INTERACTION OF CROSSFLOW INSTABILITIES AND A BACKWARD FACING STEP IN SWEPT BOUNDARY LAYER TRANSITION*. PhD thesis, Tufts University, 2014.

[26] J. Eppink. Stereo particle image velocimetry measurements of transition downstream of a forward-facing step in a swept-wing boundary layer. *AIAA Paper*, (0306):DOI: https://doi.org/10.2514/6.2017–0306, 2017.

[27] J. Eppink. The effect of forward-facing steps on stationary crossflow instability growth and breakdown. *AIAA Paper*, (0817):DOI: https://doi.org/10.2514/6.2018–0817, 2018.

[28] J. Eppink and C. Casper. Effects of forward-facing step shape on stationary crossflow instability growth and breakdown. *AIAA Paper*, (3532):DOI: 10.2514/6.2019–3532, 2019.

[29] J. Eppink and C-S. Yao. Time resolved stereo particle image velocimetry measurements of the instabilities downstream of a backward-facing step in a swept-wing boundary layer. *AIAA Paper*, (4415):https://doi.org/10.2514/6.2017–4415, 2017.

[30] J. Eppink, R. W. Wlezien, R. A. King, and M. M. Choudhari. The interaction of a backward-facing step and crossflow instabilities in boundary-layer transition. *AIAA Paper*, (0273):DOI: https://doi.org/10.2514/6.2015–0273, 2015.

[31] J. Eppink, R. W. Wlezien, R. A. King, and M. M. Choudhari. Influence of a backward-facing step on swept-wing boundary-layer transition. *AIAA Journal*, 57(1):DOI: https://doi.org/10.2514/1.J057437, 2019.

[32] J. H. Ferziger and Perić. *Computational Methods for Fluid Dynamics*. Springer, 2002.

[33] K. D. Fong, X. Wang, and Zhong. X. Numerical simulation of roughness effect on the stability of a hypersonic boundary layer. *Computers and Fluids*, 96:350–367, DOI: https://doi.org/10.1016/j.compfluid.2014.01.009, 2014.

[34] M. Gaster. The structure and behaviour of laminar separation bubbles. Tech Report: Reports and Memoranda 3595, Aeronautical Research Council, 1967.

[35] M. E. Goldstein. Scattering of acoustic waves into tollmien-schlichting waves by small streamwise variations in surface geometry. *JFM*, 154:509–529, DOI: https://doi.org/10.1017/S0022112085001641, 1985.

[36] E. R. Gowree, M. S. Mughal, E. E. Cooke, H. Xu, and C. J. Atkin. Linear and non-linear insability of tollmien-schlichting waves over a localised three-dimensional surface indentation. Underconsideration for publification in JFM.

[37] K. J. Groot, J. Serpieri, F. Pinna, and M. Kotsonis. Secondary crossflow instability through global analysis of measured base flows. *JFM*, 846:605–653, DOI: https://doi.org/10.1017/jfm.2018.253, 2018.

[38] M. GUBISCH. Analysis: Why airbus foresees laminar wings on next-gen aircraft, July 2018. URL https://www.flightglobal.com/news/articles/analysis-why-airbus-foresees-laminar-wings-on-next-448911.

[39] J. L. Guermond and J. Shen. A new class of truly consistent splitting schemes for incompressible flows. *Journal of Computational Physics*, 192(1):262–276, DOI: 10.1016/j.jcp.2003.07.009, 2003.

[40] P. Hall, M. R. Malik, and D. I. A. Poll. On the stability of an infinite swept attachment line boundary layer. *The Royal Society Journal*, 395(1809):DOI: https://doi.org/10.1098/rspa.1984.0099, 1984.

[41] D. A. Hammond and L. G. Redekopp. Local and global instability properties of separation bubbles. *European JFM*, 17(2):145–164, DOI: https://doi.org/10.1016/S0997–7546(98)80056–3, 1998.

[42] R. Hartmann. Discontinuous galerkin methods for compressible flows: higher order accuracy, error estimation and adaptivity. In *DLR: VKI Lecture Series*, pages 1–50, https://elib.dlr.de/44203/, 2005.

[43] M. A. Z. Hasan. The flow over a backward-facing step under controlled perturbation : laminar separation. *JFM*, 238:73–96, DOI: https://doi.org/10.1017/S0022112092001642, 1992.

[44] T. Herbert. Stability and transtion on swept wings. Technical report, Defense Technical Information Centre, DOI: 10.2514/6.1993-78, 1994.

[45] T. Herbert. Parabolized stability equations. *Ann. Rev. Fluid Mech. Journal*, 29: 245–283, DOI: https://doi.org/10.1146/annurev.fluid.29.1.245, 1997.

[46] S. Hosseinverdi and H. F. Fasel. Numerical investigation of laminar–turbulent transition in laminar separation bubbles: the effect of free-stream turbulence. *JFM*, 858:714–759, DOI:10.1017/jfm.2018.809, 2018.

[47] P. Huerre and P. Monkewitz. Absolute and convective instabilities in free shear layers. *JFM*, (159):151–168, DOI: https://doi.org/10.1017/S0022112085003147, 1985.

[48] G. Karniadakis and S. J Sherwin. *Spectral h/p element methods for CFD*. Oxford University Press, 1999.

[49] G. E. Karniadakis, M. Israeli, and S. A. Orszag. High-order splitting methods for the incompressible navier-stokes equations. *Journal of Computational Physics*, 97(2):414–443, DOI: https://doi.org/10.1016/0021–9991(91)90007–8, 1991.

[50] H. B. Keller and T. Cebeci. Accurate numerical methods for boundary-layer flows. ii: Two-dimensional turbulent flows. *AIAA Paper*, 10(9):DOI: https://doi.org/10.2514/3.50349, 1972.

[51] P. S. Klebanoff, D. Tidstrom, K., and L. M. Sargent. The three-dimensional nature of boundary-layer instability. *JFM*, 12(1):1–34, DOI: https://doi.org/10.1017/S0022112062000014, 1962.

[52] Fei Li and M. R. Malik. On the nature of PSE approximation. *Theoretical and Computational Fluid Dynamics*, 8(4):253–273, 1996.

[53] M.R. Malik and Chang CL. Li F. Nonlinear crossflow disturbances and secondary instabilities in swept-wing boundary layers. *IUTAM Paper in Fluid Mechanics and Its Applications*, 35:257–266, 1996.

[54] C. B. Moler and G. W. Stewart. An algorithm for generalized matrix eigenvalue problems. *SIAM Journal on Numerical Analysis*, 10(2):241–256, DOI: https://doi.org/10.1137/0710024, 1973.

[55] M. V. Morkovin. Experiments on transition enhancement by distributed roughness. *Physics of Fluids Paper*, 29(10):DOI: https://doi.org/10.1063/1.865838, 1986.

[56] M. V. Morkovin. Recent insights into instability and transition to turbulence in open-flow systems. Technical Report NASA-CR-181693, ICASE-88-44, NAS 1.26:181693, NASA Langley Research Centre, 1988.

[57] D. Moxey. *Spatio-Temporal Dynamics in Pipe Flow*. PhD thesis, University of Warwick, 2011.

[58] S. M. Mughal. Active control of wave instabilities in three-dimensional compressible flows. *Theoretical and Computational Fluid Dynamics*, 12(4):195–217, DOI: 10.1007/s001620050106, 1998.

[59] S. M. Mughal. Advanced transition prediction – development of linearised navier-stokes receptivity methods, validation and application. *EADS: Institute for Mathematical Sciences*, 2011.

[60] S. M. Mughal. *CoPSE/BL-MiPSecR User Manual*. Imperial College London, 2015.

[61] S. M. Mughal and R. Ashworth. Uncertainty quantification based receptivity modelling of crossflow instabilities induced by distributed surface roughness in swept wing boundary layers. *AIAA Paper*, (3106):DOI: https://doi.org/10.2514/6.2013–3106, 2013.

[62] J. P. Nenni and G. L. Gluyas. Aerodynamic design and analysis of an lfc surface. *Astronautics and Aeronautics*, 1966.

[63] P. Paredes, V. Theofilis, D. Rodríguez, and J. A. Tendero. The pse-3d instability analysis methodology for flows depending strongly on two and weakly on the third spatial dimension. *AIAA Paper*, pages DOI:10.2514/6.2011–3752, 2011.

[64] D. Park and S. O. Park. Influence of two-dimensional smooth humps on linear and non-linear instability of a supersonic boundary layer. *Computers and Fluids*, 79:140–149, DOI: https://doi.org/10.1016/j.compfluid.2013.03.018, 2013.

[65] D. Park and S. O. Park. Linear and non-linear stability analysis of incompressible boundary layer over a two-dimensional hump. *Computers and Fluids*, 73:80–96, DOI: https://doi.org/10.1016/j.compfluid.2012.12.007, 2013.

[66] J. Peiró and S. J. Sherwin. *FINITE DIFFERENCE, FINITE ELEMENT AND FINITE VOLUME METHODS FOR PARTIAL DIFFERENTIAL EQUATIONS*, pages 2415–2446. Springer, 2005.

[67] J. Perraud. Effects of steps and gaps on 2d and 3d transition. In *European Congress on Computational Methods in Applied Sciences and Engineering*, pages 11–14, 2000.

[68] J. Perraud, D. Arnal, A. Séraudie, and D. Tran. Laminar-turbulent transition on aerodynamic surfaces with imperfections. *: Int. J. Engineering Systems Modelling and Simulation*, 6(3/4):162–170, DOI: 10.13140/RG.2.1.3532.1364, 2004.

[69] J. Perraud, D. Arnal, and W. Kuehn. Laminar-turbulent transition prediction in the presence of surface imperfections. *International Journal of Engineering Systems Modelling and Simulation*, DOI: 10.1504/IJESMS.2014.063129, 2014.

[70] R. H. Jr. Radeztsky, M. S. Reibert, and W. S. Saric. Effect of isolated micron-sized roughness on transition in swept-wing flows. *AIAA Journal*, 37(11):DOI: https://doi.org/10.2514/2.635, 1999.

[71] H. Raposo, S Mughal, and R. Ashworth. Acoustic receptivity and transition modeling of tollmien-schlichting disturbances induced by distributed surface roughness. *Physics of Fluids Journal*, 30(1070-6631):DOI: https://doi.org/10.1063/1.5024909, 2018.

[72] H. L. Reed and W. S. Saric. Stability of three dimensional boundary layers. *Ann. Rev. Fluid Mech. Journal*, 21:235 – 284, DOI: https://doi.org/10.1146/annurev.fl.21.010189.001315, 1989.

[73] H. L. Reed and W. S. Saric. Linear stability theory applied to boundary layers. *Ann. Rev. Fluid Mech. Journal*, 28:389–428, DOI: https://doi.org/10.1146/annurev.fl.28.010196.002133, 1996.

[74] H. L. Reed, E. Reshotko, and W. S. Saric. Receptivity: The inspiration of Mark Morkovin. *AIAA Paper*, (2471):DOI: https://doi.org/10.2514/6.2015–2471, 2015.

[75] D. P. Rizzetta and M. R. Visbal. Numerical simulation of excrescence generated transition. *AIAA Journal*, 52(2):385–397, DOI: https://doi.org/10.2514/1.J052530, 2014.

[76] D. Rodríguez and V. Theofilis. Structural changes of laminar separation bubbles induced by global linear instability. *JFM*, 655:280–305. DOI: 10.1017/S0022112010000856, 2010.

[77] D. Rodríguez, E. M. Gennaro, and M. P. Juniper. The two classes of primary modal instability in laminar separation bubbles. *JFM*, 737:DOI: https://doi.org/10.1017/jfm.2013.504, 2013.

[78] A. Ruban. On the generation of tollmien-schlichting waves by sound. In *Laminar-Turbulent Transition*, pages 313–320. Springer, Berlin, Heidelberg, 1984.

[79] A. Ruban. *Fluid Dynamics Part 3 : Boundary Layers*. Oxford University Press, 2017.

[80] A. Ruban and J. S. B. Gajjar. *Fluid Dynamics Part 1 : Classical Fluid Dynamics*, volume First Edition. Oxford University Press, 2014.

[81] T. I. Saeed and J. F. Morrison. 2d roughness effects on crossflow instabilities. *Transition and Shear Flow Phenomena Paper*, 2019.

[82] T. I. Saeed, S. M. Mughal, and J. F. Morrison. The interaction of a swept-wing boundary layer with surface excrescences. *AIAA Paper*, (2065):DOI: https://doi.org/10.2514/6.2016–2065, 2016.

[83] W. S. Saric. Görtler vortices. *Annual Review of Fluid Mechanics*, 26:379–409, DOI: https://doi.org/10.1146/annurev.fl.26.010194.002115, 1994.

[84] W. S. Saric, H. L. Reed, and E. J. Kerschen. Boundary-layer receptivity to freestream disturbances. *Ann. Rev. Fluid Mech.*, 34:291–319, DOI: https://doi.org/10.1146/annurev.fluid.34.082701.161921, 2002.

[85] W. S. Saric, H. L. Reed, and E. B. White. Stability and transition of three-dimensional boundary layers. *Ann. Rev. Fluid Mech.*, 35:413–440, DOI: https://doi.org/10.1146/annurev.fluid.35.101101.161045, 2003.

[86] G. B. Schubauer and P. S. Klebanoff. Contributions on the mechanics of boundary-layer transition. Technical Report NACA-TR-1289, NASA Technical Reports Server, 1956.

[87] J. Serpieri and M. Kotsonis. Three-dimensional organisation of primary and secondary crossflow instability. *JFM*, 799:200–245, DOI: https://doi.org/10.1017/jfm.2016.379, 2016.

[88] A. M. O. Smith and A. H. Gamberoni. Transition, pressure gradient and stability theory. Technical Report No. ES26388, Douglas Aircraft Co. Rep, 1956.

[89] A. F. Sumariva, J and S. Hein. Adaptive harmonic linearized navier-stokes equations used for boundary-layer instability analysis in the presence of large streamwise gradients. *AIAA Paper*, (1548):DOI: https://doi.org/10.2514/6.2018–1548, 2018.

[90] A. F. Sumariva, J, S. Hein, and E. Valero. Effect of humps and indentations on boundary-layer transition of compressible flows using the ahlns methodology. *7th European Conference on Computational Fluid Dynamics*, 18.

[91] R. Sunderland and D. Sawyers. Evaluation of aerast large scale wind-tunnel test results. Technical report, Airbus, 2009.

[92] J. Tannehill, J. Miller, and S. Lawrence. Iterative pns algorithms for solving 3-d supersonic flows with upstream influences. *AIAA Paper*, (0821):DOI: https://doi.org/10.2514/6.2000–821, 2000.

[93] V. Theofilis, S. Hein, and U. Dallmann. On the origins of unsteadiness and three-dimensionality in a laminar separation bubble. *Proceedings of the Royal Society*, 358:3229–3246, DOI: https://doi.org/10.1098/rsta.2000.0706, 2000.

[94] C. Thomas, S. Mughal, H. Roland, R. Ashworth, and A. Martinez-Cava. The effect of gap deformations on the stability of TS wave disturbances. *AIAA Journal*, 56(6):2157–2165, DOI: https://doi.org/10.2514/1.J056821, 2017.

[95] M. W. Tufts, H. L. Reed, Crawford B. K., G. T. Duncan Jr., and W. S. Saric. Computational investigation of step excrescence sensitivity in a swept-wing boundary layer. *AIAA Journal*, 54(2):602–626, DOI: https://doi.org/10.2514/1.C033892, 2017.

[96] J. L. Van Ingen. A suggested semi-empirical method for the calculation of the boundary layer transition region. Technical Report VTH-74, Delft University of Technology, 1956.

[97] O. Vermeersch and D. Arnal. Klebanoff-mode modeling and bypass-transition prediction. *AIAA Journal*, 48(11):DOI: 10.2514/1.J050002, 2010.

[98] A. F. R. Vidales, M. Kotsonis, A. Antunes, and R. Cosin. Effect of two-dimensional surface irregularities on swept wing transition: Forward facing steps. *AIAA Paper*, (3075):DOI: https://doi.org/10.2514/6.2018–3075, 2018.

[99] P. E. Vincent and A. Jameson. Facilitating the adoption of unstructured high-order methods amongst a wider community of fluid dynamicists. *Mathematical Modelling of Natural Phenomena Journal*, 6(3):97–140, 2011.

[100] Y. Wang and M. Gaster. Effect of surface steps on boundary layer transition. *Experiments in Fluids*, 39(4):679–686, 2005.

[101] J. H. Watmuff. Evolution of a wave packet into vortex loops in a laminar separation bubble. *JFM*, 397:119–169, DOI: https://doi.org/10.1017/S0022112099006138, 1999.

[102] J. H. Watmuff, D. A. Pook, T. Sayadi, and X. Wu. Fundamental physical processes associated with bypass transition. *Physics of Fluids Journal*, 2010.

[103] A. Wörner, U. Rist, and S. Wagner. Humps/steps influence on stability characteristics of two-dimensional laminar boundary layer. *AIAA Journal*, 41(2): 192–197, DOI: https://doi.org/10.2514/2.1960, 2003.

[104] X. Wu and M. Dong. A local scattering theory for the effects of isolated roughness on boundary-layer instability and transition: transmission coefficient as an eigenvalue. *JFM*, 794:68–108, DOI: https://doi.org/10.1017/jfm.2016.125, 2016.

[105] X. Wu and L. W. Hogg. Acoustic radiation of tollmien–schlichting waves as they undergo rapid distortion. *JFM*, 550:307–347. doi:10.1017/S0022112005008220, 2006.

[106] H. Xu, J. W. Lombard, and S. J. Sherwin. Influence of localised smooth steps on the instability of a boundary layer. *JFM*, 817:138–170, DOI: https://doi.org/10.1017/jfm.2017.113, 2016.

[107] H. Xu, S. M. Mughal, E. R. Gowree, C. J. Atkin, and S. J. Sherwin. Destabilisation and modification of tollmien–schlichting disturbances by a three-dimensional surface indentation. *J. Fluid Mechanics*, 819:592–620, 2017.

[108] D Zhao. *INSTABILITY AND RECEPTIVITY OF BOUNDARY LAYERS ON CONCAVE SURFACES AND SWEPT WINGS*. PhD thesis, Imperial College London, 2011.